Contribution to the Modelling and Simulation of Aircraft Structures Impacting on Water

A thesis accepted by the Faculty of Aerospace Engineering and Geodesy of the Universität Stuttgart in partial fulfilment of the requirements for the degree of Doctor of Engineering Sciences (Dr.-Ing.)

by

Nathalie Renée Solange Toso

born in Saint-Dié, France

Main referee:	Prof. Franz Joseph Arendts
Co-referee:	Prof. Dr.-Ing. Siegfried Wagner
Date of defence:	22nd July 2009

Institute of Aircraft Design
Universität Stuttgart
2009

Acknowledgements

I acknowledge the German Aerospace Center (DLR) and in particular the Institute of Structures and Design in Stuttgart for making this work possible and for their financial support.

I would like to also thank the Zonta committee and the members of the Fakultät Luft- und Raumfahrt und Geodäsie, Universität Stuttgart for delivering me respectively an Amelia Earhardt grant and a Hermann-Reissner-Stipendium, which supported me during the starting phase of this thesis and without which this work would have never taken place.

I am particularly grateful to my supervisor Prof. Dipl.-Ing Franz Joseph Arendts, former director of the Institute of Aircraft Design, for his confidence in my work, his constant support and being the principal examiner. Additionally, I acknowledge Prof. Dr Siegfried Wagner, former director of the Institute of Aerodynamics and Gasdynamics for accepting to act as a co-examiner.

I am grateful to Christof Kindervater who enabled me to start the topics in the "Structural Integrity" department and provided me the opportunity to carry out this work with considerable freedom.

I would like to express my deep gratitude to Dr Alastair Johnson for his valuable advices and tips, for the constructive discussions during the whole work and finally for the useful comments on the manuscript.

My thanks also belong to Dr Paul Groenenboom and Dr Argiris Kamoulakos from ESI Group for their technical and scientific support concerning the use of the FE software.

I am thankful to my colleagues of the "Structural Integrity" department for bearing me and for contributing to the pleasant working atmosphere.

Finally, I especially thank my parents for their confidence in my capacities and my husband Yves for his encouragement and patience during the writing phase of the thesis in the last months.

To our son Sascha

Contents

Abbreviations

AC	Advisory Circular
ALE	Arbitrary Lagrange Euler
APP	Approach
BLI / BLO	Butt Line In / Butt Line Out
CARAT	Computer Aided Research Analysis Tool
CAST	Crashworthiness of Helicopters on water: Design of Structures Using Advanced Simulation Tools (EU Project)
CFC60	Channel Frequency Class Filter (cut-off frequency: 100 Hz)
CFC180	Channel Frequency Class Filter (cut-off frequency: 300 Hz)
CFC600	Channel Frequency Class Filter (cut-off frequency: 1000 Hz)
CFIT	Controlled Flight Into terrain
COG	Centre of Gravity
CRASURV	Commercial Aircraft Design for Crash Survivability (EU Project)
DLR	Deutsches Zentrum für Luft- und Raumfahrt
DRI	Dynamic Response Inc.
EOS	Equation of State
FAA	Federal Aviation Administration
FAR	Federal Airworthiness Regulations
FE	Finite Element
FEM	Finite Element Method
FVM	Finite Volume Method
FSI	Fluid Structure Interaction
JAR	Joint Aviation Requirements
LDG	Landing
NACA	National Advisory Committee for Aeronautics
RHOSS	Review of Helicopter Offshore Safety and Survival
SPH	Smoothed Particle Hydrodynamics
STN	Station
T/O	Take-off
VOF	Volume fraction (method)

Abstract

The impact on water of aeronautical structures is of concern as soon as an aircraft is designed to operate over sea. For the need of the ditching certification, it can be summarised that the structure should be able to land on water and float long enough to enable the passengers and crew members to evacuate. Until the middle of the 90's, compliance to the regulations was mainly shown by tests performed in a basin using a mock-up structure completed by relative simple theoretical evaluations often based on in-house knowledge.

Due to the enormous improvement in computational capacity and simulation tools in the last decade, crashworthiness investigations are increasingly conducted through numerical analysis in order to support the testing activities. From the industrial point of view, this means a reduction of cost because the number of tests can be significantly reduced. In addition, numerical investigations offer the possibility to virtually optimise the structural design before any manufacturing, and considerably diminish the risk of any mistakes at test. The development phase is then favourably shortened. To support this trend in A/C design, it is proposed in this work to develop and validate numerical methodologies to assess the specific behaviour of aeronautical structures at impact on water.

In a first phase, the various aspects of ditching in aeronautics are addressed in order to fix the context. This comprises statistical analysis of accident conditions, a discussion concerning the typical damage observed in a ditching event, themes relevant to the certification and finally a description of current practices in the industry to show compliance with the regulations.

Due to the inter-disciplinary character of the subject, a full chapter is devoted to the extensive review of the knowledge concerning the assessment and the modelling of fluid structure interaction. This part gathers the knowledge from various disciplines including ship building and offshore technologies. Valuable analytical works started in the 30's considering the impact of rigid bodies (wedge, cone) on water are presented. To complete the state of the art, two hybrid techniques involving simple but effective numerical treatments in use in the industry are described. Finally, the capabilities and problems of current advanced numerical methods (ALE, general Euler/Lagrange coupling) emerging on the market and able to treat simple problems of impact on water are discussed.

Based on the various aspects discussed above, this thesis proposes to treat the modelling of water/structure interaction problems by using a fully Lagrangian formulation, which has already proved its robustness in the general resolution of crashworthiness problems. To that aim, the classical finite-element (FE) method and the meshless Smoothed Particle Hydrodynamic (SPH) techniques, especially suitable for problems dealing with large deformations, are applied for the modelling of the water. In addition two material models basing on an elastic plastic hydrodynamic law and on a Murnaghan equation of state are adjusted to describe the specific behaviour of water with a structural explicit code. Various methodologies involving a pure FE mesh and a combined SPH-FE mesh are investigated and their domains of validity examined in an extensive benchmark study. This latter comprises various body shapes (wedges with various deadrise angles, cylinder, spheres with various

radius) impacting on water, for which test results are available in the literature. Finally, modelling guidelines and recommendations for the use of the various strategies are listed.

The methodologies and strategies previously investigated on rigid bodies are then applied to real full-scale aeronautical structures, which were “crashed” on water. In the first part, a WG30 metallic sub-floor structure and a full-scale WG30 helicopter are simulated when impacting vertically on water. The challenge of these simulations is to model the damage and energy absorbing capabilities of these complex structures while impacting on water. Based on the available test results comprising acceleration time histories, pressure time histories and observation on the crash components, it is possible to analyse in details the degrees of correlation between the simulation and the test results. In particular, specific problems (air cushioning effects) relating to the measurement of pressures on the structure are addressed from both test and computational point of view. In a second part, a local/global methodology combining FE and hybrid techniques is investigated for the ditching case involving a forward velocity at impact. In this work, the feasibility of the methodology is shown by applying it to the case of a full-scale transport aircraft. Unfortunately, validation work could not be conducted because no test data are available. The simulation of the landing on water of an aircraft, where the forward speed is large compared to the vertical speed remains a challenge due to the size of the overall models, which can hardly be treated for computational reasons (large running time, large models for the water basin). This problem is accentuated when very detailed structural FE-models have to be investigated, which are necessary to model local damage.

Nevertheless, based on a ditching test campaign conducted with various scaled rigid fuselage shapes, it was possible to simulate a test with a combined FE-SPH mesh. This shows that the consideration of additional physical effects like suction forces to capture the kinematics of the ditching event are necessary. These forces, which act at the structure/water interface, are caused by phenomena of cavitation, whose magnitude depends on the impact velocity and on the fuselage shape at the point of impact. Additional effects such as the phenomena of ventilation may also be important but cannot be included in the current analysis, because air entrapped between the structure and the water surface is not taken into account in the modelling.

Zusammenfassung

Der Wasseraufschlag einer Luftfahrtstruktur soll systematisch betrachtet werden sobald diese über Wasser eingesetzt wird. Zur Zertifizierung lässt sich der Wasseraufschlag wie folgt zusammenfassen: Flugzeug/Hubschrauber sollen in der Lage sein, auf dem Wasser zu landen und lang genug schwimmen, damit Passagiere und Besatzung evakuiert werden können. Bis in die 90er Jahre wurde die Erfüllung der Vorschriften hauptsächlich über experimentelle Tests mit einem Mock-up-Modell in einem Wasserbecken nachgewiesen. Begleitende theoretische Untersuchungen wurden auf der Basis von firmeninternen Erfahrungen/ Kenntnissen durchgeführt.

Aufgrund erheblicher Fortschritte im Computerbereich und in der Simulationstechnik der letzten zehn Jahre, erfolgten Crash-Untersuchungen immer mehr durch numerische Analysen, um die Testaktivitäten zu unterstützen. Vom industriellen Standpunkt her bedeutet diese Vorgehensweise eine Verminderung der Entwicklungskosten, da die Anzahl an Tests stark reduziert werden kann. Zusätzlich ermöglichen die Simulationswerkzeuge, die konstruktive Bauweise der Strukturen vor dem Beginn der Fertigung zu optimieren. Dadurch wird das Risiko eines Misserfolges minimiert und die Entwicklungsphase verkürzt. Um diesen Trend zu verfolgen, ist es das Ziel der vorliegenden Dissertation, eine numerische Methodik zu entwickeln und zu validieren, um das spezifische Verhalten einer Luftfahrtstruktur beim Wasseraufschlag zu ermitteln.

Zu Beginn der Arbeit werden praktische Aspekte des Ditchings (Wasseraufschlag) diskutiert. Darunter zählen statistische Untersuchungen von Ditching-Ereignissen, ein Katalog der typischen Schädigungen infolge des Wasseraufschlags, Themen relativ zu der Zertifizierung und eine Beschreibung der Vorgehensweise bzw. Praxis der Industrie, wie die Vorschriften dort erfüllt werden.

Wegen des interdisziplinären Charakters des Themas, dient ein weiteres ausführliches Kapitel dazu, einen Überblick der Kenntnisse im Bereich Bewertung und Modellierung der Fluid/Struktur Interaktion zu schaffen. Es erfasst verschiedene Disziplinen, einschließlich Schiffbau und Meerestechnik. Wertvolle analytische Arbeiten, beginnend in den 30er Jahren hinsichtlich des Aufschlages auf Wasser von einfachen starren Körpern (Keil, Konus, Kugel) werden dabei dargestellt. Als Ergänzung zum Stand der Wissenschaft im Modellierungsbereich werden hybride Techniken erläutert. Diese Verfahren auf der Basis einfacher, aber effektiver numerischer Bearbeitung finden Anwendung in der Industrie. Letztlich werden das Potential und die Probleme von aktuellen, fortgeschrittenen Techniken (ALE, Euler/Lagrange- Kopplung), die das Problem des Impacts auf Wasser berechnen können, ausdiskutiert.

Mit Hilfe der im vorherigen Kapitel erörterten Ausführungen zum Ditching-Thema, wird in dieser Arbeit die Modellierung der Fluid/Struktur-Interaktionen mit Lagrange-Formulierungen durchgeführt und ausführlich untersucht. Grund dieser Wahl ist die Robustheit der Technik bei der Ermittlung des Aufnahmevermögens der Aufprallenergie von Strukturen. Zwei Techniken für die Modellierung des Wassers werden eingesetzt: die

klassische Finite-Elemente (FE) Methode und die netzfreie Smoothed Particle Hydrodynamics Technik (SPH). Letztere hat sich bei Problemen mit starken Verformungen bewährt. Zusätzlich werden zwei Materialmodelle, basierend auf einem elastisch-plastisch hydrodynamischen Gesetz und auf einer Murnaghan-Zustandgleichung angewandt, um das spezifische „mechanische“ Verhalten von Wasser in einem expliziten Programm zur Strukturberechnung anzupassen. Verschiedene Methodiken, in denen reine FE und FE-SPH kombiniert eingesetzt werden, werden untersucht und ihr Gültigkeitsbereich anhand einer aufwendigen Benchmark-Studie geprüft. Im Besonderen wurde der Aufschlag auf Wasser von Körpern mit einfacher Geometrie (Keil mit verschiedenen Öffnungswinkeln, Zylinder und Kugel mit verschiedenen Durchmessern) anhand dieser Methodiken rechnerisch ermittelt und mit Testdaten verglichen. Zum Schluss dieser Studie werden Modellierungsrichtlinien und Empfehlungen für die Benutzung der einzelnen numerischen Strategien aufgelistet.

Die verschiedenen Methodologien, die mit einfachen starren Körpern bewertet wurden, werden dann auf verschiedene Luftfahrtstrukturen angewendet, die auf das Wasser aufschlagen.

In einer ersten Studie wird zuerst die metallische Unterbodenstruktur, daran anschließend der komplette WG30-Hubschrauber in Originalgröße beim vertikalen Aufschlag auf das Wasser simuliert. Die Herausforderung dieser Simulationen liegt in der Tatsache, das Schädigungsbild und das Aufnahmevermögen der Aufprallenergie der Struktur richtig zu erfassen. Aufgrund vorhandener Testdaten, Verzögerungs- und Druckkurven sowie Beobachtungen an den gecrashten Strukturen, ist es möglich, die Güte der Korrelation zwischen Test und Simulation zu diskutieren. Spezifische Probleme in Bezug auf die Druckmessungen (Luftkissen Effekt) auf der Struktur werden besprochen.

In einer zweiten Studie, wird eine lokale/globale Methodologie, die die FE Methode mit einer hybriden Technik kombiniert, auf den Wasseraufschlag angewendet und zwar für den speziellen Fall, in dem eine Längsgeschwindigkeit beim Impact vorhanden ist. Dazu wird die Übertragbarkeit auf ein Transportflugzeug in Realgröße geprüft. Leider konnte keine Validierung der Methodik durchgeführt werden, weil keine Testdaten vorhanden sind. Die Simulation des Verhaltens eines Luftfahrzeuges mit der FE Methode beim Ditching, in dem die Längskomponente der Geschwindigkeit viel größer als die entsprechende Vertikalkomponente ist, bleibt eine Herausforderung. Grund dafür ist die Größe des Gesamtmodells (Wasserbecken), das sehr lange Rechenzeiten erfordert. Diese Problematik wird verstärkt, wenn detaillierte Strukturmodelle untersucht werden sollen, damit lokales strukturelles Verhalten erfasst werden kann.

Dennoch war es mir möglich den Vorwärtsaufschlag auf Wasser anhand von Testergebnisse aus der Literatur unter Anwendung des kombinierten FE-SPH Netzes rechnerisch zu erforschen. Dies geschah in einer NACA-Versuchskampagne mit verschieden skalierten und starren Flugzeugrumpfmodellen. Es wird gezeigt, dass Saugkräfte auf die Impactfläche einwirken und als zusätzlich wirkender physikalischer Effekt betrachtet werden müssen. Ursache ist wahrscheinlich Kavitation, die von der Aufschlaggeschwindigkeit und der Form des Rumpfes beeinflusst wird. Zusätzliche Ventilationsphänomene werden vermutet, die aber im Simulationsmodell nicht berücksichtigt werden können, da die eingeschlossene Luftschicht, zwischen Struktur und Wasseroberfläche, nicht modelliert wird.

1 Introduction

1.1 Motivation

Even if the impact on water of an aircraft is fortunately a very rare event, it is nevertheless a case which should be covered for the certification of an aircraft operating over sea. In that case, the manufacturer should show compliance to the specific regulations relating to ditching, which can be roughly summarised as in the following: the aircraft should be able to land on water as safely as possible and to float long enough in order to enable the passengers to evacuate. For economic reason, the industry wants to fulfil these standards while limiting the very high test costs. Indeed proving the ability of an aircraft to "land" on water is a very expensive matter including extensive impact and floatation test campaigns with a scaled aircraft model. This latter should define a likely configuration or best a range of configurations, under which an aircraft is able to ditch.

From the crashworthiness point of view, loads applied to the structure during an impact on water are clearly different from those occurring during an impact on a rigid floor (Fig. 1-1). This fact eventually leads to the necessity of developing new or extra structural devices to increase the survivability of the passengers in case of an impact on water. On a rigid floor, the structure is loaded locally at the position of the bulkheads or the frames designed to absorb a part of the impact energy whilst in the case of an impact on water the load is distributed along the skin, which must transmit it to the energy absorbing structural components. As a matter of fact, a rupture of the skin or the inability of the skin to transmit the impact load would dangerously compromise the efficiency of the structural energy absorbing devices required for the safety of the occupants.

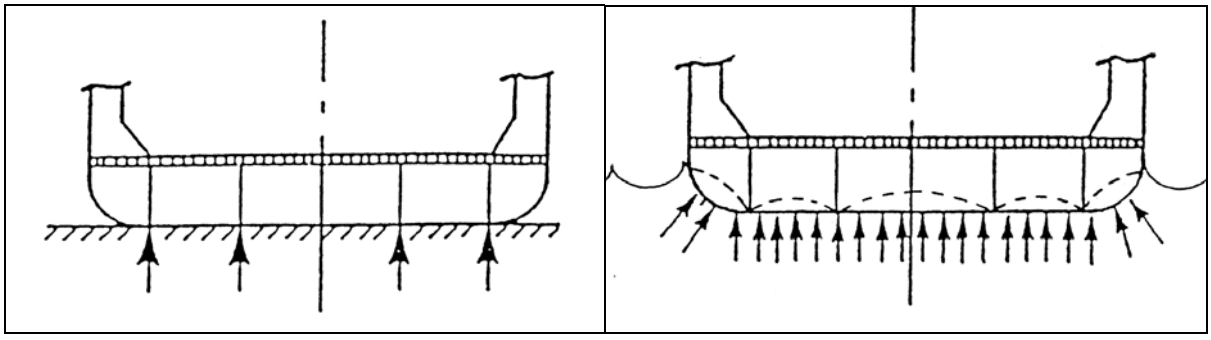

Figure 1.1: Comparison between impact on a rigid floor and on water [1]

The investigation of new crashworthy structures is intimately linked to the development and validation of simulation tools. As test campaigns are time-consuming and very expensive, the use of simulation tools capable of predicting the response of aeronautical components, or complete aircraft, to dynamic crash loads facilitates the development and the evaluation of new designs. Besides the fact that such simulation tools help to fix the final design, they decisively contribute to the determination of the test conditions and are therefore able to minimize the risk of a setback. Moreover, they offer through their flexibility the possibility to quantify the energy absorbing behaviour of the structure under various scenarios, which is not economically feasible through tests.

Present knowledge is still insufficient to predict with confidence a crashworthy design capable of coping with the impact on water. A reason for this is notably linked to the multi-disciplinary character of the problem including structural mechanics and fluid dynamics. Currently, the specific problems are firstly an insufficient knowledge of the phenomenon of impact on water in aeronautical structures, secondly the simulation limiting factors such as inadequate material models for crash investigation purposes, limited modelling possibilities for the fluid structure interaction and finally the absence of an extensive validation programme for the simulation tools.

1.2 Objectives and structure of the thesis

Since the middle of the 90's, the assessment of the safety standard for certification by simulation has been emerging in the crashworthiness area and is being extended to the specific problem of impact on water. The main objectives of this thesis are to contribute to the comprehension and to the evaluation of aeronautical structures impacting on water from the crashworthiness point of view. Within the framework of this thesis, numerical methodologies are developed and validated in order to simulate the impact of aircraft components or full-scale aircraft on water, in crash conditions relevant to the ditching event of aircraft and helicopters. In particular, the emphasis is put on the finite element and the smooth particle methods, which are common techniques used in the crash domain. The challenge is then to apply them to the specific domain of "crash on water" of real aeronautical structures.

The thesis has the following structure:

Chapter 2 points out the relevance of the impact on water in aeronautics. It analyses ditching data of the last five decades for fixed wing aircraft and rotorcraft. Ditching regulations and current certification procedures in practice are briefly reviewed in order to illustrate the expectations of the certification authorities and the industry.

Chapter 3 is devoted to the state of the art concerning the modelling of the impact on water. The physical background and complexity of the problem are introduced in relation to the problem of impact of aeronautical structures on water. Some analytical practices available in the literature and used in the ship building and offshore technologies are presented. Numerical codes basing on simplified water/structure interaction models are described in order to show their strengths and weaknesses. Finally the working principles of advanced numerical codes able to treat fluid/structure interaction problems are exposed and simulation results available in the literature discussed.

Chapter 4 deals with the use of fully Lagrangian formulations to model the water/structure interaction problems and constitutes the core contribution of this work to the subject of impact on water. It presents and validates various strategies to model the impact of structures on water using the pure finite element method and the smoothed particle hydrodynamic method. In addition two material models basing on an elastic plastic hydrodynamic law and on a Murnaghan equation of state to describe the water behaviour are investigated. The domain of validity of the methodologies is investigated in an extensive benchmark study involving

various body shapes impacting on water, for which test results are available in the literature. As a result, modelling guidelines were deduced.

Chapter 5 finally applies the strategies developed in Chapter 4 to real aeronautical structures, which deform under the water loads. In a first part, A WG30 sub-floor structure and a full-scale WG30 helicopter (Fig. 1-2) are simulated when impacting vertically on water. Based on the available test results, the quality of the simulations is extensively discussed. In a second part, a local/global methodology combining FE and hybrid techniques is investigated for the ditching case involving a forward velocity at impact. For this latter specific case, an additional analysis is performed in order to show the extent of the problem.

Chapter 6 summarises the main results of the work and discusses the achievements of the goals. Suggestions for further improvements are listed in the outlook.

Figure 1-2: Impact sequence of the full-scale WG30 helicopter [2]

2 Relevance of impact on water in aeronautics

2.1 Background

As many airports are close to water and many flights, not only transcontinental, happen partly overseas, impact on water is an event, which can be encountered by all aircraft. Like soft ground (sandy, ploughed), vegetation (e.g. trees), prepared surface (paved, hard dirt; gravel), etc …, water is also considered as a possible impact terrain. Due to its very special behaviour as impact environment, the event of impact on water has to be treated separately from the impact on hard ground in the certification phase of a new aircraft.

The event of impact on water can be classified into two categories: ditching (planned event) and unplanned impact on water. Ditching qualifies as an emergency/forced landing on water. Under these circumstances, the aircraft occupants have some time to prepare for the impact. Nevertheless, this preparation time can be, of course, very variable (from some minutes to half an hour). In contrast, when the impact on water is unplanned, the crew is not aware of the imminent crash. This very frequently means higher impact velocities, higher loads and damage and subsequently high probability for severe injury levels. Although unplanned ditching is less frequent than unplanned ground impact, it is more frequent than planned ditching.

In contrast to a ground impact accident, the quantity of information (e.g. fuselage remains) to reconstruct and analyse the chain of events, which have led to the impact on water, is often very small. When impact on water happens over an ocean, the hull of the aircraft sinks and is very rarely recovered from the ocean bed. In addition, there is very little post crash information for unplanned emergency landing on water in contrast to planned emergency landing, where communication into the cockpit and with the control deals with the upcoming impact event. The reasons for an impact on water, planned or unplanned, can be very diverse:

- controlled flight into terrain (CFIT),
- technical failure/maintenance error,
- crew incapacity (seldom in transport aircraft),
- unknown.

In the CFIT case, the crew is not aware of the situation and therefore of the imminent impact on water. The CFIT's have predictable components and result from a chain of inadequate actions or reactions to warning signals of the crew. When technical failure or maintenance error is concerned, the crew has to urgently land the aircraft due to one or several technical problems preventing choice of an adequate terrain for the landing. In that case, the control on the aircraft is limited. Here also, the degree of control can extend from some control to almost no control, so that the room for manoeuvre can be very different from one accident to another within this category. When incapacity of the crew is involved, this has a dramatic end (complete loss of the structure) in single-pilot-airplanes, where the uncontrolled impact is inevitable. In a transport aircraft [3], where the crew is composed of at least two pilots, this incapacity should never lead to any serious accident even less to an impact on water.

In order to have a better comprehension for the extent of the event, the next paragraph proposes a review of accident data, where the accident scenarios and associated risks for the

occupants are identified. Water impact accidents of fixed wing aircraft and rotorcraft are analysed separately.

2.2 Review of accident data

FIXED WING AIRCRAFT

The accident databases available in [4] and [5], respectively covering the intervals 1959-1979 and 1980-1991 were enriched by additional investigations [6]. These latter not only concentrate on the period 1992-2006 but also revealed new data completing the records of the period 1959-1991. Only information on accidents involving civil jet transport aircraft in domestic and international flights as well as scheduled and non-scheduled flights is considered. This means that flights, whose nature was ferry, positioning, executive, cargo and military of course, are not included in the study. A list of these water impact accidents data is available in Appendix A.

In [4], Johnson reviewed 933 ground/water accidents data for the period 1959-1979 obtained from FAA/Civil Aeronautics Board (CAB), National Transportation Safety Board (NTSB), foreign government organisations, airlines and aircraft manufacturers. 153 of them were declared as survivable accidents. This selection was based on the following criteria: a sufficient airframe volume around the occupants after the crash (prior to fire), the capability of at least one occupant to withstand the accident environment, the possibility for occupant escape and/or the demonstration of structural system performance under the crash loads.

Table 2-1 shows the assessment of the fatalities and serious injuries resulting from survivable impacts on water between the years 1959-1979. This information is very interesting because the number of fatalities and injuries could be assessed for this period. Three additional survivable impact accidents on water complete the eleven already collected in [4]. The demonstration is made that about 10% of the accidents are water impact accidents and that 28% of the on-board occupants perished in a survivable land impact accident compared to 20% in a water impact accident. One major statement for impact events in deep water is that drowning is the main cause of fatalities representing 218 of the 224 listed fatalities. Drowning can already happen in the aircraft, because the occupants are unable to escape due to injuries or disorientation for example but also after evacuation due to malfunctions of emergency flotation equipments or inappropriate actions of the cabin crew.

	Land impact	Water impact	Total
Accidents	142	14	156
On-board occupants	12648	1097	13745
Fatalities	3573	224 (218 by drowning)	3797
Serious injuries	1046	at least 80	1126

Table 2-1: Survivable accident database summary for civil jet transport aircraft (1959-1979)

Based on the 42 water impact accident data summarized in Appendix A over the period 1959-2006, the 32 survivable ones are analysed in the following. For informatin, no non-survivable accident on water has been reported since 1987. According to Table 2-2, the number of injuries related to water impact accident over the last 45 years is very variable from one decade to another. In addition there is no relation between the number of accidents and the percentage of injuries.

The water impact accidents can be divided into three types: off-runway, CFIT and ditching. By “off-runway”, the aircraft runs off the end of the runway or was turned off the runway and comes to stop in water. This may be due to a technical problem e.g. landing gear failure, to a touchdown far down the runway or to bad weather conditions. In a CFIT situation, the crew has a false opinion about the position of the aircraft in its surroundings and flies towards the water surface without knowing it. Finally, ditching corresponds to the emergency landing in water. Figure 2-1 shows the repartition of the accident types per decade within the last 45 years. In this period, 17 (53% of the overall water events) from the 32 survivable water accidents are due to off-runway action and ditching occurred once every decade apart from the interval 1980-1989. Since 1980 the number of water accidents of type “off-runway” has been dominant compared to the other types. Finally the number of CFIT occurrences on water has been decreasing since 1970.

Period	Accidents	On-board	Fatalities	Percentage of fatalities
1959-1969	9	786	55	7 %
1970-1979	5	311	174	56 %
1980-1989	9	1343	36	3 %
1990-1999	6	989	192	19 %
2000-2006 (6 years)	3	408	173	42 %

Table 2-2: Database summary of water related impact (survivable) accident for 1959-2006

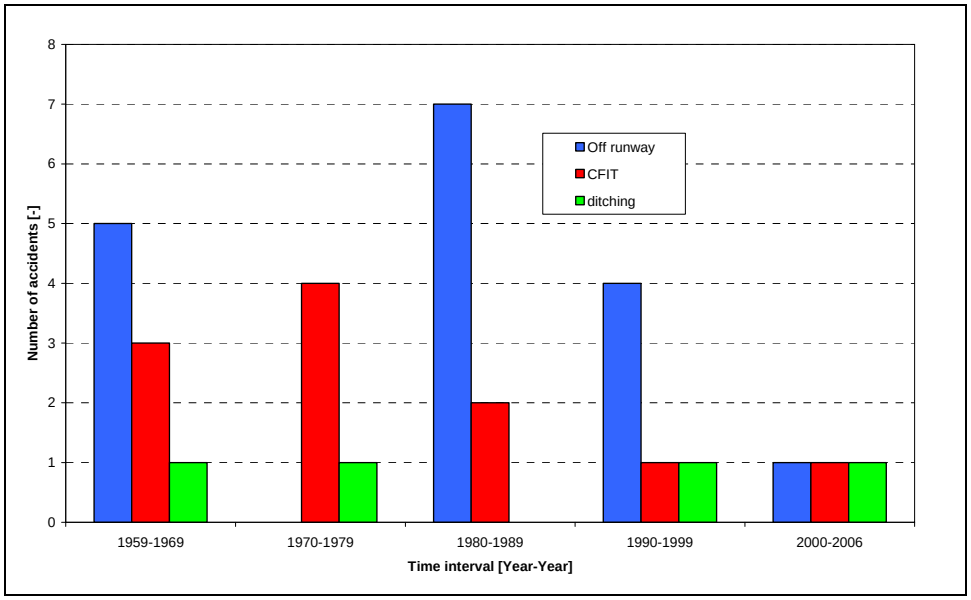

Figure 2-1: Repartition of the accident (survivable) types within each decade

Figure 2-2 shows the percentage of fatalities attributed to an accident type within each decade in the last 45 years. The CFIT events on water are mainly responsible for the fatalities apart from the period 1990-1999. Nevertheless, CFIT consequences in term of fatalities can be very variable. For example, there was only one CFIT event on water in 2000-2006, which caused the death of 169 occupants (from 179 on-board) whereas two CFIT’s events on water in 1980-1989 led to 25 fatalities (from 342 on-board).

Due to their unplanned nature, the CFIT’s are essentially characterised by an improper configuration for water impact and generally belong to the class of the high energy impacts.

This can make them fatal due to the accelerations sustained by the passengers being mainly above the survivable limits, the ejection of the passengers from their seats if unrestrained at the moment of impact and the high risk of passengers trapped in a sinking fuselage. In addition, post ditching progress may be problematical due to carry-on debris blocking the evacuation line and jammed exit doors, and structural failures which make the progression in the fuselage difficult.

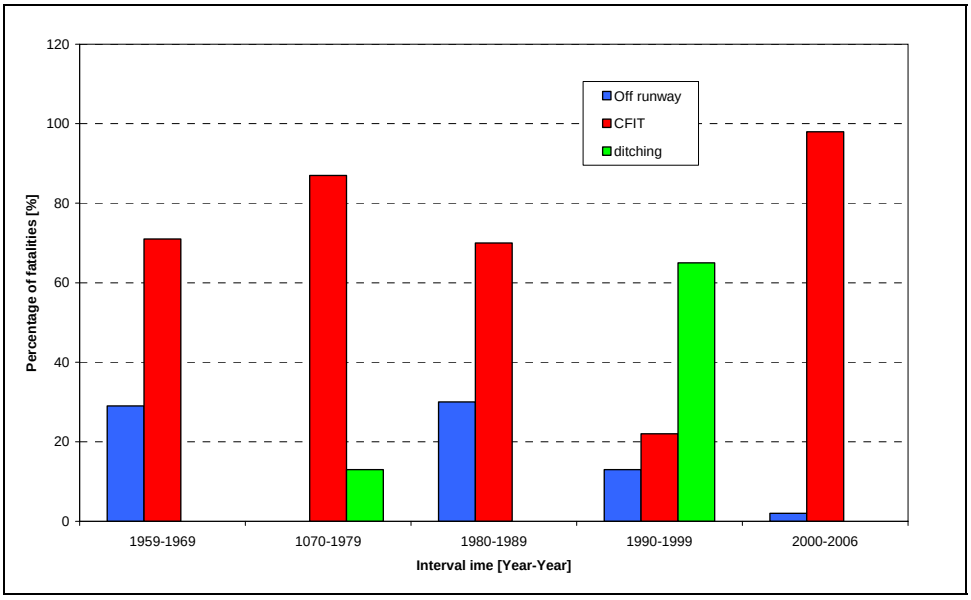

Figure 2-2: Percentage of fatalities attributed to an accident type within each decade

In the last four decades, only four intentional ditching of civil jet transport aircraft could be listed. As ditching is concerned in this work, a brief summary about each of those ditching events is presented in the following. It is interesting to notice that three of them were due to running out of fuel.

21 August 1963, Aeroflot Tu124, Leningrad, USSR
The aircraft was ditched on the 300m wide river Neva because it ran out of fuel. It could be towed to shore, which means it remained floating. All 52 occupants (7 crew members and 45 passengers) survived.

2 May 1970, ALM DC9-33CF, near Saint-Croix, Virgin Islands [7]
The aircraft was ditched on the Caribbean Sea because it ran out of fuel and sank about 1,600 m deep within five to six minutes. Due to communication problem between the flight and cabin crews, several occupants were not belted at the time of the ditching event. This is partly responsible for the number of fatalities. Five of the six crew members and 35 of the 52 passengers survived.

23 November 1996, Ethiopian Airlines 767-200ER, near Moroni, Comoros Islands
On a flight from Ethiopia to Kenya, the aircraft was hijacked and ran out of fuel due to a change in the route. The aircraft was then ditched in the shallow sheltered waters near a beach. Based on the film of the ditching event filmed from the beach, the left engine and wingtip struck first the water, causing the aircraft to break up. Only six of the 12 crew members and 44 of the 163 passengers survived.

16 January 2002, Garuda Indonesia Airways B737-300, near Yokyarta, Indonesia,
Due to the burn out of both engines, the aircraft was ditched with flaps and landing gear extracted into a shallow, one metre deep part of the Bengawan Solo River. Five of the six crew members and all 54 passengers survived.

The major statement is that CFIT's events on water and ditching are responsible for 91% of the fatalities. This underlines the importance of considering both planned (ditching) and unplanned (CFIT) water impact accidents when trying to improve the crashworthiness in a water environment.

ROTORCRAFT

According to reviews conducted in the 90's [1], it has been stated that over 24% of the world civil helicopter accidents occurred on water. In the military area, this was 27% of the UK helicopters and 40% of the US navy helicopters accidents. Statistics [8] available for helicopters operating for the offshore oil and gas industry in UK state that 90,000 hours are approximately flown each year. Between 1976 and 2004, 12 fatal accidents associated with offshore operations occurred claiming a total of 118 lives. The last accident happened in 2002 resulting in 11 fatalities. Previously, there had not been a fatal offshore accident since 1992. This is considered as a good safety level because operations over long distances and often in hostile environments are concerned. Unfortunately, the reasons and circumstances for the rotorcraft accidents on water over the last three decades could not be assessed precisely enough. For this reason, it is not possible to conduct a similar study to the one performed for aircraft.

In a helicopter water impact accident, the primary class of injuries is characterised by injuries to the body extremities like legs, arms and heads. This is caused mainly by structural failure of the seats and/or collision with the confined cockpit structure. The second most significant injury type is trauma due to excessive deceleration forces, in particular spinal injuries (compression fractures). In contrast to an impact on land, deceleration forces lead to few fatalities, which indicate that crash forces are lower on water than on the land. Regarding fatalities, drowning is a leading cause of death. In an assessment [9] conducted by Westland Helicopters over the period 1971 to 1992, drowning represented respectively 57% and 83% of the fatalities in both world civil and UK military helicopter impacts on water. Similar to fixed wing aircraft most of the fatalities in crashes on water are due to the post crash events.

The main factors for drowning are:

- injuries to legs, arms and heads, which handicaps the egress
- the strong tendency of the helicopter to capsize/to completely invert (and sometimes immediate inversion after contact with water)
- entrapment (e.g. difficulties in releasing seat-belts) and/or jammed/obstructed exits
- difficulties in reaching and opening the escape hatches
- disorientation of the occupants due to the inrush of water.

In many impacts on water, all the occupants do not have the time to evacuate before the helicopter submerges. It is therefore not rare that underwater evacuation has to be carried out with all the risks it contains (e.g. cold water shock). This shows the importance of improving the capability of helicopters to remain afloat and if possible upright after impact to allow survivors to escape "safely".

As it is clear that improved flotation makes a major contribution to survivability, efforts are concentrating on the robustness and reliability of the floatation systems. It was noticed that

inflation mechanisms very often failed at impact under the crash loads. At the same time, investigations are conducted to install extra flotation devices high on the fuselage in the vicinity of the main rotor gear box and engines to prevent complete inversion. This measure may be especially considered for helicopters operating in severe weather conditions. The stability of the helicopters on water is a real challenge when realistic wind speeds and severe sea states (over sea state 4) have to be taken into account. Finally some studies are dealing with the deployment of floatation bags before contact with water in order to limit the damage to the helicopter belly structure and also the deceleration loads transmitted to the occupants. All these measures have to remain, of course, within acceptable additional structural weights and costs.

The RHOSS (Review of Helicopter Offshore Safety and Survival) report [10] shows that no significant distinction can be made between the rate of occurrence between ditching described as a controlled descent and survivable crash on water including the control descent into a hostile sea, and all uncontrolled and unintended impacts on water. Among world civil and UK military helicopters, it is nevertheless possible to distinguish between four categories of impact on water [1]:

- the controlled ditching associated with an autorotative landing with partial or total loss of power,
- the vertical descent with limited control associated with a tail rotor failure and no autorotation,
- the fly-in impact resulting from a pilot error or disorientation,
- out of control accidents or unknown cause.

The three first categories represent approximately 70% of the world civil helicopter accidents over the period 1971 to 1992 [1]. 29% of water impacts belong to the first category, where no real damage to the airframe is observed, 26% to the second and 15% to the third. Table 2-3 gives the data defining these different categories including typical range of forward and vertical speeds, pitch angle and attitude.

Accident categories	Forward speed	Vertical speed	Pitch angle	Roll and yaw attitude
Controlled ditching	Below 10 m/s	Below 3 m/s	0°-5° nose up	Level roll attitude Minimal yaw angle
Vertical descent with limited control	0-35 m/s	Up to 8 m/s	±10°	±20° roll angle Significant yaw angle
Fly-in impact	Up to 50 m/s	Usually below 3 m/s	0°-5° nose down	

Table 2-3: Data characterizing the controlled ditching, the vertical descent with limited control and the fly-in impact

2.3 Typical damage

Based on the accident data collected in § 2.2, it is obvious that fixed wing aircraft and helicopter behave very differently when impacting on water. The structural arrangement of a fixed wing aircraft has the advantage of a large cargo volume under the passenger floor, which can absorb impact energy. Depending on configuration (high/middle/low-wing, presence of sponsons) natural flotation devices may be available or not. In the case of a low-wing aircraft, the wing may provide buoyancy (flotation volume) and the centre of gravity located in the lower half of the fuselage contributes to the aircraft stability in water. In the

case of helicopters, the mass is in most of the cases concentrated on the top of the structure where the rotor gear box and motor are located. This leads to a high positioned centre of gravity and consequently to stability problem in water, which have to be solved with deployed external flotation bags after an emergency landing on water. In addition, the volume under the floor is very restricted, which limits the capacity to absorb crash energy. The landing gear or skids of a helicopter, which are normally able to absorb impact energy in ground impact events, are useless when impact on water is concerned.

The flight conditions of both structures are also very different. A significant aspect is that the forward velocity is always preponderant compared to the vertical velocity in the case of a fixed wing aircraft. These proportions may not be so significant when considering a helicopter. Whereas the civil jet transport aircraft has to land on water with velocities above 55 m/s, the helicopter may ditch with a forward speed below 10 m/s.

The shape [11], [12] and the size [12] of the aircraft structure impacting on calm water have been investigated with scaled models in water tank. It is shown that they have a significant influence on the behaviour during the impact on water. They determine the level of accelerations reached during the event and the stability of the landing.

Before focusing exclusively on the impact on water, it is interesting to briefly analyse where the main discrepancies are when considering impacts on ground and on water. Whereas the impact forces are higher for impact on ground than on water, the levels of structural damage are higher for an impact on water. This is due to the different mechanisms with which the forces are applied to and reacted by the structure. In a crash on a solid surface, the impact forces are due to the inertial response of a system consisting of high masses. The crash loads are then a function of the structure stiffness. They are concentrated at high stiffness structural elements, which can be designed to crush progressively to absorb energy. In the case of an impact on water, it is the water pressure acting on the outer surface of the structure, which is responsible for the impact forces. These latter are then distributed over the part of the structure in contact with water. They are dependent on the velocity, the current geometry (skin intact, deformed or failed) and the structure drag in water. Another feature of the crash on water originates from the constant interactions between the structure and the fluid inducing continuous changes in the loads applied to the structure during the water crash event. For example, when the water progresses inside the structure after failure of skin panels, this leads to a new loading case, which may influence the kinematics of the whole aircraft structure. This then exposes new parts of the aircraft structure to water pressure loads. It may follow that the newly loaded parts make matters worse or better by additionally loading or unloading a critical component. When the structure finally comes to rest, the flotation phase, if any, starts and is followed in most cases by sinking. Compared to an impact on ground, impact on water is a long-term event. It is then clear that the different loadings due to crash on water and on land inevitably lead to various specific failure modes in the structure.

FIXED WING AIRCRAFT

The behaviour of a fixed wing aircraft “landing” or “crashing” on water is highly dependent on the integrity of the lower fuselage structure. If the structure remains intact without excessive deformations and, above all, without any major skin rupture, the deceleration forces remain relatively low. If the skin panels fail, the water comes into contact with internal structures which drastically increase the drag forces and subsequently the deceleration loads. In the cases, where the failure of skin panels is extensive, the event becomes very hazardous

due to the unpredictable chain of failures propagating in the structure. At the same time, fracture of devices means absorption of crash energy.

Based on the damage magnitude, the water impact events can be classified into slides/rolls into water involving quite low impact energy levels and high energy impacts. The first group primarily corresponds to the off-runway and successful ditching whereas the second includes the CFIT's and the unsuccessful ditching events. In the case of a slide/roll into water, the lower fuselage may be torn or ruptured but the fuselage does not break. Figure 2-3 shows a typical damage of the lower structure of a B707 after a ditching event. When not ruptured, buckling of the aircraft skin due to the interaction with the water is characteristic of the water loading whatever the intensity of the impact event on water.

In a high energy impact on water, higher loads and therefore higher damage in the structure are expected. At a first level, the skin extensively fails, floor structure collapse with subsequent seat track fractures and seats dislocation probably occur due to water hydrodynamic loading coming from the broken /failed belly of the fuselage. In the worst case, the fuselage may break followed by separation, which is in direct correlation with a high number of fatalities. At impact, if extended, the landing gear is torn away and the engines, if located under the wings, detach. The engine pylons are normally designed to fail at a specified longitudinal loads preventing dramatic damage to the wings. More critical is the separation of the wings from the fuselage due to an unfavourable "landing" on water (e.g. unsymmetrical impact).

Figure 2-3: Damage sustained by a Boeing 707-351 Cargo after a ditching event in Victoria Sea (Tanzania) on 3rd February 2000 [6]

In [13], a heavy jet transport high-wing airplane model (full-scale parameters: ~337 tons, 75 m long and ~67.9 m wing span) with a scaled strength fuselage lower structure was investigated under ditching. To that aim, its configuration was varied: landing gear retracted or extended, 0° or 40° flaps, two different failure strengths for the removable fuselage bottom. When ditching on a calm water surface, 40° flaps, 12° attitude and 64.8 m/s speed, the maximum longitudinal and vertical accelerations (near the pilot's compartment) amounted to 17 g and 3 g in average. The rear section of the scale strength fuselage suffered damage causing large drag loads when water contacted the internal bulkheads. By running the test with 7° attitude and 70.5 m/s landing speed, the maximum longitudinal and vertical acceleration levels diminish to respectively 6 g and 3 g. In that case, the rear section and the front half of the scale strength fuselage were considerably damaged but the motion of the aircraft remained smooth. Between both test conditions, the longitudinal acceleration is

reduced by a factor of three. These results show how much accelerations are sensitive to the kinematics and the damage on the lower structure during an impact event on water.

ROTORCRAFT

As already mentioned for the fixed wing aircraft, the response of a helicopter to impact on water also depends on the structural shape and the integrity of the lower fuselage panels. In a helicopter, there is a restricted volume under the sub-floor to absorb energy and eventually delay the sinking. When impacting on water, the lower skin panels are primarily loaded and therefore deform under the water loads. If they do not fail, they may transmit forces to the high stiffness elements (designed for ground impact) to absorb crash energy. If they fail, water rushes in and internal structures are directly exposed to water loads. Floor areas may be disrupted with subsequent distortion of seat attachments. Based on [1], the probable damages sustained by a helicopter when impacting on water are listed below according to the various categories of impact on water described in Table 2-3.

In a controlled ditching (forward speed < 10 m/s, vertical speed < 3 m/s), a minor damage is expected on the lower fuselage panels. The skin buckles under the water loads and low strength fairings and access panels may fail. The floatation system can be also damaged, which may result in inversion or sinking of the helicopter. The vertical decelerations are expected to be in the range 4 to 6 g.

When vertical descent with limited control (forward speed in the range 0-35 m/s, vertical speed < 8 m/s) is concerned, the integrity of the airframe is kept. Low to moderate structural failures are expected: substantiate damage to the lower panels resulting in inrush of water, possible failure of the cone or tail fuselage, probable damage to fuselage frames and/or under-floor keel beams. The lower forward panels probably fail due to the horizontal impact velocity component. The flotation system is partially or fully damaged. Vertical decelerations are expected to be in the range 5 to 25 g. Figure 2-4 shows the damage sustained by a WG30 helicopter after a pure vertical impact test on water at 7.95 m/s [2]. Skin buckling, frame and sub-floor deformations could be observed. In addition, the starboard door was torn away. A similar test conducted on a UH-1H helicopter is described in [14].

Figure 2-4 : Damage sustained by a WG30 helicopter after a vertical impact test at 7.95 m/s

In a fly-in impacts event (forward speed < 50 m/s, vertical speed < 3 m/s), the forward and low fuselage skin extensively fail, which enables water to come in direct contact with internal frames. This results in high drag forces causing further structural failures and can end up in a catastrophic break up of the airframe. The flotation system is expected to be fully damaged.

2.4 Ditching regulations

If certification is requested, the aircraft/rotorcraft must meet the requirements listed in the various regulations, standards, advisory circulars and/or military specifications. The FAR (Federal Airworthiness Regulations) provided by the US Department of Transportation and its equivalent European JAR (Joint Aviation Requirements) include design guidelines to meet airworthiness and crashworthiness objectives. Whereas the airworthiness design standards deal with the airframe to withstand design loads and safety of the airplane in its operational environment, the crashworthiness approach [15] in the FAR involves the three following points: protection of airplane occupants from crash impact, minimizing development and severity of potential crash fire and rapid evacuation of the airplane occupants. The main objective of all these regulations is to maximize the passenger survivability.

FIXED WING AIRCRAFT

Although only “ditching” is mentioned in the certification texts, both planned and unplanned impacts on water have to be investigated to certify an aircraft/rotorcraft for overwater flight. The major ditching requirements for large transport aircraft are mainly described in the FAR Part 25 [16] for transport category airplanes. The section 251 of Advisory Circular AC25-17 [15] gives some additional guidance for demonstrating ditching compliance. The sections of FAR25 dealing with ditching are listed in the following:

- §25.561 Emergency Landing conditions
- §25.801 Ditching
- §25.803 Emergency evacuation
- §25.807 Emergency exits
- §25.1411 Safety equipment
- §25.1415 Ditching equipment

Other sections of the FAR Parts 121 and 125 have also to be considered for emergency evacuation. They include requirements about equipments and evacuation procedures:

- §121.291 Demonstration of emergency evacuation procedures
- §121.339 Emergency equipment for extended over-water operations
- §121.340 Emergency floatation means
- §121.417 Crewmember emergency training
- Appendix D to part 121 Criteria for demonstration of emergency evacuation procedures
- §125.209 Emergency equipment: extended overwater operations
- Appendix B to part 25 Criteria for demonstration of emergency evacuation procedure

From the structural point of view, the aircraft must be designed in order to maintain as far as possible crash forces within human tolerances. This can be achieved by providing energy absorbing devices in the aircraft structure itself but also in the seats. In contrast, the structural integrity of the passengers space should be guaranteed in order to avoid injuries due to direct structural deformation and to allow the occupants to reach as easily as possible the emergency exits. In addition, the structural standards integrate requirements about the seats and seatbelts. Finally, external doors and windows must be designed to withstand the maximum load

pressure in order to avoid immediate water ingress in the cabin. Sometimes, cargo or equipments are located in the passenger compartments. In that case, they should be positioned so that they would cause no direct injury to occupants and not jam any escape facilities (when broken loose).

The kinematics of the aircraft during the impact on water strongly depends on its configuration at the moment of the event. It is therefore required to thoroughly investigate the influence of flaps position, location of the centre of gravity, weight and/or eventual damage on the structure for the forced "landing" on water. External factors like a rough sea may have to be taken into account. Based on these studies, best recommendations on configurations, speed and pitch are made. This work is conducted by means of model testing or comparisons with airplane of similar configurations for which ditching characteristics are known (see § 2.5).

When the aircraft comes to rest on water after the impact, the trim of the aircraft in water should allow the occupants to reach the emergency exits above the water level. The number of exits should be sufficient and their size adequate to allow a rapid evacuation of the airplane. In addition, the flotation time should be sufficient to allow the occupants to enter the liferafts. In the evaluation of the flotation time, structural damage and leakage have to be taken into account but also rough sea conditions.

Requirements about the type of emergency equipments for aircraft operating over water are also available. They concern life preservers, liferafts, emergency locator transmitters among other items.

ROTORCRAFT

When manufacturers have to substantiate ditching compliance, they have to demonstrate that the helicopter mainly fulfils the following requirements of FAR 29 [17] for transport category rotorcraft (FAR27 for normal category rotorcraft):

- §29.801 Ditching
- §29.807 Passenger emergency exits
- §29.1411 Safety Equipments
- §29.1415 Ditching equipments

As in FAR25, FAR29.801 delivers a short summary of the overall objective a designer should keep in mind with regard to ditching: structural integrity, kinematics during the ditching event and flotation characteristics. The previous comments on these topics made for the fixed wing aircraft apply also for rotorcraft.

As an interesting point, the advisory circular AC29-2A [18] specifies that the rotorcraft in ditching condition is assumed to be intact prior to impact on water with all controls and essentials systems functioning properly except engines. This may not be the case in a real impact on water, for which severe technical problems are highly probable. In addition, it is stated that at least sea state 4 (1.25 m-2.5 m wave height) is assumed to be representative of reasonably probable water conditions to show compliance with flotation and trim requirements. This means for the manufacturer that compliance at sea state 4 is sufficient, which considerably helps prove the flotation capacity of a rotorcraft. Another regulation, the "British Civil Airworthiness Requirement" [19], requires good flotation capability until sea state 6 (4 m-6 m wave height).

Matters relating to safety and ditching equipments are described in sections §29.1411, §29.1415, §29.1561 and in the operating rules in part 91, 121, 127 and 135. These occupant water survival equipments are required for operations more than 50 nautical miles from the nearest shoreline or an offshore heliport structure.

2.5 Current certification procedures

For both aircraft and rotorcraft, the demonstration of compliance to ditching requirements may be realised by either testing or comparison to aircraft/rotorcraft of similar design, for which the ditching behaviour has already been certified. Some full-scale tests have been performed. They remain nevertheless rare as they are costly. In [20], pictures of typical damage sustained by a full-scale high-wing aircraft named Liberator, which was ditched by NACA, are available. For economical and also flexible reasons, the use of aircraft/rotorcraft models launched in a water tank is nowadays more common for investigating various ditching conditions. This is all the more interesting since the FAA recognise model test results to prove the kinematical behaviour at impact, the flotation and trim characteristics of a full-scale aircraft/rotorcraft.

Model testing

Those model tests are essentially used to determine the best configuration to ditch and investigate critical configurations. One of them may be the ditching case at maximum gross weight, which reproduces a “landing” on water resulting from a take-off abort.

The scale models are built (very often by hand) from design data sent by the manufacturer and accurately represent the aircraft’s external shape. Typical models are made out of balsa wood covered with glass-fibre cloths and are internally reinforced with simple plywood sections. A ditching model around 1/10 scale is usual whereas flotation models can be smaller (until 1/24). For fixed wing, the wing must be able to support the aircraft during the short free flying phase and for helicopters, rotor blades with correct aerodynamic profile are included. In addition, a mechanism enables the blade to be rotated at an appropriate velocity when released in the water. The models are designed with access panels on their sides to enable equipment to be fitted and accessed. Accelerometers (at least at the fore part, centre of gravity and rear part of the aircraft), strain gauges, gyroscopes and pressure transducers may equip the model. For the test, the model is launched as a free body by means of a catapult and has a short free flight before contacting the water surface.

In a typical test campaign, the behaviour of the model at ditching is investigated by varying the position of the centre of gravity and the weight. In order to better capture reality, damage may be taken into account. To that aim, scale strength elements can be built, which fail when a specified load level is reached. This should take into account the damage of particularly sensible parts of the aircraft (e.g. engine mountings, belly structure components), which may have an influence on its further behaviour during the ditching event. An example showing how the previous factors influence the ditching behaviour of a high-wing C5 airplane is given in [21]. The effects of retracted or extended landing gear and flaps setting on the kinematics are also of interest. The ditching conditions are also varied by modifying pitch, roll and yaw angles, velocity and rate of descent. The tests are performed in calm and also in rough sea.

At each test run, a high speed video registers the kinematics of the model. The accelerations at various locations in the aircraft are measured and pressure loads are usually recorded on the belly structure. The measured data are then scaled back to the full-scale value using the

Froude similarity. Inertia and gravity forces are assumed to be the major forces involved. Dynamic similarity is then fulfilled if the Froude number remains the same between test and reality. This leads to the relationships in Table 2-4, which convert the model data to full-scale values. With the full-scale data, the integrity of the structure in particular of the skin, doors and bulkheads on the full-scale structure can then be assessed.

Physical parameters	Full-scale value	Scale factor	Model value
Length	l	λ	λl
Force	F	λ^3	λ^3 F
Moment of inertia	I	λ^5	λ^5 I
Mass	m	λ^3	λ^3 m
Time	t	$\lambda^{1/2}$	$\lambda^{1/2}$ t
Speed	V	$\lambda^{1/2}$	$\lambda^{1/2}$ V
Linear acceleration	a	1	a
Angular acceleration	α	λ^{-1}	λ^{-1} α
pressure	p	λ	λ p

Table 2-4 : Scale relationships between ditching model and real aircraft (model 1/l scale)

Besides the ditching behaviour, the model is also used for flotation testing in smooth and rough sea conditions. This kind of test is crucial especially for helicopters. Due to their high centre of gravity, they are consequently highly unstable when their rotors are stationary. For this type of investigations, replicas of flotation bags have to inflate, which means additional instrumentations for the scale model. For fixed wing aircraft, the flotation tests help to determine the static flotation water line at various weights and locations of centre of gravity. The dynamic flotation behaviour is evaluated analytically. It results from the evolution of loss-of-buoyancy at various locations due to leakage in the airplane. Its investigation leads to a time-dependent weight-centre of gravity -attitude picture, which should show the position of the (emergency) exit doorsill towards the sea level.

Comparison with airplanes of similar configuration

Other methods to show compliance with FAR25 ditching requirements are to use for comparison the hydrodynamic characteristics of prior certified designs and/or to evaluate ditching accidents involving comparable aircraft. An example is given in [22], where the ditching capabilities of a DC-10 airplane are compared to the ones of a DC8.

If the aircraft, which should be certified for ditching, has a similar design to other designs used for prior certifications, qualitative appreciation may be conducted. The manufacturer can show that the additional features of the new structure are only beneficial to the ditching behaviour compared to the existing aircraft. Some structural aspects favourable for ditching are listed in the following:

- if the new aircraft has a similar design in geometry and size for the fuselage but a longer wing span, it is clear that the new design can only provide additional buoyancy and subsequently improve the floatation.
- in a low-wing aircraft, there is a large surface area in contact with water, which therefore provides buoyancy. This surface shares therefore a portion of the impact load with the fuselage during a ditching event. At the same time, a large wing means a reduced impact speed and consequently reduced impact loads.

- in a study [11] about the influence of fuselage shape on ditching behaviour, it is reported that a circular cross section with a minimum longitudinal curvature gives the best behaviour at higher landing speed. At lower landing speeds, the flattened cross section is better if there is a longitudinal moderate curvature of the fuselage bottom. These results can be used by the manufacturers for the qualitative ditching assessment of the new design.
- some design features can also improve ditching safety. This is the case when strut mounted nacelle are designed to fail at a certain load, because this diminishes the ditching weight. The same considerations may be valid for flaps, engines and tail plane.

Current practices

The ditching certification at the moment is based in most of the cases on a mixing of model tests, analytical investigation and simulations, with the proportion of numerical simulations in the certification process increasing. With the progress of the computation capabilities and the development of multidisciplinary tools, the trend is to replace model tests by numerical assessments: the manufacturers are going now towards virtual testing.

3 Modelling fluid-structure interactions

3.1 Theoretical background

3.1.1 The phases of water impact

Impact on water depends on various parameters, which can be divided into two groups: the parameters related to the configuration of the impactor (e.g. aircraft structure) and the parameters related to the boundary conditions of the impact. Configuration parameters include geometry information like slenderness ratio, size, weight, moment of inertia whereas boundary conditions parameters are impact velocity, angle of entry, angle of pitch, roll and yaw, angular velocities, etc.

In hydroballistics, it is common to divide the phenomenon of water-entry into a number of phases linked to specific flow patterns [23]: the shock wave phase, the flow forming phase, the closed cavity phase, the collapsing cavity phase, etc. Applied to the phenomenon of impact on water, only the shock wave and the flow forming phases are relevant. Korobkin & Pukhnachov [24] also distinguishes between two characteristic stages at the initial state of water impact: a supersonic and a subsonic stage, which agrees with the previous statements. In some cases, it may happen that there is no supersonic stage at all.

The shock wave phase

This phase is also called in the literature pre-flow line phase, shock wave phase or supersonic phase. Its duration is about 50 to 100 microseconds. It is characterised by the fact that the area of the body in contact with water expands with a velocity exceeding the sound velocity in water. A compressive shock wave is transmitted from the impacting structure to the water. In this problem, which is of an acoustic nature, the elastic properties of the fluid namely compressibility effects constitute an essential factor. In this phase, the high pressure, which builds up at the very beginning of the impact, is expressed by the water hammer formula [23]:

$$P = \rho\, c\, V \tag{3-1}$$

where ρ is the density of water, c its sound velocity and V the impact velocity. P corresponds to “the pressure on a compressible half-space boundary if it is immediately accelerated to normal velocity V” [24]. Eq. (3-1) was the first to be used for sizing structures which undergoes impact with liquid masses. Zukas [25] wrote nevertheless that "the impact pressure peak can exceed the water hammer pressure by a considerable amount” whereas May [23] found experimental results for which the pressure did not reach such a high value. Although forces are very large in the shock wave phase, the transmitted structural shockwave has very short duration and as a result, this phase is considered of small practical importance for the structure.

The flow forming phase

This phase is also called flow line establishment phase. It is a subsonic mechanism which is of the order of several milliseconds and corresponds to the stage at which loads are transmitted to the structure. Pressures and accelerations are not as large as in the shock phase but the duration of the phase is long enough to cause damage to the impacting structure.
In this stage, the body establishes a flow by entering water which is initially at rest. The impact force acting on the body is primarily due to the reaction of accelerating a mass of water called induced mass, virtual mass or added mass. This reaction causes a sudden deceleration of the body and may lead to damage on the structure. The main problem is then the determination of this induced mass, to which the impact force is directly connected. As the flow forming phase is determinant for the integrity of the impacting structure, it will be focussed on this phase.

3.1.2 Order of magnitude of the acting forces

Considering impact of aeronautical structures in water, it is useful to first assess the force mechanisms associated with fluid inertia, its weight, viscous stresses and secondary effects such as surface tension. Let us consider the following physical parameters: the characteristic length *l* (diameter of the fuselage for single wing aircraft / width of the rotorcraft's hull), the velocity U, the water density ρ (1000 kg/m^3), the gravitational acceleration g (9.81 kg/m^2), the kinematic water viscosity ν (10^{-6} m^2/s), the sonic velocity in water (c=1,500 m/s) and the surface tension σ between water and air (7.4 10^{-2} N/m). For two sets of data, one related to helicopter and one related to fixed wing aircraft, the order of magnitude of the acting forces are evaluated by calculating the Froude, Reynolds, Mach and Weber numbers. Results are summarised in Table 3-1. This short study shows that in first approximation the viscous forces, compressibility and surface tension effects are negligible. These assumptions were also examined by various authors and are shortly discussed in the following.

Ratios		**Fixed-wing aircraft l = 2 m / U = 50 m/s**	**Rotorcraft l = 2 m / U = 10 m/s**
Froude number	$F = \frac{U}{\sqrt{g\,l}}$	11	2
Reynolds number	$R = \frac{l\,U}{\nu}$	$100\text{x}10^{6} >> 1$	$20\text{x}10^{6} >> 1$
Mach number	$M = \frac{U}{c}$	$0.3\text{x}10^{-1} << 1$	$7\text{x}10^{-3} << 1$
Weber number	$W = \frac{U}{\sqrt{\sigma/(\rho\,l)}}$	8,220 >> 1	1,644 >> 1

Table 3-1 : Evaluation of the Froude, Reynolds, Mach and Weber numbers for characteristic impact on water of fixed wing aircraft and rotorcraft

Viscosity

During the supersonic phase of the impact, only a negligible part of the body is in contact with water. Therefore water viscosity can be neglected. During the subsonic phase (flow

forming phase) inertial forces are preponderant in comparison to viscous ones as far as vertical impacts are considered. In this case, loads acting on the impactor are primarily caused by the reaction of accelerating an "induced mass" of fluid, which moves with the body. Nevertheless, when the impact is oblique (impact velocity with vertical and horizontal impact velocity components), Troesch and Kang [26] found out that effects of viscosity may not be negligible anymore. When comparing simulation results assuming the fluid to be inviscid and test results of a sphere dropped into water under an angle of 45°, the calculated impact force horizontal component was under-predicted by the simulation, whereas the calculated and measured vertical ones agreed quite well. They attributed the discrepancy to viscosity forces and splash effects not taken into account in the simulations.

Compressibility

Depending on the geometry of the bodies impacting on water, it may be required to consider compressibility in the subsonic stage of an impact. This latter particularly applies to bodies with a plane front section impacting water when the front plane is parallel to the water surface at impact.

Surface tension

Surface tension is an important factor in the case of impact on water of small light-weighted bodies (with a diameter smaller than ¼ inch and $V < 6$ m/s [23]), which does not correspond to the range of impactors investigated in this work. It has also an effect on the water flow around the body, as it forms a spray sheet or droplets. As the impact loads primarily result from the action of pressures acting on the main part of the body situated under water, it is assumed that the spray sheet does not contribute significantly to the impact forces.

Air entrapment

As investigated by Verhagen [27] and Lewison [28], air entrapment between the impactor and the water free surface is a factor, which should be taken into consideration, as it may provide a cushioning effect. This phenomenon could be demonstrated, when bodies impact water with their flat bottom/nose at near 0° angles. In that case, the air layer situated between the flat part of the body and the water surface deforms the water surface, which starts accelerating downwards before any physical contact (Figure 3-1). This latter consequently diminishes the pressure applying on the impacting structure. Nevertheless, considering air compressibility is not necessary since the velocity of the moving entrapped air is likely to be much less than the speed of sound in air.

The factor of air entrapment may be important when flat- or nearly flat-bottomed bodies (e.g. wedges with deadrise angle less than 1 degree) strike the water surface. Nevertheless, it is negligible for two-dimensional wedges with deadrise angle bigger than 3 degrees and for three-dimensional bodies according to [29, 30].

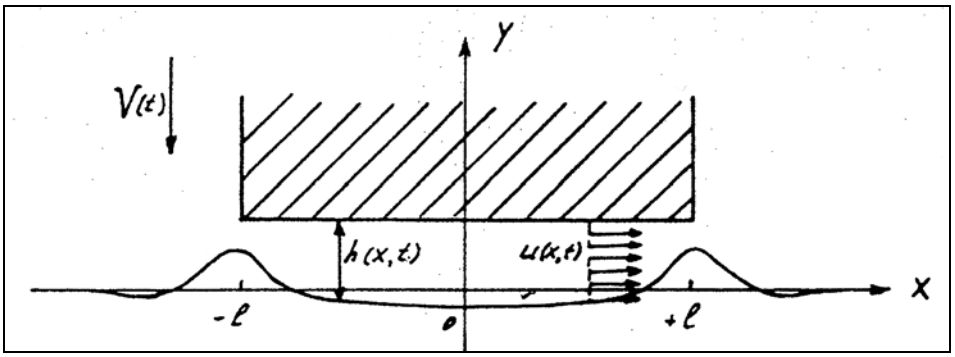

Figure 3-1 : Effects of the air layer on the water surface [27]

3.1.3 Mathematical formulation of the problem of impact on water (Eulerian description)

The impact pressures on a perfectly rigid body (no hydro-elastic interactions) entering a calm ideal fluid are considered in this paragraph, where a mathematical formulation of the problem is proposed. The flow is assumed to be irrotational (no vortices generation). Viscosity, surface tension, air entrapment, compressibility of air and water are neglected. A right-handed co-ordinate system is chosen so that its origin is located on the calm free surface. Consider a fluid where V describes the velocity of fluid particles. As the fluid motion is irrotational, the velocity in the fluid can be expressed by a velocity potential function $\phi(x,y,z,t)$ as

$$\vec{V} = \text{grad}\,\phi \tag{3-2}$$

The continuity equation, which expresses the conservation of mass in a given space occupied by a fluid, is expressed in the general case by:

$$\frac{\partial \rho}{\partial t} + \text{div}\,(\rho V) = 0 \tag{3-3}$$

where ρ is the fluid density. As the fluid is assumed incompressible and the flow potential, it results that the fluid field is governed by the Laplace equation:

$$\Delta\phi = 0 \tag{3-4}$$

The Momentum equation equating the applied forces to the inertia forces for a unit volume of an inviscid and incompressible fluid is defined by the following Euler equation

$$\rho \frac{DV}{Dt} = -\text{grad}(p + \rho g z) \tag{3-5}$$

where p is the pressure in the fluid, g the gravity, z the coordinate of the fluid particle in the z-direction and D/Dt is the material time derivative defined in § 3.4.1.2. Due to the assumption of a potential flow, this leads to the Bernouilli's equation

$$\frac{p}{\rho} + \frac{\partial \phi}{\partial t} + \frac{1}{2}\text{grad}\phi.\text{grad}\phi + gz = f(t) \tag{3-6}$$

where f is independant of the space coordinate but may be dependent on time. This equation is valid everywhere in the fluid.

Free surface:
The next step consists of determining the boundary conditions at the free surface η, which is itself unknown. Two conditions are specified: a kinematic and a dynamic condition [31, 32]. Let us assume that the vertical elevation of any point on the free surface is defined by

$$z = \eta(x,y,t) \tag{3-7}$$

The kinematic boundary condition states that the particle at the free surface remains at the free surface. This can also mathematically be formulated as follow: the normal velocity of the fluid and of the boundary surface must be equal e.g. it is required that the derivative of z-η vanishes on the free surface

$$\frac{\partial\phi}{\partial z} - \vec{\text{grad}}\phi . \vec{\text{grad}}\eta - \frac{\partial\eta}{\partial t} = 0 \text{ on } z = \eta(x,y,t) \tag{3-8}$$

The dynamic boundary condition is obtained from the Bernouilli's equation. It states that the pressure on the free surface must be atmospheric. By choosing f(t) suitably, the exact condition to be satisfied on the free surface is

$$\frac{-1}{\rho}(p - p_a) = \frac{\partial\phi}{\partial t} + \frac{1}{2}\vec{\text{grad}}\phi . \vec{\text{grad}}\phi + gz = 0$$

Substituting z by η leads to

$$\eta = -\frac{1}{g}\left(\frac{\partial\phi}{\partial t} + \frac{1}{2}\vec{\text{grad}}\phi . \vec{\text{grad}}\phi\right) \tag{3-9}$$

Boundary conditions
As the fluid is inviscid, the normal velocity component of the fluid at the impacting structure surface must be equal to the corresponding component of the structure surface itself. The velocity of a fluid particle on the instantaneous wetted surface of the structure is then determined by

$$\vec{V} = \vec{V_S} \cdot \vec{n} \quad \Leftrightarrow \quad \frac{\partial\phi}{\partial n} = \vec{V_S} \cdot \vec{n} \text{ on the wetted structure} \tag{3-10}$$

$\vec{V}_S$ and $\vec{n}$ are respectively the velocity and the normal of the surface.

At a fixed and rigid boundary if any, no fluid can flow through the boundary surface. That is the normal velocity component is zero

$$\vec{V} \cdot \vec{n} = \frac{\partial\phi}{\partial n} = 0 \text{ on a fixed boundary} \tag{3-11}$$

The radiation conditions require that the fluid velocity components generated by the impacting structure approach zero at large distances from the impact region:

$$\vec{\text{grad}}\,\phi \to \vec{0} \text{ when } \left(x^2 + y^2 + z^2\right)^{1/2} \to \infty \tag{3-12}$$

At time t = 0, the free surface is an horizontal plane and at rest

$$\eta(x,y,0) = 0 \tag{3-13}$$

$$\phi(x, y, z, 0) = 0 \tag{3-14}$$

The boundary value problem, for which a schematic illustration is available in Figure 3-2, is properly posed by equations (3-4), (3-8) to (3-14). Even with the simplifications that the liquid is ideal and incompressible, the flow potential and the structure rigid, the equations are nonlinear (quadratic terms). Nevertheless, the main difficulties are that the free surface and the wetted part of the structure are both additional unknowns changing in time and space. A three-dimensional analytical solution to this boundary value problem has not yet been found and the numerical solution remains nowadays a challenge for research.

If a velocity potential satisfying the above equations can be found, the pressures can be calculated from the Bernouilli's equation (3-6). Assuming a pure vertical impact, the acceleration $\ddot{z}_S$ sustained by the impacting structure are then determined by the following equation of motion

$$M_S \ddot{z}_S = -\iint \vec{p}\,\vec{n}_z dS - M_S g \tag{3-15}$$

where M_S is the structure mass and $\vec{n}_Z$ the unit vector on the z-axis. The velocity V_S and the displacement z_S are calculated by further integrations:

$$\dot{z}_S = V_S = \int_0^t \ddot{z}_S(t)dt \tag{3-16}$$

$$z_S = \int_0^t \dot{z}_S(t)dt \tag{3-17}$$

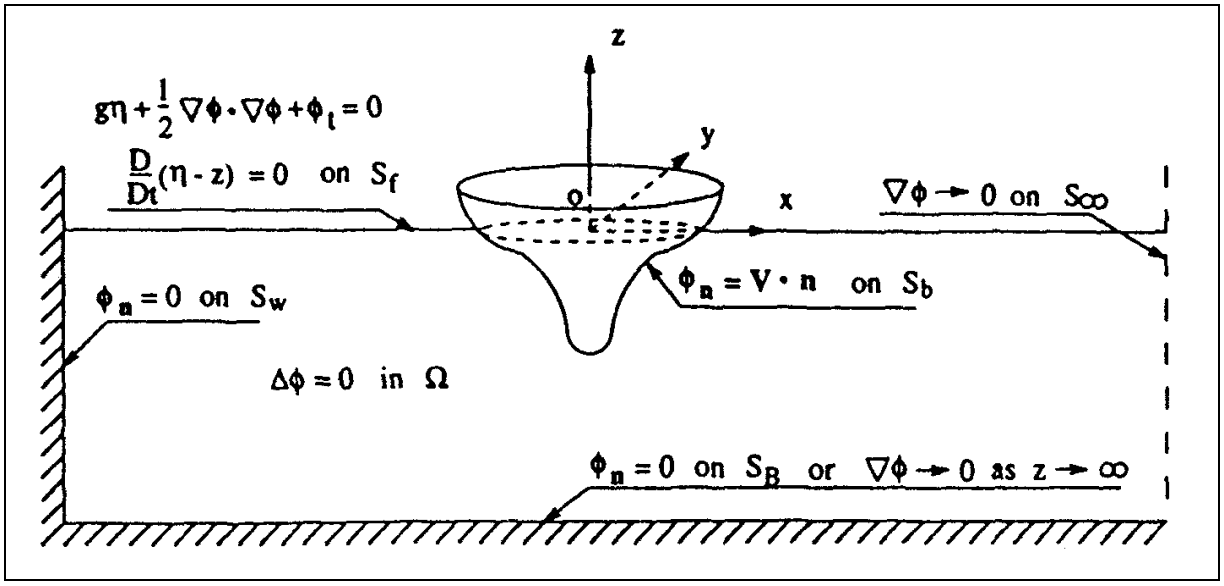

Figure 3-2 : Schematic illustration of the problem of impact on water [33]

The above-mentioned equations are the typical equations solved for the hydrodynamic loadings and are the subject of a very large number of publications. In naval application, they describe the phenomenon of slamming, which concerns the impact of the forebody/bottom of ships or floating structures on the water surface. This type of loading is a matter of concern because it is capable of causing structural damage to ship structures. As developed in § 3.2, the slamming problem is related to rapid changes of the added mass of submerged part of a structure. The second application is the impact of waves on structures. This concerns offshore

or coastal structures essentially of tubular types or structures on decks of ship in heavy weather.

3.2 Analytical methods for vertical impact of simple rigid bodies on water

This paragraph reviews the main analytical work treating the problem of impact. Aim is to have a better understanding of the complexity of the problem and not to give an exhaustive list of the current methods in use. Nevertheless, some recent developments are briefly discussed to show the well foundation of the early intuitive works.

3.2.1 2D-Analytical estimate of the force acting on a body impacting on water

Th. Von Karman [34] and H. Wagner [35] were the pioneers in determining an estimate of the virtual mass and therefore of the impact force. Historically, they first made an estimation of the forces applied to seaplanes at landing. Their works were the basis of numerous extensions. For example, F. H. Collopy [36] proposed an extension of the solution for the impact of three dimensional simple bodies and Shiffman & Spencer [37] a semi empirical graphic method including deformation of the free surface. As these works are still the basis of calculation tools used to estimate the impact force in the pre-development phase of structures susceptible to impact on water, they are briefly presented in the next paragraphs. They are used since aircraft may be geometrically approximated slice-wise by a series of wedges with different deadrise angles. The aim is to show, what the procedures behind the methodologies are and how they help improving understanding.

The basis of the theories presented is the conservation of momentum between the moment of first contact on water and the time t of interest (after the penetration of the body into water). This leads to the following equation:

$$M_{body}\, V_0 = (M_{body} + m_{water})\, v \tag{3-18}$$

where M_{body} is the mass of the body, V_0 the impact velocity, m_{water} the induced mass and v the actual velocity of the body at time t. The momentum lost by the impactor is converted into momentum of the added mass of water. This induced mass is the mass of water, which would have the same kinetic energy as that of the flow, if it travels with the body speed.

Through derivation of (3-18) and some mathematical transformations, it comes out for the acceleration undergone by the body that:

$$\frac{dv}{dt} = \frac{-v}{M_{body} + m_{water}} \frac{dm_{water}}{dt} \tag{3-19}$$

The force on the body is then expressed by

$$F = -\left(\frac{M_{body}}{M_{body} + m_{water}}\right)^3 V_0^2 \frac{dm_{water}}{dz} \tag{3-20a}$$

$$F = -\left(\frac{1}{1+\mu}\right)^3 V_0^2 \frac{dm_{water}}{dz} \text{ where } \mu = \frac{m_{water}}{M_{body}} \tag{3-20b}$$

dm_{water}/dz accounts for the rate of change of the induced mass as the depth of penetration changes. Eq. (3-20a) approximates the force applying on a body impacting on water in the subsonic phase. To that aim, the flow around the body is mainly considered.

3.2.2 Von Karman's analytic solution for wedges

Based on the conservation of momentum during water impact, Von Karman [34] proposed in the early thirties a solution to the two-dimensional problem of a wedge-shaped horizontal cylinder impacting on water.

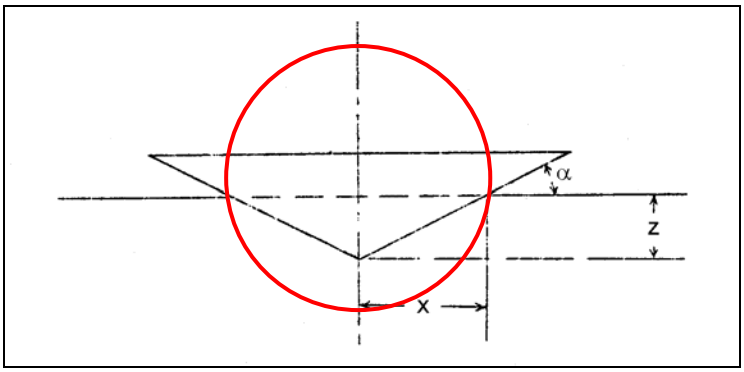

Figure 3-3 : Wedge parameters used in Von Karman estimate [34]

Von Karman approximates the mass per unit length of the induced water by half the mass of fluid contained in a circular cylinder of diameter 2x, where x is the half width of the body at the level of the free surface of water (Figure 3-3). The induced mass according to Von Karman is expressed by:

$$m_{Von\,Karman} = \frac{1}{2} x^2 \rho \pi = \frac{1}{2} \rho \pi z^2 ctg^2 \alpha \qquad (3\text{-}21)$$

$m_{Von\ Karman}$ corresponds to half the increase of inertia sustained by an infinitely long plate of width 2x when it is suddenly accelerated in a fluid. As only half of the cylinder is immerged into water and as the effect of air is negligible, only half of the inertia is considered. After some mathematical transformations, Von Karman formulates the force per unit length acting on the wedge as:

$$F = \frac{V_0^2 \cot \alpha}{\left(1 + \frac{\rho \pi x^2}{2M_{body}}\right)^3} \rho \pi x \qquad (3\text{-}22)$$

where α is the deadrise angle of the wedge and M_{body} the wedge mass per unit length. The maximum pressure is reached at the moment of impact and is then equal to:

$$P_{max} = \frac{\rho V_0^2}{2} \pi \cot \alpha \qquad (3\text{-}23)$$

3.2.3 Wagner's intuitive work for two-dimensional bodies

Wagner's correction takes into account the formation of a splash contour around the impactor. In order to explain the importance of this correction, a brief description of the splash effect follows.

At first, drops of spray are formed. This is a phenomenon of impact rather than of flow. This is followed by the formation of a sheet of splash, which results from the separation of the flow around the impactor. In the case of a sphere, "a thin sheet of water travels up the surface of the sphere and then detaches to form the splash sheath. It is mainly assumed that the pressure in the water is high up to some point P (Figure 3-4) and that the area above this thin layer of sheath is approximately at atmospheric pressure" [23].

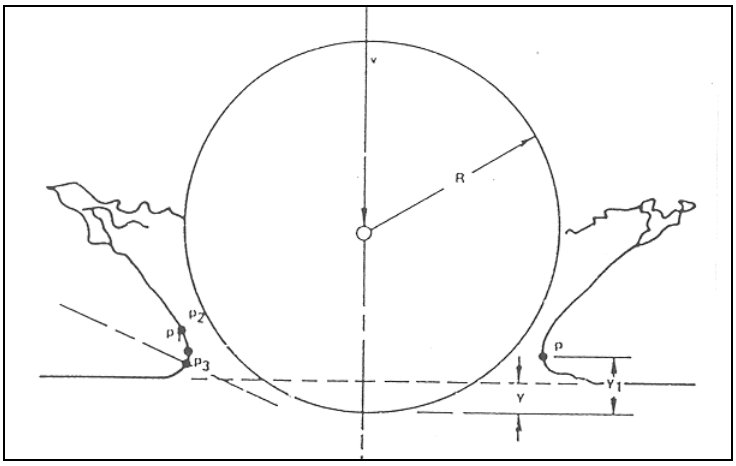

Figure 3-4 : Splash formation around a sphere impacting on water [23]

In the case of a sphere hitting water, a splash forms while the slope of the contact surface is still small. Then the increasing contact slope and the establishment of a flow pattern leads to the formation of a sheet of splash with a maximum angle of 60 degrees. The notion of wetting factor is introduced, which is the ratio of the penetration y_1 of the sphere determined from the point P to the penetration y of the sphere determined from the undisturbed free surface. This wetting factor is taken into account in numerous analytic solution given in the literature concerning the problem of impact on water.

Wagner proposes a solution to the impact problem of a two-dimensional symmetric wedge of small deadrise angle, where he computes the jet thickness, water free surface elevation and pressure distribution.

Unlike Von Karman, Wagner [35] considers for the calculation of the induced mass the wetted width 2c (Figure 3-5) of the immersed body instead of the width of the body at the level of the free surface of water.
The induced mass of water can then be calculated from equation (3-21) by replacing x by half the wetted width of the impactor, namely c:

$$m_{Wagner} = \frac{1}{2}\pi\rho c^2 \tag{3-24}$$

In order to take this correction into account, the problem consists then in evaluating the function $\eta(x)$ corresponding to the elevation of water at the body surface.

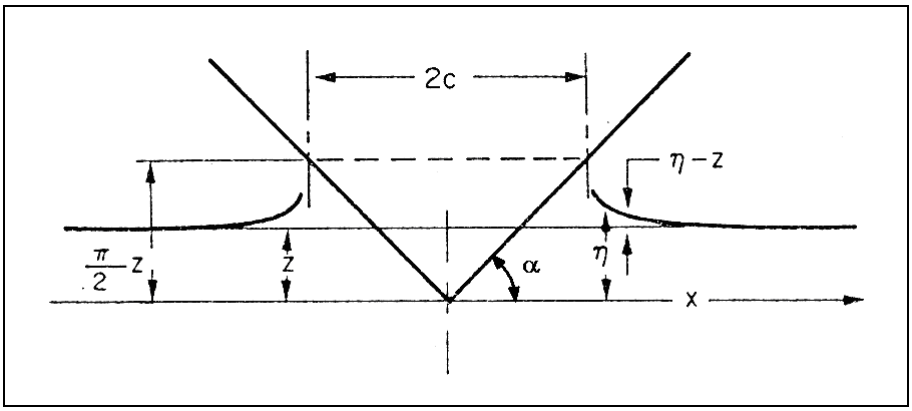

Figure 3-5 : Parameters relating to the water elevation around the impactor

During the impact, Wagner assumes that the flow velocity remains in the z direction on the free surface (no tangential component). He then replaces the body entering water by a motionless "expanding equivalent flat plate" placed in a normal uniform flow with velocity V. In the impact case, the flow is directed in the upward z-direction and the current plate width is 2c according to Figure 3-5. The complex potential F for a flow normal to a flat plate of width 2c is well known and determined by the following expression [32]:

$$F = -iV\sqrt{z^2 - c^2} \tag{3-25}$$

where z is the complex co-ordinate of any point in the complex plane (z = x + iy). The velocity at any point of the free surface is given by

$$u - iv = \frac{-iVz}{\sqrt{z^2 - c^2}} = \frac{-iV}{\sqrt{1 - c^2/z^2}} \tag{3-26}$$

The normal velocity (perpendicular to the x-axis) of any point (y = 0, x > c) of the surface is finally given by:

$$V_n = \frac{V}{\sqrt{1 - \frac{c^2}{x^2}}} \tag{3-27}$$

The elevation η(x,t) of any point on the free surface is then determined by:

$$\eta = \int_0^t V_n \, dt = \int_0^t \frac{V \, dt}{\sqrt{1 - \frac{c^2}{x^2}}} \tag{3-28}$$

The problem is reduced to the one of a plate whose width 2c(t) changes in time. Taking c as an independent variable (t = t (c) and V=V(c)), Eq.(3-28) can be re-written as

$$\eta = \int_{t=0}^{t} \frac{V\left(\frac{dt}{dc}\right) dc}{\sqrt{1 - \frac{c^2}{x^2}}} = \int_{c=0}^{c \le x} \frac{\omega(c)\, dc}{\sqrt{1 - \frac{c^2}{x^2}}} \tag{3-29a}$$

$$\text{where } \omega(c) = V(t)\frac{dt(c)}{dc} \tag{3-29b}$$

When a water particle reaches the plate, following equalities are valid: x = c, $\eta = \eta_b$ where η_b is the equation of the impactor/body contour. The following equality applies:

$$\eta_b = \int_0^x \frac{\omega(c)\,dc}{\sqrt{1-\frac{c^2}{x^2}}} \tag{3-30}$$

where ω is the unknown. ω is a geometric parameter without dimension and depends only on η_b and not on V(t). Eq. (3-30) should be fulfilled for every x on the body contour. Wagner assumes that the shape of every body contour in contact with water can be described by the following polynomial development:

$$\eta_b = \beta x + \beta_1 x^2 + \beta_2 x^3 + \beta_3 x^4 + \beta_4 x^5 + \ldots \tag{3-31}$$

and finds the following expression for ω as solution of (3-30):

$$\omega(c) = \frac{2}{\pi}\beta + \beta_1 c + \frac{4}{\pi}\beta_2 c^2 + \frac{3}{2\pi}\beta_3 c^3 + \frac{16}{3\pi}\beta_4 c^4 + \ldots \tag{3-32}$$

If the normal velocity V_n is given as a function of time t, it is possible to determine c=c(t) from Eq. (3-29b). The contour of the free surface is then determined by solving the equation (3-28) where c (t) is known.

By applying the previous methodology to a wedge of deadrise α, the following expressions are obtained:

$$\begin{cases} \eta_b = \tan\alpha\, x \text{ which leads to the following expression} \\ \omega(c) = \dfrac{2}{\pi}\tan\alpha \quad (\omega \text{ is here constant}) \\ \eta = \displaystyle\int_{c=0}^{c\le x} \frac{\frac{2}{\pi}\tan\alpha}{\sqrt{1-c^2/x^2}}\,dc = \frac{2}{\pi}x\tan\alpha\arcsin\left(\frac{c}{x}\right) \text{ for a given width } 2c \\ c = \dfrac{\pi}{2}\cot\alpha\displaystyle\int_0^t V(t)dt + K = \frac{\pi}{2}\cot\alpha\ z(t) = \frac{\pi}{2}x(t) \end{cases}$$

If the wedge pit is Δz under the calm free surface, the wetted surface considered by Wagner for the calculation of the force is

$$c = \frac{\pi\cot\alpha}{2}\Delta z\,,$$

whereas it is estimated by Von Karman to $c = \cot\alpha\,\Delta z$. This inevitably leads to a higher force in Wagner's calculation.

By approximating the mass per unit length of the induced water by half the mass of fluid contained in a circular cylinder of diameter 2c, the rate of change of the induced mass can be written as a function of c and ω:

$$\frac{dm_{water}}{dz} = \frac{dm_{water}}{dc}\frac{dc}{dz} = \frac{\pi\rho c}{\omega} \tag{3-33}$$

From (3-33), (3-20b) can be re-written as follow:

$$F = -\frac{\pi \rho c V_0^2}{\omega(1+\mu)^3} \tag{3-34}$$

$$\text{where } \mu = \frac{m_{water}}{M_{body}} \text{ and } \omega = \frac{dc}{dz}$$

From the geometry of the impactor and the boundary conditions/kinematics of the impact, it is possible to make a first estimation of the global effort applying on the impacting body by using Eq. (3-34). Wagner introduces additionally correction for large deadrise angles to better approximate the experimental results. Fabula [38] extended the Wagner's approximation by fitting ellipses instead of an extending flat plate to the wetted portion of a two dimensional body. The basis idea of ellipse fitting is a better approximation to the shape of the wetted contour, which eliminates the corrections linked to large deadrise angles. He applied this method to elliptic cylinders and wedges (Figure 3-6).

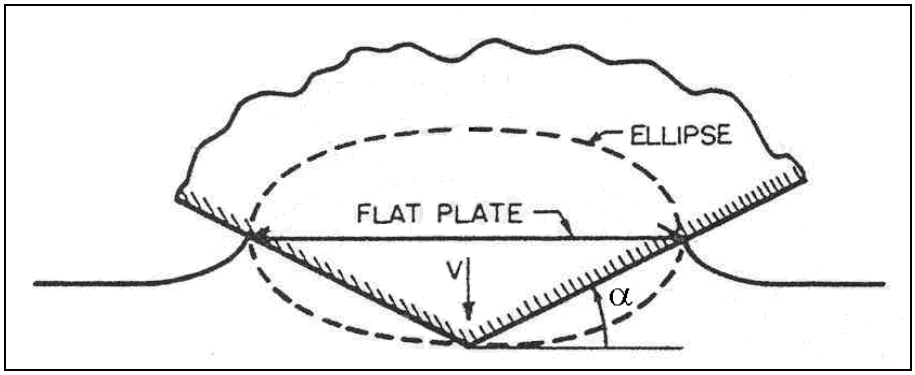

Figure 3-6 : Normal symmetric impact of wedge of deadrise angle α showing ellipse fitting by Fabula [38]

Nevertheless the previous methods do not furnish the pressure distribution on the body which is of real importance for the designer. The intuitive work of Wagner, applicable for wedge with small deadrise, has been put 50 years later on a firm theoretical basis using the method of matched asymptotic expansions by Cointe [39, 40]. Following [40], it is concluded that the wetting correction introduced by Wagner is very important and can double the effective penetration depth. Additionally, the maximum impact pressure is always reached in the vicinity of the water line and is equal to ½ ρ $(dc/dt)^2$, where c is the half wetted width of the structure. With this theoretical background, it is possible to calculate a pressure distribution.

Numerous publications about the calculation of impact forces and therefore of the added mass for various body shapes using the matched asymptotic expansion method are available. In [41,42], the added mass of two dimensional bodies (wedge, parabola and wedge with flattened end) is analytically assessed and results for a wedge and a parabola are shown in Table 3-2. For the impact of wedges with larger deadrise angles at constant velocity, Zhao and Faltinsen [30] present solutions of the free surface elevation and the pressure variation for a larger range of deadrise angles than Wagner/Cointe covering angles between 4° and 81°. To that aim, they use a nonlinear boundary element method with a jet flow approximation. Water entry of circular cylinder relevant to offshore structures and pipeline are studied by Greenhow [43], Greenhow and Yanbao [44] and Cointe [39]. In all these works, the effects of gravity,

viscosity, compressibility and air cushion are neglected. The impacting structures are considered rigid and the flow around the structure and especially the jet flow are of interest. This latter is important for the calculation of the maximum loads, which occurs in the region of the jet.

Body shape	Wetted length "c"	Pressure distribution
$f(x) = \tan\alpha \; x$ 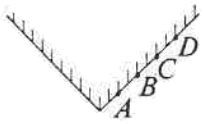	$\frac{\pi}{2}\frac{Vt}{\tan\alpha}$	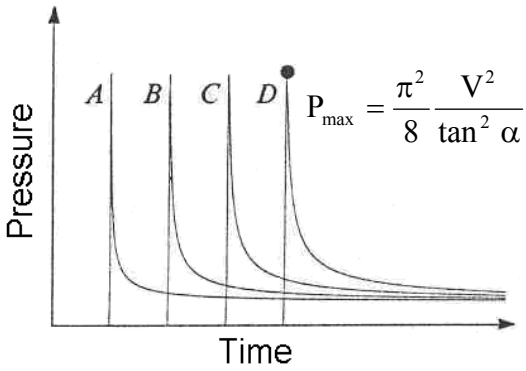
$f(x) = a\,x^2$ 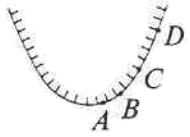	$\sqrt{\frac{2Vt}{a}}$	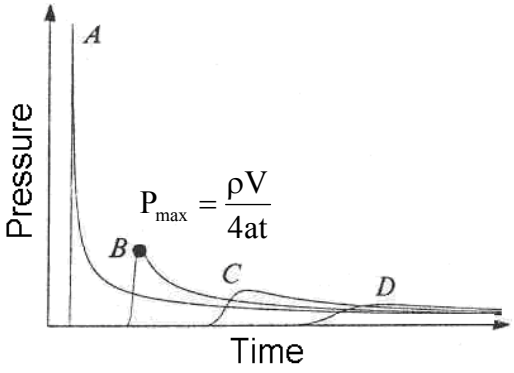

Table 3-2 : Analytic results for the pressure distribution of various two-dimensional bodies resulting from impact on water (based on [41])

3.2.4 Collopy's approach for three dimensional bodies

Following the same procedure as Von Karman, Collopy [36] proposed expressions to determine the force behaviour applying on a three-dimensional impactors of revolution. To that aim, he makes the same assumptions as Von Karman:

- the gravitational force, the buoyant force, the friction drag, the viscosity and the surface tension effects are negligible,
- the impacting body is rigid,
- the fluid is incompressible.

He deduces the expression impact force F and the velocity during impact of the impactor by applying the conservation of momentum. He approximates the added mass of a revolution body to half that of an expanding fully submerged disk. According to Lamb [45], the added mass of a fully submerged disk of radius r is defined by $8\rho r^3/3$. As half of the disk is in contact with water, this leads to the following added mass for a body of revolution:

$$m_{water} = \frac{4\,\rho\,r^3}{3} \tag{3-35}$$

where r is the radius of the body at the intersection with the undisturbed water free surface (Figure 3-7). The vertical velocity is deduced from the conservation of momentum (§ 3.2.1) and is given by

$$\dot{z} = \frac{dz}{dt} = \frac{1}{1 + \frac{m_{water}}{M_{body}}} V_0 \tag{3-36}$$

where V_0 is the impact velocity, M_{body} the mass of the impactor, m_{water} the induced mass of water and z the penetration distance of the body in water.

Depending on the shape of the impactor and the penetration distance, it is possible to calculate the wetted width r analytically. The force F can be calculated using Eq. (3-20a) and t from Eqs. (3-36) and (3-35). Comparisons of the calculated forces with test results are presented in Appendix B.

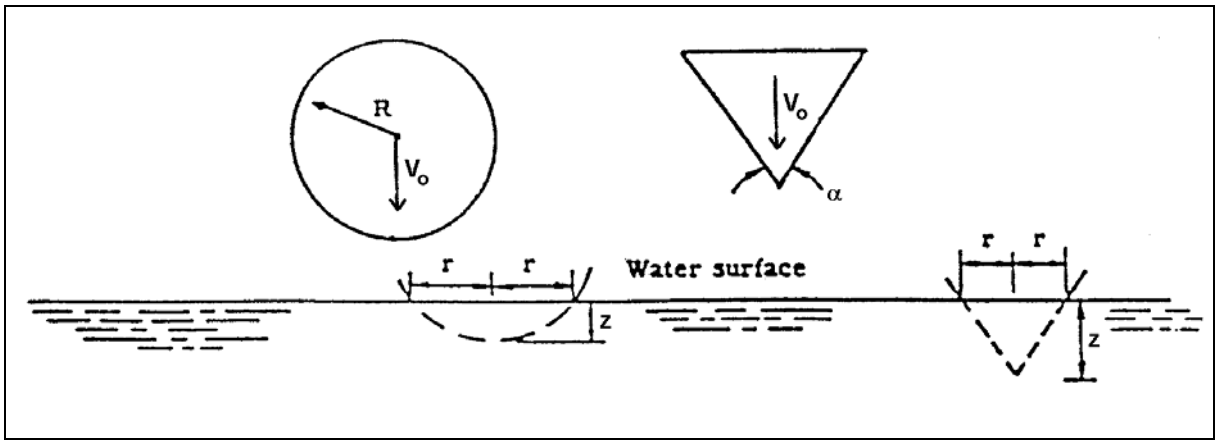

Figure 3-7 : Parameters' definition for Collopy's estimate (sphere and cone) [36]

The Collopy's method gives the overall force applying on the rigid structure and no pressure distribution on the body surface in contact with water. In addition, no flow rise around the body is taken into account in the calculation.

3.2.5 Shiffman-Spencer's analysis for three dimensional bodies including corrections

Based on the conservation of momentum and assuming that the gravitational force is negligible, Shiffman & Spencer determine the force F applying on various bodies impacting on water like sphere [46] and cone [37]. They introduce the dimensionless impact drag coefficient C_d defined as:

$$F = \frac{1}{2} C_d\, A\, \rho\, V^2 \tag{3-37}$$

where A is the cross-sectional area (surface defined by the intersection of the impacting body with the undisturbed water surface), ρ the density of water and V the velocity of the sphere. C_d depends on the depth of penetration of the sphere in water and of the Reynolds number.

After some manipulations, Shiffman & Spencer come to the following definition of C_d for a sphere impacting on water:

$$C_d = \frac{dm_{water}/db}{\left(1 + 3m_{water}/8\sigma\right)^3} \tag{3-38}$$

where $$m_{water} = \frac{M_{water}}{\left(\frac{1}{2}\pi\rho R_{sphere}^{\ 3}\right)}, \sigma = \frac{M_{sphere}}{\left(\frac{4}{3}\pi R_{sphere}^{\ 3}\rho\right)} \tag{3-39a, 3.39b}$$

b is the ratio of the penetration depth of the sphere in water to its radius R_{sphere}, M_{water} the virtual mass of water, r the radius of the disk formed by the intersection of the sphere and the water free surface and M_{sphere} the mass of the sphere. σ is the effective specific gravity of the sphere relative to the liquid. It is interesting to notice that for a sphere with a very high mass ($\sigma >> 1$), the approximation $C_d = dm_{water}/db$ is valid. The expressions (3-37) to (3-39b) have been developed for a sphere and are valid until a penetration depth of half the radius of the sphere (no flow separation from the sphere).

To determine dm/db, they firstly approximate the velocity potential [47] by the flow around a lens shape for a sphere and secondly, in contrast to Collopy, introduce corrections for the rise of the free surface and for the wetted factor (ratio between the elevations of the actual and the undisturbed free surface above the lowest point of the body). Their results are presented through graphs from which C_d can be directly read knowing the depth of penetration of the sphere into water and the specific gravity of the sphere. This unfortunately supposes that the current velocity corresponding to a specific penetration is known. As a consequence, they introduce a more practical formula for the impact force F:

$$F = \frac{1}{2}\rho\, V_0^{\,2}\, C_D^*\, A \tag{3-40}$$

for which the impact velocity V_0 is considered instead of the instantaneous velocity of the sphere. The variations of C^*_D are presented in form of a graph from which the force (acceleration) applying on various sphere can be directly read. Figure 3-8 shows one of these graphs.

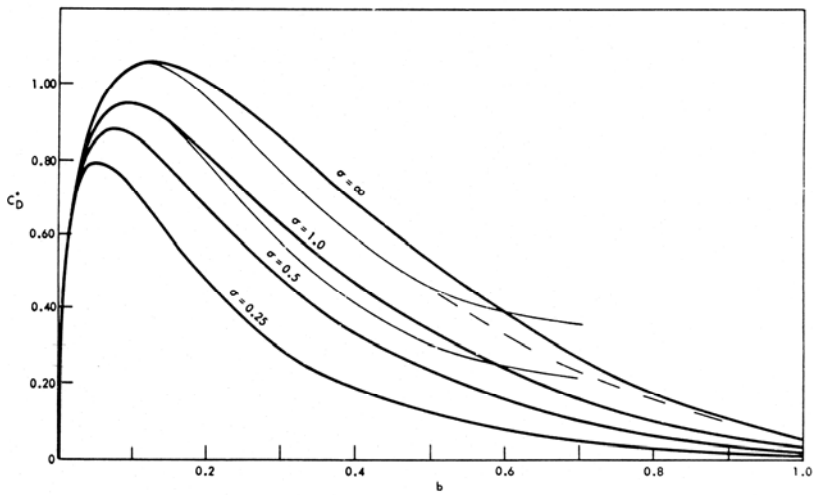

Figure 3-8 : Drag coefficient against normalised depth of immersion b
(light lines correspond to experimental results) [23]

It can be noticed that the maximum force applying on a sphere impacting on water is reached when the depth of penetration is between 10% and 20% of the radius. In appendix B, calculated results based on Shiffman-Spencer analysis are compared with test measurements. The agreement between test and calculation are very good. An analytical solution for the added mass, splash contour and wetted factor for a sphere are available in [48].

Shiffman and Spencer [37] use a similar principle to the sphere for cones with various vertex angles impacting vertically on water. They estimate the impact force F to

$$F = \frac{3M}{B(1 + M / M_0)^3} U_0^2 \tag{3-41}$$

where $M = k\rho B^3 \tan^3(\theta/2)$, k is a dimensionless constant gained from the graph in Figure 3-9, ρ the water density, B the immersion depth, θ the vertex angle of the cone and M_0 the mass of the cone. The factor k is determined by considering the flow around an expanding ellipsoid and is presented by Shiffman and Spencer in a graphic way.

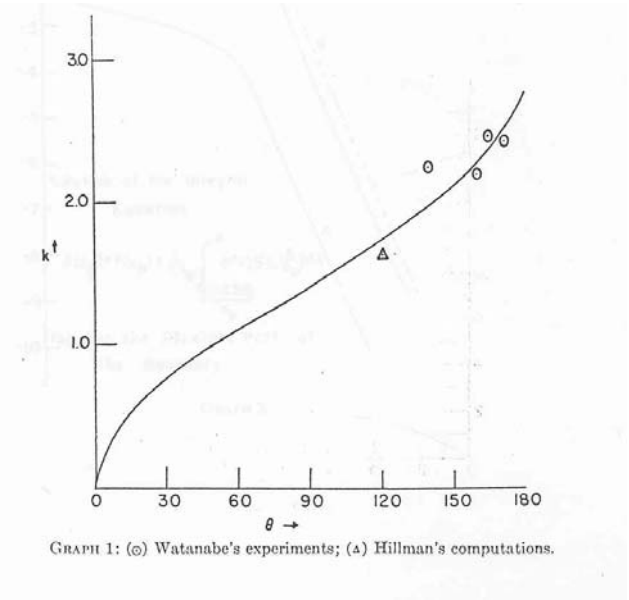

GRAPH 1: (o) Watanabe's experiments; (Δ) Hillman's computations.

Figure 3-9 : Graphical determination of factor k depending on the vertex angle θ of a cone [37]

Using the matched asymptotic expansion method, Wilson [49] and Korobkin [50] determine the analytical solution for the wetted surface and the pressure for a cone and an elliptic paraboloid. It can be noticed that the maximum pressure is also reached in the region of the jet for a cone (Figure 3-10). Finally, in [42], a numerical method is presented in order to solve the asymptotic problem for 3D arbitrary rigid geometries.

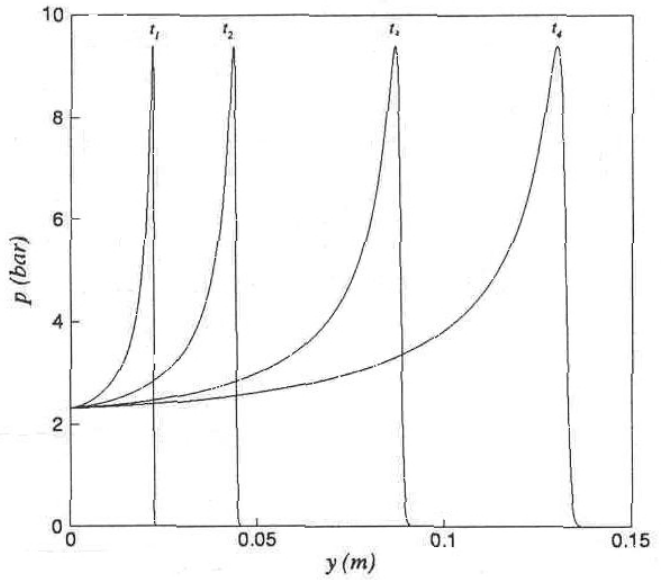

Figure 3-10 : Example of pressure distribution on a cone impacting on water at various times (y: distance between the axis and the skin of the cone) [42]

3.3 Numerical techniques for ditching simulation

As seen in the previous paragraph, it is possible to solve analytically a certain number of problems. They concern 2D- and 3D-solutions using the potential flow theory for rigid simple shapes (wedge, parabola, cylinder, sphere, cone etc…). As analytical results for arbitrary 3D geometries impacting on water and including deformation resulting from the water loads are not available, the use of numerical methods is required.

For the resolution of impact on water of 3D complex flexible structure shapes, a great variety of possible numerical treatments are available but have not been always used for the specific case of an aircraft/rotorcraft fuselage impacting on water. The following review will be restricted to techniques available at the moment in the aeronautical area. These latter can be divided into two classes:

- hybrid techniques involving simple numerical methods and semi-empirical formulas (e.g. DRI-KRASH and DITCHER codes) based on known results from tests or analytical studies for simple bodies.
- numerical techniques which are able in most cases to solve the nonlinear partial differential equations governing the fluid field through a set of algebraic equations (discretization in space and time). The limitations of the geometry of the problem are removed and nonlinearities may be taken into account. In contrast to hybrid techniques, they need different data (e.g. material behaviour, exact description of the geometry), rather than impact test results for calibration.

3.3.1 DRI-KRASH (semi-empirical procedure for water analysis)

The DRI-KRASH code (being continuously developed since 1971 by Dynamic Response Inc.) is an analytical tool, which assists in the performance of structural crash dynamics analysis of general aviation airplanes. Modified under FAA sponsorship, it has the advantage to be well recognised by the certification authorities.

DRI-KRASH models basically consist of masses, nodes and beams (nonlinear or linear), which are able to reproduce the stiffness and mass distribution of the structure. A typical DRI-KRASH model of a full-scale airplane is presented in Figure 3-11. Depending on the type of impact/crash case being investigated, additional features are available. In the case of an impact on rigid floor, floor-structure interactions are modelled with springs. Concerning the modelling of structure-water interactions either "hydrodynamic" elements or springs are introduced in the model. Finally specific springs can be used to model the impact on soft soil.

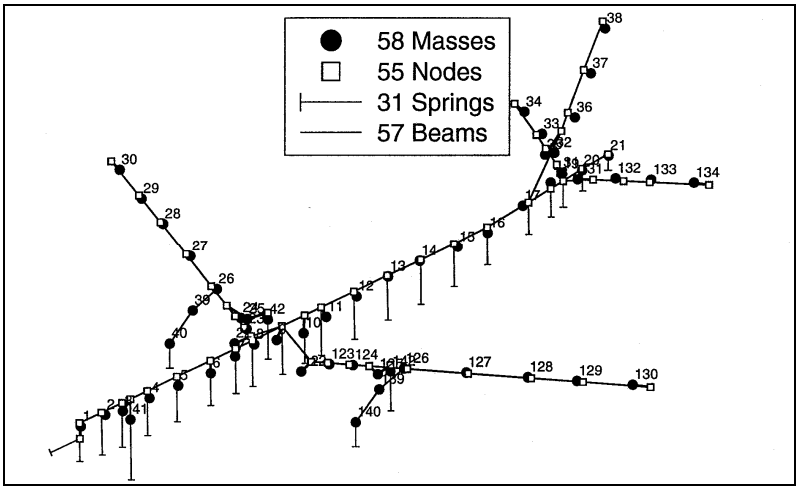

Figure 3-11 : Example of a DRI-KRASH model [51]

As the impact on water is concerned in this work, this paragraph exclusively deals with the principle of the hydrodynamic elements and "water-springs" available in the code. There are two ways of modelling impact on water in DRI-KRASH. A coupled and an uncoupled option are available as depicted in Figure 3-12.

The coupled option is based on two models: a lift surface model and a drag surface model. The uncoupled one uses springs to model vertical reaction of the water and drag surface models to model horizontal reaction as in the coupled option.

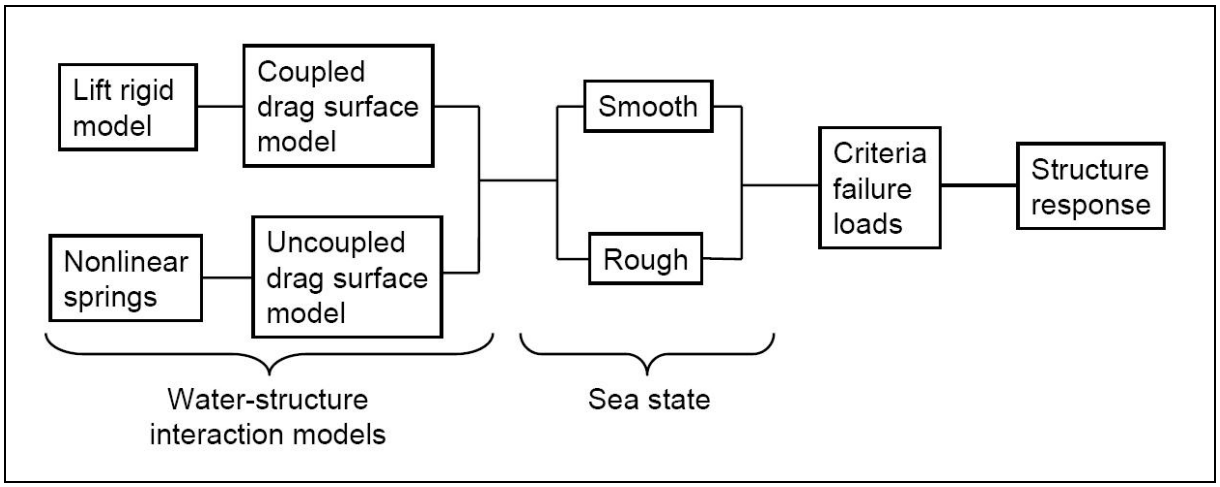

Figure 3-12 : Modelling water-structure interaction in the hybrid code DRI-KRASH (Version 9601 [52])

3.3.1.1 Principle of the water impact module

The **lift surface model** [52] is based on the studies of planning surface developed by Mercier [53] for seaplanes, where a 3D-float having the shape of a wedge is concerned. For the case of impact with smooth water, it is assumed that:

- the trim remains constant throughout the impact.
- the inertia forces are predominant (gravity and viscous forces are neglected and consequently the loads act normal to the keel).
- the float is weightless (the wing lift support the weight of the float during the impact).
- the virtual mass is a function solely of the geometry of the float in contact with water ($m_w = f(z)$).
- the water surface is initially smooth.

Based on these assumptions, Brown [54] states that the resultant force normal to the keel is equal to the total rate of change of the momentum of virtual mass of fluid. This latter can be additionally split into a rate of change of momentum of virtual mass m_w moving with the float and a rate of shedding of momentum of the virtual mass of wake and splash. This leads to:

$$F_y = \frac{d}{dt}\left(m_w \frac{dy}{dt}\right) + \left(\frac{dm_w}{dL}\right)\frac{dx}{dt}\frac{dy}{dt} \tag{3-42}$$

As the motion of the float is determined by the differential equation

$$-\frac{d^2y}{dt^2} = \frac{\cos\tau}{a+\mu}\frac{d\mu}{dz}\left(\frac{dy}{dt}\right)^2 \tag{3-43}$$

the following expression for the reaction load normal to the planning surface F_y in the case of a constant velocity component parallel to the keel is given by:

$$F_y = \frac{1}{1+\mu} m \cos\tau \frac{d\mu}{dz}\left(\frac{dy}{dt}\right)^2 \tag{3-44}$$

where m is the mass of the planning surface, μ the ratio of virtual water to m, z the instantaneous penetration depth, dy/dt the velocity perpendicular to the keel of the planning surface.

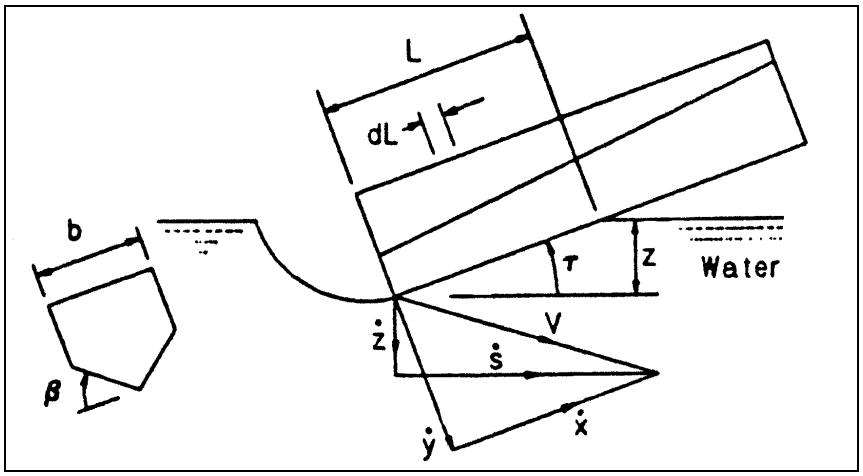

Figure 3-13: Lift surface models used for the hydrodynamic elements [53]

Expressing F_y as a function of the vertical and horizontal velocity components (z- and s-directions in Figure 3-13) leads to the relation used to calculate the hydrodynamic lift surface force in DRI-KRASH.

$$F_y = m\cos\tau\left[\cos^2\tau\,K_z\left(\frac{dz}{dt}\right)^2 + 2\cos\tau\sin\tau\,K_{zs}\frac{dz}{dt}\frac{ds}{dt} + \sin^2\tau\,K_s\left(\frac{ds}{dt}\right)^2\right] \quad (3\text{-}45)$$

$$\text{where } K_z = \frac{1}{1+\mu_z}\left(\frac{d\mu}{dz}\right)_z \quad (3\text{-}46)$$

$$K_s = \frac{1}{1+\mu_S}\left(\frac{d\mu}{dz}\right)_s \quad (3\text{-}47)$$

$$K_{zs} = \frac{1}{1+\mu_{zs}}\left(\frac{d\mu}{dz}\right)_{zs} \quad (3\text{-}48)$$

The virtual masses in the expressions (3-46) to (3-48) are calculated differently. They are each applicable for restricted impact conditions.

In the expression of K_z, the added mass is derived from the theory of planning surface (high forward velocity, zero vertical velocity) by Mercier [53] and Brown [54] and is evaluated from the following empirical relation

$$\mu_s = \frac{0.6\,\rho}{m}\frac{(1-\sin\tau)\cot^2\beta}{\sin\tau\ \cos\tau}z^3 \quad (3\text{-}49)$$

where ρ is the density of water, m the mass of the impactor, β the deadrise angle, τ the trim angle relative to the horizontal and z the instantaneous penetration distance (Figure 3-13).

In $K_{s,}$ the added mass is calculated by using Collopy's expressions for the sphere or a cone impacting on water vertically. As an example, the estimated induced mass of a sphere impacting on water is calculated with (3-50) in DRI-KRASH.

$$\mu_z = \frac{4\rho}{3m}\left(2Rz - z^2\right)^{\frac{3}{2}} \quad (3\text{-}50)$$

where R is the radius of the sphere.

Finally K_{sz} is determined from the following weighted average.

$$\frac{1}{1+\mu_{zs}}\left(\frac{d\mu}{dz}\right)_{zs} = \frac{V_z}{V_t}K_z + \frac{V_s}{V_t}K_s \quad (3\text{-}51)$$

$$V_t = \sqrt{V_z^2 + V_s^2} \quad (3\text{-}52)$$

where V_z is the vertical velocity of the lift surface model, V_s the horizontal velocity of the lift surface model and V_t the total velocity .

The determination of the drag loads in **the drag surface model** is based on surfaces standing perpendicular to the horizontal velocity or defined with an inclination towards the vertical

axis as shown in Figure 3-14 [52]. Each of these surfaces is defined by a lower curved surface of radius R and two lateral limit lines defined by BLI and BLO.

The input data of each drag surface consist of the radius R, the position of the lateral lines, the position to the mass to which it is attached, a drag coefficient and the failure pressure.

The hydrodynamic drag force is then calculated by:

$$C_D = \frac{1}{2} \rho_{water} V_n^2 A C_D \tag{3-53}$$

where ρ_{water} is the density of water, V_n the normal velocity to the drag surface and A the submerged area of the drag surface. At each time step, the program calculates the current submerged area of the drag surface and subsequently the drag force. Each hydrodynamic drag surface is linked to a single mass in the DRI-KRASH model and stands predominantly normal to the horizontal velocity.

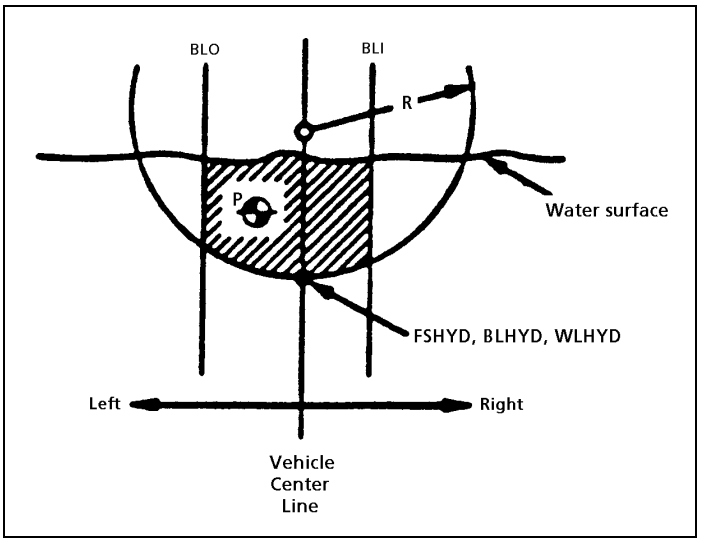

Figure 3-14 : Drag surface models used for the hydrodynamic elements [55]

3.3.1.2 The coupled option

The coupled option consists in using so-called hydrodynamic elements. Each of them is defined by up to two lift surface models and up to two drag surface models. The lift surface model is mainly responsible for the vertical deceleration whereas the drag surface model is mainly responsible for the horizontal deceleration. Both lift and drag surface models are coupled in the program as depicted in Figure 3-15.

When two lift surface models and two drag surface models in a hydrodynamic element are defined, they are activated in the following way. At the beginning of the impact on water, only the primary lift surface model is active. The structure only undergoes vertical loads and drag loads are neglected. It is implied that the structure is still undamaged.
In a second step, when the maximum pressure given in the input card of the lift surface model is reached, the primary lift surface model fails and lift loads are then modelled by the secondary lift surface model. As DRI-KRASH very strongly derives from practical experience of its developers, a drag surface model called primary drag surface model becomes then active. This corresponds to the moment at which the structure skin has failed and

therefore drag loads very strongly increase due to the leakage of water in the structure (the water flow against vertical obstacles). The next step corresponds to the moment at which the primary drag surface model fails (maximum pressure reached) and is replaced by the secondary drag surface model. Both the secondary lift and drag surface models are active till the secondary lift surface model fails. At that moment, only the secondary drag surface models acts on the structure and no lift loads are applying anymore.

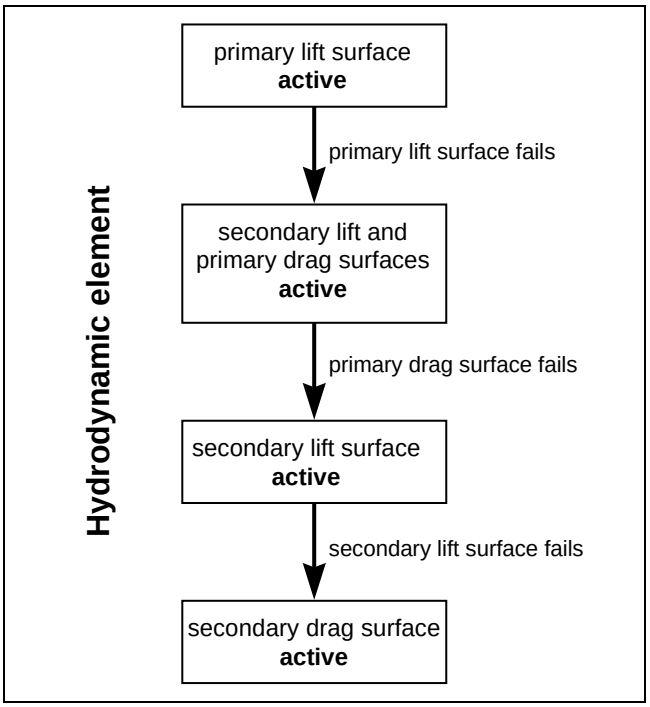

Figure 3-15 : Principle of the coupled option

In addition, it is possible to consider only the drag of a hydrodynamic element to model the drag of protuberances like engine nacelles, landing gear, etc..., which do not produce any lift. In this case the primary and secondary lift surface models as well as the primary drag surface model are defined as failed from the beginning.

3.3.1.3 The uncoupled option

The uncoupled option (Figure 3-16) available in DRI-KRASH to model the water-structure interactions consists in using two external springs in series at each mass concerned. One spring attached to the structure mass is responsible for the structure deformation and the other one for the water free surface action on the (un)deformed structure.

Drag forces responsible for the structure deceleration in the horizontal direction are still modelled with drag surfaces as described in the previous paragraph. Both spring deformations and drag models are acting independently from each other. In addition as many drag surface models attached to a single mass can be defined, in contrast to the coupled option for which only two were possible.

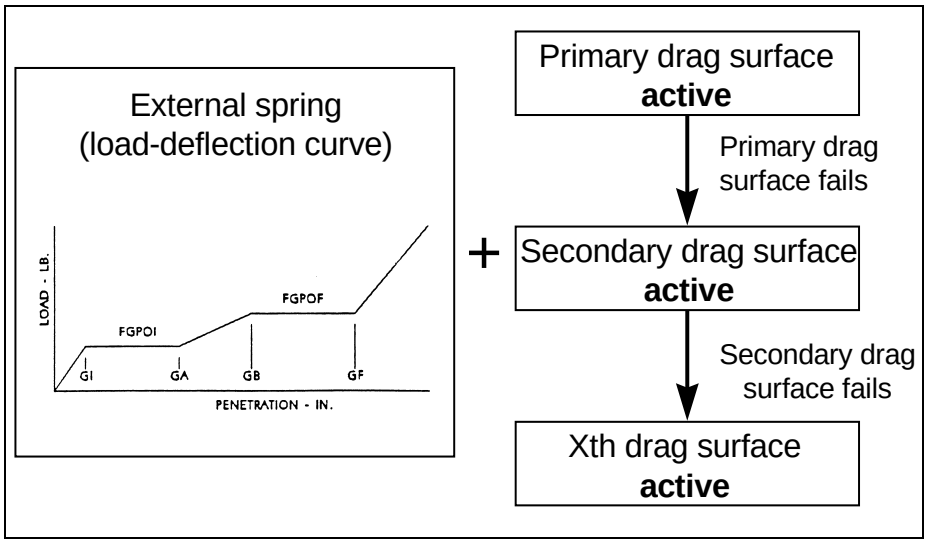

Figure 3-16 : Principle of the uncoupled option

Within this option, it is possible to simulate the structural deformation but the structure as well as the water spring characteristics have to be known. This implicitly supposes that information about the structure behaviour during impact on water is known. In addition, this option does not give the possibility to consider the state of the water surface (smooth or rough), which very strongly influences the behaviour of a structure impacting on water

3.3.1.4 Advantages and disadvantages of the code

Advantages

- the code is very attractive from the point of view of computation time, which can vary from some seconds to an hour on a PC depending on the size of the model.
- the coupled option enables the simulation of the impact on rough water. Different sea state conditions can be very easily described in the code by the definition of the wave characteristics (wave height, wavelength, orientation, propagation velocity).
- a DRI-KRASH model gives the possibility to assess the global behaviour of a whole structure.

Disadvantages

- from the geometry point of view, it is not easy to model the geometry of the structure part in contact with water through springs (uncoupled option) or with hydrodynamic elements (coupled options). The decision should be made at which masses these features should be attached.
- it is necessary to roughly know the chain of events to rationally define the characteristics of the hydrodynamic elements. This strongly influences the rupture sequence and therefore the global behaviour of the model during the impact.
- it is not possible to assess the local damage of the structure because the drag and lift surfaces (coupled option) are rigid elements. The same applies for the uncoupled option.
- previous experiences in design and on former structure behaviour are necessary to use properly the code.

3.3.1.5 Some applications

DRI-KRASH simulation results of the impact on water of a UH-1H helicopter are available in [56], which shows the technique to generate the DRI-KRASH model. The overall structural stiffness is checked by comparison with a FE model and the structural response of the helicopter can be verified by comparison with full-scale tests conducted on the structure or components with similar design. The hydrodynamic elements are placed according to the geometry and the location of expected damage. Their definitions are based on the panel properties and the user judgment, which need a certain experience.

After improvement of the model, the code is very useful to conduct parameterised studies. It is very easy to carry out changes in the model in order to investigate the influence of global parameters (masses, stiffness variation, etc…) which is not possible with the FE technique. The computation time remains very low: 1 to 2 minutes computation on a PC for a model composed of 138 masses, 290 beams, 37 node points and 27 hydrodynamic surfaces. Other DRI-KRASH analyses of water impact compared with tests are available in [57] for the ditching investigation of the V-22 Osprey.

3.3.2 DITCHER code

The DITCHER [58] code developed by D2M for EUROCOPTER France assumes the helicopter structure to be rigid during ditching. The input parameters necessary for the computation of the ditching event are the following:

- helicopter speed (longitudinal, vertical),
- wave speeds and direction (a wave model is also included in order to include a kinematic representation),
- helicopter attitude (roll, pitch and yaw angles),
- lift forces which may be constant or time-dependent,
- known quasi-static behaviour of floats under progressive penetration in water from computation or measurements.

The external forces acting on the helicopter and considered for the calculation include the helicopter weight, the lift force, the hydrostatic fluid force obtained from hydrostatic pressure and the dynamic fluid force gained itself from a hydrodynamic model.

The time dependent **hydrostatic forces** are computed by direct integration over the instantaneous submerged volumes. The centre of buoyancy is also determined.

The **dynamic fluid forces** are computed from a hydrodynamic model, for which the evaluation of the relative motion between fluid and body based on motion parameters of the COG and wave parameters is necessary. The time varying hydrodynamic force is expressed under the form of the so-called Morisson equation, which is used in the DITCHER code under the following form:

$$F_{hyd}(t) = \rho.W.C_m.\frac{d\vec{V}_{RM}}{dt} + \frac{1}{2}\rho.S_T.C_d.\vec{V}_{RM}.\left|\vec{V}_{RM}\right| \qquad (3\text{-}54)$$

where ρ is the water density, W the displaced volume, C_m an added mass coefficient matrix, V_{RM} the velocity of any point M of the body relative to water including wave kinematics, S_T

the exposed area under the basic body and C_d a drag coefficient matrix. The matrixes C_m and C_d are dependent on the shape of the wetted body, which itself depends on time.
The strip theory is applied in order to simplify the calculation. This means that the helicopter and its floats are assumed slender enough to approximate the flow at each section or strip of the bodies locally two-dimensional. This assumes that at each instantaneous position of the water line, the hydrodynamic coefficients of each strip shape are tabulated (known from analytical expressions or from 2D hydrodynamic models based on Von Karman approach). Knowing these instantaneous coefficient values along the bodies and the position and velocity of each section relative to water including wave kinematics, it is possible to calculate the hydrodynamic force on each section of the helicopter and its floats in contact with water and then compute the forces applying on the whole immersed part of the helicopter. Finally, the equations of motion are solved in order to determine the new position, rotational and translational speeds of the COG and deduce the new attitude of the helicopter. The code was validated by a full-scale ditching test conducted with a SUPER PUMA helicopter.

3.4 Advanced numerical techniques

A lot of numerical methods have been developed or adapted to the impact on water during the last 40 years. This includes the use of equivalent external static pressures, which are applied to the structure in order to simulate the hydrodynamic loads. In [59], this method was employed to verify the integrity of the skin panels of the Space Shuttle. At the same time, codes involving panel methods are extended in order to take into account for the presence of a free surface. In [60], based on linear flow theory the flow of air and water around an aircraft is simulated by correcting the lower flow describing the water by accounting for the density differences between air and water. In [61], the panel method is extended in order to analyse hydrodynamics in the presence of a free surface. These are a non-exhaustive list of some techniques applied in the aeronautical area to simulate water impact aspects. Finally, in the 90's a new generation of codes emerged involving the coupling between finite volumes for the fluid and finite elements for the structure. These are the beginning of the so-called Euler/Lagrange coupling. The following will focus on this class of codes, which are currently used nowadays to treat problem of fluid-structure interactions (FSI). Nevertheless, their use for extensive industrial application like impact on water with detailed structural models for the aircraft has not yet been published. This may be due to limitation in computation time or treatment limitation between the Lagrangian and Eulerian meshes.

In continuum mechanics, two descriptions are possible to describe the motion in a media: the Eulerian and the Lagrangian descriptions. These latter differ from each other due the reference co-ordinate system, in which the equations of motion are written. Fluid analyses are traditionally described in a Eulerian formulation with a spatial coordinate system and structural analyses in a Lagrangian formulation with a coordinate system fixed in the structure. The next step consists of the coupling e.g. the transmission of the contact forces and/or displacements between the fluid and the structure described with different formulations and therefore computed with different solvers.

3.4.1 Lagrangian, Eulerian and ALE formulations

Consider a body B occupying at time t = 0 a region R_{S0} with boundary ∂R_{S0} corresponding to the initial or reference configuration. The boundary ∂R_{S0} is divided into two parts, ∂R^{v}_{S0}

where the velocity is specified and ∂R_{S0}^{t} where the traction vector is specified. The index "0" indicates the time t = 0 (corresponding to the initial configuration). The movement of the body B described by the function φ (Figure 3-17) transforms at time t the reference configuration R_{S0} into the current configuration R_S with boundary ∂R_S.

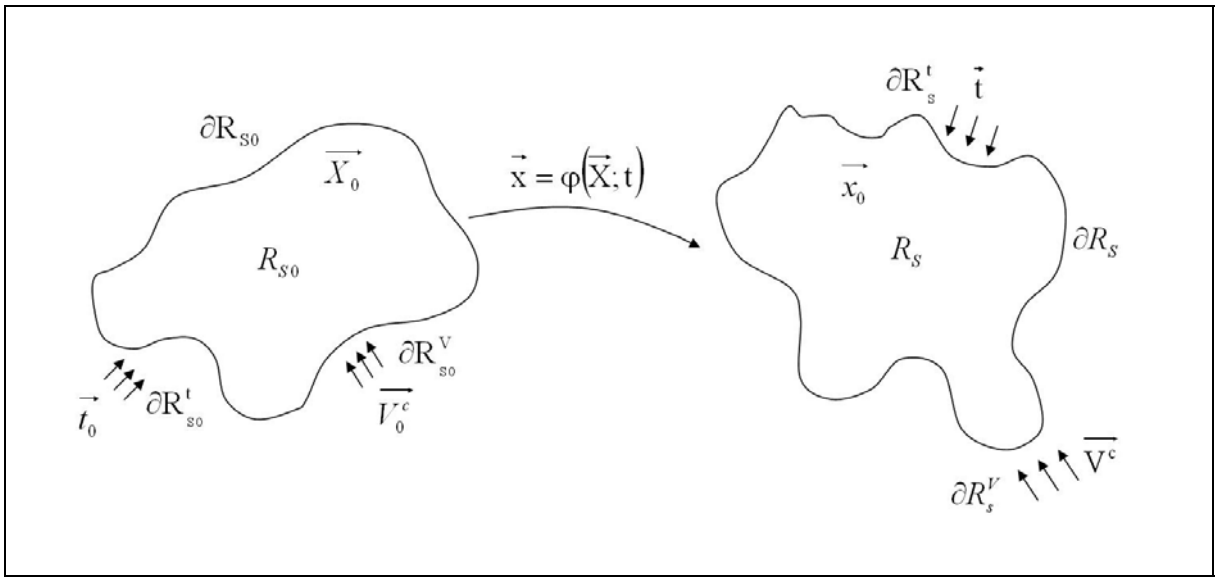

Figure 3-17 : Definition of the initial and current configurations

3.4.1.1 Lagrangian formulation for the structure

In the Lagrangian description, a volume of identified material, moving in the space during the course of time, is of interest. In this formulation, this volume changes in shape while its mass remains constant e.g. the material shape coincides with the shape of the elements. The mesh of the computational domain moves with the particle velocities e.g. it coincides with material points and has time dependent coordinates. This formulation is interesting in solid mechanics, because boundary conditions can be very easily defined (The mesh is coincident with the physical material domain). The structural deformations remain in most of the cases small enough to use the Lagrangian formulation. If the initial position of a particle of material at time t_0 is defined by $A(X_0,Y_0,Z_0)$, a physical quantity measured at the location of this particle A after an elapsed time $t\text{-}t_0$ is given by $f(X_0,Y_0,Z_0,t\text{-}t_0)$. As a consequence the material time derivative of a field quantity (scalar, vector or tensor) is equal to the partial time derivative of the field quantity:

$$Df / Dt = \partial f / \partial t .$$

In the Lagrangian approach, the conservations of mass and energy are automatic. Only the equations of momentum have to be solved.

The equations (strong form) governing the motion of a structure in the Lagrangian formulation and the applied boundary conditions are established in the following.

Conservation of mass

$$\rho\left(\vec{X}, t\right) J\left(\vec{X}, t\right) = \rho_0\left(\vec{X}, t\right) J_0\left(\vec{X}, t\right) = \rho_0\left(\vec{X}, t\right) \tag{3-55}$$

ρ is the density of the structure and J the Jacobian of the transformation φ. $\vec{X}$ is the coordinate of the initial configuration (Lagrangian coordinate).

As the mesh is Lagrangian, no material moves to or out of a cell, the conservation of mass is automatically satisfied.

Conservation of momentum

$$\rho \frac{Dv_i}{Dt} = \frac{\partial \sigma_{ji}}{\partial x_j} + \rho b_i \text{ in } R_S \tag{3-56}$$

The index "i" represents the coordinate directions, v_i the velocity component and x_j the coordinate of the current configuration (Eulerian or spatial coordinates), b_i the volume force component and σ_{ji} the Cauchy stress tensor (second order stress tensor)

Constitutive law

In the case of elastic materials, the stress rate and strain rate are related by

$$\dot{\sigma}_{ij} = C_{ijkl}\dot{\varepsilon}_{kl} \tag{3-57}$$

$\dot{\sigma}_{ij}$ is the stress rate and $\dot{\varepsilon}_{kl}$ the strain rate. C_{ijkl} is a fourth order tensor called the constitutive material tensor.

$$\dot{\varepsilon}_{kl} = \frac{1}{2}\left(\frac{\partial v_k}{\partial x_l} + \frac{\partial v_l}{\partial x_k}\right) \tag{3-58}$$

Boundary conditions

$$n_j(\vec{X},t)\sigma_{ji}(\vec{X},t) = t_i(\vec{X},t) \quad \text{on } \partial R_S^t$$

$$v_i(\vec{X},t) = v_i^c(\vec{X},t) \quad \text{on } \partial R_S^v$$

t is the force imposed on ∂R_S^t and v^c the velocity imposed on ∂R_S^v. The coupling is applied on ∂R_S^t.

Initial conditions

$$\vec{v}(\vec{X},0) = \vec{v}_0(\vec{X})$$

$$\sigma_{ij}(\vec{X},0) = \sigma_{ij0}(\vec{X})$$

3.4.1.2 Eulerian formulation (Eulerian mesh fixed) for the fluid

In the Eulerian description, a particular space volume, fixed with respect to a spatial frame, is of interest. In this formulation, the material is studied as it passes through this fixed space volume, which remains unchanged during the course of the time. The mesh of the computational domain remains fixed. This formulation is especially interesting in fluid mechanics, where material displacements are very large. At a given point A(x,y,z) in space, a field quantity is given by f(x,y,z,t). The material time derivative of a field quantity (scalar, vector or tensor) is given by:

$$Df / Dt = \partial f / \partial t + \partial f / \partial x \,.\, v$$

The equations (strong form) governing the motion of a fluid in the Eulerian formulation and the applied boundary conditions are established in the following.

Conservation of mass

$$\frac{\partial \rho}{\partial t} = -\rho \frac{\partial v_i}{\partial x_i} - v_i \frac{\partial \rho}{\partial x_i} \tag{3-59}$$

ρ is the density of the structure The index "i" represents the coordinate directions, v_i the velocity component and x_j the coordinate of the current configuration. (= Eulerian or spatial coordinates).

Momentum equation for a fluid

$$\rho \frac{\partial v_i}{\partial t} = \sigma_{ij,j} - \rho v_i \frac{\partial v_i}{\partial x_j} + \rho b_i \tag{3-60}$$

b_i is the volume force component and σ_{ij} the stress tensor (second order stress tensor).

Constitutive law

The stress tensor for Newtonian fluid is composed of a hydrodynamic pressure and a viscous term

$$\sigma_{ij} = -p\delta_{ij} + \mu(v_{i,j} + v_{j,i}) = -p\delta_{ij} + 2\mu\dot{\varepsilon}_{ij}^{dev} \tag{3-61}$$

δ is the kronecker function and μ the dynamic viscosity. Whereas in solid mechanics the stress rate is a function of the strain rate, in fluid mechanics the stress is a function of strain rate $\dot{\varepsilon}_{ij}$ and/or velocity gradient.

Energy equation

$$\rho \frac{\partial E}{\partial t} = \sigma_{ij} v_{i,j} - \rho v_j \frac{\partial E}{\partial x_j} + \rho b_i v_i \tag{3-62}$$

Boundary conditions

$$n_j(\vec{x},t)\sigma_{ji}(\vec{x},t) = t_i(\vec{x},t) \quad \text{on } \partial R_F^t$$

$$v_i(\vec{x},t) = v_i^c(\vec{x},t) \quad \text{on } \partial R_F^v$$

t is the force imposed on ∂R_F^t and v^c the velocity imposed on ∂R_F^v.The coupling is applied on ∂R_F^t.

Initial conditions

$$\vec{v}(\vec{x},0) = \vec{v}_0(\vec{x})$$

$$\sigma_{ij}(\vec{x},0) = \sigma_{ij0}(\vec{x})$$

In contrast to a Lagrangian mesh, it should be kept in mind that the Euler mesh should be large enough to contain the material after deformation.

3.4.1.3 ALE formulation (Eulerian mesh movable) for the fluid

The Arbitrary Lagrange-Euler (ALE) technique combines both Lagrangian and Eulerian approaches. The mesh moves and the material "flows" through the moving mesh. An arbitrary

referential coordinate system is introduced in addition to the Lagrangian and Eulerian coordinates. The material derivative of a function f with respect to the reference coordinate is given by:

$$\frac{Df}{Dt} = \frac{\partial f(X_i, t)}{\partial t} = \left(\frac{\partial f^{ALE}}{\partial t} \right)_{\bar{\chi}} + w_i \frac{\partial f(x_i, t)}{\partial x_i}$$

where X_i is the Lagrangian coordinate, x_i the Eulerian coordinate, w_i the relative velocity. This so-called convective velocity, is defined by **w** = **v**-**u** where **v** is the velocity of the material and **u** the velocity of the mesh.

The equations (strong form) governing the motion of a fluid in the ALE formulation and the applied boundary conditions are established in the following. This formulation is based on three domains (Figure 3-18): a reference domain (or ALE domain) R_χ, a standard material domain R_X (Lagrangian) and a spatial domain R_x (Eulerian). The standard material and spatial domains respectively correspond to the initial and current configuration introduced at the beginning of this paragraph.

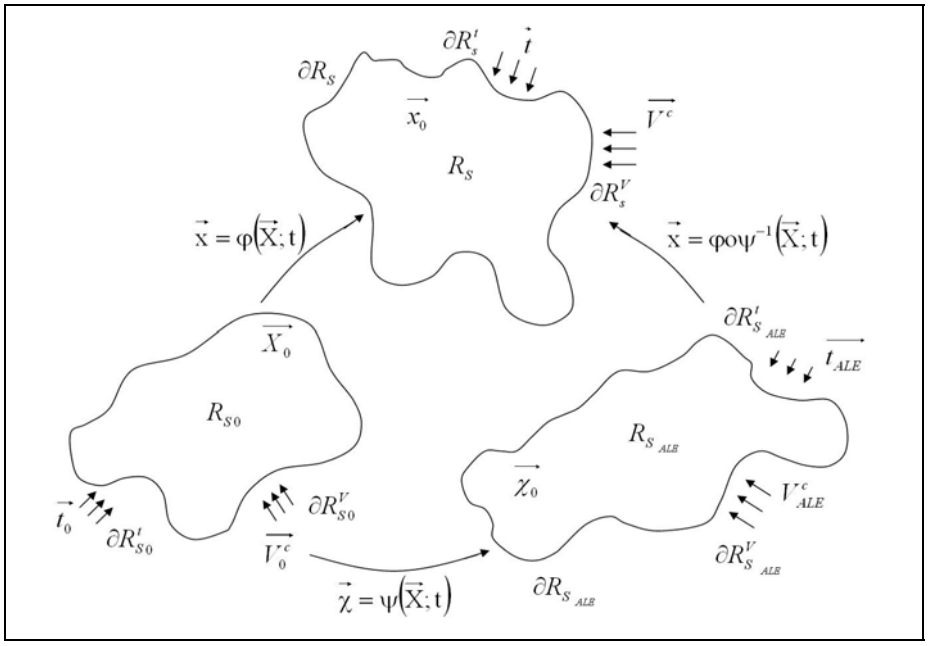

Figure 3-18 : Definition of the initial, current and arbitrary configurations

Conservation of mass

$$\left(\frac{\partial \rho^{ALE}}{\partial t} \right)_{\bar{\chi}} = -\rho \frac{\partial v_i}{\partial x_i} - w_i \frac{\partial \rho}{\partial x_i} \tag{3-63}$$

Momentum equation for a fluid

$$\rho \left(\frac{\partial v_i^{ALE}}{\partial t} \right)_{\bar{\chi}} = \sigma_{ij,j} + \rho b_i - \rho w_i \frac{\partial v_i}{\partial x_j} \tag{3-64}$$

The stress tensor is composed of a hydrodynamic pressure and a viscous term

$$\sigma_{ij} = -p\delta_{ij} + \mu(v_{i,j} + v_{j,i}) = -p\delta_{ij} + 2\mu d_{ij}^{dev} \tag{3-65}$$

Energy equation

$$\rho\left(\frac{\partial E^{ALE}}{\partial t}\right)_{\vec{\chi}} = \sigma_{ij} v_{i,j} + \rho b_i v_i - \rho w_j \frac{\partial E}{\partial x_j} \tag{3-66}$$

Constitutive law for a Newtonian fluid flow

$$\sigma_{ij} = 2\mu e_{ij}^{dev} - p\delta_{ij} \tag{3-67}$$

δ is the kronecker function, μ the dynamic viscosity

Boundary conditions

$$n_j(\vec{\chi}, t)\sigma_{ji}(\vec{\chi}, t) = t_i(\vec{\chi}, t) \quad \text{on } \partial R_F^t$$

$$v_i(\vec{\chi}, t) = v_i^c(\vec{\chi}, t) \quad \text{on } \partial R_F^v$$

where t is the force imposed on ∂R_F^t and v^c the velocity imposed on ∂R_F^v.The coupling is applied on ∂R_F^t.

Initial conditions

$$\vec{v}(\vec{\chi},0) = \vec{v}_0(\vec{\chi})$$

$$\sigma_{ij}(\vec{\chi},0) = \sigma_{ij0}(\vec{\chi})$$

The extra term in the conservation of mass and momentum equations involving the relative velocity **w** in Eq. (3-63), (3-64) and (3-66) is called advective term. It accounts for the transport of material through the mesh. These equations can be numerically solved in two ways. The first method consists in fully solving the coupled equations in “one” step. Only one material can be handled in an element with this approach according to [62]. The second method known as a split operator technique consists in dividing the calculation into two phases for each time step. First, a Lagrangian calculation is performed in which the mesh moves with the material. The changes in velocity and internal velocities due to internal and external forces are computed. In this phase, the mass is automatically conserved. In the second phase, the advection phase, the transport of mass, internal energy and momentum across cell boundaries are computed. This can be seen as remapping the mesh to its original or arbitrary position. This phase is characterized by the transport of physical quantity from the Lagrangian mesh to the new mesh. Discretization details about the ALE technique are available in [63, 64]. In that case, the fluid problem can be solved in a first phase with a finite element method and then with a finite volume method for the advection phase.

The Eulerian equations are derived from (3-63) to (3-66) by assuming that the velocity **u** of the reference configuration is zero e.g. the mesh is fixed. The relative velocity between the material and reference configurations is therefore the material velocity. In the Lagrangian description, the velocity of the reference configuration is the velocity of the material e.g. the convective velocity is null.

3.4.2 Principle of the contact algorithms

The aim of the contact algorithms is to prevent the nodes of one mesh from penetrating the element(s) of another mesh or the nodes to interpenetrate the element of the same mesh. They can be decomposed into two sub-phases:

- detect and locate the contact/impact boundaries (contact search algorithm)
- impose the condition of contact/impact, sliding/friction and separation (contact interface algorithm).

The notions of slave and master are commonly used. The nodes of the slave interface are checked as they move towards the nearest element of the master interface. If penetration of the nodes is detected, a normal force is applied to prevent further penetration and remove it. Depending on the nature of the contact, one-sided or two-sided, the slave nodes belong to the slave interfaces and the master nodes to the master interface, whilst for two-sided interface no distinction is made between slave and master interfaces. The forces at the interface are calculated only if the contact is detected.

Let us consider a two-dimensional contact case (The three-dimensional contact case works according to the same principle). Assuming a slave node S penetrating a master segment defined by two nodes M1 and M2, the local co-ordinate system is defined by the normal (z-direction) and the tangent (x-direction) to the master segment. By considering only the normal force to the master segment, when the system is in equilibrium, the force applying on the slave nodes $F_{M->S}$ is equal to the force applying on the master nodes $F_{S->M}$. The equations of the systems are given by:

$$F_{S->M1} = -(1-\xi)F_{M->S} \tag{3-68}$$

$$F_{S->M2} = -\xi F_{M->S} \tag{3-69}$$

$$\xi = \frac{y_S - y_{M1}}{y_{M2} - y_{M1}} \tag{3-70}$$

where y_S, y_{M1} and y_{M2} are the coordinates of the slave and master nodes in the local co-ordinate system, $F_{S->M1}$ and $F_{S->M2}$ are the reaction forces applying on the nodes M1 and M2. The aim is to calculate the contact force $F_{M->S}$. Two usual methods are presented in § 3.4.2.1 and § 3.4.2.2: the Lagrange multiplier method and the penalty method, which are commonly used in the explicit FE codes.

3.4.2.1 Lagrange multiplier method

The Lagrange multiplier method [65] introduces the following function in the momentum equation at the contact location

$$\phi = y_S - (1-\xi)y_{M1} - \xi y_{M2}$$

so that the force at the node i is then determined by $\lambda \partial\phi / \partial y_i$. The equations (3-68) and (3-69) are then expressed

$$F_{S->M1} = -(1-\xi)\lambda$$

$$F_{S->M2} = -\xi\lambda$$

This leads to

$$F_{M->S} = \lambda$$

Iterative methods are then used to determine λ. The contact force at time t = n is then determined by:

$$F^n_{M\to S} = -F^n_{S\to M} = \frac{M_M M_S}{(M_M + M_S)}\left(\frac{F^{ext,n}_S}{M_S} - \frac{F^{ext,n}_M}{M_M} + \frac{\left(v^{n-1/2}_S - v^{n-1/2}_M\right)}{\Delta t} + \frac{d^n}{\Delta t^2}\right) \qquad (3\text{-}71)$$

where the $F^{ext,n}_S$ and $F^{ext,n}_M$ are the external nodal forces applying on the slave and master nodes respectively, $F^n_{M\to S}$ and $F^n_{S\to M}$ are the contact forces acting on these nodes, d the distance between them, M_M and M_S their masses.

3.4.2.2 Penalty method

In the penalty method, the contact condition is relaxed and penetration of the slave node into the master segment is allowed. The slave node when penetrating the master segment is then subjected to a recovering force proportional to the penetration according to

$$F_{M->S} = -k(z_S - z_M) \qquad (3\text{-}72)$$

where k is a penalty factor and z_S - z_M represents the distance of penetration of the slave through the master segment. $F_{S->M}$ is applied to remove the penetration. k represents a spring stiffness and is calculated by:

$$k = \frac{\alpha K A^2}{V} \qquad (3\text{-}73)$$

where α is a scaling factor (default 0.1), K the bulk modulus, A the surface of the contact area and V the volume of the master element. It can be noticed that this method does not satisfy the zero gap condition while the Lagrange multiplier method does.

3.4.3 Coupling methods

Two different approaches are available: a fully monolithic scheme referred also as strong coupling and a partitioned or staggered procedure referred also as loose coupling. In the partitioned coupling, two different codes already existing in some cases can handle the fluid-structure interaction problem: one code solving the fluid problem and one solving the material problem. The fluid and the structure are handled sequentially. This technique is very flexible but has the disadvantage of sometimes having convergence problems [66]. In the monolithic coupling, the fluid and the structure are computed simultaneously. Compared to the partitioned coupling, the monolithic method is more precise and has an optimal convergence but is more difficult to implement. For a same time step, the monolithic method is more CPU intensive than the partitioned method. Nevertheless, both coupling procedures are successful.

Another interesting aspect of fluid-structure interactions problems is the time scales involved in the structure and the fluid system, which are quite different. As the computation time may be very important when considering coupling methods, the coupling strategy may be adapted so that a local time loop is run for the smaller time step system before realizing the coupling (e.g. transfer of the kinematic boundary conditions) with the bigger time step system.

Depending on the context and the availability of existent adequate tools, the monolithic or the partitioned procedure is implemented. In [67], Wagner described various partitioned couplings developed at the Institute of Aerodynamics and Gasdynamics at the University of Stuttgart, which couples aerodynamic and structure codes for helicopter applications (e.g. DYNROT-INROT strong coupling and FLOW-HOST weak coupling). Even a mixed monolithic/partitioned coupling is possible as in the case of the commercial explicit FE code LS-DYNA [66].

In highly non linear fluid-structure interaction problem, the aim of the coupling algorithm is mainly to transmit the forces or pressures between two formulations in the most suitable way (between a Lagrangian formulation and a Eulerian formulation or between a Lagrangian formulation and an ALE formulation). These interactions are controlled by contact algorithms, which work similarly to the ones described in § 3.4.2. The contact treatment is CPU intensive and represents very often the main part of the computation time. Like the usual contact treatment, the coupling can be divided into two phases:

- a phase of contact tracking, where the interface between the structure and the fluid is searched,
- a phase of contact computation, where the required interaction forces are calculated at the interface surface.

3.4.3.1 Contact tracking/search

Depending on the various codes, different strategies are used to locate the contact: geometrical detection and the VOF method (method of volume fractions) are the most commonly used for the water impact applications. The choice of one of them depends on the way the structure and the fluid are modelled.

When solely the water is modelled (meshed), the structure and fluid meshes are not superposed at any time of the simulation (it is assumed that the contact algorithm functions correctly). The contact interface between the structure and the fluid can then be detected by a pure geometrical search between the nodes of one mesh and the segments of the other. This is the technique used in the explicit FE code RADIOSS provided by Mecalog.

When the structure mesh is superposed to the fluid mesh, the cells of the fluid mesh may be occupied by only the structure, only by the fluid, only by void or any gas, or a combination of them. The notion of material interface, which is the equivalent of the geometric interface in the case of a contact is introduced. It acts as a boundary to the flow of material in the Eulerian mesh. In parallel, the stresses in the Eulerian elements cause forces to act on the coupling surface. These forces load then the Lagrangian mesh, which can distort. The difficulty is then to find the position of these interfaces in each fluid cell. The interface tracking can be made by using the method of volume fractions in the fluid elements/cells. In the specific case of a fluid partially occupying a cell, the interface is positioned so that it divides the element into two volumes, which correctly match the element volume fraction of the fluid. If the volume fraction is equal to 1, the cell is fully filled. If it is equal to 0, it is empty. The volume fraction with a value between 0 and 1 means the cell is partially filled. A nodal volume fraction is calculated at each node based on the fraction volumes of the elements sharing the same node. This volume fraction determines the slope of the material interface in the elements. This technique can be used to determine the position of the free surface or the position of the

structure within the cell. Its advantage is that it is possible to have more than two "materials" in one Eulerian cell. The VOF method can be divided into three steps: localize the interface, determine the position of the interface in the element and apply the "sufficient" condition at the boundary. The explicit FE code LS-DYNA [64] provided by LSTC (Livermore Software Technology Corp.) uses this technique. The advantage is that the Lagrangian and the Eulerian mesh can be generated independently from each other. In addition, the VOF method enables to solve the fluid problem in a fixed mesh, which is very interesting when large fluid motions are expected (e.g. sloshing in a moving tank [63]).

3.4.3.2 Contact computation between the fluid and the structure meshes

In most of the explicit finite element codes, the penalty or the Lagrangian multiplier coupling is used to compute the fluid-structure interaction forces. The choice of the method is independent of the interface tracking technique and the principles are very close to the ones used for treating contact within a usual FE structure model as described in § 3.4.2.

In general the fluid is considered master and the structure slave. It is nevertheless possible to inter-change the role even during a calculation. In the penalty coupling, when the penetration is determined, a recovering force is applied to the fluid particle to "replace" it out of the structure mesh. At the interface, the spring stiffness per surface unit in LS-DYNA [64] is determined by the properties of the fluid:

$$k = \frac{p_f \rho c}{\Delta t_f} \tag{3-74}$$

where c is the sound velocity in the fluid, ρ the fluid density, Δt_f the time step in the fluid and p_f a scalar factor to be defined. It should be noted that the penalty coupling allows some penetration.

By using the Lagrange multiplier method on the coupling, the interaction force applying on the structure to prevent penetration in LS-DYNA [64] is again given by (3-71) multiplied by an additional scale factor p_r.

In the following, FE results reported by several authors are discussed together with modelling strategies and codes they are using.

Aquelet notices, that depending on the angle of incidence between the structure and the water surface at impact, the spring stiffness has to be adjusted in order to better represent reality. In the FE code LS-DYNA [66], he therefore defines specifically the parameter p_r and p_f according to the angle of incidence of each structural element at impact on water. Nevertheless, the calculated value of the pressure peak remains 40% above the analytical results in the case of a wedge impacting on water (2D) whatever the coupling method used (penalty or Lagrange multiplier). He also shows that the pressure pulse varies very slightly when the coupling parameters p_r and p_f are changed.

In the simulations presented by Ribet [68], which were conducted with the explicit FE code RADIOSS, the penalty method is used to calculate the impact force applying on wedges (30°, 20°, 10° and 5° deadrise angle) and a cone (160° opening angle) impacting on water. The simulations are based on an ALE formulation for the fluid and a geometric contact detection.

The ALE formulation is mainly used to reproduce the deformation of the free surface around the impacting structure. The calculated deformation of the free surface and the calculated pressure distribution are found to be qualitatively and quantitatively comparable to test measurements. Nevertheless, the computations were prematurely aborted due to the high deformation of the water mesh leading also to a dramatic decrease of the time step. A solution to this problem could be to re-mesh the deformed region. However this task is time consuming and the re-meshing does not always improve the mesh quality due to the high deformation of the free surface ([69], [70], [71])

Finally, in a third code MSC-Dytran [72] provided by MSC Sofware, two ways are available to calculate the interaction between the Euler (finite volume) and the Lagrangian meshes (classical FE): a so-called "general coupling", where the Euler mesh is fixed, and an ALE coupling. Initially the Euler and the Lagrangian solver are entirely separate. In the general coupling, a coupling surface, which should be a closed volume, is created on the Lagrangian structural mesh. This coupling surface transfers the force between both solvers. In the ALE technique available in MSC-Dytran, the Eulerian mesh is deforming by means of the ALE moving algorithm so that it follows the structure at the contact interface. The restriction is that the Lagrangian and Eulerian grid points have to coincide in physical space at the interface surface (logically different). When the Lagrangian structure deforms or simply moves (rigid body motion), the Eulerian mesh boundary also moves. Two possibilities are then available. Only the point of the Euler mesh situated at the boundary moves or the full Eulerian mesh is allowed to deform. This type of coupling is not very simple to apply on complex structures. Anghileri [73] shows, that the computation time necessary for the simulation of the impact on water of a sphere with MSC-Dytran with general coupling was 12 times as high as with the ALE method.

An important point is that whatever the commercial code (LS-DYNA, RADIOSS, MSC-Dytran) and the coupling algorithms used, no tangential forces (friction) are transmitted between the fluid and the structure. The boundary limit effects cannot therefore be taken into account independently of the fluid behaviour law chosen (inviscid or real fluid).

3.4.4 Application to the impact of aircraft/rotorcraft structure on water

Some first trials have been conducted to simulate the impact on water of aeronautical structures using the Eulerian and Lagrangian method. It is proposed in the following to reflect some experiences and facts reported in publications concerning success and encountered difficulties.

In [71], Candy et al conduct a validation study with water impact characteristics of the Gemini capsule and the orbiter space shuttle during a horizontal fly-in using the LS-DYNA3D code, which contains an Euler/Lagrange coupling algorithm. They come to the conclusion that the water modelled with a Lagrangian mesh is too "hard" and therefore that the Euler mesh delivers better results. They also conduct the simulation of the impact of a helicopter on water by using a pure Lagrangian mesh. Unfortunately, no validations are conducted because no experimental data are available. Although the helicopter airframe model includes stringers, ribs and panel stiffeners in the lower fuselage section and is defined as deformable, the FE-model remains coarse and is in my opinion not adequate for detailed crash analysis. It

comprises 6000 elements, mainly shells, whereas the water pool was modelled with 200,000 solid brick elements. A 0.1 sec simulation needs approximately 12 hrs on a Silicon Graphics Origin 2000.

In [74] Clark and Shen reported a MSC-Dytran simulation of a Sikorsky S92 helicopter impacting on water using a Eulerian-Lagrangian coupling, where the helicopter is defined as a rigid body. They correlate the impact pressure predictions with test data recorded during scaled-model ditching tests. Whereas air and water are both modelled with 25,200 solids (air modelled only at the surface of the water), the helicopter is modelled with 2,851 shell elements. The simulations for different rotorcraft configurations need 26 to 40 hours on an IBM machine RS6000 model 590. They obtain higher calculated pressure levels than those recorded in the tests and recommend the modelling of air in order to take into account for air-entrapment. To that aim, if entrapped air is to be taken into account, it is necessary to simulate the free fall, at least a part of it, so that the air flow around the body is somehow established at the moment of contact.

In [75], Sareen et al. also use both Lagrangian and Eulerian processors with a general coupling in order to simulate the impact of an energy-absorbing subfloor on water (§ 3.4.3.2) with MSC-Dytran. In contrast to the previous publication, it is possible to use a finer Eulerian solid element mesh and the structure is deformable. Because of computation time, the Euler mesh is constructed so that only a part of the structure is "immersed" in it and comprises 9,600 Eulerian solid elements from which 1600 for air. Two mesh densities are investigated for the structure (a coarse one with 503 nodes, 174 bars, 576 shells and a fine one with 15,900 nodes, 15,200 shells and 400 bar elements). The authors show that the refined models could achieve better correlation but presents numerical instability.

Using MSC-Dytran, Vignjevic et Meo [76] conduct a similar analysis to assess the crashworthiness performance of a helicopter underfloor metallic structure. To that aim, they use an ALE coupling, where the Eulerian mesh is made to follow the structure mesh by means of a ALE moving algorithm (§ 3.4.3.2). At the coupling surface, the Lagrangian (structure) and the Eulerian mesh have coinciding nodes. The authors show that a failed structural element is removed from the internal force calculation within the Lagrangian mesh but not from the contact calculations through the coupling surface. When this element is eliminated, there is no longer resistance to the movement of the contact interface inside the structure, which inevitably leads to extremely distorted Eulerian elements and therefore a termination of the run due to a dramatic drop of the time step. The simulation of fluid ingress in the structure is not possible.

In [69], Ribet et al. present the results of the impact of an ellipsoid **rigid** body impacting obliquely on water (forward velocity of 60 m/s and 5 m/s sink speed in a nose down attitude) using an ALE formulation for the water in RADIOSS. The Eulerian mesh is allowed to move/deform and the fluid is also allowed to move in the mesh. This is off course very interesting to model the deformation of the free surface. For an order of magnitude, this simulation necessitates the following CPU time on a 2-processor Cray j916:

- 1h50 for a full Lagrangian model (100 ms simulation time)
- 2h15 for a model using the ALE formulation (46 ms simulation time).

The ALE simulation prematurely stops due to extreme deformation of the Eulerian mesh (because of the extreme shear deformation linked to the horizontal impact velocity component) leading to a dramatic drop in the time step. Using the Lagrangian mesh, it is possible to run the simulation longer due to the fact that Lagrangian elements which are severely distorted and which do not participate further to the fluid structure interaction contact can be eliminated. Nevertheless, the deformation of the mesh remains restrictive in all cases. This shows the challenge to develop algorithms for mesh displacement management. In fact, the choice of the mesh velocity constitutes one of the major problem in the ALE description. Literature relating to this topic and a possible solution to the problem are available in [77].

Based on the previous experiences, it is clear that the simulation of impact on water is not a solved problem. The problems remain on the one hand in the computation of the fluid flow and on the other hand on the coupling between the structure and the fluid in order to compute the fluid-structure interactions. In the next chapter, two approaches are evaluated to simulate the impact on water: one based on a pure Lagrangian method and another one based on a meshless method (Smoothed Particle Hydrodynamics). The advantage of both methods is that the same solver is used for the computation of the fluid and structure problems.

4 Simulation of the impact on water with fully Lagrangian techniques

4.1 Motivation

In order to reduce time for the generation of structural models, which is time consuming, it is necessary to confirm the compatibility between the methods used to model the water medium and the common structural models, namely FE-models available in the different aeronautical disciplines (static and dynamic loads). For these latter problems, the structure deformations are computed with the classical finite element method, which has already proved its robustness. The difficulties remain on the one hand in the computation of the fluid flow and on the other hand the coupling between the structure and the fluid in order to compute the interactions. Two approaches to model water were presented in the previous chapter:

- the pure Eulerian technique,
- the ALE technique.

In some codes, where the water medium is modelled using the ALE technique, the problem of deformation of the fluid mesh following the deformation of the free surface still remains. This is shown in the work of Ribet et al. [69], who found extensive mesh shear deformation leading to a dramatic drop of the time step especially when a forward impact velocity component is involved. When the ALE technique is used to model the water and its environment (air above water, or void, in order to allow the water to splash up or to form waves), the structure model is practically immerged in the ALE mesh. The problem of mesh deformation is then solved because the mesh may deform independently of the water displacement. In the case of simulation of impact on water, a pure Eulerian mesh is also adequate. Nevertheless, problem of stability may be encountered when the mesh is too fine [74].

To solve some of these problems, it is proposed as an alternative, in this chapter, to use Lagrangian techniques to model the water medium: a classical FE technique and the Smoothed Particle Hydrodynamics (SPH) method, which is a meshfree method. In this way, the problem of mesh deformation is overcome. Concerning the impacting structure, it is modelled with a classical finite element method in the same way as in standard crash simulations. As shown in § 4.2.3, the definition of the contact between the structure and the water media will be simplified as both the structure and the water are modelled using a Lagrangian technique.

It is shown that the use of a classical Lagrangian technique may be sufficient to model the water media in the very beginning of the impact, as long as the deformation of the water mesh remains acceptable. The results of both methods (classical FE and SPH) will be compared in order to assess their domain of validity.

Finally, as the behaviour of the structure during impact on water is of prime interest, it is important to use a code capable of treating structural dynamic problems, whose common characteristics are:

- loading and response times from microseconds to seconds,
- the typical strain rates in the range of 10^{-2} s^{-1} to 10^{2} s^{-1},
- typical strains on the order of 0.5% to 10%,
- the magnitude of the hydrodynamic pressure of the order of the material strength,
- resulting global deformations,
- material or structure failure infered from the global deformations.

These characteristics are best covered by crash codes.

For the fluid structure interaction (FSI) problems of interest in this work, it was then decided to use the commercial finite element explicit code PAM-CRASH, which presents the following advantage:

- proved capacity to treat nonlinear dynamic analysis of structures, which makes it particularly suited for crashworthiness simulations in transportation industry,
- SPH solver for applications in solid mechanics (§ 4.2.2.2),
- FE and SPH can be used simultaneously and easily coupled within the same model,
- the material models of interest for water are already implemented but were not used so far to investigate the impact on water in detail.

The version used for this study is three-dimensional and purely Lagrangian.

4.2 Modelling water with Lagrangian techniques

4.2.1 Classical solid finite element (FE)

As a recapitulation of the theory of the standard finite element method is beyond the scope of this work, explanation will remain very brief. For specific information concerning the implementation of the element used (discretisation scheme, numerical integration, etc, …) in the code chosen for the following simulations, it is recommended to consult [78].

In nonlinear crash analysis, only the “simplest” finite elements are used because the experience shows that “higher order” elements with improved interpolation shape functions are not better at modelling high-gradients of three-dimensional stress and plastification than dense nets of simple finite elements. Increasing the density of the “high order” elements improves the results but requires increased computation time. For this reason, “simple” eight node solid elements are used to model the water pool. They are based on tri-linear shape functions for the interpolation of the coordinate. The same shape functions are used to interpolate the displacements. As mentioned before, first order C^0 solid elements are used for computation efficiency. This means that the displacement and its gradient fields are continuous within the elements. Across element boundaries, the displacements are also continuous while their gradients can be discontinuous at the element edges.

4.2.2 Smoothed Particle Hydrodynamics/ SPH formulation

The smoothed particle hydrodynamics (SPH) method was first presented in 1977 [79, 80]. It belongs to the meshfree particle methods and is therefore very suitable for many problems with extremely large deformations. It was mainly applied in the astrophysics [81] to simulate

complex phenomena like the collision between stars, the explosion of supernovae, etc…. Since then, its application has extended to problems of continuum solid and fluid mechanics (underwater explosion shock, high velocity impact of projectiles upon space structures with penetration ([82] to [84]). Due to the specificity of the method, which is not as well known as the finite element technique, some theoretical background is given in the following.

Despite redundancy, the term of SPH particle will be used instead of SPH "element" in the following text in order to emphasize the particle character of the method in contrast to the finite element method.

4.2.2.1 Fundamentals

The basic idea of the SPH method is to replace the fluid "material" by a set of arbitrarily distributed particles (meshfree) with individual mass and assigned properties (e.g. stress state). As a Lagrangian technique, the mass associated to a SPH "element" remains unchanged during the whole simulation. The variation of velocity, density and position of the particles are determined by the equations of continuity, of conservation of momentum and of conservation of energy. The key step is to approximate the derivatives of these equations at any point by using information on a finite number of particles within a given area. To that aim, two approximations are the fundamentals of the SPH formulation: the Kernel approximation and the particle approximation, which are described in the following.

Kernel approximation

Field functions can be approximated by using the integral representation method termed as the Kernel approximation in the SPH method. Consider a field function A(x) continuous on the integration domain Ω and x a three dimensional position vector. A(x) can be exactly represented by the following integral

$$A(x) = \int_{\Omega} A(x')\,\delta(x - x')\,dx'$$

where δ(x-x´) is the Dirac Delta function defined by

$$\delta(x - x') = \begin{cases} 1 \text{ if } x = x' \\ 0 \text{ if } x \neq x' \end{cases}$$

If the Dirac Delta function is replaced by a well behaved smoothing function W(x, h), whose properties will be listed later, the integral representation of A(x) is given by

$$\langle A(x) \rangle = \int_{\Omega} A(x')\,W(x - x', h)\,dx' \qquad (4\text{-}1)$$

where W is the so-called Kernel approximation and h the smoothing length defining the influence area of the smoothing function W. The use of the Kernel approximation W for the integral representation of A(x) delivers an approximation of A(x) written <A(x)>, which is the origination of the term of Kernel approximation.

The smoothing function W must satisfy the following conditions

- even function: $W(x) = W(-x)$
- normalization or unity condition: $\int_{\Omega} W(x - x', h)\,dx' = 1$
- Delta function property: $\lim_{h \to 0} W(x - x', h) = \delta(x - x')$
- compact condition: $W(x - x', h) = 0$ when $|x - x'| \rangle h$

where h is the smoothing length defining the influence area of the smoothing function W.

Based on the compact condition, the integration domain Ω becomes the same as the support domain. In this chapter, the Kernel function is a so-called cubic spline W4, which is expressed by:

$$\begin{cases} W(r, h) = C\left(1 - \frac{3}{2}x^2 + \frac{3}{4}x^3\right) & \text{if } x \le 1 \\ W(r, h) = \frac{1}{4}C(2 - x)^3 & \text{if } 1 < x \le 2 \\ W(r, h) = 0 & \text{if } x > 2 \end{cases}$$

where x=r/h and C is chosen to give the correct normalization corresponding to the dimension of the simulation.

The integral representation of the derivative of a function is then given by

$$\langle \nabla . A(x) \rangle = \int_{\Omega} [\nabla . A(x')] W(x - x', h)\,dx' \tag{4-2}$$

By reformulating the derivative and using the divergence theorem applied to the integrated domain Ω delimited by the surface S, Eq. (4-2) can be re-written as

$$\langle \nabla . A(x) \rangle = -\int_{\Omega} A(x') \nabla W(x - x', h)\,dx' \tag{4-3}$$

As W has a compact support and the support domain is located within the integration domain Ω, the surface integral is null. It shows a very important point: the spatial derivatives of a field function can be expressed from the values of this function and the derivatives of the smoothing function W.

Particle approximation

The continuous integral approximation <A(x)> and $<\nabla.A(x)>$ can be converted into discretized forms. They can be expressed as summation over all the particles in the support domain. Figure 4-1 illustrates the principle of the particle approximation.

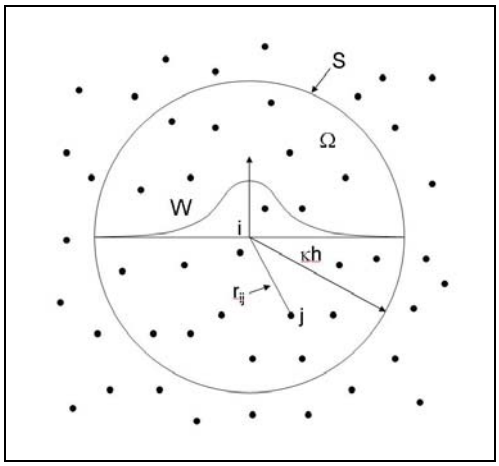

Figure 4-1 : Particle approximation [85]

As the mass of the particle m_j can be calculated from the finite volume ΔV_j of the particle j

$$m_j = \rho_j \, \Delta V_j \quad \text{for j=1, …, N}$$

the continuous integral representation of A(x) can be written in discretized form as

$$\langle A(x) \rangle \cong \sum_{j=1}^{N} A(x_j) \, W(x - x_j, h) \, \Delta V_j$$

$$\langle A(x_i) \rangle \cong \sum_{j=1}^{N} \frac{m_j}{\rho_j} A(x_j) \, W_{ij} \tag{4-4}$$

where

$$W_{ij} = W(x_i - x_j, h) = W(|x_i - x_j|, h)$$

Eq. (4-4) shows that the value of a field function at a particle i is approximated by the sum of the values of this field function at all particles in the support domain weighted by the smoothing Kernel function.

In the same way, by using the particle approximation, the continuous integral representation of the derivative of a function A(x) can be written as

$$\langle \nabla . A(x_i) \rangle = \sum_{j=1}^{N} \frac{m_j}{\rho_j} A(x_j) . \nabla_i W_{ij} \tag{4-5}$$

where

$$\nabla_i W_{ij} = \frac{x_i - x_j}{r_{ij}} \frac{\partial W_{ij}}{\partial r_{ij}}$$

r_{ij} is the distance between particles i and j.

Eq. (4-5) shows that the value of the gradient of a field function at a particle i is approximated by the sum of this field function at all particles in the support domain weighted by the gradient of the smoothing Kernel function. From Eq. (4-4), the density of a particle i is given by

$$\rho_i = \langle \rho(x_i) \rangle = \sum_{j=1}^{N} m_j \, W_{ij}$$

4.2.2.2 SPH formulation used for the governing equations of the fluid problem

The well-known basic governing equation for the mechanic and fluid problems can be written as the following set of partial differential equations in Lagrangian description:

$$\frac{D\rho}{Dt} = -\rho \frac{\partial v^{\beta}}{\partial x^{\beta}} \tag{4-6}$$

$$\frac{Dv^{\alpha}}{Dt} = \frac{1}{\rho} \frac{\partial \sigma^{\alpha\beta}}{\partial x^{\beta}} \text{ (no external force)} \tag{4-7}$$

$$\frac{De}{Dt} = \frac{\sigma^{\alpha\beta}}{\rho} \frac{\partial v^{\alpha}}{\partial x^{\beta}} \tag{4-8}$$

where α and β are used for the coordinate directions and repeated indices stand for summation, v the velocity, ρ the density, x the position and σ the total stress tensor. e describes the intern energy. The rates of change of physical quantities are calculated by spatial derivatives.

The total stress tensor σ is then decomposed into an isotropic pressure p and an anisotropic stress τ.

$$\sigma^{\alpha\beta} = -p\delta^{\alpha\beta} + \tau^{\alpha\beta} \tag{4-9}$$

where $\delta^{\alpha\beta}$ is the Kronecker delta function. Eq. (4-6) to (4-9) are general and apply in both for solid and fluid mechanics problems.

In both following paragraphs, the SPH formulations of the fluid dynamics and solid mechanics equations are listed for comprehension. Aim is to emphasize, where the differences are between the formulations in both fields and therefore to understand, where the limitations are when using the formulation of solid mechanics to describe the water behaviour in § 4.4 and § 4.5.

SPH formulation for fluid dynamic

For Newtonian fluids, the stress is proportional to the strain rate

$$\tau_{ij} = \mu \dot{\varepsilon}_{ij} \tag{4-10}$$

where $\dot{\varepsilon}_{ij} = \frac{\partial v_j}{\partial x_i} + \frac{\partial v_i}{\partial x_j} - \frac{2}{3}(\nabla . v)\delta_{ij}$ is the shear strain rate and μ the dynamic viscosity.

Taking into account for an artificial viscosity (to make the algorithm able to model shock waves), a well-established SPH formulation of the fluid dynamics equations is given by:

- Conservation of mass

$$\frac{D\rho_i}{Dt} = \sum_{j=1}^{N} m_j \left(v_i^{\beta} - v_j^{\beta}\right) \frac{\partial W_{ij}}{\partial x_i^{\beta}} \tag{4-11}$$

- Conservation of momentum

$$\frac{Dv_i^{\alpha}}{Dt} = -\sum_{j=1}^{N} m_j \left(\frac{p_i}{\rho_i^2} + \frac{p_j}{\rho_j^2} + \Pi_{ij} \right) \frac{\partial W_{ij}}{\partial x_i^{\alpha}} + \sum_{j=1}^{N} m_j \left(\frac{\mu_i \dot{\varepsilon}_i^{\alpha\beta}}{\rho_i^2} + \frac{\mu_j \dot{\varepsilon}_j^{\alpha\beta}}{\rho_j^2} \right) \frac{\partial W_{ij}}{\partial x_i^{\alpha}} \tag{4-12}$$

- Conservation of energy

$$\frac{De_i}{Dt} = \frac{1}{2} \sum_{j=1}^{N} m_j \left(\frac{p_i}{\rho_i^2} + \frac{p_j}{\rho_j^2} + \Pi_{ij} \right) \left(v_i^{\beta} - v_j^{\beta} \right) \frac{\partial W_{ij}}{\partial x_i^{\beta}} + \frac{\mu_i}{2\rho_i} \dot{\varepsilon}_i^{\alpha\beta} \dot{\varepsilon}_i^{\alpha\beta} \tag{4-13}$$

where

$$\varepsilon_i^{\alpha\beta} = \sum_{j=1}^{N} \frac{m_j}{\rho_j} \left(v_j^{\beta} - v_i^{\beta} \right) \frac{\partial W_{ij}}{\partial x_i^{\alpha}} + \sum_{j=1}^{N} \frac{m_j}{\rho_j} \left(v_j^{\alpha} - v_i^{\alpha} \right) \frac{\partial W_{ij}}{\partial x_i^{\beta}} - \left(\frac{2}{3} \sum_{j=1}^{N} \frac{m_j}{\rho_j} \left(v_j - v_i \right) . \nabla_i W_{ij} \right) \delta^{\alpha\beta}$$

$$\varepsilon_j^{\alpha\beta} = \sum_{i=1}^{N} \frac{m_i}{\rho_i} \left(v_i^{\beta} - v_j^{\beta} \right) \frac{\partial W_{ji}}{\partial x_j^{\alpha}} + \sum_{i=1}^{N} \frac{m_i}{\rho_i} \left(v_i^{\alpha} - v_j^{\alpha} \right) \frac{\partial W_{ji}}{\partial x_j^{\beta}} - \left(\frac{2}{3} \sum_{i=1}^{N} \frac{m_i}{\rho_i} \left(v_i - v_j \right) . \nabla_j W_{ji} \right) \delta^{\alpha\beta}$$

α and β are used to define the coordinate direction, i and j are references to particles i and j respectively. Π_{ij} is a viscous dissipation term for removing numerical oscillations. Π_{ij} is a common numerical artifice used in FVM and FEM and helps to diffuse sharp variations in the flow (e.g. from shock wave), to dissipate the energy of high frequency term or to prevent interpenetration of particles [86].

The equations (4-11) to (4-13) are not the unique expressions for describing conservation of mass, momentum and energy. Depending on the nature of the problem, other SPH formulations may be more appropriate. If we consider the motion inviscid (perfect fluid), the equation for conservation of momentum and energy gives:

$$\frac{Dv_i^{\alpha}}{Dt} = -\sum_{j=1}^{N} m_j \left(\frac{p_i}{\rho_i^2} + \frac{p_j}{\rho_j^2} \right) \frac{\partial W_{ij}}{\partial x_i^{\alpha}} \text{ (conservation of momentum)} \tag{4-14}$$

$$\frac{De_i}{Dt} = \frac{1}{2} \sum_{j=1}^{N} m_j \left(\frac{p_i}{\rho_i^2} + \frac{p_j}{\rho_j^2} \right) v_{ij}^{\beta} \frac{\partial W_{ij}}{\partial x_i^{\beta}} \text{ (conservation of energy)} \tag{4-15}$$

(4-14) is the SPH formulation of the Euler equations.

For extended details about the choice of an adequate smoothing Kernel function, consistency, time integration and implementation issues, it is recommended to refer to [87 to 89].

SPH formulation for solid mechanic problems

In solid mechanics, the anisotropic stress (shear stress) is a function of strain and strain rate and is determined by the constitutive law. For small displacements, the shear stress rate is a function of the strain rate and is defined by:

$$\dot{\tau}^{\alpha\beta} = G \left(\dot{\varepsilon}^{\alpha\beta} - \frac{1}{3} \delta^{\alpha\beta} \dot{\varepsilon}^{\gamma\gamma} \right) \tag{4-16}$$

where G is the shear modulus, $\dot{\tau}$ is the stress rate and $\dot{\varepsilon}^{\alpha\beta}$ the strain rate tensor defined by

$$\dot{\varepsilon}^{\alpha\beta} = \frac{1}{2}\left(\frac{\partial v^{\alpha}}{\partial x^{\beta}} + \frac{\partial v^{\beta}}{\partial x^{\alpha}}\right)$$

The SPH formulation of the equations governing the solid mechanics is given by:

- Conservation of mass

$$\frac{D\rho_i}{Dt} = \sum_{j=1}^{N} m_j \left(v_i^{\beta} - v_j^{\beta}\right) \frac{\partial W_{ij}}{\partial x_i^{\beta}} \tag{4-17}$$

- Conservation of momentum

$$\frac{Dv_i^{\alpha}}{Dt} = -\sum_{j=1}^{N} m_j \left(\frac{p_i}{\rho_i^2} + \frac{p_j}{\rho_j^2} + \Pi_{ij}\right) \frac{\partial W_{ij}}{\partial x_i^{\alpha}} + \sum_{j=1}^{N} m_j \left(\frac{\tau_i}{\rho_i^2} + \frac{\tau_j}{\rho_j^2}\right) \frac{\partial W_{ij}}{\partial x_i^{\alpha}} \tag{4-18}$$

- Conservation of energy

$$\frac{De_i}{Dt} = \frac{1}{2}\sum_{j=1}^{N} m_j \left(\frac{p_i}{\rho_i^2} + \frac{p_j}{\rho_j^2} + \Pi_{ij}\right)\left(v_i^{\beta} - v_j^{\beta}\right) \frac{\partial W_{ij}}{\partial x_i^{\beta}} + \frac{1}{\rho_i} \tau_i^{\alpha\beta} \dot{\varepsilon}_i^{\alpha\beta} \tag{4-19}$$

where α and β are used to define the coordinate direction, i and j are references to particles i and j respectively. Π_{ij} is a viscous dissipation term for removing numerical oscillations.

By considering a material without strength ($G << 1$) in the equations of solid mechanics, the Euler equations (inviscid fluid) of the fluid dynamics are obtained back.

Followed strategy to model the water behaviour

As the instant of impact is of interest for the investigations performed in this work, the inertial forces are preponderant compared to the viscous ones. It follows that a SPH formulation of the governing equations for an inviscid flow is sufficient to solve the problem of impact in the initial phase, which is of interest for first dimensioning. Due to the fact that the SPH formulation of the code used for the investigations of the impact on water in this report is implemented for solid mechanics problems (with strength), the material model for the fluid will be suitably defined so that the Euler equations of fluid mechanics are solved. This means that the shear behaviour of the material will be kept negligible and only volumetric components of the stress tensor will be considered. In that case, the total stress tensor σ solely consists of the isotropic pressure components

$$\sigma^{\alpha\beta} = -p\delta^{\alpha\beta} \tag{4-20}$$

where the pressure p is defined by the material model.

4.2.3 Contact modelling between structure and water

As a part of the theory is already explained in § 3.4.2, a brief explanation follows to describe the functioning of the algorithm. A standard node to segment contact algorithm, commonly employed in crash simulation, is used to compute the contact between the impacting structure and the water surface. At each time step, each node on the slave surface is checked and the nearest master is located. If the slave node has penetrated the master segment, forces are

applied in a direction normal to the master surface to prevent further penetration. The magnitude of the force depends on the amount of penetration and the properties of the elements on each side of the contact surface. This is known as the penalty method.

A friction force is also applied to each of the surfaces (here between the surfaces of the water element and of the structure in contact). The magnitude of the force during sliding is equal to the magnitude of the normal force multiplied by the coefficient of friction using the standard Coulomb friction law. The direction of the friction force is opposite to the relative motion of the surfaces.

4.3 Water material models/laws

Two laws can be used in the explicit code PAM-CRASH to model the behaviour of the water medium:

- isotropic elastic plastic hydrodynamic law
- Murnaghan equation of state

4.3.1 Isotropic elastic plastic hydrodynamic law

The isotropic elastic plastic hydrodynamic law was originally developed to apply for ballistic impact in metals, where the material behaves like a fluid above a certain impact energy level. It describes an isotropic elastic plastic material at low pressures with an equation of state (EOS) describing the 'hydrodynamic' pressure-volume behaviour at high pressures. To model water, the elastic plastic contribution to the material behaviour is neglected so that the model reduces to the EOS for the pressure p, which is assumed to have the polynomial form:

$$p = C_0 + C_1\mu + C_2\mu^2 + C_3\mu^3\,,\ \mu = \rho/\rho_0 - 1 \tag{4-21}$$

where C_0, C_1, C_2 and C_3 are material constants and μ is a dimensionless parameter defined in term of current density ρ to initial density ρ_0.

Determination of the C_i coefficients of EOS (4-21):

For most solids and fluids, the relationship (called "linear Hugoniot") between the shock velocity u_S and particle velocity u_p (velocity of the material) can be expressed as

$$u_S = c_0 + k\,u_p \tag{4-22}$$

where c_0 is the normal sound speed in the material and k a constant for the material. Wilbeck [90] shows that the pressure density across a shock can be approximated by

$$p = \rho_0\, c_0^2\, \eta/(1 - k\eta^2)\,,\ \eta = 1 - \rho_0/\rho = \mu/(1+\mu) \tag{4-23}$$

It follows for nearly incompressible flow ($\eta << 1$) that Eq. (4-23) takes the form of the polynomial EOS by expanding for small μ:

$$p = \rho_0 c_0^2 + (2k-1)\rho_0 c_0^2\,\mu + (k-1)(3k-1)\rho_0 c_0^2\,\mu^2 \tag{4-24}$$

Identifying Eq. (4-24) with Eq. (4-21) leads to the following expressions for the coefficients C_1, C_2 and C_3.

$$\left.\begin{aligned} C_1 &= \rho_0 c_0^2 \\ C_2 &= (2k-1)\, C_1 \\ C_3 &= (k-1)(3k-1)\, C_1 \end{aligned}\right\} \qquad (4\text{-}25)$$

C_0 is the initial equilibrium pressure in the material and is generally assumed to be negligible in impact.

Based on Heymann [91], Eq. (4-22) takes the following specific form for water up to Mach= 1.2

$$u_S = c_0 + 2\,u_p$$

and delivers the value of parameter k = 2 necessary to calculate the coefficients C_i using Eqs. (4-25). Table 4-1 compares the new calculated coefficients of the equation of state based on Wilbeck's expression (4-23) to data available from the literature obtained from measurements [92]. It appears that results agree well with measurements.

Coefficents of the EOS (4-21)	**Calculated data from Eqs. (4-25)**	**Measurements [92]**
C_0 [GPa]	0	0
C_1 [GPa]	2.5	2.723
C_2 [GPa]	7.5	7.727
C_3 [GPa]	12.5	14.66

Table 4-1 : Comparison between the measured data and data deduced from Wilbeck'stheory for the water continuum

A third cross-check to determine the coefficient C_1 in Eq. (4-21) is the determination of the bulk modulus. Per definition, the degree of compressibility of a substance, which does not change its phase, is characterised by the bulk modulus of elasticity, which is defined by the equation [93]

$$K = -\frac{\partial p}{\partial V / V} = \rho \frac{\partial p}{\partial \rho} \qquad (4\text{-}26)$$

Identifying Eq. (4-21) to Eq. (4-26) shows that C_1 exactly corresponds to the bulk modulus of the material considered.

Determination of the virtual "elastic" properties of the water medium:

Based on the definition of the shear modulus G and the bulk modulus K

$$G = \frac{E}{2(1+\nu)} \qquad (4\text{-}27) \qquad \text{and} \qquad K = \frac{E}{3(1-2\nu)} \qquad (4\text{-}28)$$

where E is the Young modulus and ν the Poisson's ratio, the shear modulus can be re-written as a function of E and ν in

$$G = \frac{3(1-2\nu)}{2(1+\nu)} K \tag{4-29}$$

This leads, in the case of an incompressible fluid ($\nu \rightarrow 0.5$), to the following approximation for the shear modulus

$$G \approx 0.01\ K \tag{4-30}$$

Finally the yield stress σ_y and the tangent modulus E_t are set to negligible values, 1.0 Pa and 0.0 Pa respectively, in order to control the water behaviour essentially by the EOS (4-21) of the material model.

It is important to mention that no viscosity is available in the hydrodynamic elastic plastic material model. This does not present any problem as the interest is in the first milliseconds of the impact on water for which inertial forces dominate viscous ones.

4.3.2 Murnaghan law

This material law developed by Murnaghan [94] corresponds to a liquid with an artificially increased compressibility to perform a certain class of hydrodynamic simulations, where the flow velocities remain well below the physical sound speed, and where compressibility effects are of minor importance.

As water has a high sound velocity (1,500 m/s), the computational time step in the case of an explicit solution scheme is very small compared to the typical duration of the flow phenomena. In addition, assuming the liquid to be incompressible requires a solution of the Poisson equation over the entire flow regime and an implicit solution. For these reasons, the Murnaghan material is an alternative to the hydrodynamic elastic plastic material model to reduce computation time for the simulation of the impact on water. In this case the artificial fluid must be given a speed of sound which is below the true sound speed but still well above the speed of the bulk flow. The advantage of the Murnaghan law over the hydrodynamic elastic plastic material model is a gain in computational time due to the artificially reduced sound speed and reduced pressure oscillations. This Murnaghan material model is described by the following pressure-volume equation of state:

$$p = p_0 + B\left[\left(\frac{\rho}{\rho_0}\right)^{\gamma} - 1\right] \tag{4-31}$$

where B is the parameter defining the sound velocity, ρ the current density, ρ_0 the initial mass density, p_0 the reference pressure and γ a parameter set to 7.

In the simulations performed, B has been determined according to the criteria (4-32). The condition on B is required to ensure that pressure waves are still much faster than the material velocity and therefore do not affect the flow.

$$B \geq 100 \frac{\rho_0\ v_{max}^2}{\gamma} \tag{4-32}$$

where v_{max} is the expected maximum material flow speed. In this case, the inequality (4-32) states that the sound speed of the medium is a factor 10 times higher than the bulk flow velocity.

The Murnaghan material model is adequate to simulate gravity and inertia driven flow of liquids e.g. outflow from a cavity, sloshing of liquids in partially filled containers. It will be also tested in § 4.4 and § 4.5 towards its adequacy to model impact on water

4.4 Benchmark validation of the fluid models (classical FE-solid and SPH-FE solid)

4.4.1 Reference tests based on a sphere impacting on water

For the studies two series of tests have been considered from the literature [73, 26], in which two spheres of different sizes and densities are dropped vertically on water (Table 4-2). Four impact velocities have been tested. The measured acceleration at the COG of a sphere dropped into water is used for comparison with the simulation results.

Test cases	Sphere diameter [m]	Weight [kg]	Velocity at impact [m/s]
Anghileri_1 Anghileri_2	0.218	3.76	11.8
Troesch_1	0.502	33.12	3.46
Troesch_2	0.502	33.12	4.89
Troesch_3	0.502	33.12	5.99

Table 4-2 : Considered three-dimensional test cases for the validation of the simulation procedure

The sphere is considered to remain undeformed during the test and the water surface is smooth (no waves) just before the contact.

4.4.2 The hydrodynamic elastic plastic material model

4.4.2.1 Investigations involving a classical FE mesh

For the investigations involving a classical FE mesh, the water pool is modelled using 8-node solid elements. For the following parameterised studies, a homogeneous mesh is considered. Nevertheless some precautions are taken in order to minimise the dramatic deformation of the water mesh: the hexahedral elements are generated so that they are elongated in the direction of the impact in order to delay their extreme compression leading to a dramatic drop of the time step after some milliseconds. The boundary conditions applied on the sides of the pool (except the top) are defined so that the normal displacement to each face is constrained. Finally, the spherical impactor is simply modelled with shell elements and is defined as a rigid body.

Gravity has been taken into account as well as damping before the contact of the sphere on water in order to damp the oscillations in the water continuum resulting from the introduction of an acceleration field. This damping is of course eliminated before the contact occurs.

Figure 4-2 shows a typical finite element model used for the calculation of the impact of a sphere on water. In particular, the elevation of the water "elements" around the sphere is shown 0.015 s after the impact. Although the circular propagation of the disturbance caused by the spherical impactor is plausible, splash effects cannot be reproduced due to the topology used in the classical Lagrangian finite element approach (Neighbouring elements have common nodes)

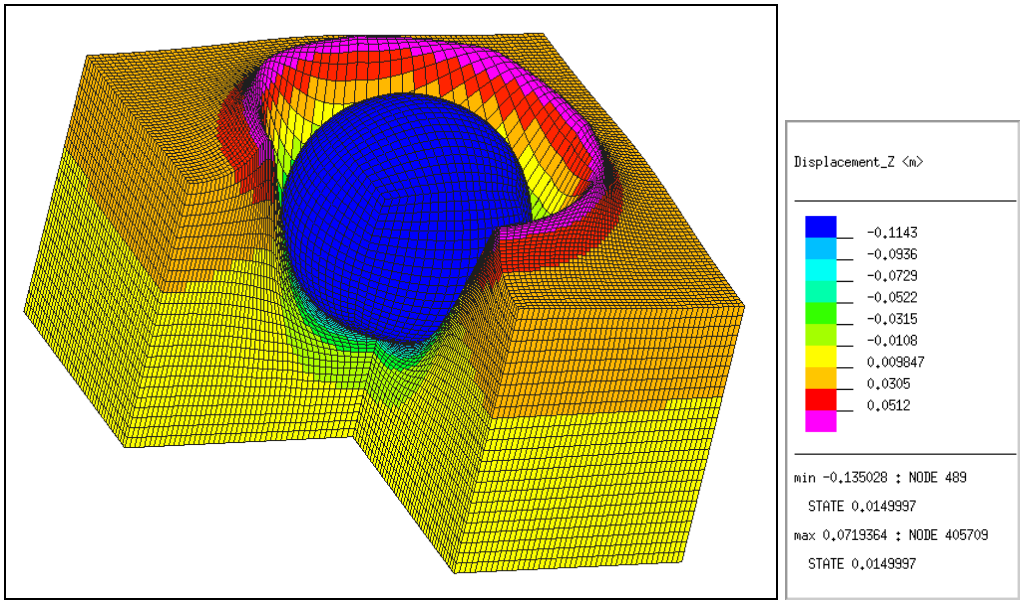

Figure 4-2 : Simulation instantaneous picture of a sphere impacting on water at t=0.015 s (pure FE model) using a hydrodynamic elastic-plastic material model

Mesh size effects

Three different meshes have been generated in order to investigate the influence of the mesh size on the calculated results. The 8-node solid elements have the following sizes:

- 0.01 m x 0.01 m x 0.02 m,
- 0.005 m x 0.005 m x 0.01 m,
- 0.003 m x 0.003 m x 0.006 m.

Figure 4-3 shows the influence of the mesh element size on the acceleration time histories at the centre of gravity of the sphere. The calculated curves are filtered with a CFC 600 filter. The coarser mesh shows high oscillations and leads to an over-estimation of the acceleration peak of 26%. The finer meshes are able to deliver acceleration time histories in better agreement with the measured data, whereas the middle-size mesh already delivers very acceptable results, where the acceleration peak is overestimated by only 9%. Finally whatever the mesh size used, the acceleration plateau following the peak is overestimated. As a compromise with the computation time, it is decided to adopt the middle-size mesh (0.005 m x 0.005 m x 0.01 m) for the following investigations.

As presented in Appendix C, it can be assumed that the mesh size of the sphere has almost no influence on the calculated acceleration time histories. Nevertheless, this assumption applies as long as the geometry of the impactor remains sufficiently close to the real one.

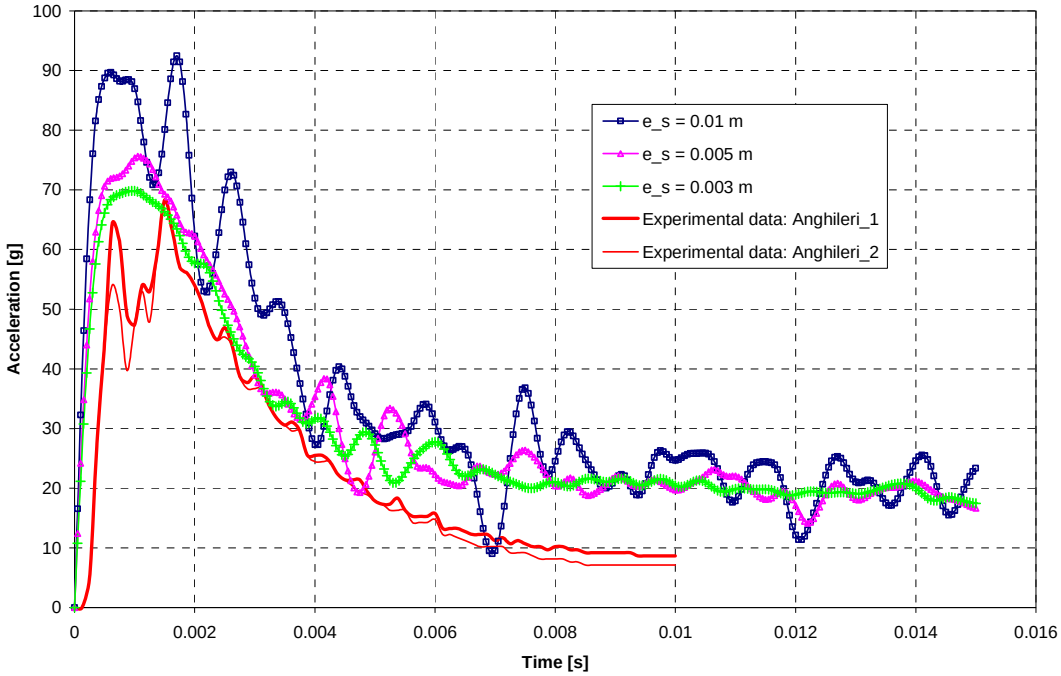

Figure 4-3 : Influence of the element size on the acceleration time histories (pure FE model) using a hydrodynamic elastic-plastic material model

Effects of pool size

In order to investigate the effects of the water pool size on the simulation results, three pool sizes have been considered corresponding to approximately 1.5, 2 and 2.5 times the diameter of the sphere. This leads to the following dimensions of water pools:

- 0.34 m x 0.34 m x 0.25 m,
- 0.44 m x 0.44 m x 0.25 m,
- 0.56 m x 0.56 m x 0.25 m.

Figure 4-4 shows the influence of the pool size on the acceleration time histories at the COG of the sphere. The calculated curves are filtered with a CFC 600 filter. Independently of the pool size, the calculated peak remains unchanged. Nevertheless, the level of the acceleration plateau following the curve peak shows a dependency. For the smaller pool size (0.34 m x 0.34 m x 0.25 m), the plateau level amounts to approximately 30 g's compared to 20 g's for both higher pool sizes. This means that for the test case studied, a pool having a width and a length corresponding to two times the diameter of the sphere should be sufficient to minimise the boundary effects. It is evident, that the bigger the pool size is, the better it is to delay the reflection of compression waves able to parasitize the calculated curves. The oscillations in the calculated time histories remain nevertheless very acceptable compared to the general shape of the acceleration curve.

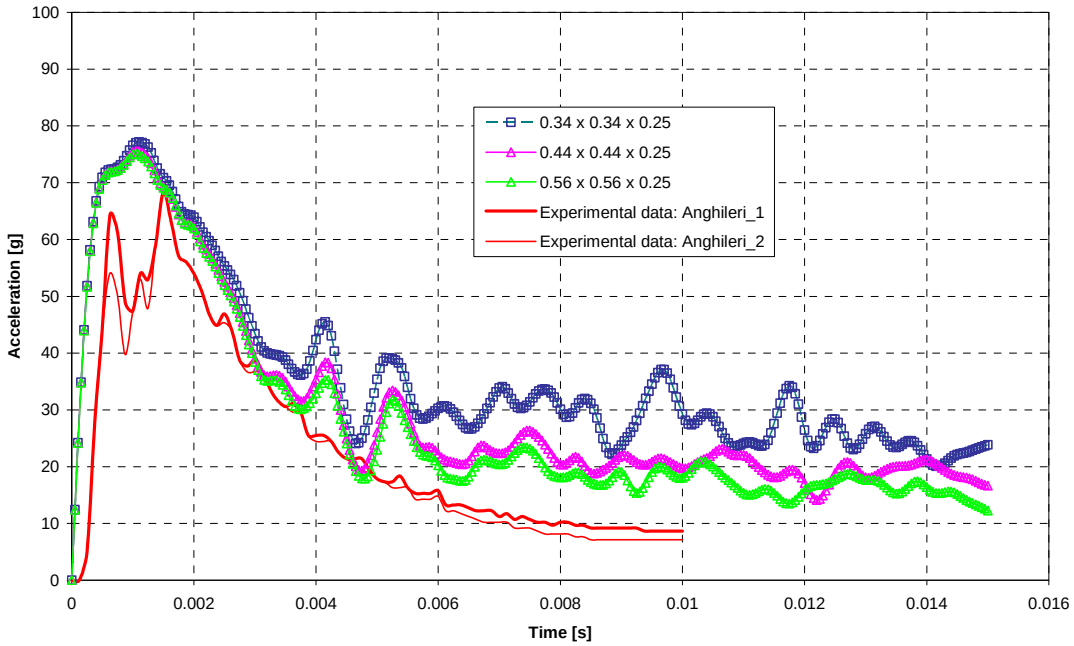

Figure 4-4 : Influence of the pool size on the acceleration time histories (pure FE model) using a hydrodynamic elastic-plastic material model

Effects of symmetry conditions

As depicted in Figure 4-5, other studies conducted with the 0.44 m x 0.44 m x 0.25 m pool show that the calculation with a half and then a quarter model does not change the quality of the simulation results. Consequently, when the impactor presents a symmetry, this latter will be used in order to reduce the computation time.

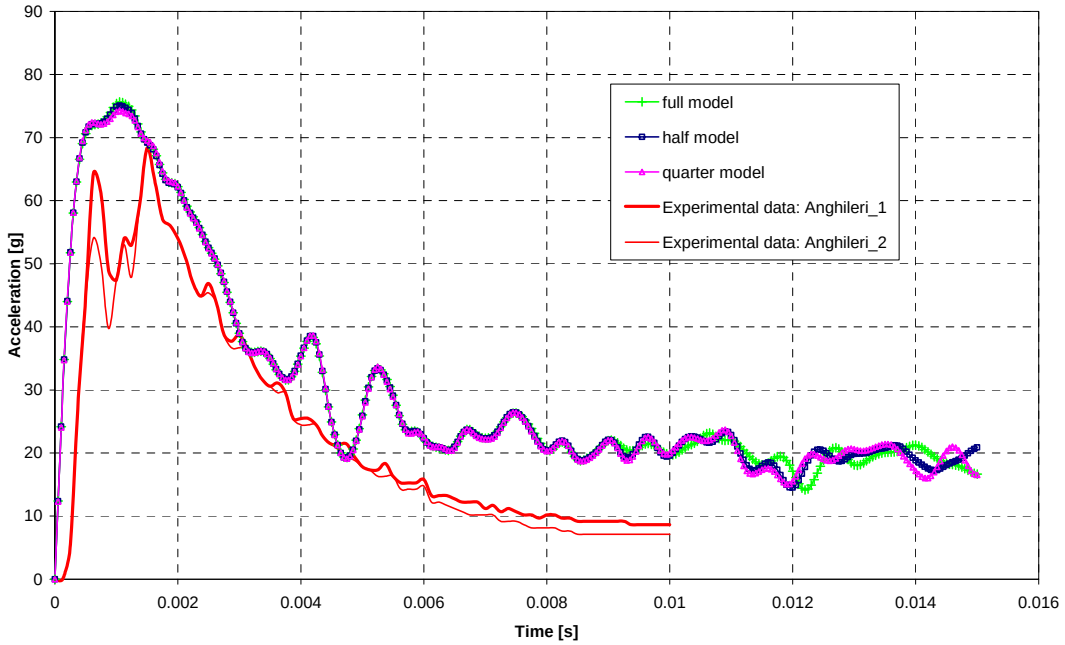

Figure 4-5 : Influence of symmetry conditions on the acceleration time histories (pure FE) using a hydrodynamic elastic-plastic material model

Simulation results of other test cases involving a sphere

Taking into account the lessons learned in the previous studies, Figure 4-6 presents a comparison between calculated and measured acceleration time histories for three other test cases [26]. A 0.5 m x 0.5 m x 0.5 m quarter model is used with an element size of 0.01 x 0.01 x 0.02 for the water mesh. The calculated and measured accelerations time histories agree very well. Contrary to the previous simulations of the Anghileri's test cases, the plateau after the peak is well reproduced by the simulations for the three velocities. The reasons for it can be many:

- relative density of the sphere compared to water is different between both spheres, which may have an influence in the FE model,
- the velocity range considered involving other phenomena,
- effects of measurement devices, which are different between the tests results obtained by Anghileri [73] and Troesch [26].

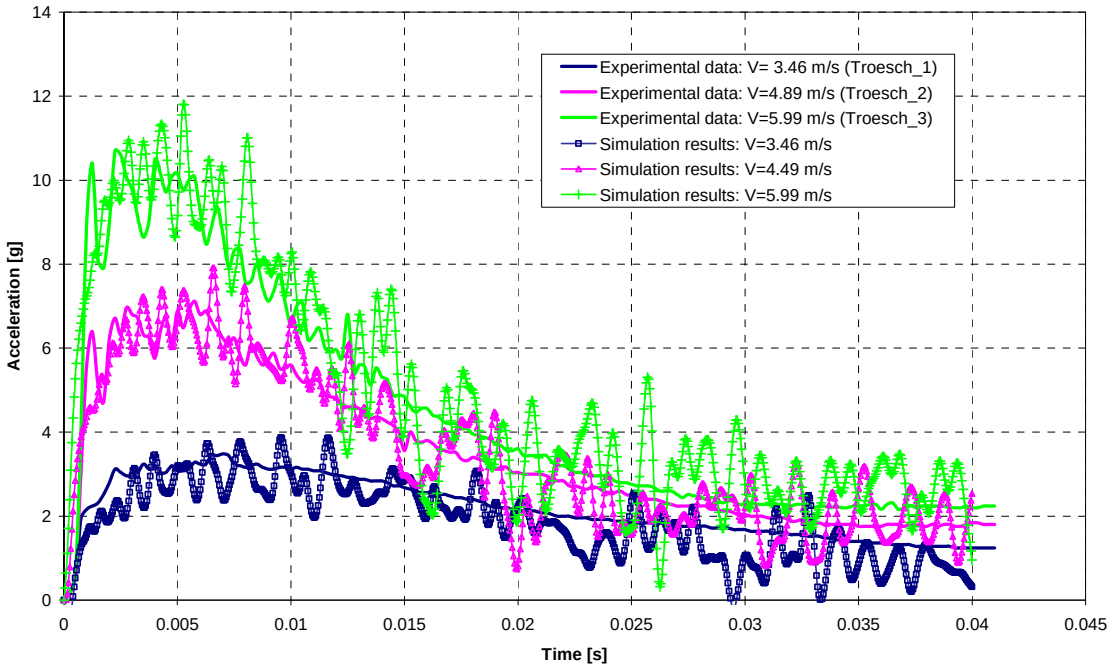

Figure 4-6: Comparison of the acceleration time histories at the COG of a sphere (Ø 0.502m) between test and simulation (pure FE model) using a hydrodynamic elastic-plastic material model

4.4.2.2 Investigations involving a SPH mesh

By the investigations involving a SPH mesh, two concepts have been considered:

- a pure SPH mesh,
- a mixed SPH/8-node solid mesh.

In the second concept the idea is to use a SPH mesh in the impacting area, where large deformations are expected and the 8-node solid mesh around it in order to extend the water pool. In order to reduce computation time, this latter mesh has been chosen to be progressively coarser towards the outside of the water pool model. For the need of the parameter study, the region of impact is always meshed with the same uniform SPH mesh in

both concepts. Figure 4-7 and Figure 4-8 show the typical meshes of a pure SPH model and of a mixed SPH/8-node solid model, whereas the SPH mesh is of the same size in both Figures. Concerning the boundary conditions applied on the sides of the pool (except the top), they are defined so that the normal displacement to each face of the water pool is constrained. For the pure SPH mesh of the water pool, a container model is necessary in order to apply these conditions on the SPH, which are topologically independent.

As in the pure FE investigations in § 4.4.2.1, the same spherical impactor modelled with shell elements and defined as a rigid body is used. The gravity is also included.

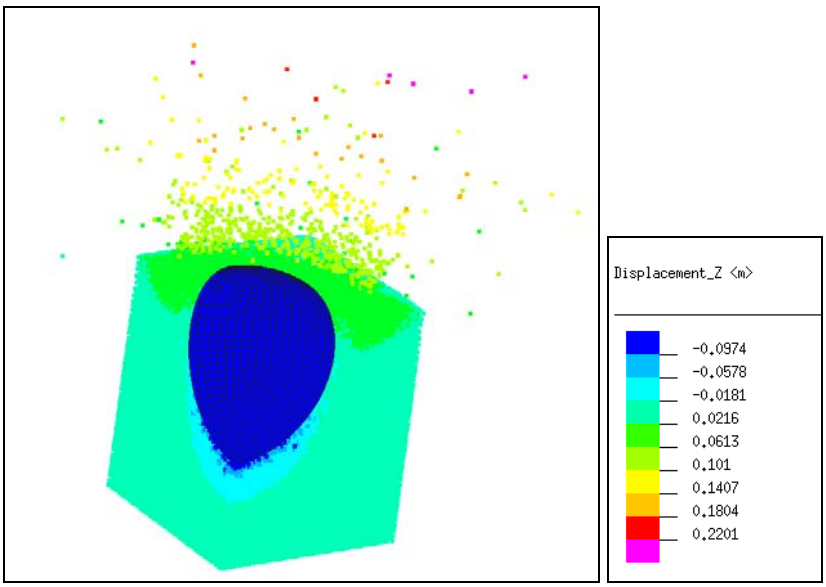

Figure 4-7 : Simulation instantaneous picture of a sphere impacting on water at t=0.015 s (pure SPH model) using a hydrodynamic elastic-plastic material model

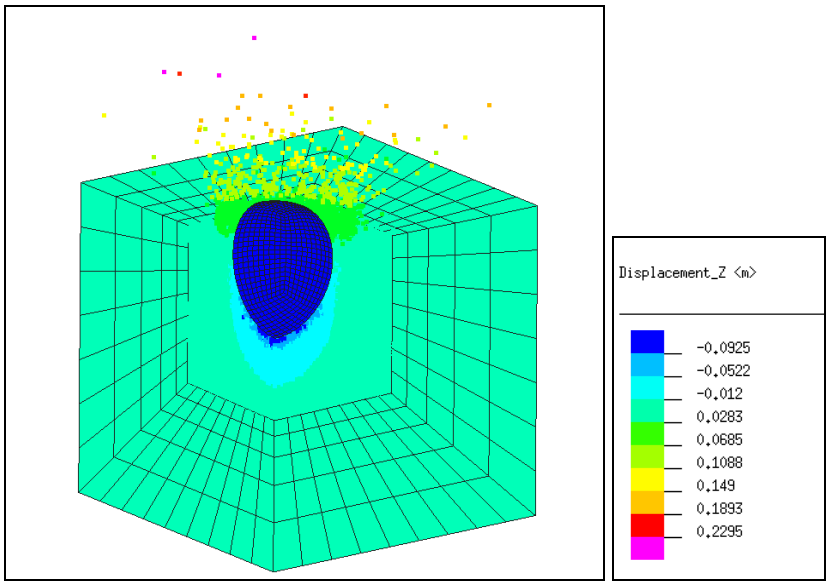

Figure 4-8 : Simulation instantaneous picture of a sphere impacting on water at t = 0.015 s (mixed SPH/8-node solid model) using a hydrodynamic elastic-plastic material model

Effects of pool size

The effects of the water pool size on the simulation results are investigated by considering three block sizes with the same dimensions considered in the study involving a FE mesh (0.34 m x 0.34 m x 0.25 m, 0.44 m x 0.44 m x 0.25 m and 0.56 m x 0.56 m x 0.25 m). No symmetry is applied.

Figure 4-9 shows the influence of the pool size on the acceleration time histories at the COG of the sphere. The calculated curves are filtered with a CFC 600 filter. Independent of the pool size, the calculated peak remains almost unchanged as is the case for the pure FE analyses (§ 4.4.2.1). Nevertheless, the level of the acceleration plateau following the curve peak shows a dependency and does not agree well with the measurements. For the smaller pool size (0.34 m x 0.34 m x 0.25 m), the plateau level amounts to approximately 40 g compared to 20 g for both higher pool sizes. All the simulations overestimate the acceleration plateau level by 100%. This means that for the test case studied involving a SPH mesh, a pool having a width and a length corresponding to two times the diameter of the sphere is not sufficient. It is evident, that a bigger pool size is required. In the next paragraph, another strategy is proposed penalising the computation time as little as possible and showing better agreements between tests and simulations.This is especially of concern when using SPH (§ 4.6).

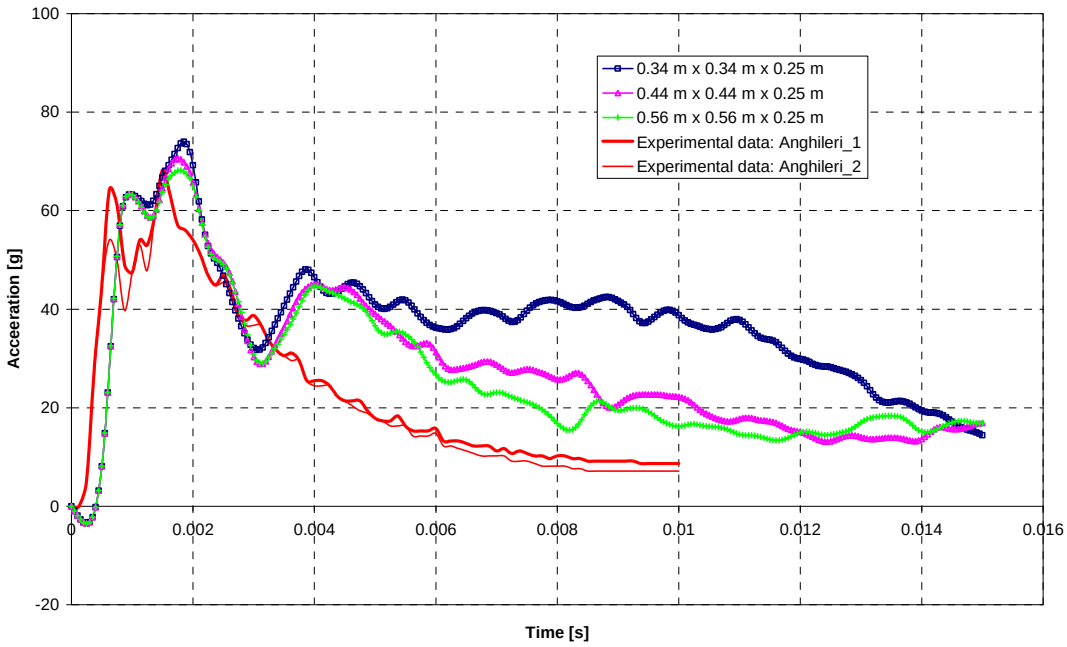

Figure 4-9 : Influence of the pool size on the acceleration time histories (pure SPH model) using a hydrodynamic elastic-plastic material model

Effects of symmetry conditions and of a mixed FE-SPH mesh (new modelling strategy)

Figure 4-10 illustrates two positive effects of the modelling strategy. Firstly, the use of a quarter model to model the impact on water of the sphere constitutes a good compromise between computation time and quality of the results. Apart from a higher acceleration peak, the simulation with the quarter pure SPH model (0.22 m x 0.22 m x 0.25 m) delivers

equivalent results to the ones obtained with the full pure SPH model. Unfortunately, both simulations overestimate by more than 100 % the measured acceleration plateau level. As discussed in § 4.4.2.1, this latter is mainly due to the effect of the water pool size.

Providing an acceptable computation time, a mixed FE-SPH model is proposed as the solution to extend the water pool size (a 0.22 m x 0.22 m x 0.22 m SPH block included in an overall 8-node solid mesh with the external dimensions of 0.5 m x 0.5 m x 0.5 m). The transition from the SPH elements to the solid elements is made by tying the external SPH particles to their neighboured solid in displacement. In that way, the deformation and stresses are transmitted from one mesh to the other. The calculated results could be really improved with this strategy.

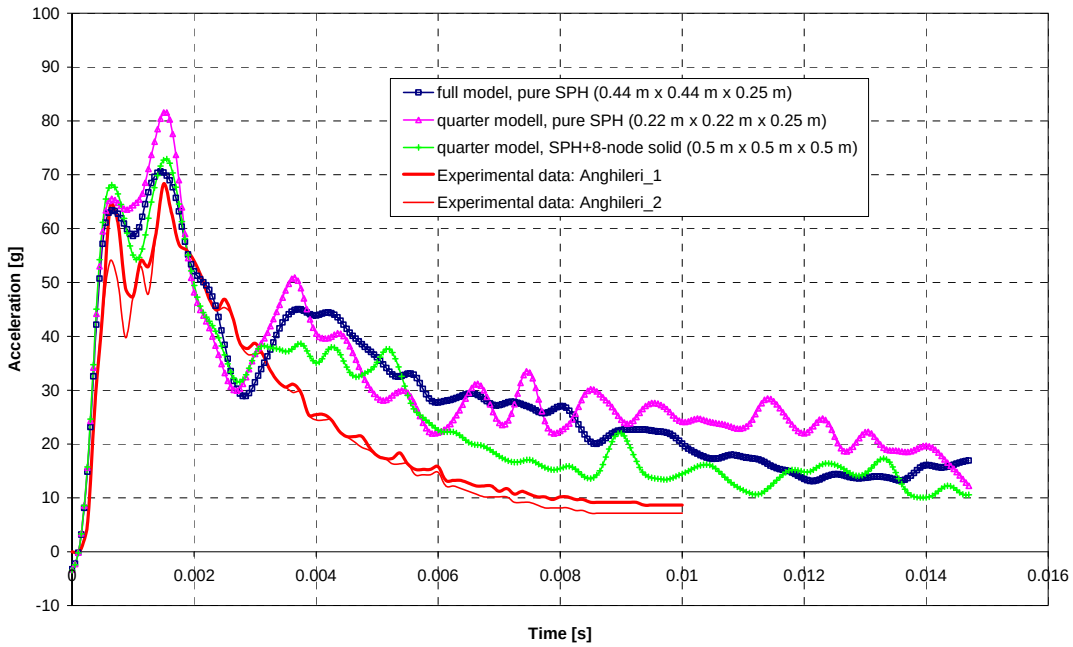

Figure 4-10 : Influence of symmetry conditions on the acceleration time histories (mixed FE-SPH model) using a hydrodynamic elastic-plastic material model

Mesh size effects

Using the same water pool size involving a mixed SPH/8-node solid mesh, the SPH size has been varied in order to quantify its influence on the simulated acceleration at the COG of the sphere. Four SPH sizes have been investigated, where various particle volumes are considered:

- 10^{-6} m^3 corresponding to a spacing of 0.01 m between two particles,
- 4.8 10^{-7} m^3 corresponding to a spacing of 0.008 m between two particles,
- 1.2 10^{-7} m^3 corresponding to a spacing of 0.005 m between two particles,
- 2.6 10^{-8} m^3 corresponding to a spacing of 0.003 m between two particles,

Figure 4-11 shows the influence of the mesh element size of the water pool on the acceleration time histories (filtered with a CFC600 filter) at the centre of gravity of the sphere. The coarser mesh shows high oscillations and leads to an over-estimation of the acceleration peak of almost 100%. For element size below 0.005 m (distance between two particles) / 1.2e-7 m^3 (volume of a particle), the calculated curves shapes are very close to each other: the acceleration peak and the plateau phase agree quite well with the experimental results.

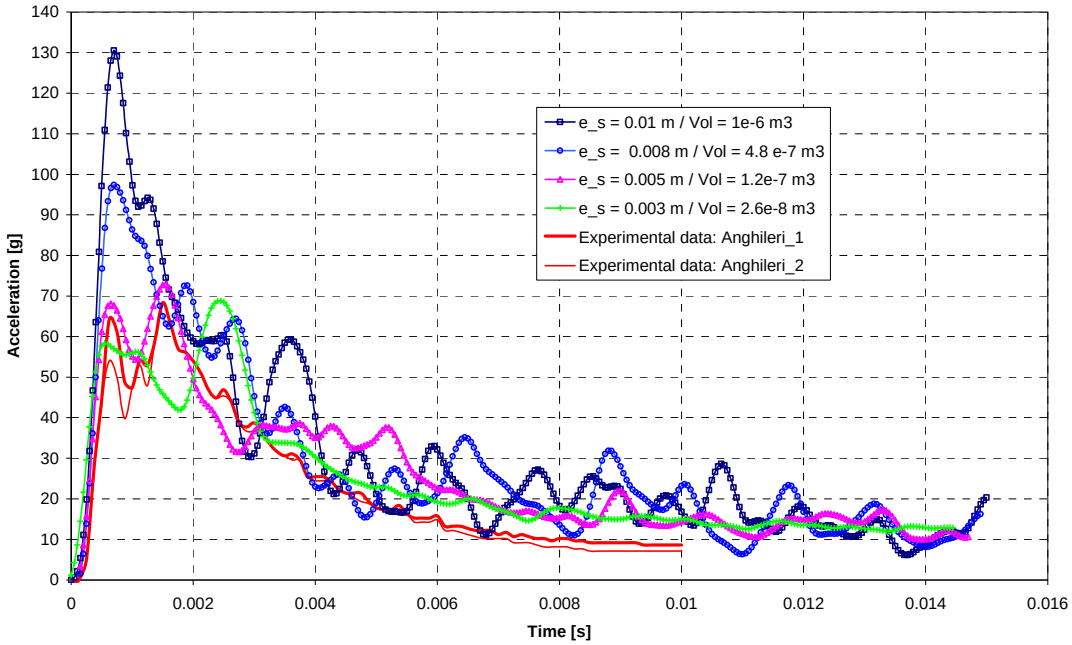

Figure 4-11 : Influence of the element size on the acceleration time histories (mixed FE-SPH model) using a hydrodynamic elastic-plastic material model

Meshing technique

For the previous studies, only uniform SPH meshes have been used. Nevertheless, various schemes are possible:

- the previous studies have been conducted with a mesh constituted of aligned SPH particles. A hexagonal distribution of the SPH particles is also possible but does not lead in our case to significantly better results. For this reason, no results involving such a mesh are chosen.
- a progressing mesh (from fine in the region of impact to coarse outside of it) can be used. This should be made, nevertheless, with caution in order to avoid instabilities in the SPH mesh. Indeed, within this work, SPH elements are defined according to their volume, which is also dependent on the spacing. Knowing the volume, the area of influence of the particle is also fixed. If a voluminous particle is located near a smaller one, the bigger one sees the smaller one but the smaller one may not see the bigger one. Interaction forces are not in equilibrium and may lead to unrealistic disturbance to the SPH mesh and even to an “explosion” of the mesh.

4.4.3 The Murnaghan law model

In this paragraph, a second material model based on the Murnaghan law and able to model the water behaviour is applied to the impact on water. As explained in § 4.3.2, this material law enables an artificial increase in the material compressibility, which increases the time step in explicit codes. Two different parameters for the Murnaghan law have been chosen for the investigations: $B = 0.144\ 10^9$ Pa and $B = 14.28\ 10^9$ Pa corresponding to expected maximum flow velocities of 100 m/s and 1000 m/s, respectively. For the calculation of the parameter B, the sound speed is assumed to be ten times higher than the flow velocity. Assuming a higher flow velocity for the simulation with the Murnaghan model is not an advantage, because the

computation time step would have the same order of magnitude as the one computed when using the hydrodynamic elastic plastic material model. Based on the experiences described in the previous paragraph, the following studies are conducted with a quarter model.

4.4.3.1 Investigations involving a pure FE mesh

The FE model (corresponding to the optimum of the investigations conducted in § 4.4.2.1) used for these investigations comprises

- a 0.22 m x 0.22 m x 0.22 m water pool meshed uniformly with 8-node solid elements, where the element size amounts to 0.005 m x 0.005 m x 0.01 m,
- a sphere with 0.218 m diameter meshed with shell elements with an average edge length of 0.008 m.

Figure 4-12 depicts a comparison between the results of three simulations, two conducted with the Murnaghan law and one conducted with the hydrodynamic elastic plastic material model, (already presented in Figure 4-3 to Figure 4-5) and the test data of the corresponding tests. The calculated acceleration curves are filtered with a CFC 600 filter. Whereas the Murnaghan law assuming a maximum flow speed of 100 m/s (B = 0.144 10^9 Pa) overestimates the measured acceleration peak by 8 %, the other simulation assuming a maximum flow speed of 1000 m/s (B = 14.28 10^9 Pa) shows an acceleration peak 22 % above the measured one. For both values of the parameter B, the simulations predict an acceleration plateau 120 % above the measured one. The choice of an "appropriate" sound speed for the simulation of the impact on water significantly influences the results and especially the acceleration peak. This shows that parameter calibration is necessary depending on the impact speed on water and probably on the geometry of the impacting structure. When comparing the results obtained with the hydrodynamic elastic plastic material model and the Murnaghan law assuming a maximum flow speed of 100 m/s (B = 0.144 10^9 Pa), the acceleration time histories are very close to each other and agree best to the test data.

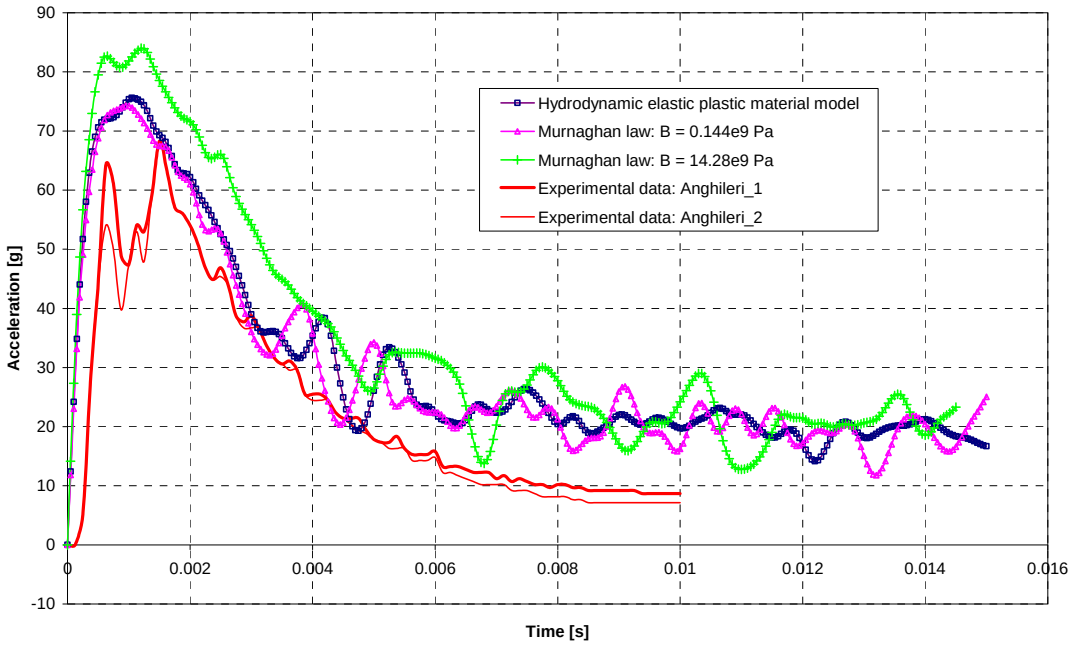

Figure 4-12 : Comparison of the acceleration time histories at the COG of the sphere between tests and the simulations (pure FE model) conducted with the Murnaghan material model and the hydrodynamic elastic plastic material model for the water medium

4.4.3.2 Investigations involving a FE-SPH mesh

For these investigations, the characteristics of the combined FE/SPH mesh are the same as those delivering the best results in § 4.4.2.2:

- a water pool with overall dimensions of 0.5 m x 0.5 m x 0.5 m meshed uniformly with SPH elements in the impact region corresponding to a total volume of 0.22 m x 0.22 m x 0.22 m and with 8-node solid elements outside of it (mixed FE-SPH mesh). Each SPH particle has an initial specific volume of 1.2 10^{-7} m^3 corresponding to a spacing of 0.005 m.
- a sphere with 0.218 m diameter meshed with shell elements with an average edge length of 0.008 m.

Figure 4-13 shows the acceleration time histories gained from two simulations conducted with the Murnaghan model and one simulation performed with the hydrodynamic elastic plastic material model (already presented in Figure 4-9 to Figure 4-11) using a combined FE/SPH mesh. These results are compared to the corresponding test data [73]. The calculated curves are filtered with a CFC 600 filter. The simulation based on the Murnaghan law assuming a maximum flow speed of 100 m/s (B = 0.144 10^9 Pa) overestimates the measured acceleration peak by 11 % whereas the water model assuming a maximum flow speed of 1000 m/s (B = 14.28 10^9 Pa) predicts an acceleration maximum 26 % higher than the measured one. In contrast, the acceleration plateaus after the peak are very similar for both variants of the Murnaghan law and amounts to an average value of 15 g, which is 33 % above the measured data. As reported in § 4.4.3.1, the Murnaghan law is able to predict the measurement after adjustment of its parameter B (see § 4.3.2) to the problem treated.

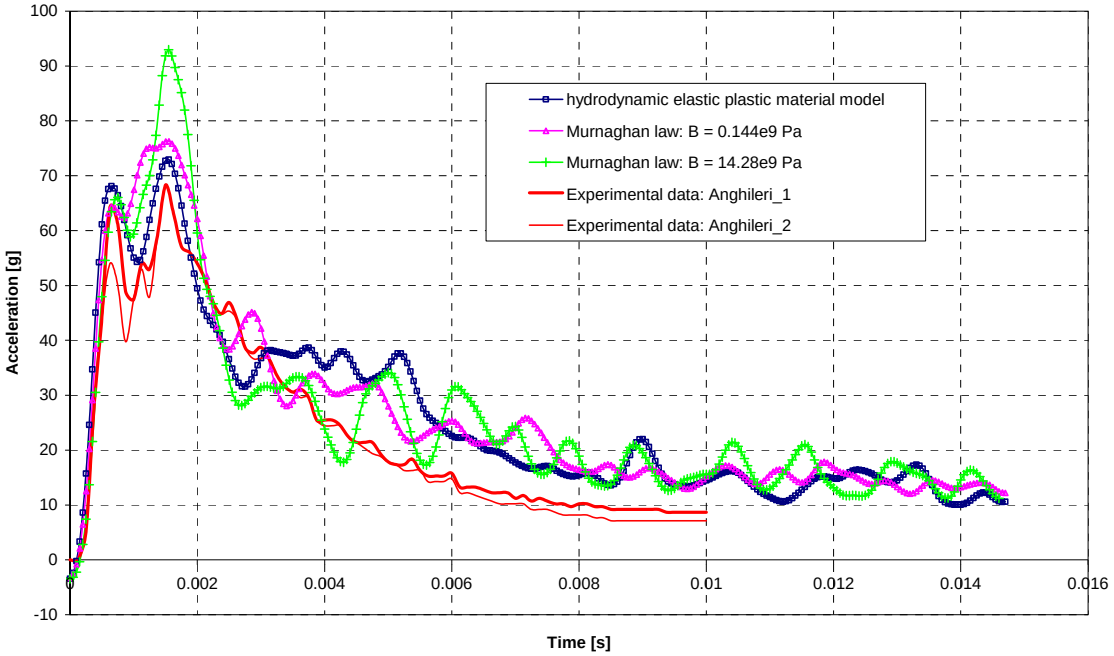

Figure 4-13 : Comparison of the acceleration time histories at the COG of the sphere between tests and the simulations (combined FE/SPH model) conducted with the Murnaghan material model and the hydrodynamic elastic plastic material model for the water medium

Based on the simulation results gained from the "best" Murnaghan law, the FE and combined FE/SPH mesh globally deliver results of similar precision when compared to the test data. Nevertheless, compared to a pure SPH simulation the mixed FE/SPH mesh predicts an

acceleration plateau level after the peak closer to the measurements when considering the test case reported in [73].

4.5 Validation of the water material model with other geometries

4.5.1 Cylinder

4.5.1.1 Reference tests

In [95], the results of the impacts on water of a cylinder are reported and are used in this paragraph for comparisons with the simulation data. A long rigid cylinder of 0.2096 m diameter is driven at a constant velocity into a quiescent water pool. The total force applied to the cylinder is the quantity measured during the tests, for which two velocities of 2.33 m/s (7.65 ft/sec) and 7.37 m/s (24.2 ft/sec) were investigated. The cylinder was sufficiently long to consider the flow to be two dimensional. Consequently, the results are given in the form of a total force per unit length for each impacting velocity.

4.5.1.2 Simulations with the hydrodynamic elastic plastic material model

Due to the symmetry of the cylinder and the two dimensional flow, two dimensional simulations with half a cylinder section were performed. The cylinder is considered rigid and a gravity field is applied on the water models. For comparison, the full FE and the combined FE/SPH simulations are based on the same mesh, whose characteristics are collected in Table 4-3. The knowledge gained from the investigations with the spheres in § 4.4 is used for the generation of the mesh. The water model is composed of two mesh zones: a fine one in the impacting zone and a coarse one outside of it. The transition between both mesh densities is modelled by a tied contact (similar to the SPH-FE transition). In this case, a finer mesh size than examined so far could be investigated involving elements with a volume of 2.5^3 mm^3 in the fine region of the mesh. This was made possible by the 2D nature of the problem, which makes the computation time still acceptable (see § 4.6).

Mesh type	**Total number of nodes**	**SPH particles or fine solid elements**		**Solid elements**
		Number	**Volume [mm^3]**	
5 mm-mesh	3,524	1,500	5^3	945
2.5 mm-mesh	8,020	6,000	2.5^3	945

Table 4-3 : Description of the meshes used for the water pool model

Figure 4-14 and Figure 4-15 show mesh plots of the simulation conducted with the hydrodynamic elastic plastic material model using respectively a pure FE and a combined FE/SPH model for the water continuum. Whereas the simulation with the pure FE mesh shows velocity magnitudes of 8.73 m/s in the jet area, velocity magnitudes up to 20 m/s are predicted by the simulation using the combined FE/SPH mesh. In addition, it is clearly visible that the mesh deformations in the case of the pure FE simulation are restricted due to the intrinsic topology of the finite element formulation.

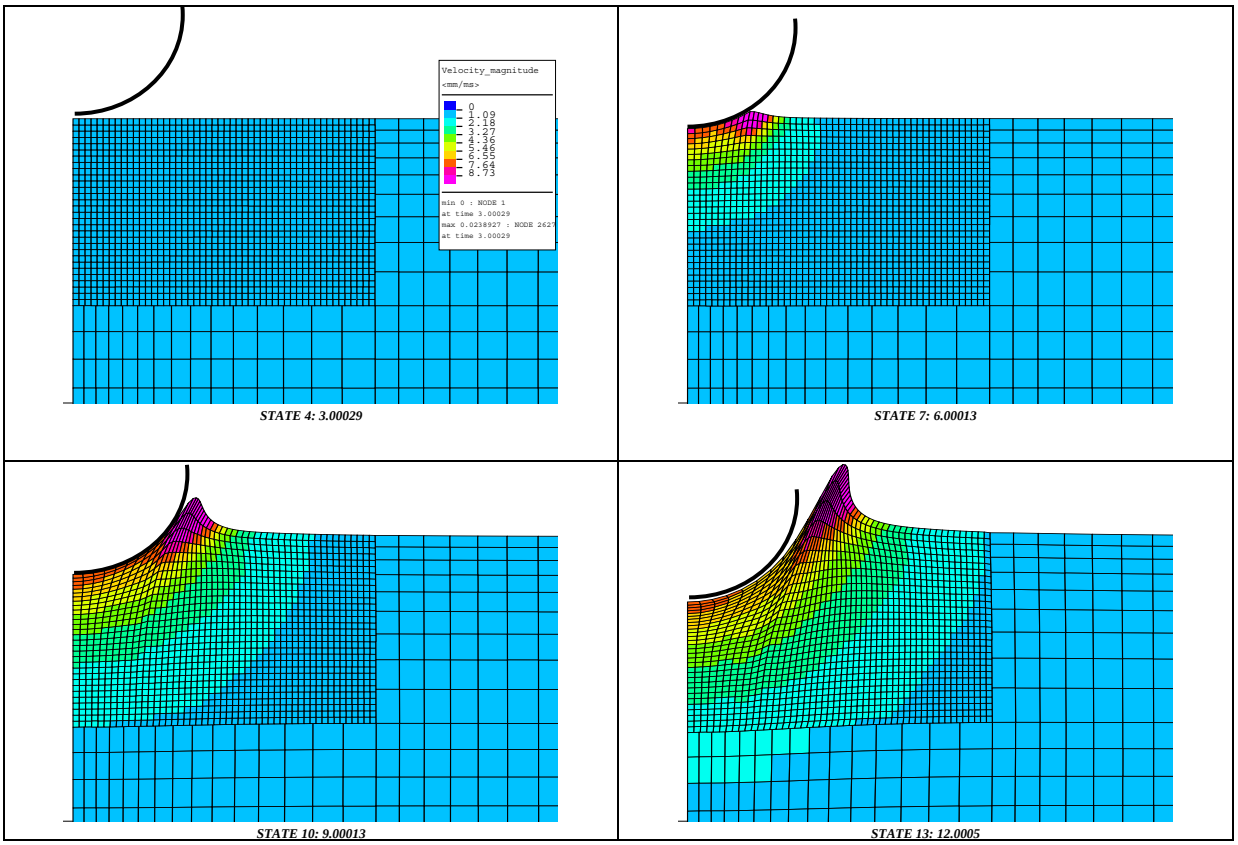

Figure 4-14 : Mesh plots of the cylinder impacting vertically on water at 7.37 m/s (hydrodynamic elastic plastic material model/full FE model/legend: velocity magnitude)

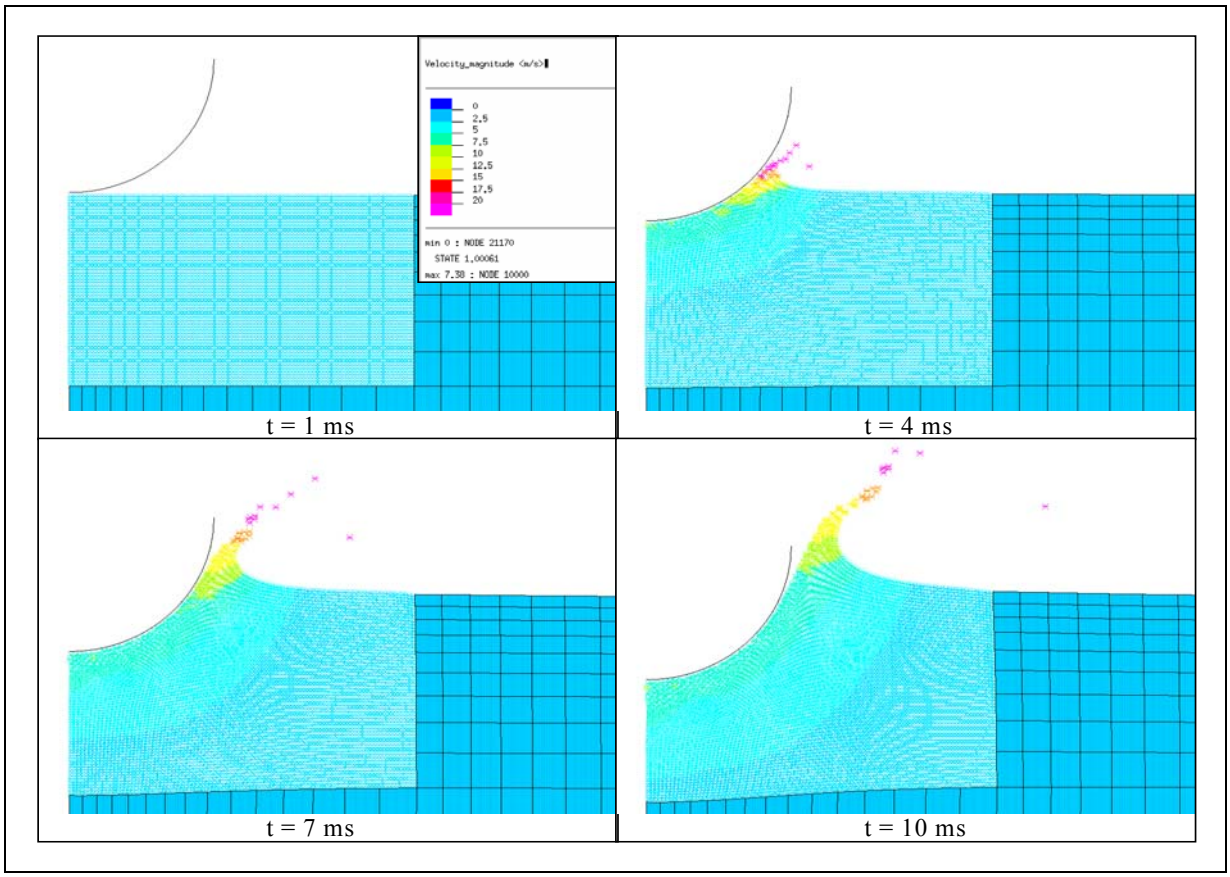

Figure 4-15: Mesh plots of the cylinder impacting vertically on water at 7.37 m/s (hydrodynamic elastic plastic material /combined SPH-FE model/legend: velocity magnitude)

Figure 4-16 and Figure 4-17 depict the contact force per unit length of the cylinder on water respectively for both impact speeds 2.33 m/s and 7.37 m/s when using the hydrodynamic elastic plastic material model. Making abstraction of the simulation case of the very fine combined SPH-FE mesh in the case of 7.37 m/s impact speed (see following explanations), the calculated forces are in fairly good agreement with the experimental data.

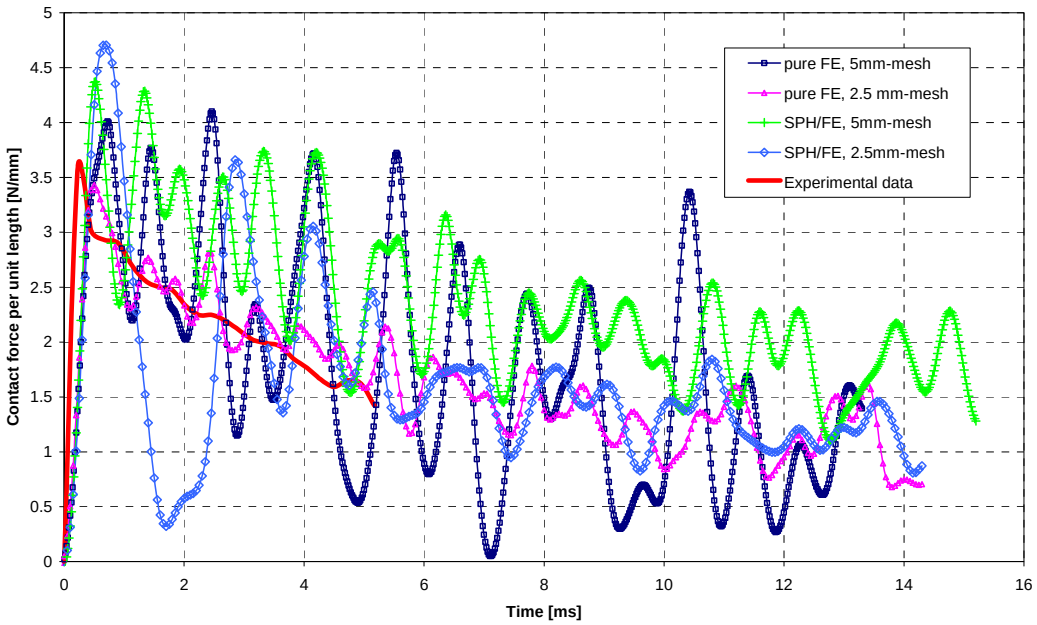

Figure 4-16 : Comparison of the contact force per unit length time histories of the cylinder between tests and the simulations (combined FE/SPH model, various mesh densities) conducted with the hydrodynamic elastic plastic material model for the water medium (impact speed: 2.33 m/s)

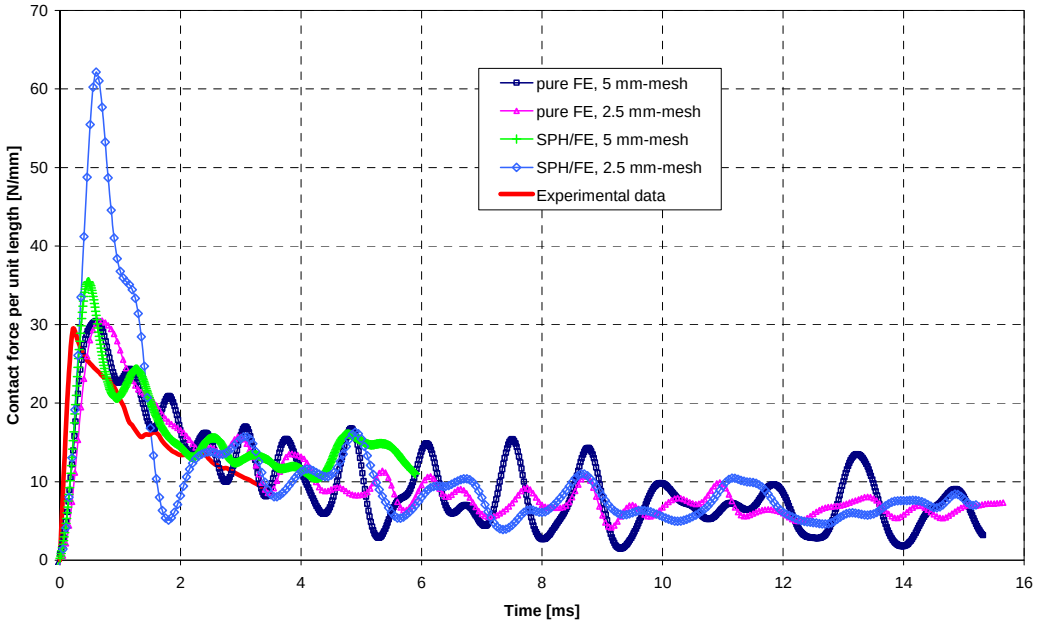

Figure 4-17 : Comparison of the contact force per unit length time histories of the cylinder between tests and the simulations (combined FE/SPH model, various mesh densities) conducted with the hydrodynamic elastic plastic material model for the water medium (impact speed: 7.37 m/s)

The effect of a finer mesh on the calculated force obtained with a pure FE mesh clearly leads to smoother curves, whereas high oscillations appear in the case of a combined FE/SPH mesh especially at the very beginning of the impact when refining the SPH mesh. This trend is particularly noticeable in Figure 4-16 where the amplitude of the oscillations is very close to the level of contact forces sustained by the cylinder. The use of a filter is nevertheless not recommended because important information gets lost such as the maximum calculated contact force. With the refined mesh, the impact force is high enough to separate the particles from each other at the point of impact. This consequently leads to uncontrolled disturbance in that region and arbitrary displacements of the "detached flying" particles, where each of them very locally causes isolated short-time contact forces on the cylinder. This phenomenon is of course amplified when the impact velocity is increased (simulation case with the very fine combined SPH-FE mesh in the case of 7.37 m/s impact speed in Figure 4-17). To sum up, a finer mesh is not always a guarantee for the best results especially when the first moments of the impact are considered. This latter especially applies for the combined FE/SPH mesh.

4.5.1.3 Simulations with the Murnaghan material model

Figure 4-18 and Figure 4-19 illustrate the contact force per unit length of the cylinder on water respectively for both impact speeds 2.33 m/s and 7.37 m/s when using the Murnaghan material model (material input - $B = 0.144\ 10^9$ Pa - corresponding to expected maximum flow velocities of 100 m/s). The water and cylinder models are the same as the ones used previously. All simulations deliver results of very similar order of magnitude to the experimental results. For the lowest impact velocity (2.33 m/s), the calculated contact forces especially agree well with the experimental data. The quality of these results is explained by the fact that the compressibility effect remains negligible due to the low impact velocity and therefore makes the Murnaghan material model particularly adequate. The amplitude of the contact force oscillations is smaller than in the simulations with the hydrodynamic elastic plastic material model (Figure 4-16). When comparing the results gained from the pure FE model with two different mesh densities, the peak of the contact force is very close to the measured peak for the 5 mm mesh and is underestimated with the 2.5 mm mesh. In contrast, the combined SPH-FE models overestimate the peak for both meshes by 26 % but simulation results remain very satisfactory.

For the higher test velocity (7.37 m/s), the predictions of the simulations using the Murnaghan material model are also very satisfactory and remain conservative towards measured data. The pure FE mesh provides contact forces in very good agreement with the experimental data whatever the mesh density used whereas the combined SPH-FE mesh overestimates the contact peak by approximately 30 % but remains in good agreement with the force plateau level after the first contact.

For both test cases, the same remark as for the hydrodynamic elastic plastic material model is valid: the refinement of the mesh attenuates the oscillations of the contact force by using pure FE whereas it increases them by using a combination of SPH and FE.

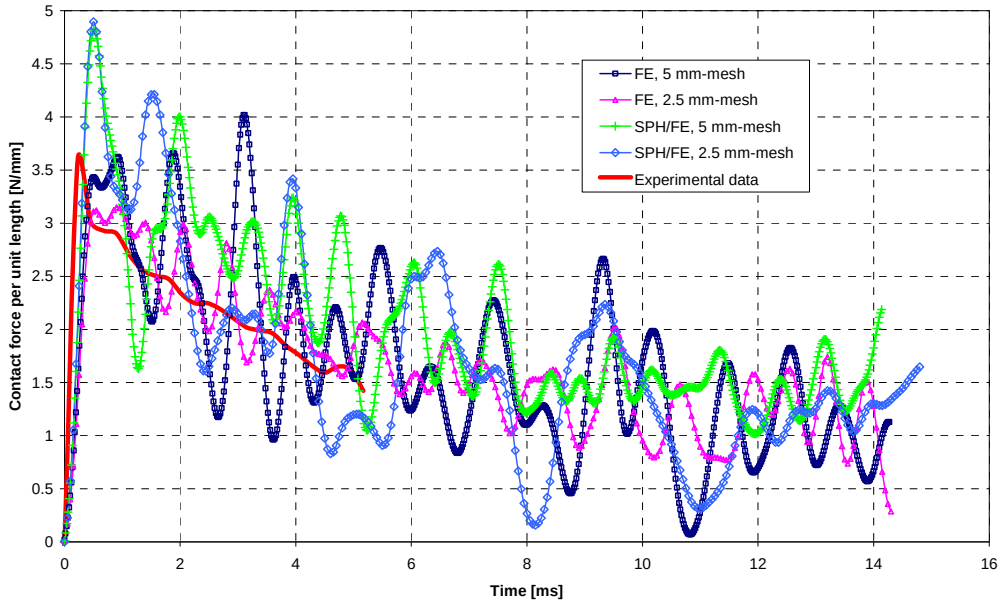

Figure 4-18 : Comparison of the contact force per unit length time histories of the cylinder between tests and the simulations (combined FE/SPH model) conducted with the Murnaghan material model for the water medium (impact speed: 2.33 m/s)

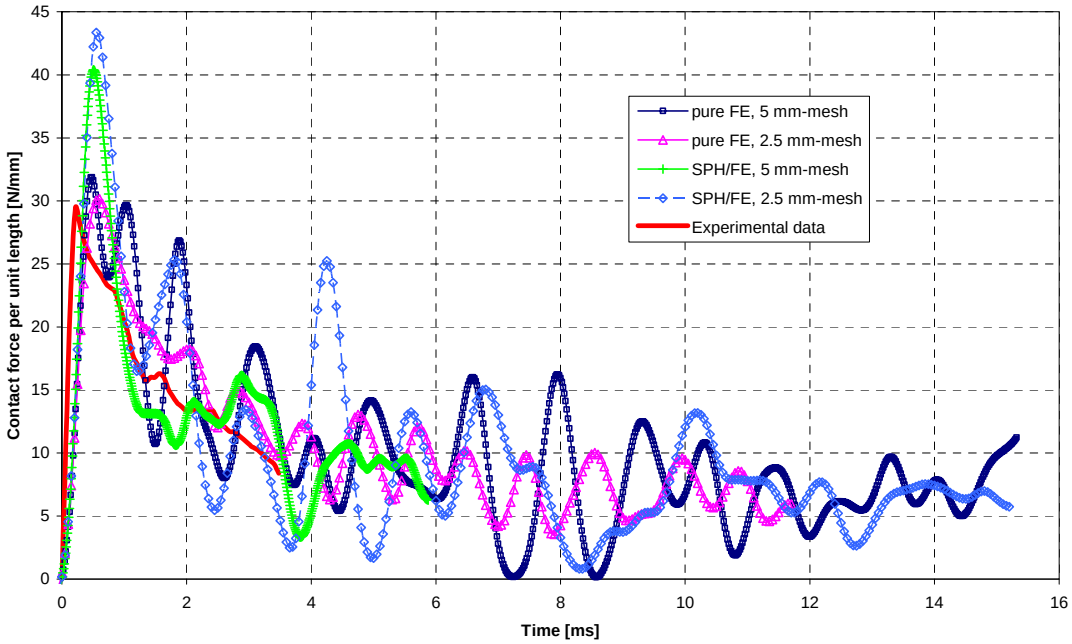

Figure 4-19 : Comparison of the contact force per unit length time histories of the cylinder between tests and the simulations (combined FE/SPH model) conducted with the Murnaghan material model for the water medium (impact speed: 7.37 m/s)

4.5.2 Wedges

4.5.2.1 Reference tests

The drop tests into water of three wedges with deadrise angles of 10°, 20° and 30°, and a weight of 2.34 kg are reported in [96]. The tested wedges have a length of 6 inches. The water container is experimentally built so that the gap between the wedge sides (parallel to the section) and the water container is kept at a minimum, so that the flow can be considered two-

dimensional. All wedges were dropped from a height of ca. 125 mm, which corresponds to an impact speed on water of 1.58 m/s. The measured quantity is the vertical acceleration time histories measured at the upper side of the wedge, where the final data for each deadrise angle are an average gained from several drops at the same height.

4.5.2.2 Simulations with the hydrodynamic elastic plastic material model

Due to the symmetry of the wedges and the two dimensional flow, two dimensional simulations with half a cylinder section were performed. The weight of the wedges has been adapted to the model dimensions in order to respect the mass to length ratio. In addition, the wedge is considered infinitely rigid and a gravity field is applied on the structure and the water model. The water model consists of 9.088 nodes and 4,392 solid elements and the average element size in the region of impact amounts to 2.5 mm x 2.5 mm x 2.5 mm, which corresponds to a relatively fine mesh.

Figure 4-20 and Figure 4-21 show the velocity contour in the horizontal and vertical direction (drop direction) in the pure FE and combined SPH-FE models respectively at the same time (t = 19.5 ms after the contact). Comparing both Figures, the SPH simulation qualitatively better describes the jet effect of water than the classical FE calculation.

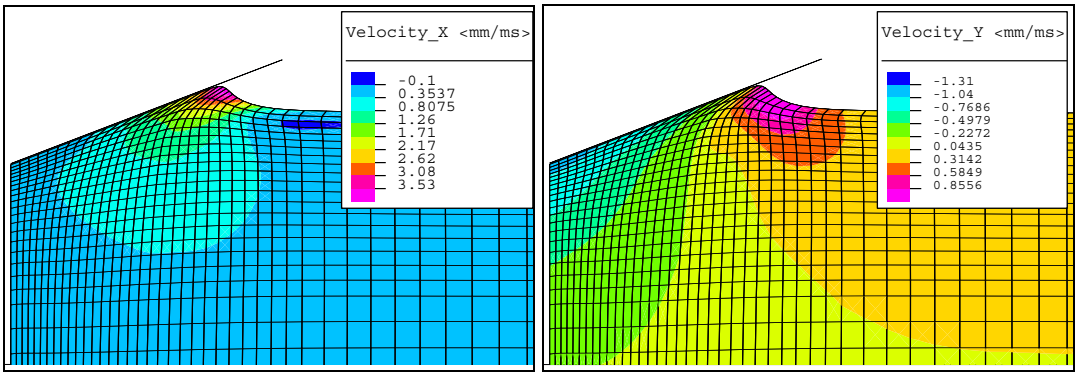

Figure 4-20 : Plots of the 20° deadrise angle wedge at time t= 19.5 ms (pure FE mesh / hydrodynamic elastic plastic material model) showing the horizontal and vertical velocity distribution in the water model

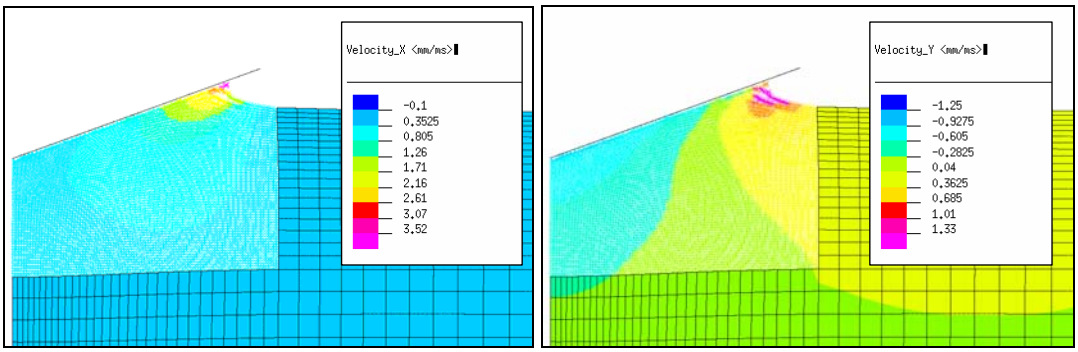

Figure 4-21 : Plots of the 20° deadrise angle wedge at time t= 19.5 ms (combined FE-SPH mesh / hydrodynamic elastic plastic material model) showing the horizontal and vertical velocity distribution in the water model

In Figure 4-20, due to the topological connectivity of the solid elements with their neighbours, the water surface remains tangential to the wedge surface in the zone, where the highest water elevation takes place, whereas in this area some SPH particles are able to go along the wedge

surface and therefore form a convex arc with the undisturbed water surface. Concerning the horizontal component of the velocity of water in the area of impact, they are exactly the same for the pure FE and the combined SPH-FE model. The range of velocities reached is also the same. In contrast to the X-velocity distribution, results are quite different between both techniques. In the case of the pure FE model, the maximum vertical velocity of the water reaches 0.85 m/s whilst it reaches 1.33 m/s for the SPH simulation. This difference is particularly sensitive in the jet region, where SPH particles tend to glide along the wedge surface. Outside this region, the distribution of the vertical component of velocity is similar whatever the techniques used.

Figure 4-22 and Figure 4-23 depict the acceleration time histories measured on the three wedges and compare them to the calculated ones using the hydrodynamic elastic plastic material model for the water when the water is meshed respectively with pure finite elements and a combination of SPH and finite elements. For both mesh philosophies, there is no major difference in the simulation results and the same tendency as in the tests is observed in all simulations: the bigger the deadrise angle, the later the maximum acceleration takes place, the lower the value of the acceleration maximum and the shorter the pulse. Although all the results are conservative compared to the test data, the agreement of the simulation data with the test data strongly depends on the deadrise angle of the wedge investigated.

For the 30° wedge, the maximum of the calculated acceleration agrees very well with the measured one and amounts to 2.6 to 2.9 g compared to 2.4 g experimentally. Nevertheless, the time of the calculated maximum is brought forward by 8 ms. The assumption that the air layer between the impacting structure and the water surface may delay the acceleration peak is not apparent because this effect is not accentuated in the simulations with the lower deadrise wedges (20° and 10°).

Concerning the 20° deadrise wedge, both calculated and measured acceleration time histories agree excellently, both from the maximum value and from the time of the maximum. For this wedge, the acceleration maximum reaches 4.8 g and 5 g at t = 8.3 ms after the contact with water for both meshes.

Finally, the calculated results for the 10° deadrise angle are quite different from the experimental one as far as the acceleration peak is concerned. The measured peak reaches 7 g at t = 5.7 ms whereas the simulation model exhibits an acceleration maximum of 11 g at approximately t = 4.5 ms. This discrepancy can be explained by the fact that the 10° deadrise wedge is in the range of shape for which compressibility effects of water cannot be neglected during the impact. It should be remembered that the hydrodynamic elastic plastic material model used to model water is based on the quasi-incompressibility of water. In addition, the presence of an air layer between the structure and the water surface may be important as reported in § 3.1.2 when the structure impacting on water has a flattened base. This has the effect to cushion the impact and therefore decrease the acceleration level. This aspect is further discussed in § 4.5.2.4.

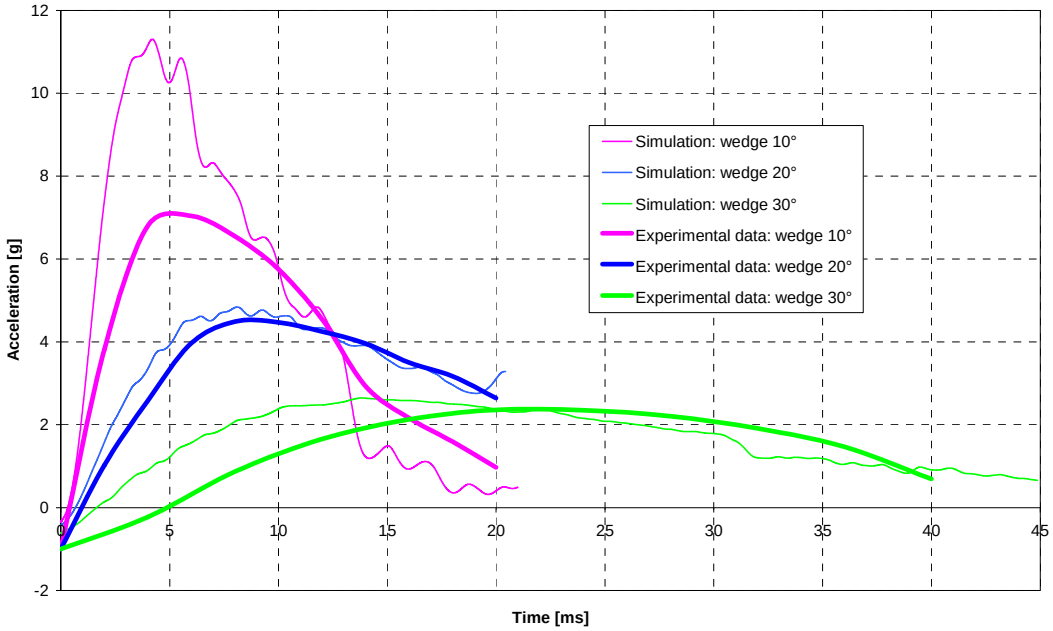

Figure 4-22 : Comparison of the acceleration time histories between tests and simulations (pure FE model) conducted with the hydrodynamic elastic plastic material model for the water medium and involving three wedge deadrise angles (10°, 20° and 30°)

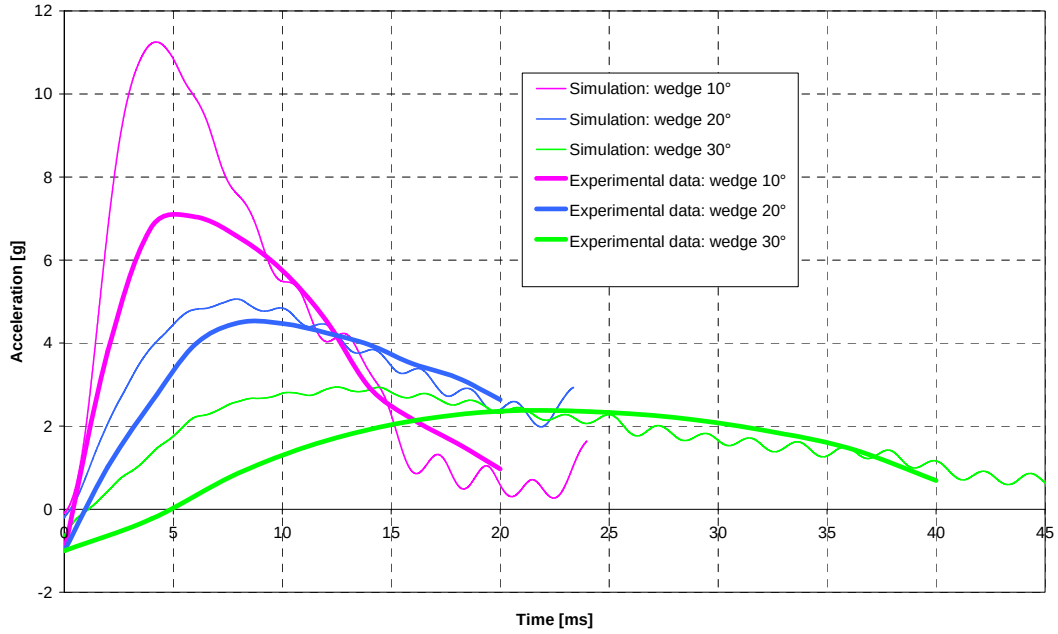

Figure 4-23 : Comparison of the acceleration time histories between tests and simulations (combined SPH-FE model) conducted with the hydrodynamic elastic plastic material model for the water medium and involving three wedge deadrise angles (10°, 20° and 30°)

4.5.2.3 Simulations with the Murnaghan material model

Figure 4-24 and Figure 4-25 depict the acceleration time histories measured on the three wedges and compare them to the calculated ones using the Murnaghan material model for the water when the water is meshed respectively with pure finite elements and a combination of SPH and finite elements. For the simulations using the the Murnaghan material model, the material input (B = 0.144 10^9 Pa compatible with expected maximum flow velocities of 100 m/s) corresponds to the best results obtained with the sphere (§ 4.4.3). The same comments as

for the simulations with the hydrodynamic elastic plastic material apply to the calculations performed with the Murnaghan material model.

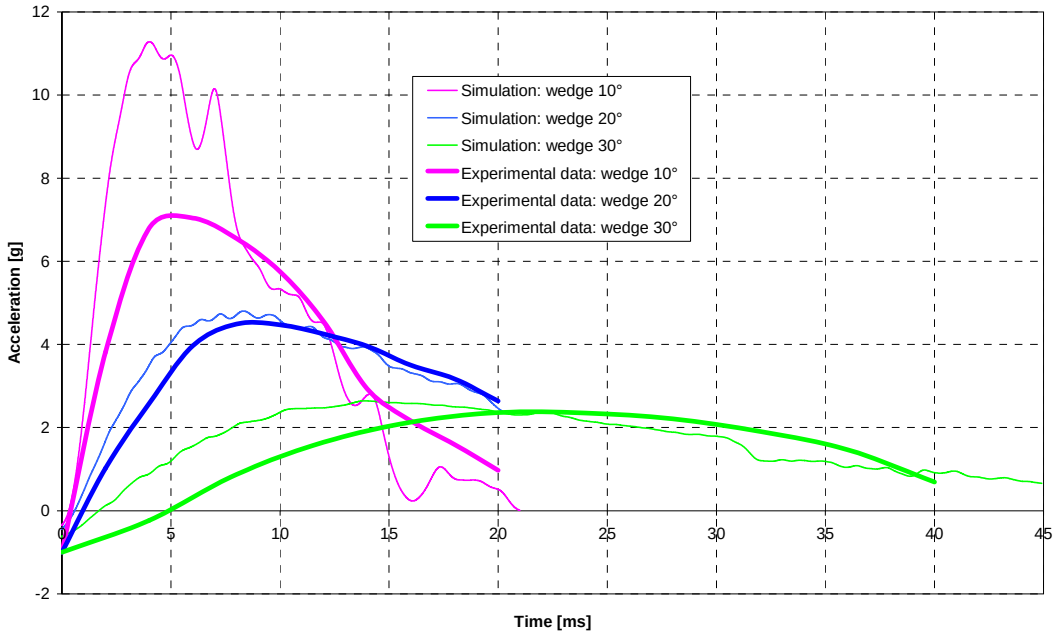

Figure 4-24 : Comparison of the acceleration time histories between tests and simulations (pure FE model) conducted with the Murnaghan material model for the water medium and involving three wedge deadrise angles (10°, 20° and 30°)

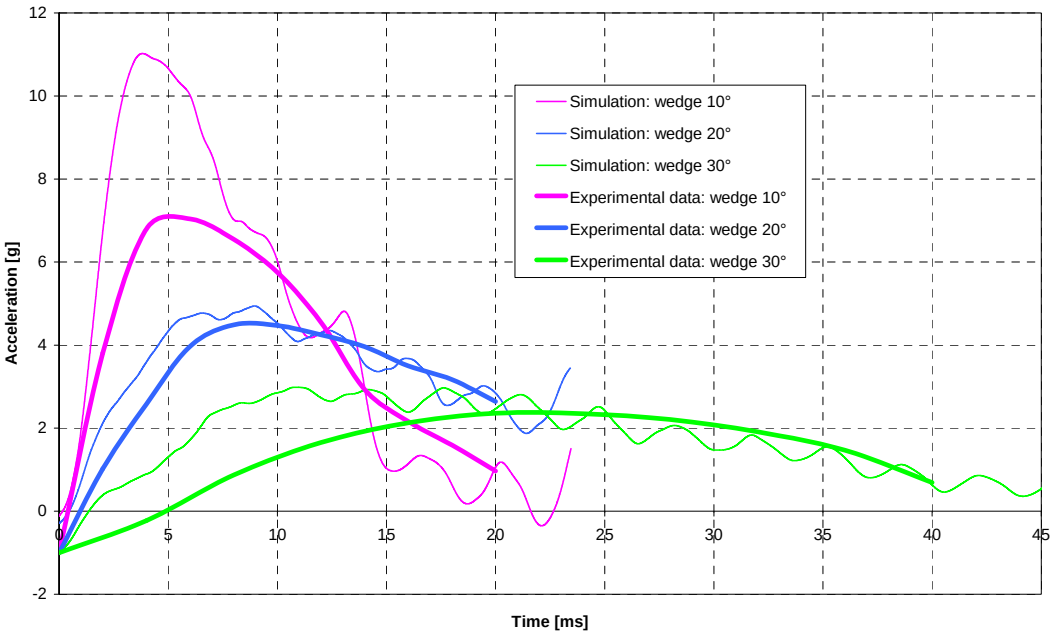

Figure 4-25 : Comparison of the acceleration time histories between tests and simulations (combined SPH-FE model) conducted with the Murnaghan material model for the water medium and involving three wedge deadrise angles (10°, 20° and 30°)

4.5.2.4 Influence of an air layer model between the impacting body and the water surface

The influence of an “air layer” on the results when a rigid body with a “flat” bottom impacts on water was partly investigated in [97] but was not applied here due to the additional

computation time linked to it and to necessary further work in the subject. It is proposed in this paragraph to briefly recapitulate the major lessons of the investigations:

- the properties of the air layer could not be used exactly for the simulations due to the strong difference in density between water and air (factor ~ 1.0 10^6 at atmospheric pressure), which causes dramatic numerical instabilities between both water and the air layers meshes. As a result, it was necessary to use a higher density for the air to run the analysis in a stable way.
- this intermediate air-like layer between the structure and the water surface can be modelled solely with SPH due to the high compressibility of air, which would cause high deformations in a classical FE mesh and consequently lead to the abortion of the simulation.
- introducing such an intermediate layer decreases the level of the loads on the structure when impacting on water.

Figure 4-26 illustrates a simulation sequence including the modelling of an air-like layer between a 10° deadrise wedge and the water surface. In a first phase (t = 8 ms), the air-like intermediate layer is compressed by the structure, which approached the water surface. At t = 16 ms, the deformation of the water surface, which takes the shape of the wedge bottom, can be observed before any contact between the wedge and the water surface has occurred. During the whole impact, the intermediate layer is progressively pushed outside the impact region due to the geometry of the wedge. All these events leads to a cushioning effect on the impact.

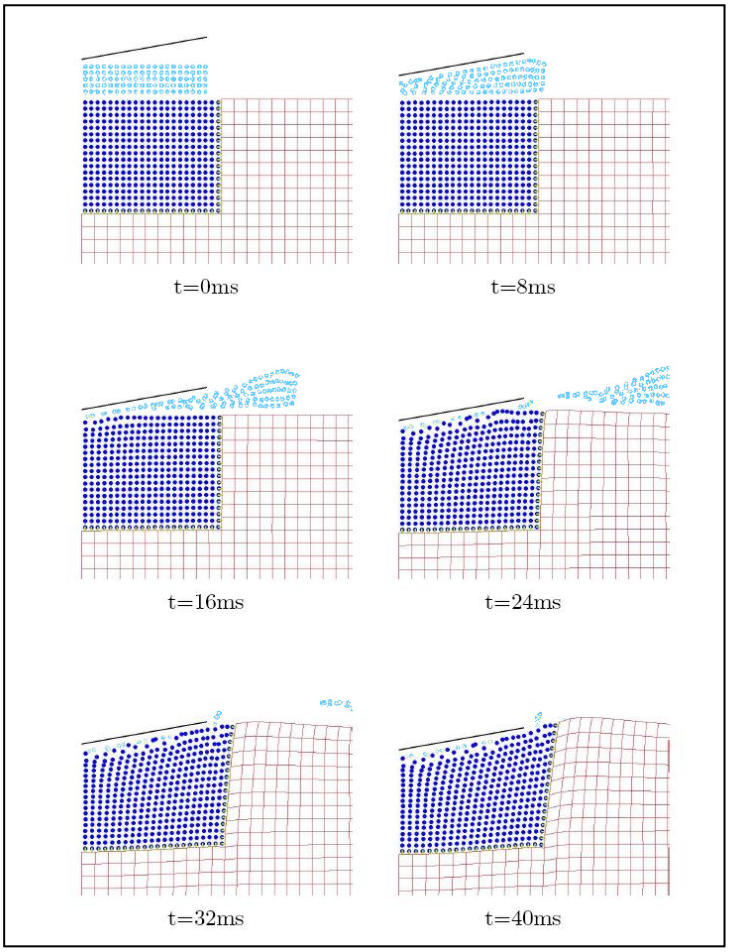

Figure 4-26 : Simulation of the impact on water with an intermediate air-like layer between the structure and the water surface (wedge with a 10° deadrise angle) [97]

4.6 Computational aspects

As the meshes with the SPH particles have been generated from the same meshes (5 mm and 2.5 mm element size) as the ones with the classical finite elements for the two-dimensional simulations with the cylinder (§ 4.5.1), CPU times can be directly compared. All the simulations were performed on a HP workstation equipped with one processor (9000/785/J5600 processor with 552 MHz frequency). Table 4-4 shows the CPU times necessary to simulate the first 20 milliseconds of a cylinder impacting on water. It can be observed that the SPH technique is very helpful to save computation time for the impact velocity of 7.37 m/s. As the Finite Element mesh of the water continuum undergoes very high deformations at early times in that case, this leads to a dramatic decrease of the time step and therefore to a higher computation times. The gain in CPU time for the SPH technique in comparison to simulations performed with a classical Lagrangian technique reaches 48 % for these simulations. For low impact velocities (e.g. V = 2.33 m/s), the combined SPH-FE technique is more time consuming in comparison to the pure FE method leading to CPU times twice to three times as high as the ones of the FE method and this whatever the mesh used.

Mesh size	**Material type**	**Impact velocity**	**CPU time [s]**		**Gain in time**
			Classical FE	**Combined SPH-FE**	
5 mm-mesh	**Hydro. elast. plast.**	**2.33 m/s**	175	512	+192 %
		7.37 m/s	415	268	- 35 %
	Murnaghan	**2.33 m/s**	109	299	+ 174 %
		7.37 m/s	288	150	- 48 %
2.5 mm-mesh	**Hydro. elast. plast.**	**2.33 m/s**	1775	5017	+ 327 %
		7.37 m/s	7089	5158	-27 %
	Murnaghan	**2.33 m/s**	-	2897	-
		7.37 m/s	-	2977	-

Table 4-4 : Comparison of CPU times between the pure FE and the combined FE-SPH techniques for the 2D simulations conducted with the cylinder (§ 4.5.1)

Nevertheless, care must be taken when 3D-simulations are considered. The previous conclusions may not apply. Knowing that the computation of the contacts represents at least 95% of the computation time in the simulations involving SPH elements, it is clear that increasing the number of SPH particles exponentially increases the total computation time. As a consequence, the gain represented by the more stable time step offered by the SPH elements is not high enough to compensate the dramatic decrease of the time step due to deformation of a pure FE solid mesh.

Table 4-5 illustrates the influence of the SPH number on the total computation time. The analyses were performed on 2-processors Linux PC (1001L AMD Opteron: 2 x AMD Opteron 242, 1.6 GHz). The mesh size amounts to 5 mm between two SPH particles. Comparing the computation times between a full model and a quarter models (using the

symmetry of the loading case), the computation time is not divided by four but here by a factor of approximately 13. This is explained by the fact that the computation time is mainly due to the computation of the contact between the individual SPH elements. When considering a regular mesh, the number of direct neighbours seen by each SPH particle increases from 8 to 26 between a 2D and a 3D model. The number of contacts, which should be computed, is then increased by a factor of three for each particle. This trend is additionally amplified by the increased number of SPH particles when considering a 3D model.

For information, supplementary results are included in Table 4-5 concerning the CPU time necessary to simulate the same test case with a combined SPH-FE mesh and a pure FE mesh. The following results can be derived:

- the use of additional FE solid elements to extend the model of the water pool costs almost no additional computation time
- a pure FE model should be chosen, when the deformation sustained by the water elements do not lead to a simulation abort or to unrealistic behaviour. To that aim, extended solid elements in the direction of the impact can be very helpful (§ 4.4.2.1).

Mesh type	Number of SPH	Number of solids	Number of nodes	CPU time [s]
Only SPH / full model	387,200	0	387,200	586,080
Only SPH / quarter model	96,800	0	96,800	43,615
SPH-FE / quarter model	96,800	1,035	98,200	41,561
Only FE / quarter model	0	49,435	54,059	1,827

Table 4-5 : Comparison of CPU times between the pure FE and the combined FE-SPH techniques for the 3D simulations conducted with the sphere (§ 4.4) / 5 mm mesh

Taking into account for the previous remarks, it is clear that including an air-like layer in a 3D model would significantly decrease the time step and therefore make the simulation impossible to compute even on a cluster of PCs.

4.7 Water modelling strategies for application to complex structures

In § 4.4 and § 4.5, two meshing strategies and two material models to describe the water behaviour were investigated and this for different basic body shapes (sphere, cylinder and wedges with various deadrise angles) impacting on water. These studies show that:

- the modelling of water with a pure FE mesh (8-node solids) is appropriate to simulate the first milliseconds of the impact on water as long as the mesh elements are not too deformed.
- a combined SPH-FE mesh for water is also well suited to the simulation of the impact on water. It has the advantage to keep the time step more stable during the whole simulation run when this latter is controlled by the water SPH elements. In some specific 2D cases, using SPH can reduce the simulation time especially compared to a pure FE run when the deformation of the mesh is getting critical.
- when using a SPH mesh in the zone of impact, the water splash looks very realistic compared to a FE mesh, which is limited by the topology of the FE method itself.

- the agreement between calculated and measured time histories depends on the material parameter used for the Murnaghan material model. After calibration based on the sphere impact case, B was set to 0.144 10^9 Pa corresponding to an expected maximum flow velocities of 100 m/s as explained in § 4.3.2.
- refinement of the mesh leads in the case of pure FE simulations to less spurious oscillations in the time histories whereas in the case of a combined SPH-FE mesh, high oscillations are amplified at the beginning of the impact. This could be observed especially in the 2D investigations.
- mesh sizes below 5 mm in combination with a pure FE mesh and the Murnaghan material model for water may under-predict the maximum forces (§ 4.5.1.3). This happens once for the test case concerning the cylinder impacting water at a velocity of 2.33 m/s.
- all simulations conducted apart from the special configuration described above are delivering conservative results compared to the test data and this for all mesh sizes investigated.
- a refined FE-mesh in combination with the hydrodynamic elastic plastic material model for the water medium predicts best the quantitative measured data.

Based on these results, the following modelling guidelines are adopted in the next chapter, where it is very important that the results remain conservative compared to test data:

- the water behaviour will be modelled with the hydrodynamic elastic plastic material model, for which the parameters remain the same for all impact velocities in contrast to the Murnaghan material model, which requires calibration.
- a pure FE mesh for the water medium will be preferred if the deformation of the water elements enables enough simulation time. If possible from the computation time point of view, a combined FE/SPH model should be used. It will be seen that in some case, solely a combined SPH-FE mesh is appropriate.
- the mesh size will be chosen as fine as possible as long as the computation time remains in an acceptable frame.

5 Numerical investigations of the impact on water of aircraft structures

Based on the knowledge gained in Chapter 4, the aim now is to apply the methods to the impact on water of aeronautical structures, which can **deform under the water loads** in contrast to the previous studies. The quality of the calculated results is judged by comparing them to test measurements and observations gained within the CAST Project [98]. In a first step, the vertical impacts on water of a WG30 helicopter sub-floor structure and then of a full-scale WG30 helicopter are investigated [99, 2]. In particular, predicted structural deformations, acceleration and pressure time histories are especially correlated to the tests and extensively discussed. In a second step, a methodology based on a local/global technique to analyse the behaviour of an aircraft landing on water is tested [100]. A forward velocity component is this time considered at impact.

5.1 Simulation of the vertical impact on water of a sub-floor component and a full-scale WG30 helicopter

5.1.1 WG30 sub-floor structure

5.1.1.1 Test component and test set-up

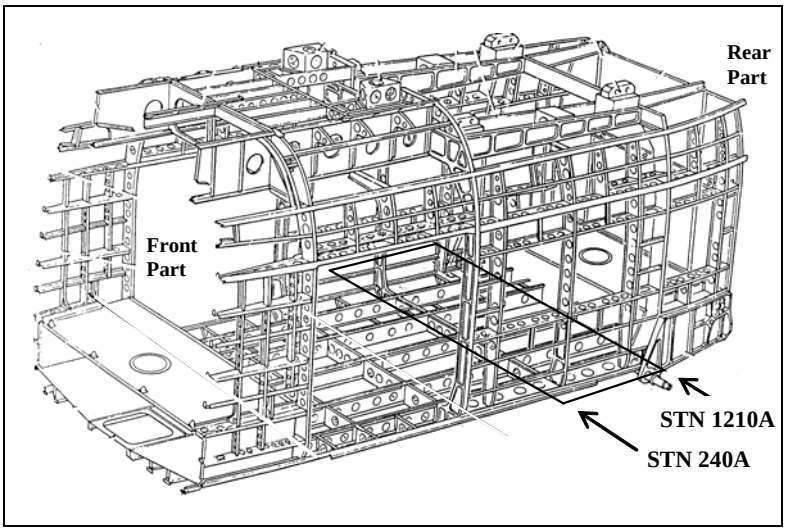

Figure 5-1 : Location of the tested sub-floor structure in the WG30 helicopter airframe [101]

The tested sub-floor structure, which was provided by Westland Helicopters, is cut between stations STN 240A and STN 1210A of a WG30 sub-floor as shown in Figure 5-1 and therefore includes two frames located at STN 380A and 1210A. This component, representative of a common sub-floor of a helicopter, has a weight of 41 kg and following dimensions: 2,170 mm (width) x 970 mm (length) x 163 mm (height). An aluminium alloy 2014T6 was used to manufacture the majority of the structure except the floor panels which are out of Fibrelam panels (unidirectional cross-plied fiberglass bonded to an aramid honeycomb core).

After pre-test simulations with different configurations and advice from the manufacturer [101], it was decided to fix the component to a guided trolley by mean of 18 rods positioned on the seat rail of the structure as shown in Figure 5-2. In addition, the weight of the structure located above the sub-floor in the overall helicopter was taken into account by adding masses above the rods. The final mass of the ballast, the trolley, the mounting and cables amounts to 607 kg.

The structure impacted vertically the water surface at a velocity of 7.85 m/s and remains in the same attitude during the test due to guide rails and a wheels assemblage as shown in Figure 5-3. This means that the structure impacts in a zero attitude the water surface representing the worst impact conditions for the structure, which is expected to undergo very high damage. The sub-floor structure was instrumented with 3 accelerometers on the seat rails, 14 pressure transducers and 6 strain gauges on the skin, whereas only the data from the pressure transducers (Figure 5-4) have been used for the validation of the simulation technique. The signal of the strain gauges was too disturbed for any reasonable exploitation and the signal of the accelerometers was not exploitable due to a too short measurement range (measurements cut).

Figure 5-2 : Test article in the test rig at CIRA, Italy [101]

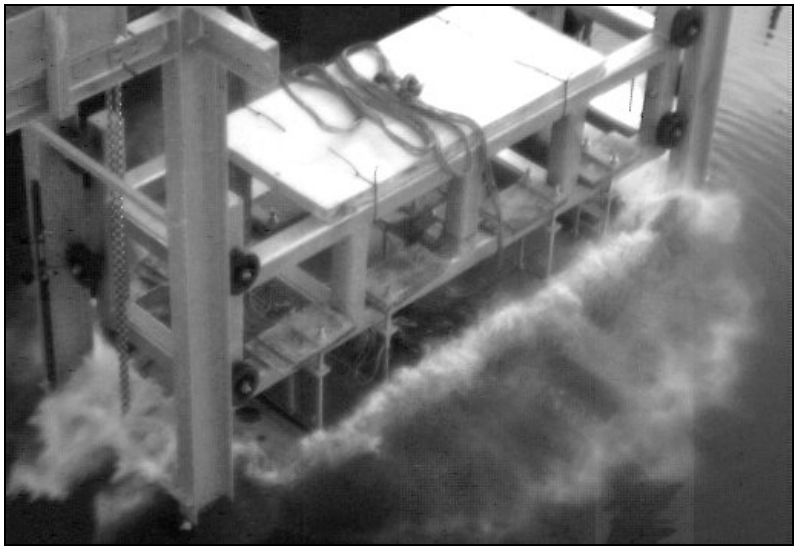

Figure 5-3 : Drop test of the WG30 sub-floor at CIRA [101]

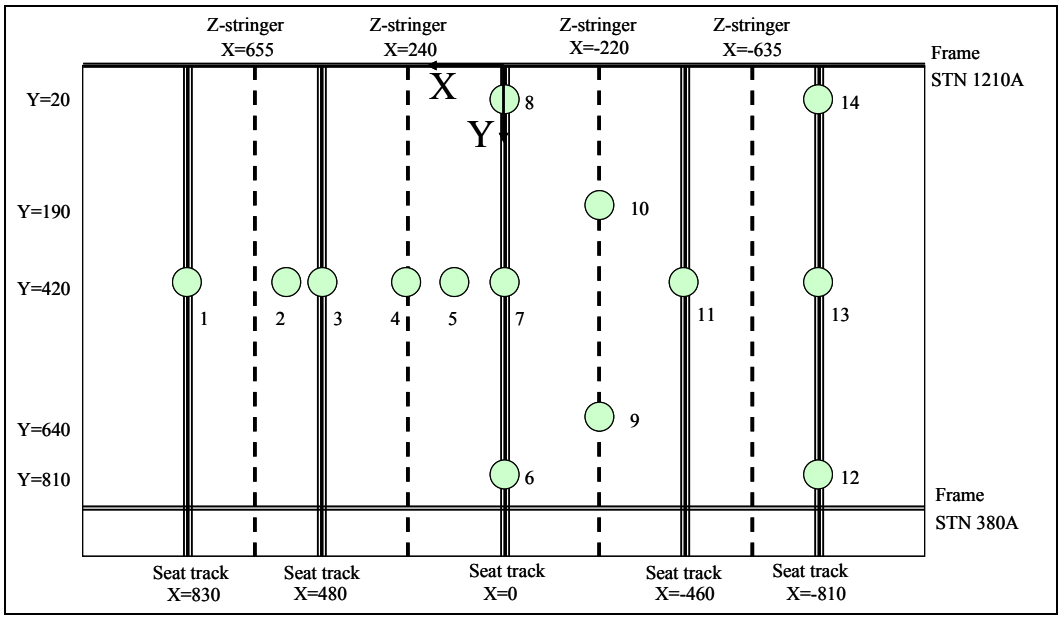

Figure 5-4 : Location of the pressure transducers on the sub-floor skin (top view)

5.1.1.2 Models used for the simulations

Finite-Element models

Two different water meshes were used to conduct the FE-analyses, one based on a pure FE mesh and one using a combined FE-SPH mesh as investigated in § 4.4:

- the pure FE mesh of the 3150 mm x 1850 mm x 550 mm water basin (Figure 5-5) consists of about 75,240 solid elements and 149,840 nodes and was generated by taking into account the size of the structure mesh. In order to save computing time, a gradually varying mesh has been used with an element size of 30mm x 30mm x 20mm in the impact zone and coarser elements outside. As most of the structural deformation occurs in the 40 ms of the simulation and taking into account the velocity decrease during the plunging of the sub-floor component into water, water elements in the impact region do not dramatically deform. Consequently, their shapes and sizes were judged adequate for the simulation.

- for computation time reasons, the impact on water of only half of the sub-floor structure was investigated using the combined FE-SPH mesh of the water basin (Figure 5-5 and D-1 in appendix D). This latter consists of 28,000 solid elements and 230,000 SPH elements leading to a total number of 261,750 nodes. The SPH elements have a volume of 20^3 mm^3. This size is mainly chosen as a compromise between computation time and required fineness of the SPH mesh. The overall dimensions of the pool SPH-FE model are 3000 mm x 3000 mm x 2500 mm (height) whereas the central SPH zone is 2000 mm x 2000 mm x 450 mm (height).

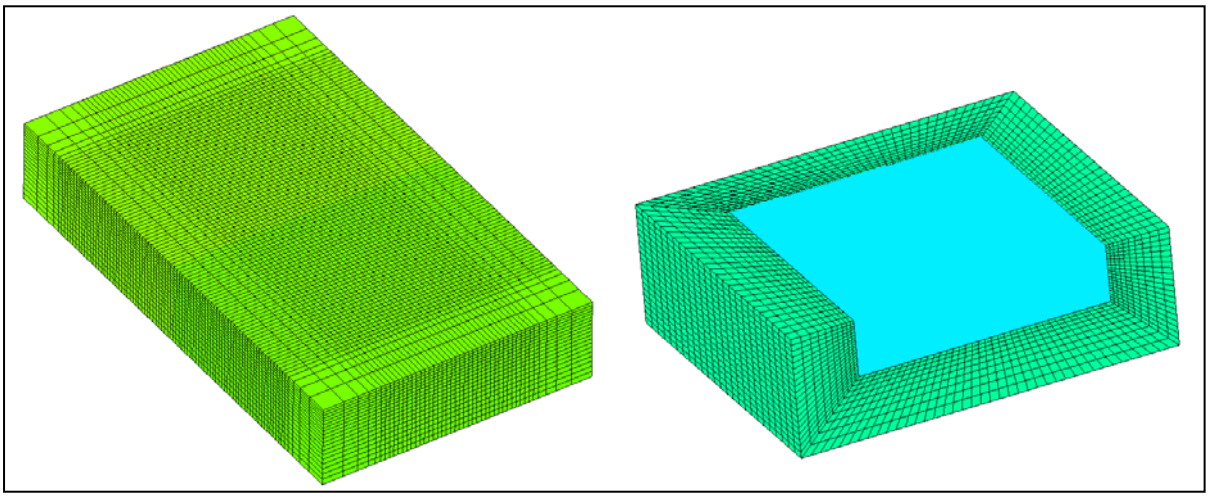

Figure 5-5 : FE model and combined FE-SPH half model of the water basin

The Finite-Element structural model, shown in Figure 5-6, consists of approximately 61,800 shell elements, 68,000 nodes and 2,260 rivets. The average size of the element edge is 7 mm with a finer mesh for the primary energy absorbing components (keel beams, frames) and a coarse mesh for the skin and the floor panel (8 to 14 mm element size). On one side, the structure was cut exactly at the location of the frame (STN 1210A) whereas it was cut 140 mm after the frame at STN 240A on the other side. It follows that the frame at STN 380A is loaded by the skin on both sides whereas the frame at STN 1210A is one-side loaded.

Rivets

As the sub-components of the sub-floor structure are joined by rivets, which fail during the test, it is necessary to explicitly model them to correctly simulate the structural behaviour during the impact event. To that aim, elements based on rigid body formulation [102] and able to fail were used. The nodes joined by such elements, are allowed to separate upon the violation of the following failure criterion:

$$\left(\frac{\text{Normal Force}}{\text{AFAILN}}\right)^{a_1} + \left(\frac{\text{Shear Force}}{\text{AFAILS}}\right)^{a_2} \leq 1$$

where AFAILN and AFAILS are respectively the ultimate tensile and shear strengths of the rivet, a_1 and a_2 are user provided constants, which enable the user to vary the influence of normal and shear failure on the failure criterion. Eighteen different types of rivets and bolts are modelled with their corresponding tensile and shear strength failures in the finite-element model of the structure. It is important to note that these elements are not able to absorb energy, which is a limitation compared to real rivets.

Boundary conditions applied to the sub-floor structure FE-model

The mass of the ballast (607 kg) on the structure is introduced through 18 surfaces corresponding to the 9 pairs of attachment points as shown in Figure 5-6. In the simulation, those surfaces are permitted to move equally in the Z-direction in order to reproduce the constraints of the trolley. Finally, a classical self-contact algorithm acting between the

different internal parts of the sub-floor model is used in order to avoid inter-penetration during collapse.

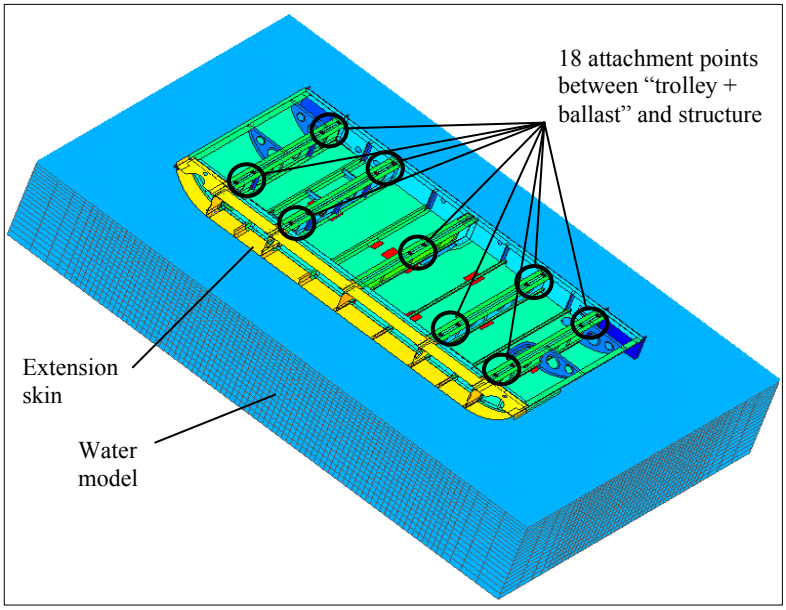

Figure 5-6 : Finite-Element model of the sub-floor structure and the pure FE water basin after removal of the floor panel (elements not shown for clearness reasons)

Computation time

Both simulations were conducted on a 2-processors Linux PC (1001L AMD Opteron: 2 x AMD Opteron 242, 1.6 GHz). The simulation using the pure FE-mesh for the water basin required 15.5 CPU hours to simulate the first 40 milliseconds of the impact, whereas the simulation with the combined FE-SPH mesh necessitated 249.2 CPU hours and this with the half sub-floor structure model. For both FE analyses, the time step remains between $0.247\ 10^{-3}$ ms and $0.286\ 10^{-3}$ ms and is determined by a shell element of the structure. These very simple facts show how time consuming the SPH formulation may be in some cases. However, a too rapid conclusion should be avoided. As long as the time step is determined by the structural mesh, a pure FE mesh for the water is more appropriate from the computation time point of view. Nevertheless, as soon as the time step is determined by the water mesh, the SPH formulation may be of interest compared to a pure FE mesh, where mesh deformations can be so large that the time step can decrease very dramatically.

Another technique based on a multi-model coupling could diminish the computation time when SPH is used. It is especially interesting when the smaller time step is defined by the elements in the structure. In this case, the calculation of the deformations in the water basin necessitates less time steps than for the calculation of the structural deformations. Practically, the structure deformations are computed with the smaller time step and forces/accelerations at the water/structure interface are exchanged at a higher number of cycles (k x time step) with the water in order to compute the resulting water medium deformation and the new resulting loads applying to the structure.

5.1.1.3 Correlation between test and analysis results

Comparisons of the deformations undergone by the structure

Figure 5-7 shows a global view of the deformations of the keel beams after removal of the Fibrelam floor panels from the sub-floor structure after the test, and of the model 30 ms after the impact. The deformations observed on the central keel beam, where two points of attachment of the trolley were placed in its middle (Figure 5-6) are the largest in the test and in the analysis. The external keel beams, on each of which the trolley is also attached through four attachment points, undergo a smaller plastic bending deformation in the test and in the simulation. The larger component bending observed in the simulation compared to the tested article after the test is explained by the fact that both elastic and plastic deformations are represented in the simulation, in contrast to the picture of the tested structure, where the test article is shown in a released state with only plastic deformation.

As seen in Figure 5-8 from the analysis and from a picture of the component after the test, the skin deforms very similarly between the keel beams under the pressure load of water. The highest vertical displacements of the skin are reached on each side of the central keel beam.

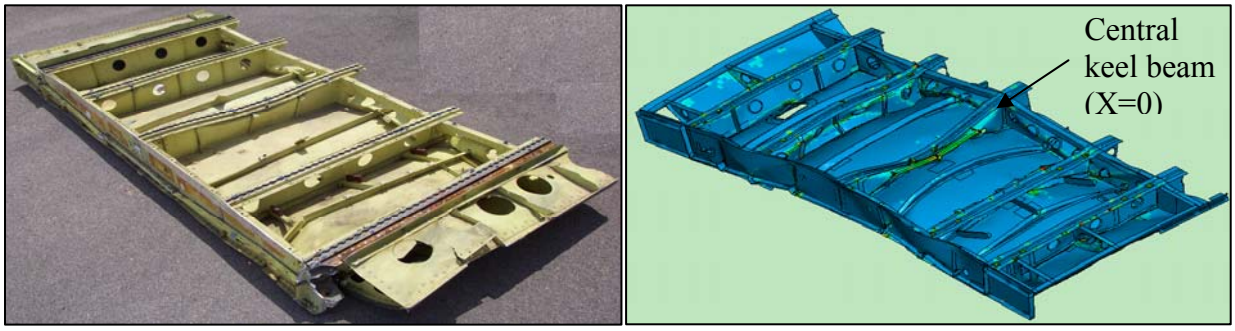

Figure 5-7 : Upper view of the sub-floor deformations after the test and in the analysis at t = 30 ms

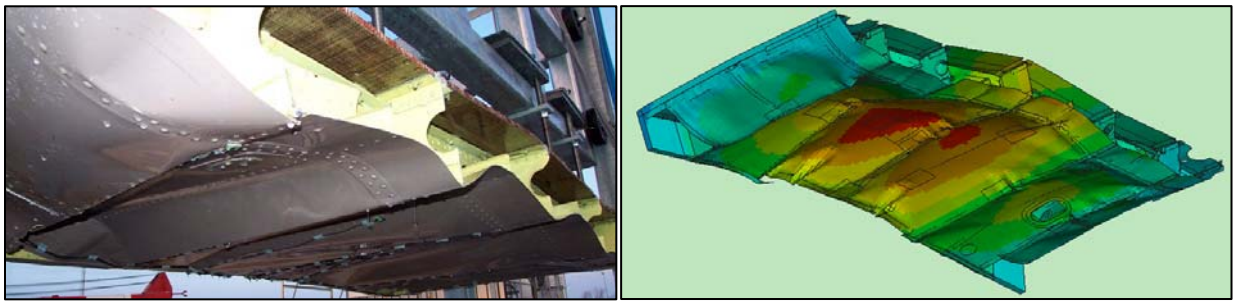

Figure 5-8 : Lower view of the sub-floor deformations after the test and in the analysis at t = 30 ms

In Figure 5-9, the deformation of the frame STN 1210A deformation at time t = 10 ms and t = 30 ms is shown and the last state of the simulation compared to the tested structure. In the simulation, the frame only sustains plastic deformations in the areas, where the Z-stringers go through it, which corresponds to the test. The higher elastic bending of the frame in the simulation is due to the idealised modelling of the frame itself, for which no reinforcements are considered.

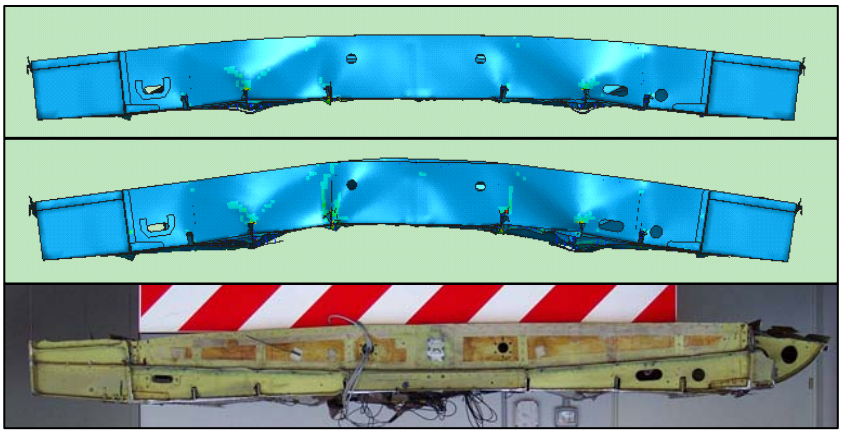

Figure 5-9 : Plastic deformation of frame STN 1210A (t = 10 and 30 ms) and side view of the test article after the test

Compared to the frame STN 1210A, the frame STN 380A shown in Figure 5-10 strongly folds between the keel beams. This is due to its smaller thickness of 1.2 mm (compared to STN 1210A) and above all to the presence of circular holes in the frame. This behaviour is also accentuated by the extension sub-floor part on this side of the structure and notably by the extension skin (Figure 5-6), which uniformly introduces the water load on each side of frame STN 380A. To sum up, qualitative results between test and simulation agree very well.

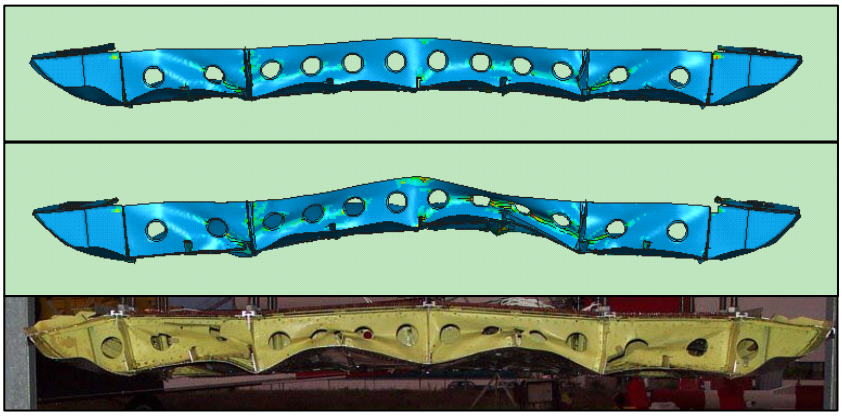

Figure 5-10 : Plastic deformation of frame STN 380A (t = 10 and 30 ms) and side view of the frame after test

Very similar calculated deformations of the sub-floor structures are obtained when the water basin is modelled with a combined FE-SPH mesh. In order to avoid redundances of figures and descriptions, the figures showing a comparison between test and simulation using the combined mesh are shown in Appendix D.

Comparisons of the Pressure Time Histories

After qualitative comparisons, three representative pressure time histories calculated in the PAM-CRASH simulations using the pure FE model and the combined FE-SPH model of the water basin are compared to the measurements. These pressure points (P7, P4 and P5) are located at characteristic locations on the structure skin:

- P7 is located under the central longeron, which corresponds to a very stiff structural region,
- P4 is located under a Z-stringer, which corresponds to a semi-stiff area,
- P5 is located under pure skin, which corresponds to a soft area.

The other pressure graphs are made available in appendix D. All curves are filtered with a CFC600 filter and the time t = 0 in the graphs corresponds to variation of pressure levels of the trolley, which is a sign of interaction between the sub-floor structure and the water surface.

Figure 5-11 depicts the calculated and measured pressure curve at location P7 (see Figure 5-4), situated on the skin directly under the central keel beam. Despite differences in the maximum of the initial peak and its instant, the shapes of the pressure time histories are similar between test and simulations. At the moment of impact, a very high pressure peak occurs followed by a globally decreasing pressure. This behaviour is characteristic of the calculated pressures in a stiff structural region. In addition, the instant of the pressure peak is advanced, the maximum is higher and the pressure increase is steeper in the simulations compared to the test. These differences are explained by the effects of air cushioning and water compressibility, which are especially important in this impact case (controlled impact at 0° pitch) and which are not considered in the calculations. Nevertheless, measured and calculated pressures agree satisfactorily if the mean level of pressure after the peak is considered.

In Figure 5-12 and Figure 5-13, which depict the measured and calculated pressure variations at location P4 and P5 (see Figure 5-4), respectively situated under a Z-stringer and pure skin, after a gradual increase the measured pressure reaches a plateau for a moment before decreasing again. This behaviour is characteristic of semi-stiff and soft areas in the structure, which strongly deform under the water load at impact. The plateau-like typical shape of the pressure time histories could be reproduced by the simulation with the pure FE mesh model of the water basin whereas the modelling with a combined SPH-FE mesh for the water shows a pressure peak followed by a gradual decrease of the pressure in the semi-stiff region (P4) and followed by a plateau in the soft region (P5). The softer the position at which the pressure transducer is placed, the better is the correlation between test and simulations. This is especially the case for the simulation case conducted with the pure FE mesh.

In the cases of the pressures at locations P7 (Figure 5-11) and P4 (Figure 5-12), the calculated pressures reach a transitory zero value. In these areas of the sub-floor structure, the contact algorithm between the water and the structure has locally pushed away a part of the skin from the water surface because of a local penetration, which has resulted in a temporary loss of contact. This behaviour occurs especially in the stiff and semi-stiff areas of the structure during the calculation and is a pure numerical effect.

At the locations of the pressure transducers, the peak of the pressure in the stiff areas and the mean level of the pressure plateau in the semi-stiff and stiff regions are always higher than the test data. In the test, the air entrapped between the structure and the water causes the deformation of the water surface before any physical contact and additionally compresses, which results in reduced contact forces compared to the simulation results. This was also observed in the simulations of Chapter 4 and is here emphasised by the type of impact investigated (controlled impact of a quite large flat-bottom structure at 0° pitch), for which the effect of air entrapment can be considered important.

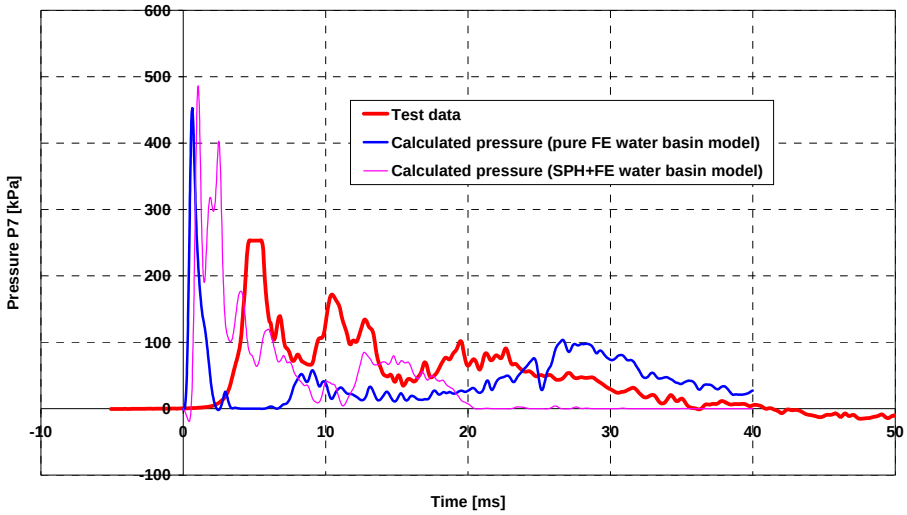

Figure 5-11 : Measured and calculated pressures at location P7 (very stiff location)

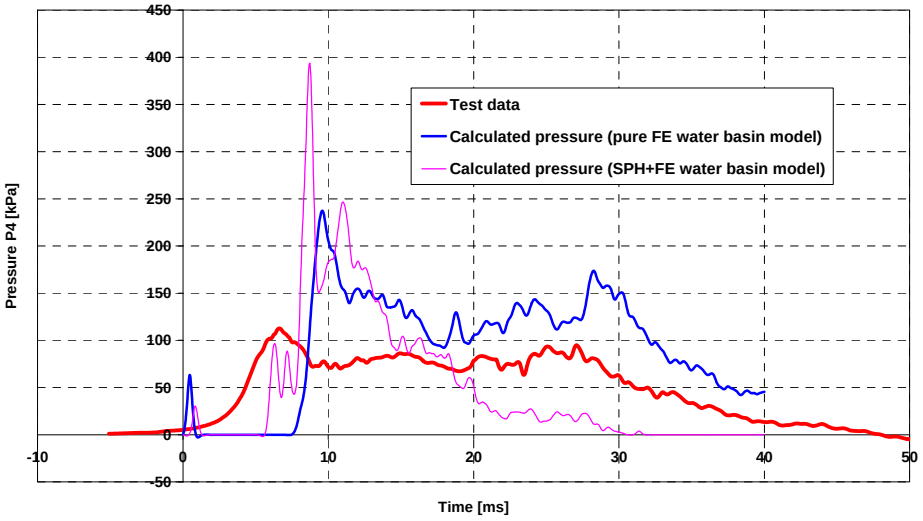

Figure 5-12 : Measured and calculated pressures at location P4 (semi-stiff location)

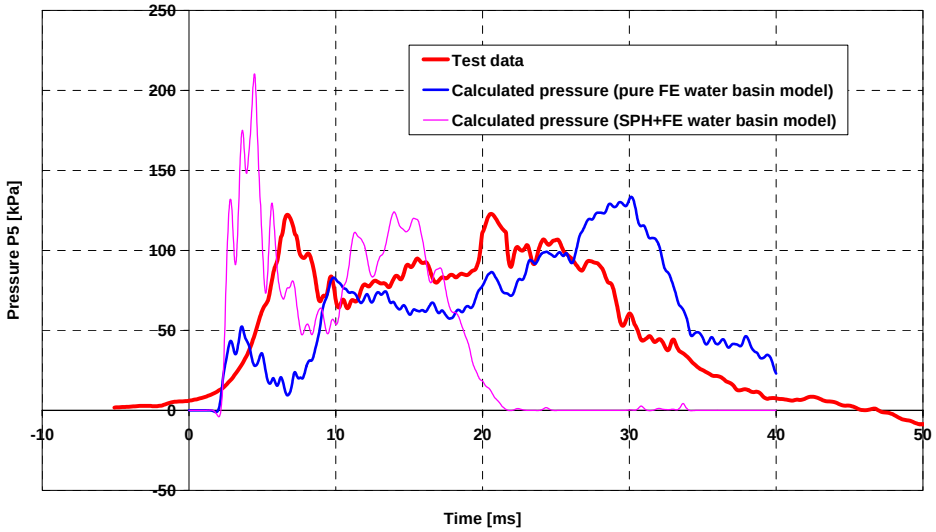

Figure 5-13 : Measured and calculated pressures at location P5 (soft location)

Comparing the curves of Figure 5-11 to those of Figure 5-12 and Figure 5-13, it can be observed that the measured pressure peak at the very beginning of the impact is much higher at location P7 (253 kPa) than at locations P4 (111 kPa) and P5 (122 kPa). The same trend is observed in the simulation results. This is explained by the fact that the structure due to its higher stiffness at location P7 can better counteract the sudden pressure load of water than at location P4 and P5 and therefore causes a higher pressure peak.
Whatever the location of the pressure transducers, the mean value of the calculated pressures are very close to the measured ones and the trend shown by the curves are in agreement with the measurements. It would be a nonsense to deduce more from the quantitative results due to the complexity of the test case. Firstly, it is not clear that repeating the impact test would deliver exactly the same test data. If the structural damage was different (e.g. the evolution of damage slightly changed), the pressure variations would consequently change. Secondly, the structure model despite its complexity (material behaviour including plasticity effects, rivet failure models) is a simplification of the real structure, which may have at some places some weaknesses due to its history (e.g. the structure was cut from a helicopter, which was in operation). These latter are not considered in the model. This, of course, may have an influence on the damage sequence in the structure and consequently on the exact pressure variation acting on the structure during the impact event. Secondly, the quality of the pressure measurements in connexion with the transducer technology has been contested by some authors [70]. Finally, the chosen test conditions (controlled impact of a quite large flat-bottom structure at 0° pitch) are very severe for the structure and therefore load the structure close to its failure limit. The mathematical models used to describe the behaviour of the materials of the structure are consequently exploited to their limits.

To conclude, the simulation results remain conservative compared to the test data and the mean pressure level could be predicted very well in the simulations. This is a very important statement, because this means that the simulation can be confidently used for pre-test investigations. All other pressure time histories are available in Appendix D for information.

5.1.2 Full-scale WG30

5.1.2.1 WG30 Helicopter and Test Set-up

The WG30 helicopter is 14.23 m long, 3.04 m wide and 3.1 m high. Its structure is mainly made of aluminium and titanium alloys. The composite part of the structure consists of the floor panels out of Fibrelam and walls out of aluminium skin/ honeycomb sandwich.

The WG30 helicopter to be tested was provided by Westland. It included 10 passenger seats, the pilot seat, the main rotor transmission, two regular engines and four floatation bags. Its weight without added masses amounts to 3,000 kg. A ballast of 1,370 kg in form of sand bags and lead plates had been added in order to represent the missing items and occupant weight, which are listed in Table 5-1. Both fuel tanks were filled with 150 litres of water. This led to a total mass of 4,370 kg for the test article. The masses were placed so that the helicopter, when suspended from the rotor head, had a zero degree pitch and roll attitude as shown on Figure 5-14. The helicopter was instrumented with 21 accelerometers, 12 pressure transducers and 6 anthropomorphic test dummy sensors in order to quantitatively analyse the impact with simulation work.

Mass designation	Added mass
Fuel in the fore fuel tank	150 kg
Fuel in the aft fuel tank	150 kg
Pilot (dummy) and co-pilot	2 x 75 kg
Nose avionics bay	40 kg
Cockpit instrument	30 kg
Inter-seat console	20 kg
10 passengers	10 x 75 kg
Electrical bay	40 kg
Extra mass	40 kg

Table 5-1 : Distribution of the added masses in the WG30 helicopter for the full-scale test

Figure 5-14 : WG30 helicopter before test

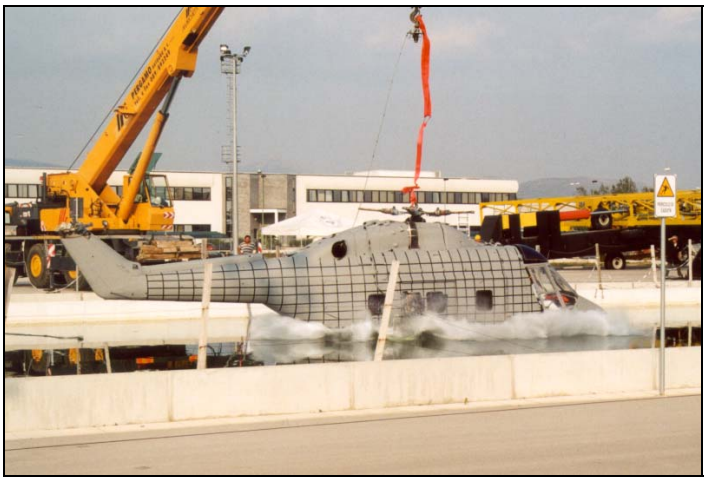

Figure 5-15 : WG30 helicopter during impact on water

The test was executed in the ditching water pool at CIRA, Italy (Italian Aerospace Research Center, Capua) with the helicopter suspended from a crane. It was a free fall test with the helicopter secured by a light flexible rope to prevent it from sinking and to avoid damage to the structure when hitting the bottom of the pool as shown in Figure 5-15. The recorded vertical impact velocity was 7.95 m/s.

5.1.2.2 Finite-element model

The Finite-Element model of the full-scale helicopter shown in Figure 5-16 with the water block consists of 359,055 nodes, 364,130 shell elements, 840 beams, 4,516 bars, 6 springs in the main rotor head area and about 2,260 rivets, which have already been defined for the sub-floor model. The average size of the element edge is the same as for the model of the sub-floor component in the area of primary energy absorbing components (sub-floor and frames).

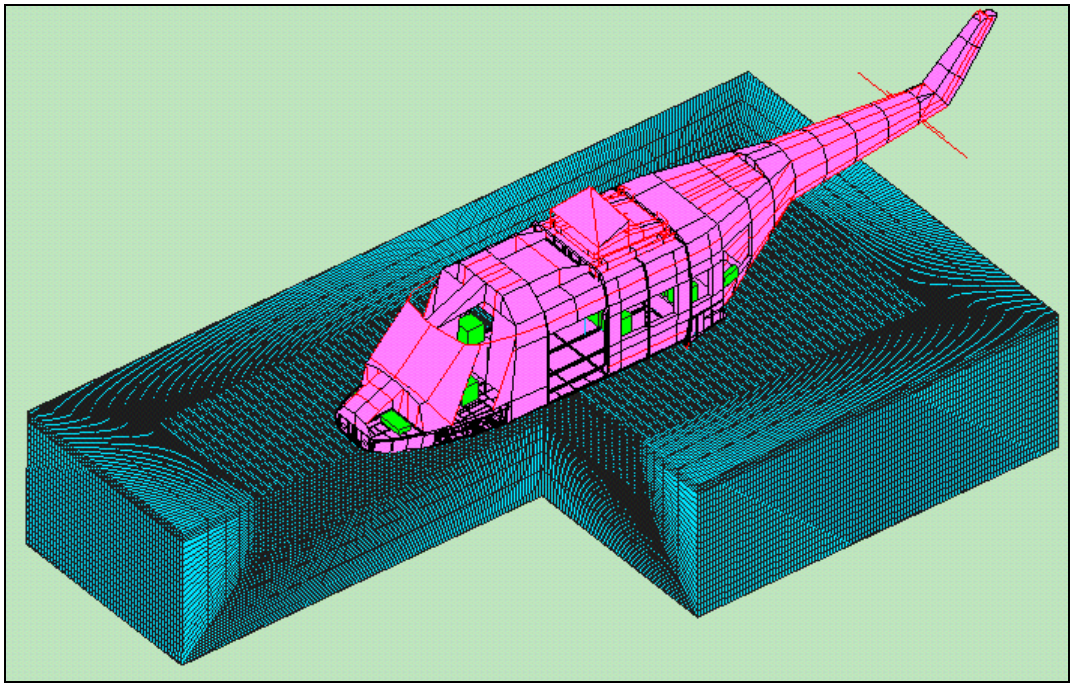

Figure 5-16 : Model of the full-scale helicopter and the water block

The water block, whose dimensions are 8.2 m x 14.9 m x 2.7 m, is modelled with 834,930 nodes and 799,888 solid elements. A gradually varying mesh from the impact zone towards the sides of the water block, as shown in Figure 5-16, is used to limit the number of elements. For reasons of computation time, the water impact analysis is conducted with a pure FE model. The isotropic elastic-plastic hydrodynamic material model is used as defined in § 4.3.1. The ten passengers, the pilot and copilot, the avionics, the instruments as well as the fuel in the tanks have been modelled with Finite-Elements as shown in Figure 5-17 in order to better represent the mass distribution on the structure parts in interaction with those added masses in the simulation.

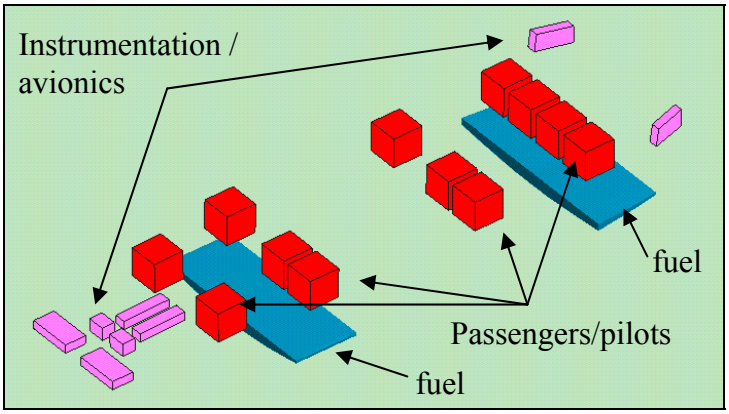

Figure 5-17 : Added masses listed in Table 5-1

The contact between the added masses and the helicopter has been modelled with a tied contact [102]) because the sand bags used in the tested structure have been held by ropes during the test. The material model used for the masses is a simple isotropic elastic material model, whereas the water placed in the fuel tanks has been modelled with the same isotropic elastic-plastic hydrodynamic material model as the one used for the water block.

The nose and main landing gears have been modelled as three added masses at a node linked to the structure with beams, because these components are not relevant to the energy absorption in the case of impact on water.

5.1.2.3 Correlation between Test and Analysis Results

In Figure 5-18, the global behaviour of the helicopter is presented. The five contour plots show the vertical velocity at time t = 0, 20, 40, 60 and 80 ms after the first contact with the water surface.

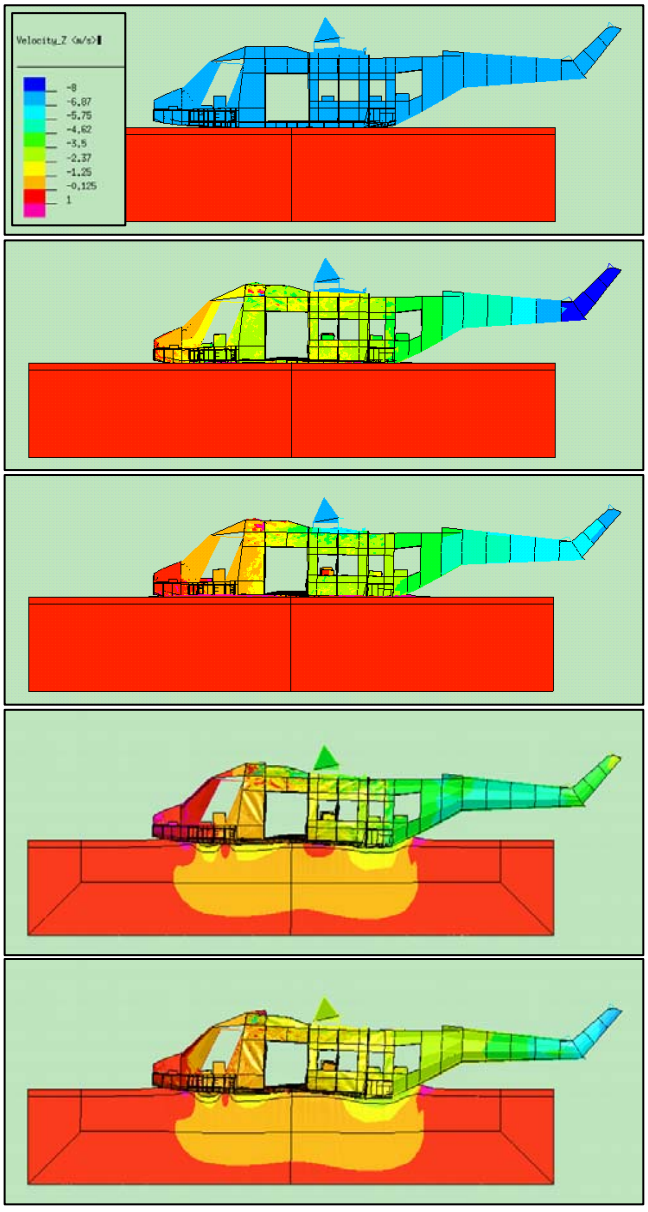

Figure 5-18 : Evolution of the vertical velocity at time t= 0, 20, 40, 60 and 80 ms

It shows that the helicopter cell could be slowed very quickly in the first 40 milliseconds of the impact while the heavy overhead and tail masses with their inertia still continue their motion at a velocity of approximately 3 m/s at time t = 80 ms. A light oscillation at the end of the tail can be observed.

Comparisons of the deformations undergone by the structure

A juxtaposition of a deformation plot sustained by the skin in the model at time t = 80 ms and of two pictures of the tested WG30 helicopter are shown in Figure 5-19. The zones of plastification are mainly at the intersection between the skin and the base of the stiffeners, the bulkheads and the frames. The relatively strong bending undergone by the skin between the frames/bulkhead and the local bending of the sub-floor shown by an arrow-headed line between both frames of the door can be observed in the simulation and in the test. However, the global bending predicted by the simulation between the door areas and the rear part of the model could not be directly recognized in the post-test pictures. As already mentioned for the sub-floor component, the total elastic and plastic deformations are shown in the simulation plots whereas the photos of the real structure show only the plastic deformation.

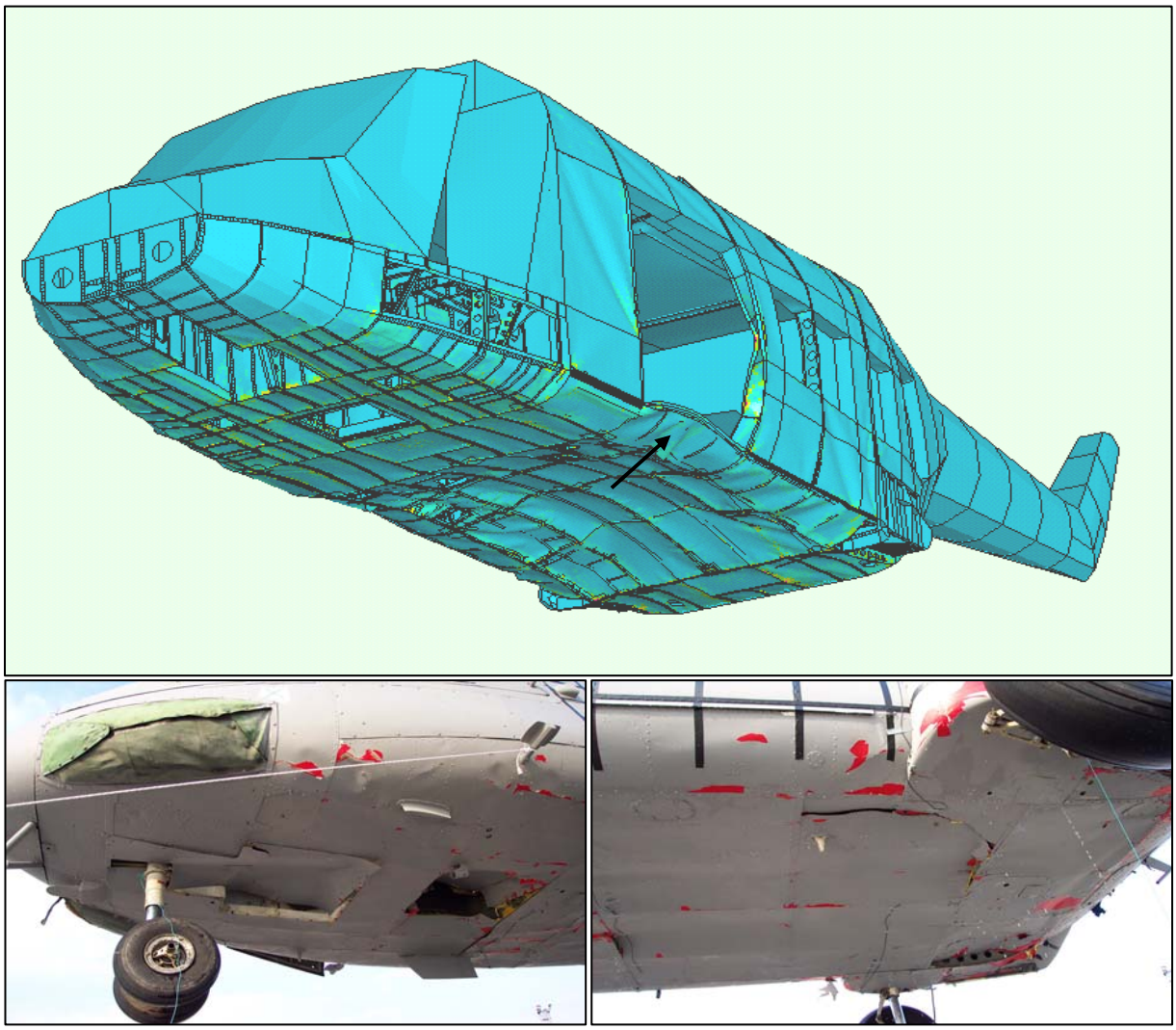

Figure 5-19 : Comparison between the skin deformation of the helicopter model and the tested one

Figure 5-20 shows the deformations of the frames and keel beams in the sub-floor area after removal of the floor panels in the test and in the simulation. It can be seen that the analysis and test results agree excellently. The frames especially on both sides of the central keel beam of the sub-floor undergo high deformations under the action of the water pressure load. Results of the simulation and structure deformations agree perfectly.

Another characteristic deformation observed on the WG30 structure concerns the deformation of frame 450 on the side of both doors as depicted in Figure 5-21. This is mainly the result of the inertia load of the rotor head. The simulation was also capable of predicting this buckling failure.

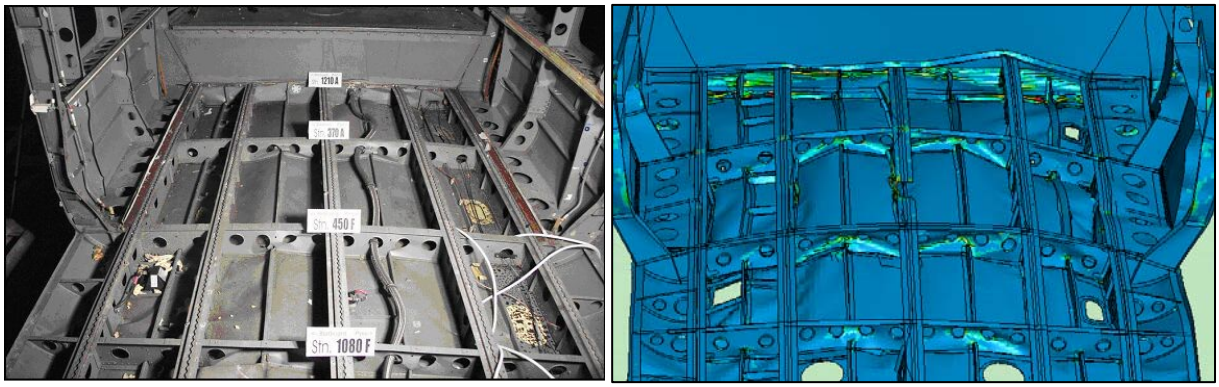

Figure 5-20 : Global internal view, rear side (t = 80 ms)

Figure 5-21 : Deformation of frame 450 on the side of each door in the simulation and after the test

Comparisons of the Pressure and Acceleration Time Histories

After comparison of the deformations, characteristic pressure and acceleration time histories respectively calculated at the locations shown in Figure 5-22 are compared to the test data. The other comparisons are available in Appendix E for information.

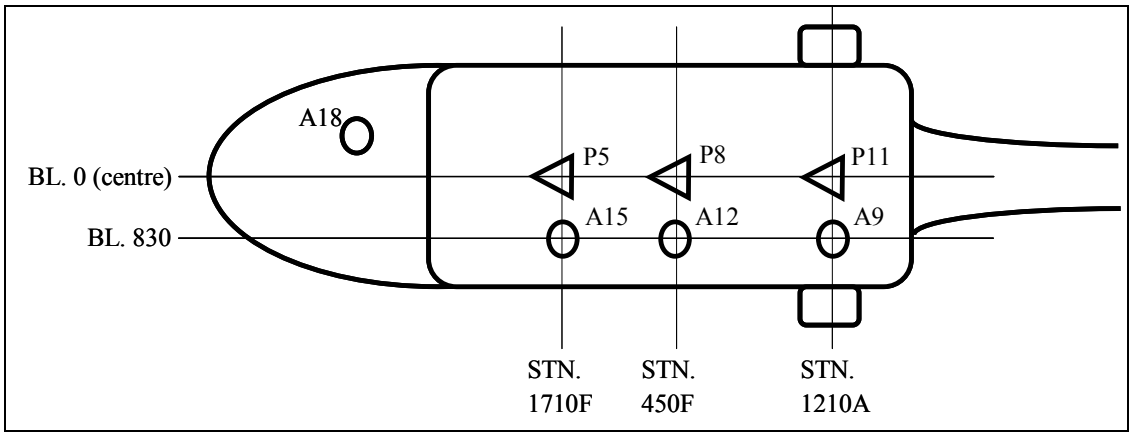

Figure 5-22 : Position of the measurement points of Figure 5-23 to Figure 5-29 (P: Pressure transducer; A: Accelerometer)

Figure 5-23 to Figure 5-26 show the measured and calculated acceleration time histories respectively calculated on the port seat rail BL 830 at stations 1210A, 450F and 1710F and on the pilot floor. On the graphs, the time t = 0 ms corresponds to the moment of impact. Acceleration data are filtered with a CFC60 filter as recommended for full vehicle test in [103, 104].

The maximum acceleration levels could be predicted by the simulations especially in the middle (location A12) and in the front part (location A15) of the port rail. At these locations, the maximum acceleration levels in the test are 92 g and 70 g respectively, whereas the PAM-CRASH model exhibits a maximum acceleration of 89 g and 70 g.
One interesting point concerns the level of acceleration reached in the rear part of the passenger cabin (location A9). At this point of the structure, the maximum acceleration in the test reaches 36 g compared to 40 g in the simulation, which is well below the maximum acceleration measured at location A12 and A15. This reduced acceleration level is explained by the particularly high deformation observed in this area in the sub-floor (Figure 5-20). In addition, the acceleration pulse in the test at location A9 remains at a mean level of about 20 g during 20 milliseconds whereas these levels are higher but shorter at the other locations.

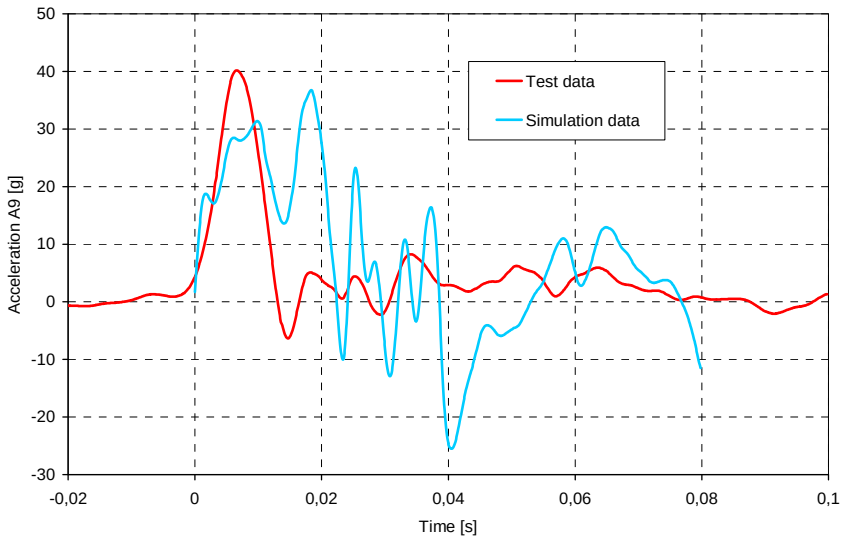

Figure 5-23 : Acceleration time histories on the cabin floor rear port STN 1210A, WL –802, BL 830 (location A9)

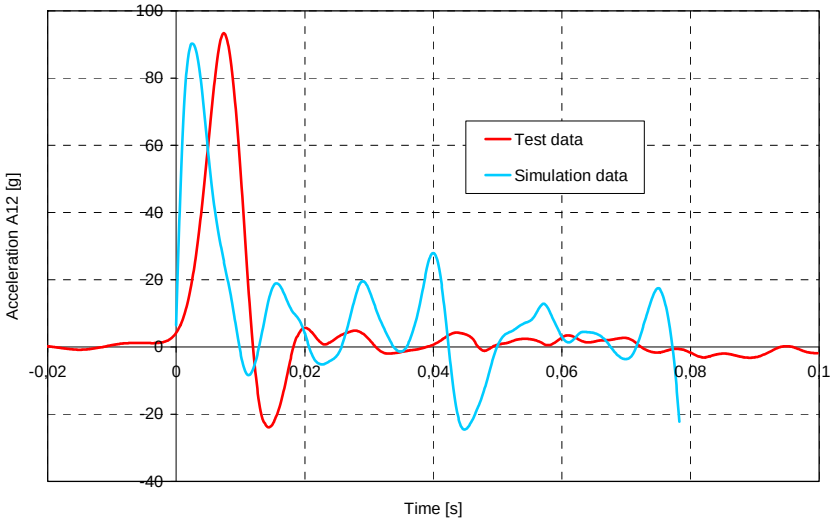

Figure 5-24 : Acceleration time histories on the cabin floor rear port STN 450F, WL –802, BL 830 (location A12)

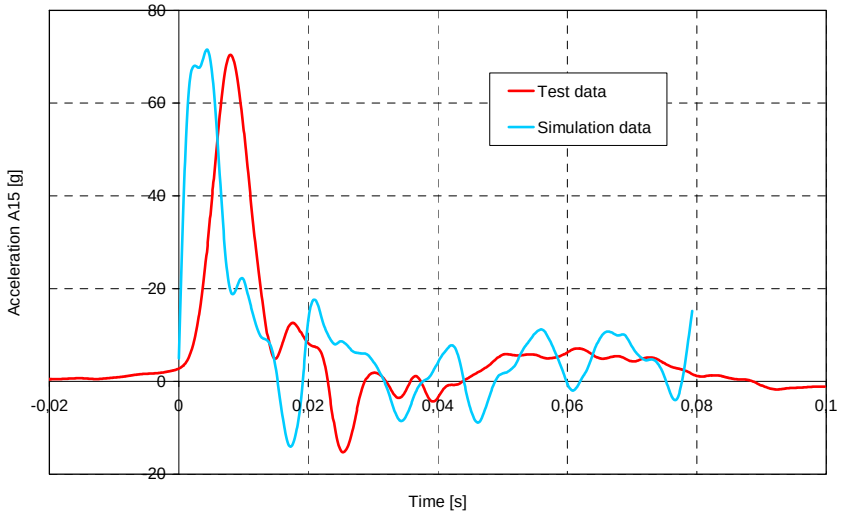

Figure 5-25 : Acceleration time histories on the cabin floor rear port STN 1710F, WL –802, BL 830 (location A15)

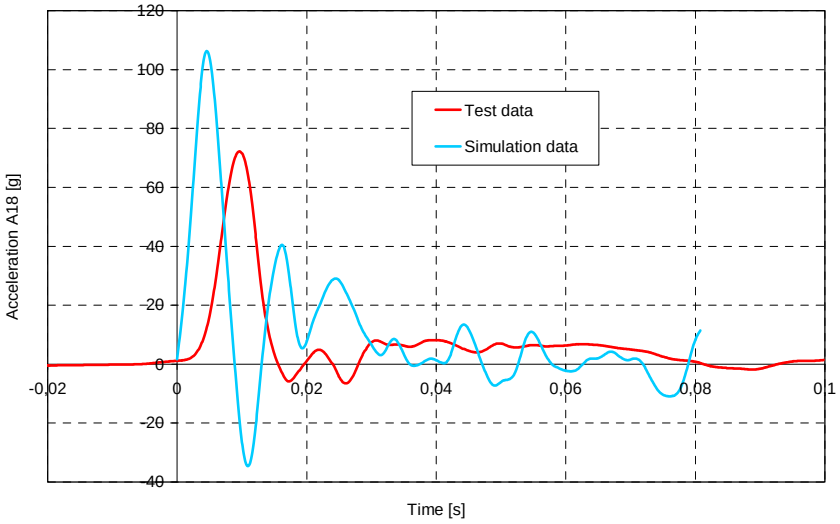

Figure 5-26 : Acceleration time histories on the pilot floor (location A18)

Concerning the acceleration measured and calculated in the pilot floor, a big discrepancy between simulation and test data can be observed concerning the value of the acceleration peak which reaches 71 g in the test and was estimated to 106 g with the explicit FE code. In this area, the modelling is not as precise as in the region of the passenger's sub-floor. The high deceleration undergone by the pilot floor can be partly explained by the fact that the pilot's cabin remains stiff compared to the rest of the structure, as can be seen in Figure 5-18.
The acceleration maxima are predicted at an earlier time in the FE code as compared with the test. The reasons are the same as mentioned for the sub-floor structure concerning the cushioning effect of the air on the sub-floor structure, which also reduces the peak load at the moment of impact.
In addition to the acceleration time histories, three calculated and measured pressure time histories are compared in Figure 5-27 to Figure 5-29 at locations P5, P8 (failed at t = 0.027 s) and P11 positioned at different stations on the centre of the helicopter (Figure 5-18). As all pressure time histories have been measured on the skin directly under a frame (very stiff locations), the problem of over-estimated pressure peak levels at the first contact, predicted by the simulation, can be observed, as already mentioned for the simulations conducted with the sub-floor structure. The same filter (CFC180) as for the test data is used for the calculated data.

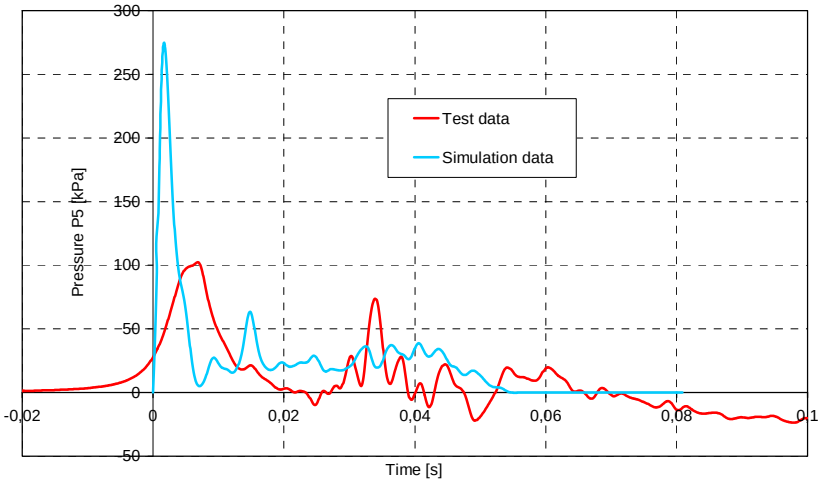

Figure 5-27 : Calculated and measured pressure time histories at location P5 (STN 1710F)

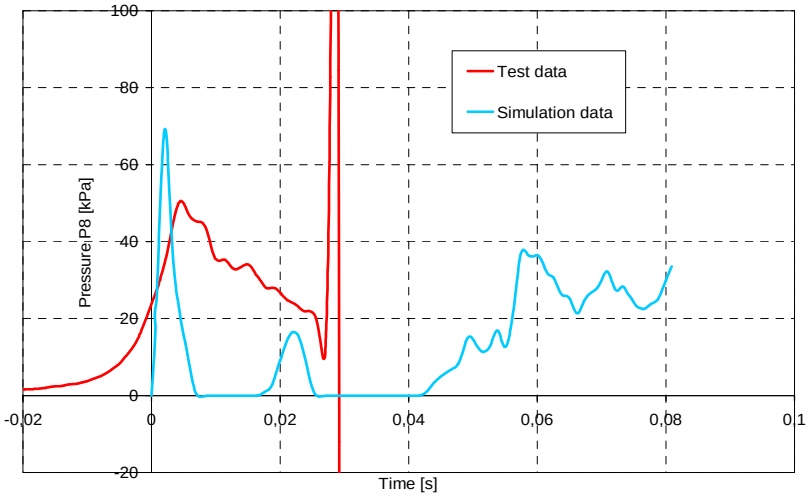

Figure 5-28 : Calculated and measured pressure time histories at location P8 (STN 450F)

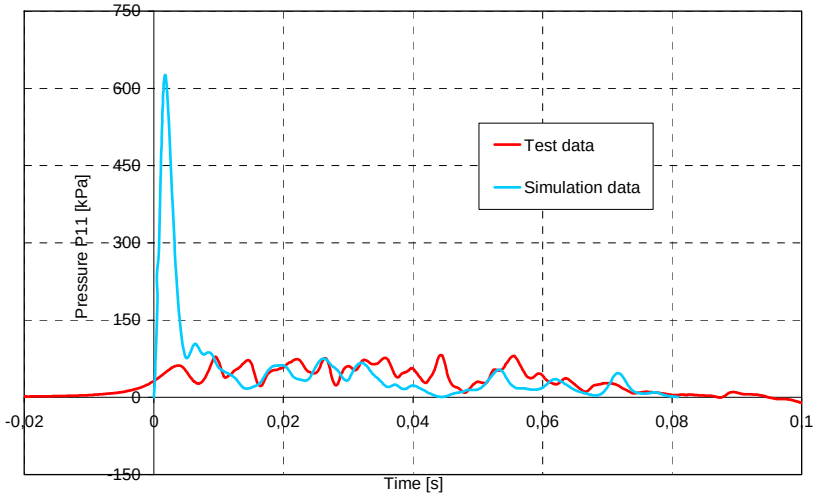

Figure 5-29 : Calculated and measured pressure time histories at location P11 (STN 1210F)

However, the average levels of the pressures calculated in the analysis after the peak match well with the measured data, showing that the simulation is able to reproduce the quantitative data after the first contact. It is important to mention that no calibration work was made for these simulations and that all calculated curves remain conservative compared to the test results.

Computation Time

The complete Finite-Element model required approximately 1,300 CPU hours to simulate the first 80 milliseconds of the impact, taking about a week on an eight-processor HP workstation.

5.2 Simulation of the ditching event of a full-scale aircraft using the local/global methodology

5.2.1 Principle of the methodology

The local/global methodology is based on the use of an explicit Finite-Element code e.g. PAM-CRASH and of a hybrid code e.g. DRI-KRASH (see § 3.3.1), and proposes to use the advantages of both techniques in order to run complex simulations at lower computation costs. On the one hand, the FE analyses are very detailed but have the disadvantages of being time-consuming due to the very high number of degrees of freedom. On the other hand, the hybrid code is able to compute global oriented solutions with less degrees of freedom ($\sim 10^2$) and therefore needs a shorter time for the analysis. Nevertheless, it necessitates the input of elaborated data such as

- force-deflection characteristics for non linear-beams,
- moment-angular deflection characteristics for the definition of plastic hinges,
- etc…

which are not always available from test campaign especially in the pre-development phase of an aircraft.

The principle of the local/global methodology is illustrated in Figure 5-30. Local behaviour on sub-components of the structure are analysed with the FE code. The acquired pieces of information are then used to determine the input data necessary to the definition of the hybrid global model (e.g. non linear structural characteristics) with which the global behaviour of the whole structure can be simulated. According to the simulation results obtained from this combination, global weaknesses of the structure can be detected and as a result modification of the design of sub-components carried out. The new designed sub-component(s) can then numerically be re-analysed with the finite-element method and results (new characteristics) re-injected in the hybrid model for a new global run. An optimisation loop can be performed in that way.

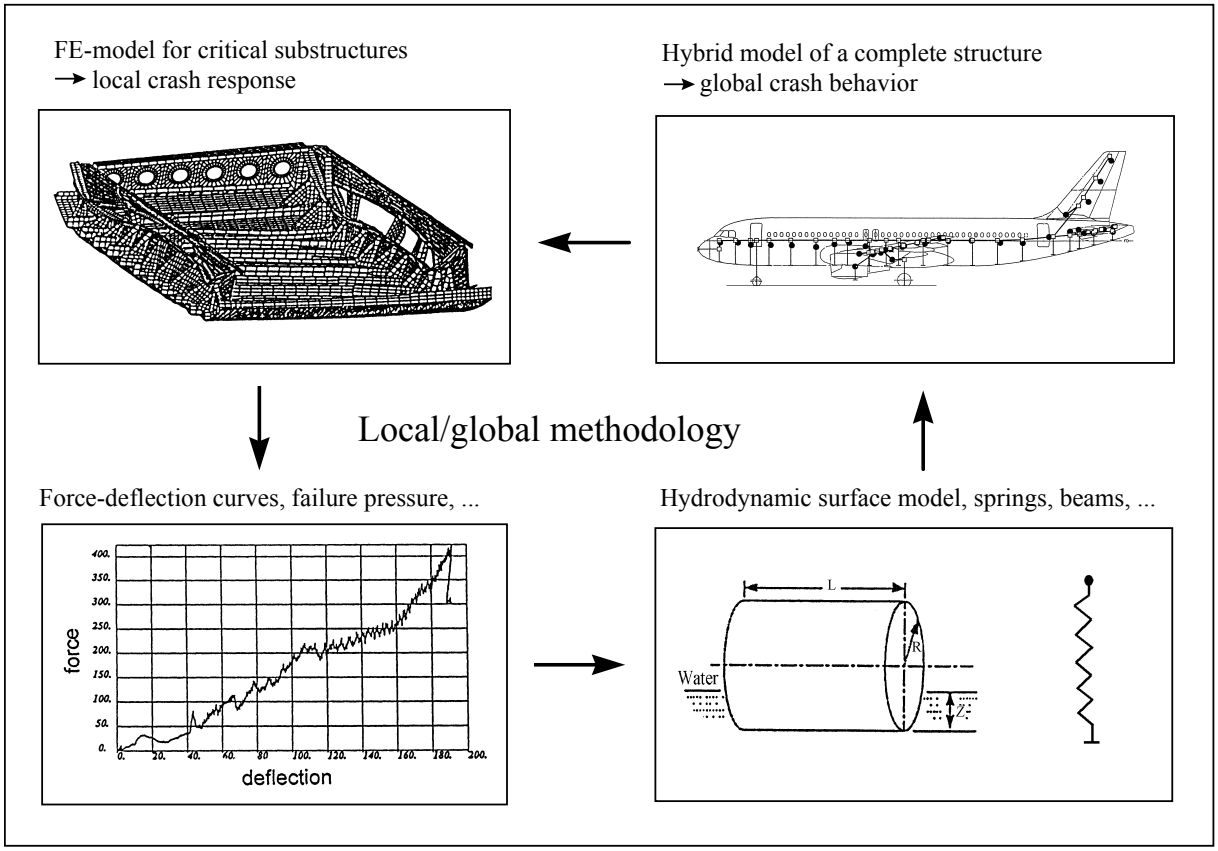

Figure 5-30 : Principle of the local/global methodology

5.2.2 Simulation of ditching events

Based on the experience gained on the full-scale WG30 helicopter (§ 5.1.2), it is clear that the investigation of the impact on water of deformable full-scale structures necessitates very large computation times. If a horizontal velocity component at impact is involved, the computation time very quickly becomes a limiting factor. For this reason, it is proposed to demonstrate the applicability of the local/global methodology by applying it to a full aircraft impacting on water according to the procedure depicted schematically in Figure 5-31.

In a first step, the global structural stiffness of the structure or of a part of the structure is assessed. Crash analyses of an aircraft fuselage have shown that most of the energy absorption occurs through the formation of plastic hinges and deformation in the sub-cargo area. The location of plastic hinges in sub-components e.g. in a cross-section of the fuselage as well as

their moment-angular deflection characteristics can be evaluated through an explicit finite element analysis by considering the angle formed by at least three nodes representative of the deformation and the moment transmitted at the cross section, where plastification takes place. The variation of the angular deflection as a function of time is calculated in an external FORTRAN program, which has been written to this aim.

In a second step, the water/structure interactions have to be included in the hybrid model. To that aim, a calibration based on FE analyses is performed. For the loads resulting from the vertical impact component on water, the lift surface model of a "Hydrodynamic Element" (§ 3.3.1.1) is calibrated from the contact force time history obtained in the Finite-Element analysis in the region to be modelled in DRI-KRASH by a mass and its attached hydrodynamic element. It is also possible to deduce the skin pressure failure from the FE analysis in order to determine the transition from a primary hydrodynamic element to the secondary one (see DRI-KRASH coupled option § 3.3.1.2). For the loads resulting from the horizontal impact component on water, the definition of the drag surface (drag coefficient) still has to be evaluated either from test data or through empirical methods.

In a third step, the behaviour of a full fuselage section can be investigated within a few minutes using the hybrid code based on the information gained from the calibration of the sub-cargo area between FE and hybrid analysis.

For investigations aiming at examining the global behaviour of a full aircraft at ditching, it is possible to pass from the section model to a typical DRI-KRASH stick model, where a section is modelled by a node/mass and its attached hydrodynamic elements, which itself has been calibrated from the hybrid full section model. The nodes of the fuselage are of course linked to each other by non-linear beams, which reproduce the stiffness of the fuselage structure. The same principle applies for the wings.

At this stage, depending on the results gained from the simulations with the DRI-KRASH stick model, change in design may be necessary and an optimisation loop may occur.

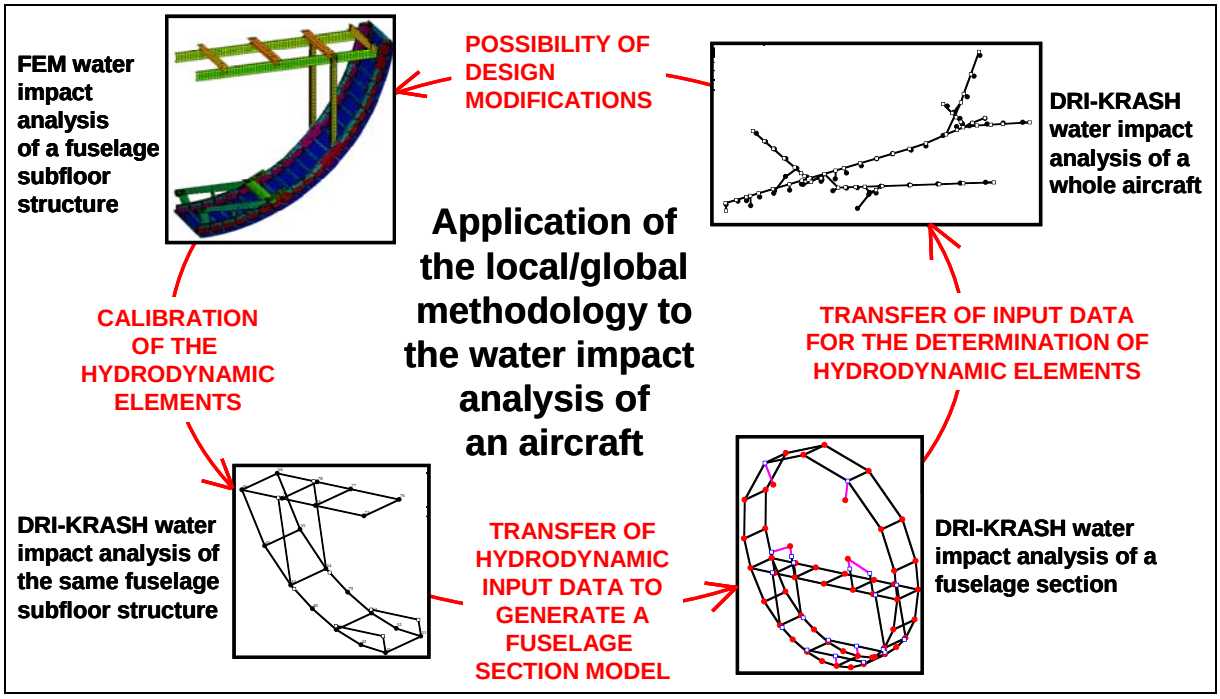

Figure 5-31 : Application of the local/global methodology to a full aircraft

5.2.2.1 Finite-Element water impact analysis of a lower half-fuselage sub-component

The structure [105] below the passenger floor of an aircraft (Figure 5-32) impacting water vertically is analysed with an explicit FE code using the methodology described in Chapter 4. The structure is made out of aluminium and has a weight of 32 kg. For the purpose of the simulation, additional masses have been distributed on the cross beams in order to take into account for the mass of seats, passengers, etc. This sub-component has been chosen for the water impact analysis because its behaviour (deformation, eventually rupture) will dictate the behaviour of the whole aircraft. The impact velocity has been set to 7 m/s in order to cause a substantial damage to the structure necessary for the definition of structural non-linearities required for the DRI-KRASH code input.

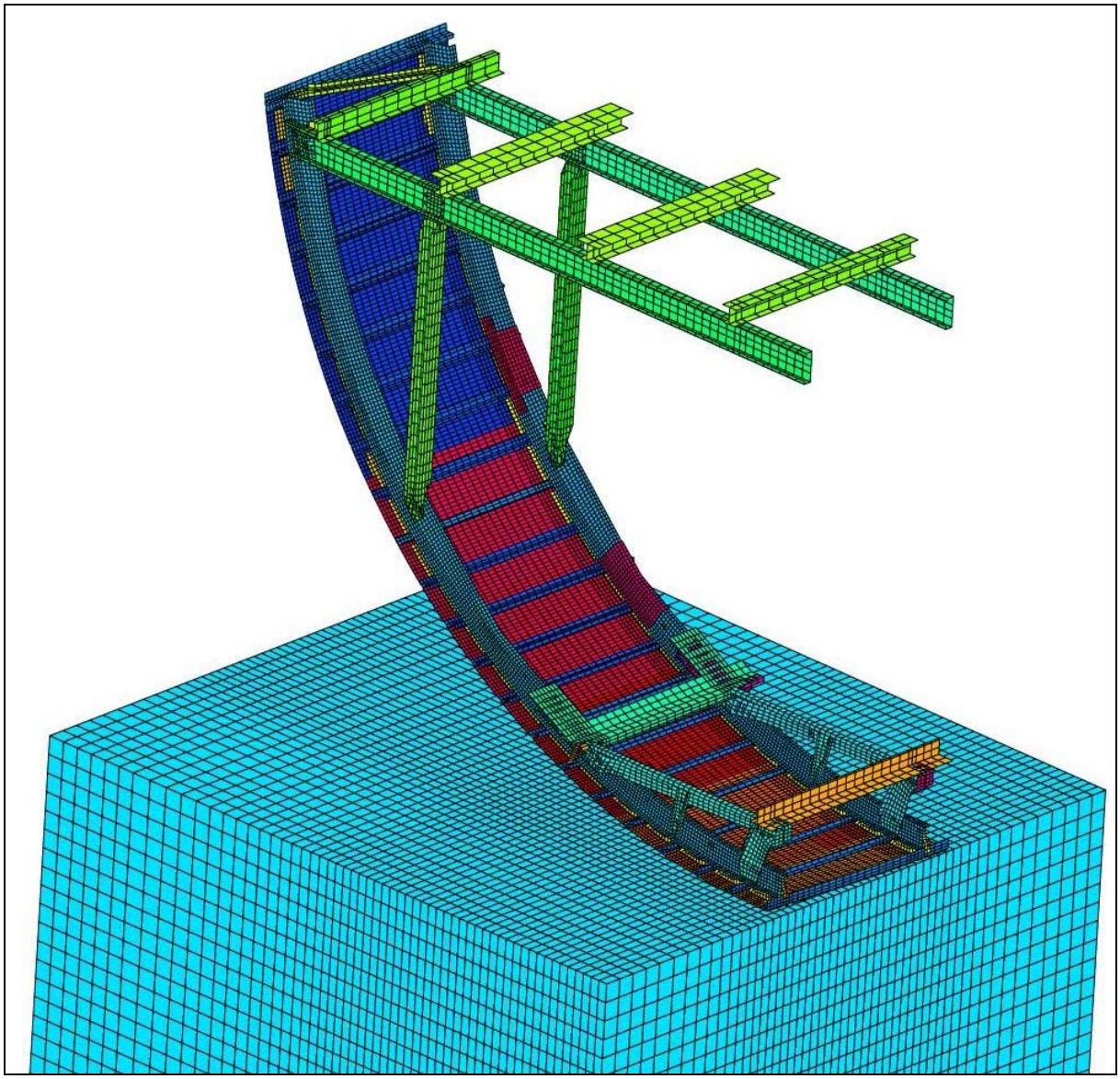

Figure 5-32 : Mesh plot of the half lower fuselage substructure of an aircraft

The half cross-section has been modelled with about 29,000 shell elements and the water block with about 93,500 hexahedral solid elements based on an element size similar to that of the structure. An elastic plastic material law with isotropic hardening has been chosen for the fuselage substructure and the hydrodynamic elastic plastic material model as described in

§ 4.3.1 for the water continuum. Gravity is taken into account in the simulation. A self-impacting contact algorithm avoids the inter-penetration within the structure and the interactions between the half section and the water surface are driven by a node to segment contact.

Figure 5-33 to Figure 5-37 show the deformations of the half cross-section sub-component 25 ms, 50 ms, 75 ms and 100 ms after the impact. In order to better appreciate the deformations of the structure, a side view of the structure is shown in the low right corner of each figure.

Hinges build up at six places: between stringers 16 and 17 above the struts' bases, at the bases of the struts themselves (stringer 13) and at the intersection between the sub-cargo floor and the frame (stringer 7). Furthermore, the unfolding of the skin in contact with water causes a horizontal displacement of the struts' base towards the outside which results in a relative rotation between the frames and the struts and therefore in the bending of the cross-beams. The outcome from the Finite-Element analysis is that most of the energy is absorbed through the formation of the plastic hinges. Moreover, it is foreseeable that the skin would fail in the area located at the intersection between the cargo floor and the frames. Nevertheless, it should be noted that the severity of the impact investigated is well above the condition encountered during a ditching procedure, for which sink velocities do not usually exceed 2 m/s.

Regarding computation time, 67.4 CPU hours are necessary for the simulation of the first 100 milliseconds of the impact on a HP 9000/780 workstation.

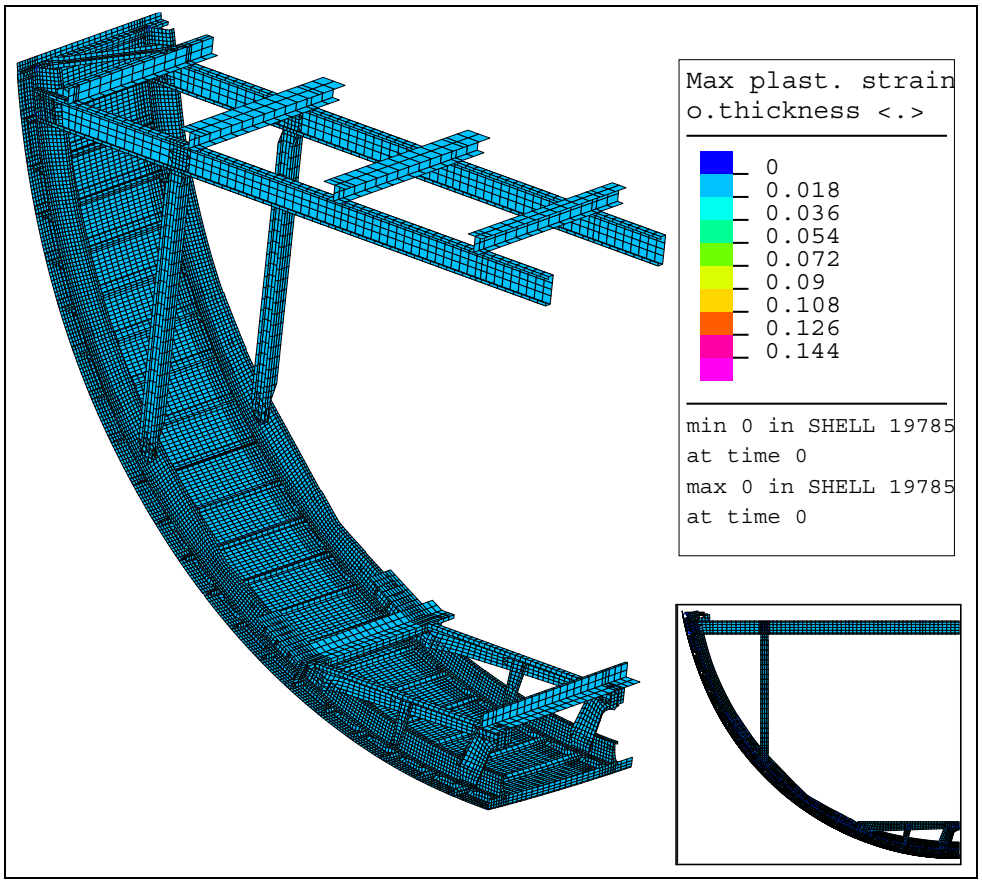

Figure 5-33 : Mesh of the half lower fuselage sub-structure before the impact

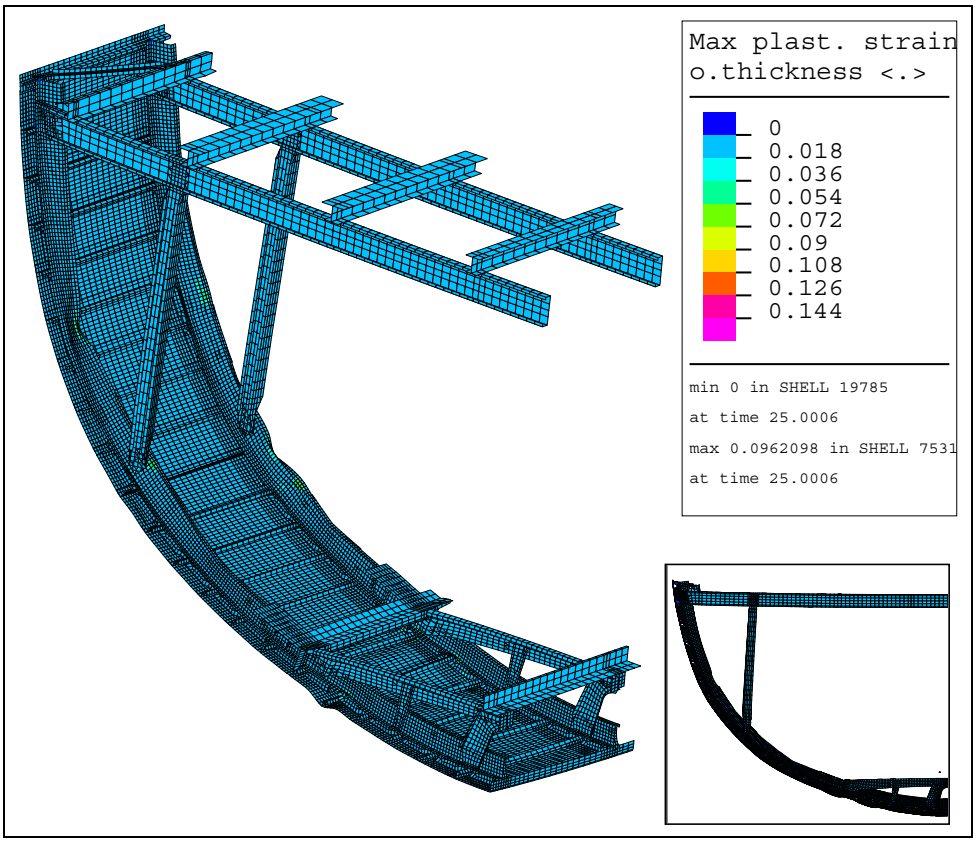

Figure 5-34 : Mesh deformation of the half lower fuselage sub-structure 25 ms after the impact

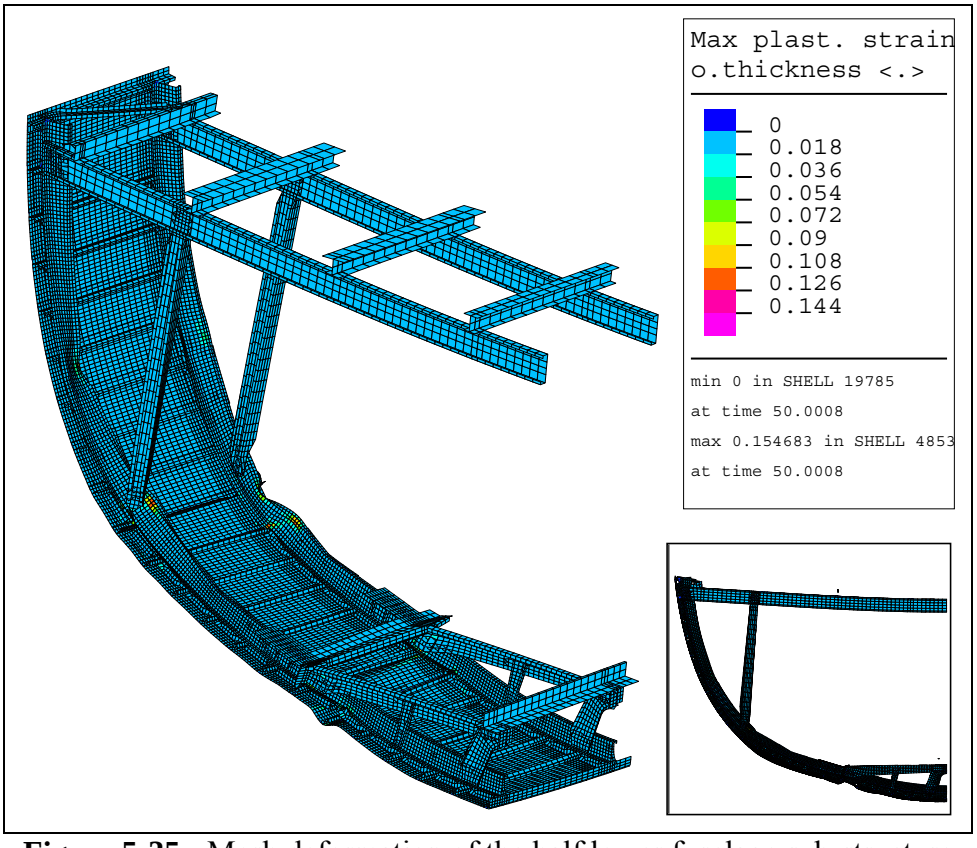

Figure 5-35 : Mesh deformation of the half lower fuselage sub-structure 50 ms after the impact

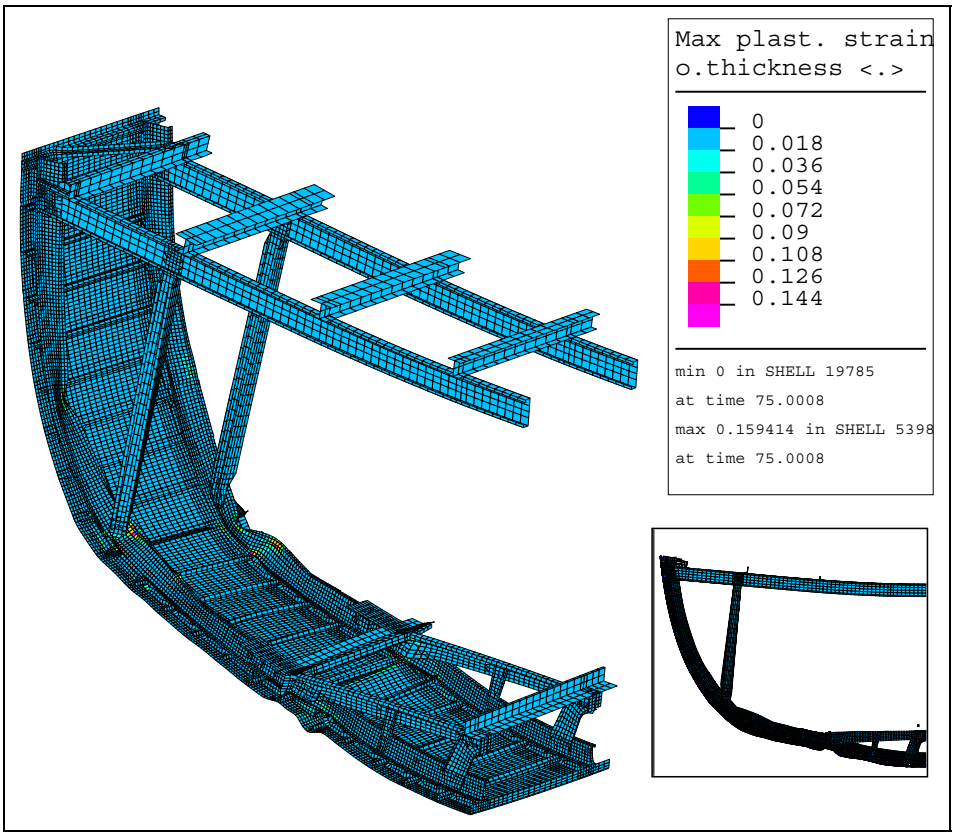

Figure 5-36 : Mesh deformation of the half lower fuselage substructure 75 ms after the impact

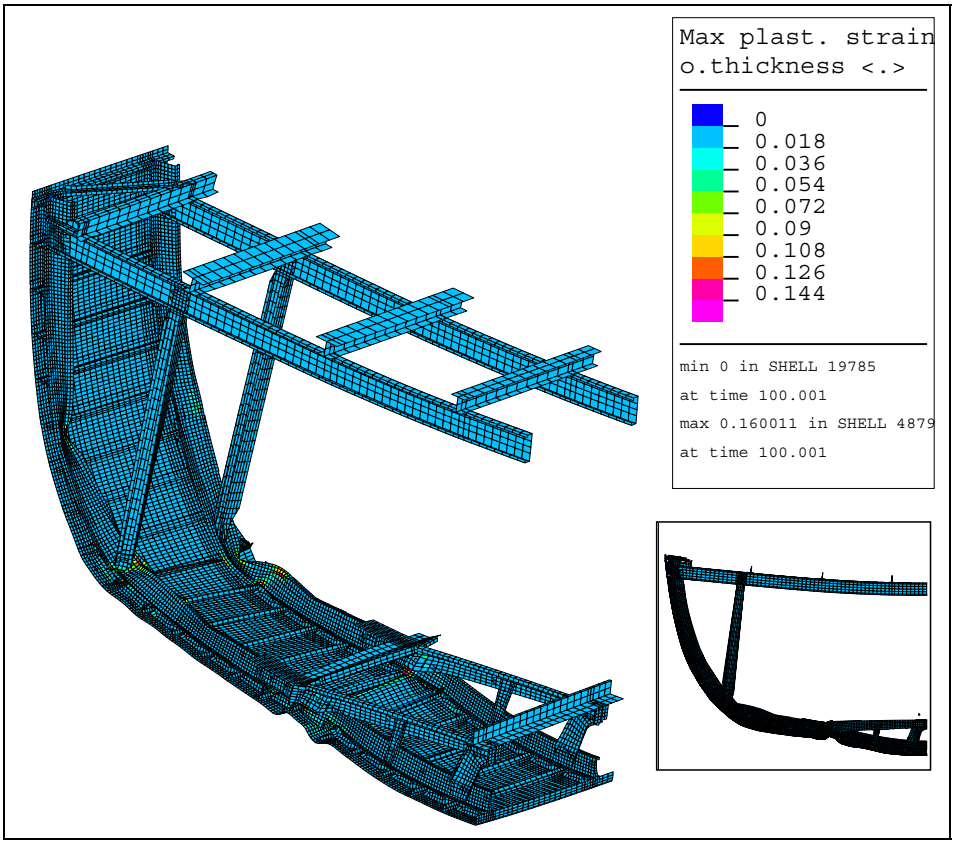

Figure 5-37 : Mesh deformation of the half lower fuselage substructure 100 ms after the impact

5.2.2.2 DRI-KRASH water impact analysis of a sub-component of a fuselage section

The same half lower fuselage sub-structure investigated in the previous section with the explicit FE code PAM-CRASH is now modelled with the hybrid code DRI-KRASH. This half model was originally generated for impact scenarios on hard surface [105, 106] and has been adapted for impact on water by replacing the structural external springs by hydrodynamic elements. It consists of 20 masses, 30 beams, 8 plastic hinges and 10 hydrodynamic elements (Figure 5-38). The impact conditions are the same as those used for the Finite-Element simulation in the previous paragraph.

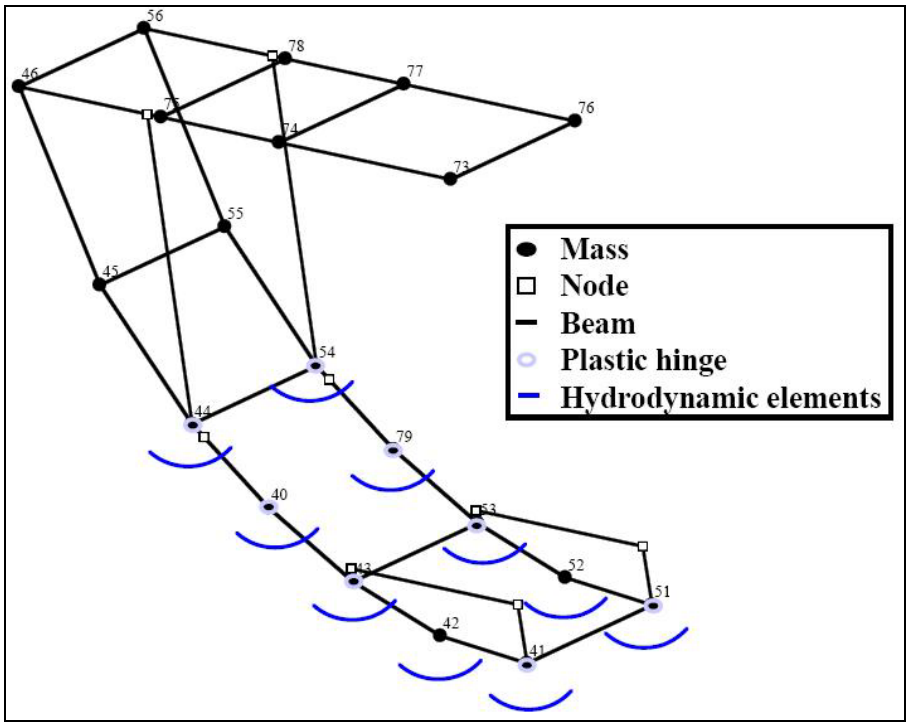

Figure 5-38 : DRI-KRASH model of the half lower fuselage sub-structure

As most of the energy is absorbed by the plastic hinges, deformation of the fuselage can be reproduced despite the use of the uncoupled option of the water module of DRI-KRASH. 2.8 min were necessary to simulate the first 100 milliseconds of the impact using a Pentium 233MHz PC whereas around 67 hours were necessary on a HP workstation for the Finite-Element analysis of the same structure.

Plastic hinge characteristics have been determined by using moment-angular deflection deduced from the FE simulation and hydrodynamic elements have been calibrated according to the contact forces as described previously.

Figure 5-39 shows a DRI-KRASH simulation sequence showing the evolution of the deformations in the lower fuselage sub-structure. The line at Z = 0 corresponds to the water surface. As expected from the FE simulation results, deformations first develop at the base of the struts and at the intersection between the sub-cargo floor and the frames, where plastic hinges are located. This then leads to a rotation of both struts around their bases and the bending of the cross beams located at the level of the passengers' floor.

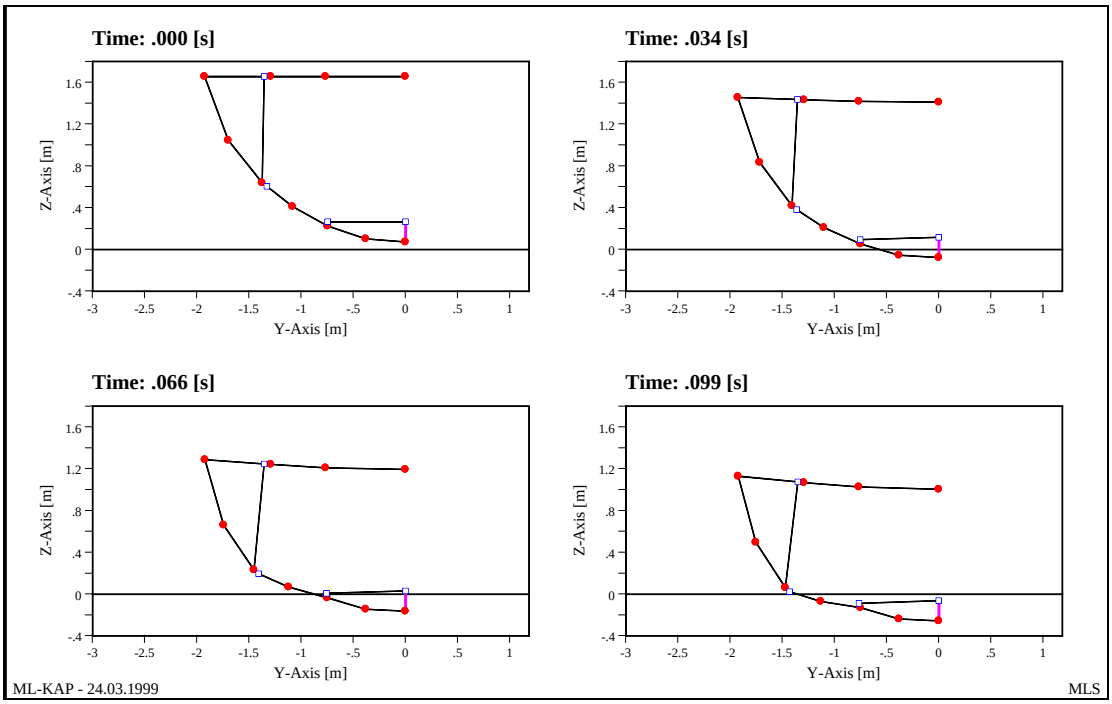

Figure 5-39 : Simulation sequence of the half lower fuselage sub-structure subjected to a vertical water impact (front view)

As an example, Figure 5-40 shows the acceleration time history at mass 46 in DRI-KRASH (Figure 5-38) and at node 1 in the FE code, centre of gravity of the corresponding floor cross beams. TheFE and the DRI-KRASH accelerations reach a peak of 14.4 g and 13.1 g respectively 9.80 ms and 11.2 ms after the impact. Both acceleration curves conform very well at this point, which demonstrates that the calibration of the DRI-KRASH model with the FE output is successful. This is also shown by similar deformations between both models as shown in Figure 5-41.

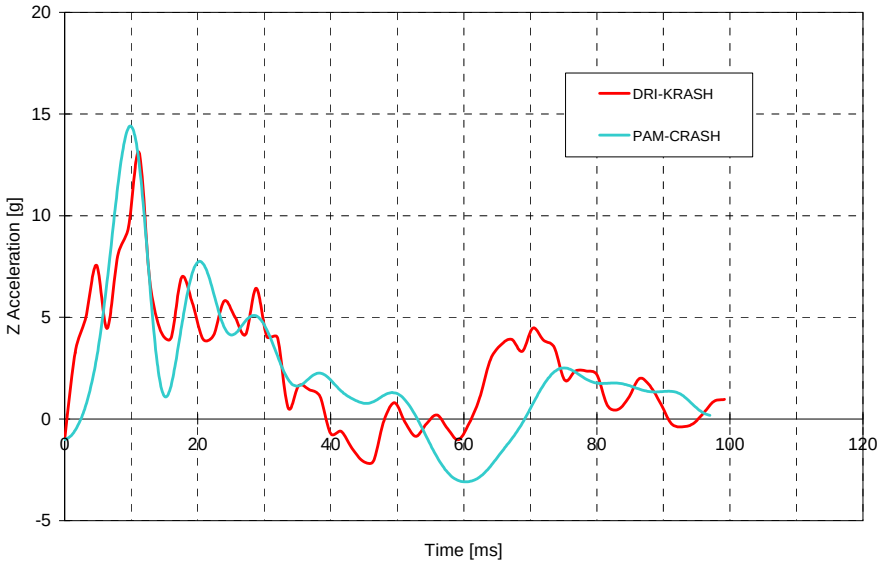

Figure 5-40 : Comparison between the acceleration time histories between the FE and the DRI-KRASH models on the external beam

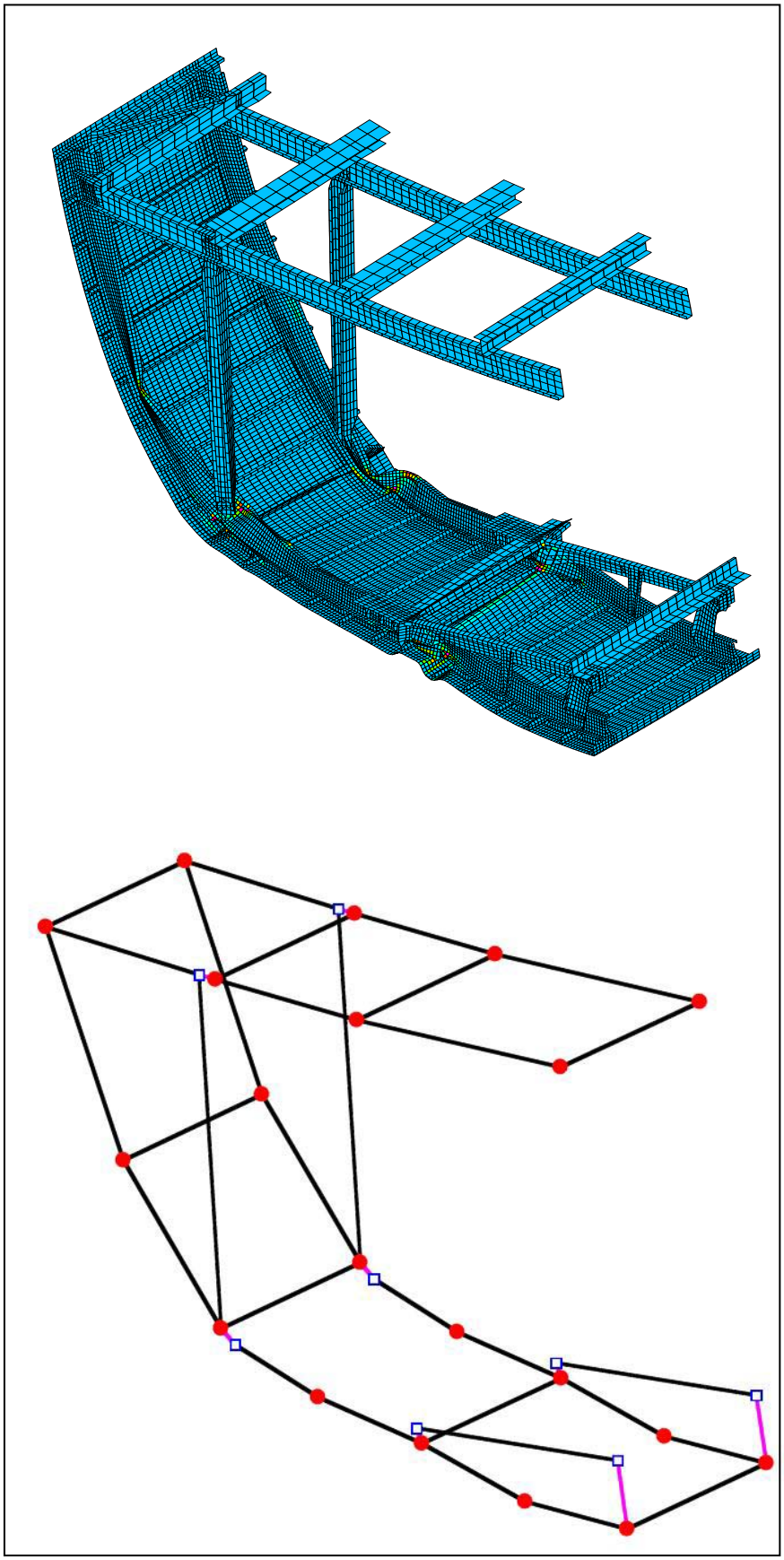

Figure 5-41 : Comparison between the PAM-CRASH (FE) and DRI-KRASH Deformations of the lower fuselage sub-structure 100 ms after the impact

5.2.2.3 DRI-KRASH water impact analysis of a full fuselage section

From the calibration of the half cross-section sub-component illustrated in Figure 5-38, the whole section of the fuselage or even a whole fuselage can be investigated. As an example, a full two-frames cross-section (Figure 5-42) comprising hat racks and seats has been generated from the previous DRI-KRASH model and has been investigated under the same impact conditions as those for the half-cross section component. The hydrodynamic elements have the same characteristics as those of the DRI-KRASH component investigated in § 5.2.2.2.

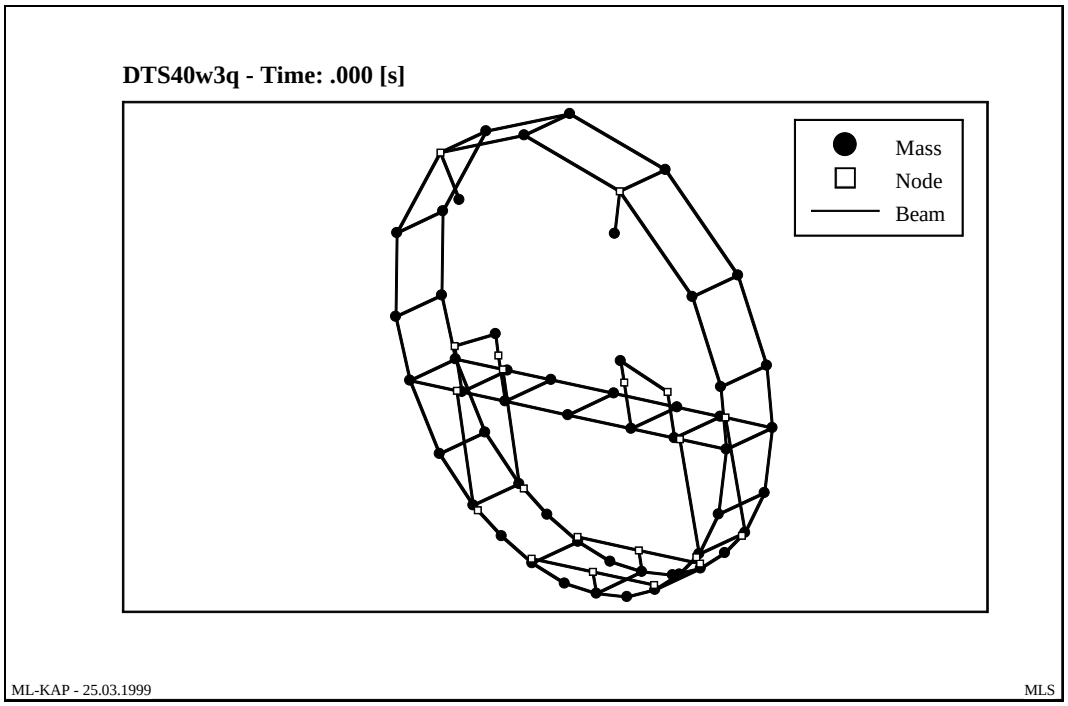

Figure 5-42 : DRI-KRASH model of a fuselage full section [107]

Similarly to the previous simulation runs, one can point out the rotation of the struts around their base and the subsequent bending of the floor as it can be observed in Figure 5-43.

Figure 5-44 shows the acceleration calculated at different masses (location to be seen in Figure 5-38) situated on the floor of the DRI-KRASH model. On the external mass of the floor, the maximum acceleration reaches 10.3 g after 11 ms and remains between –8g and 2 g subsequently. The mass number 75 situated on the floor between the external and the middle masses undergoes accelerations between –7.7 g and 2 g. In addition, the middle mass reaches two maxima: one of –10 g at t = 50 ms and one of –11 g at t = 83 ms. Finally, the accelerations niveau reached at the centre of gravity of the whole section remains between -5 g and 1 g. This 1 g observed at t = 0 ms corresponds to the gravity acting on the fuselage section during the simulation.

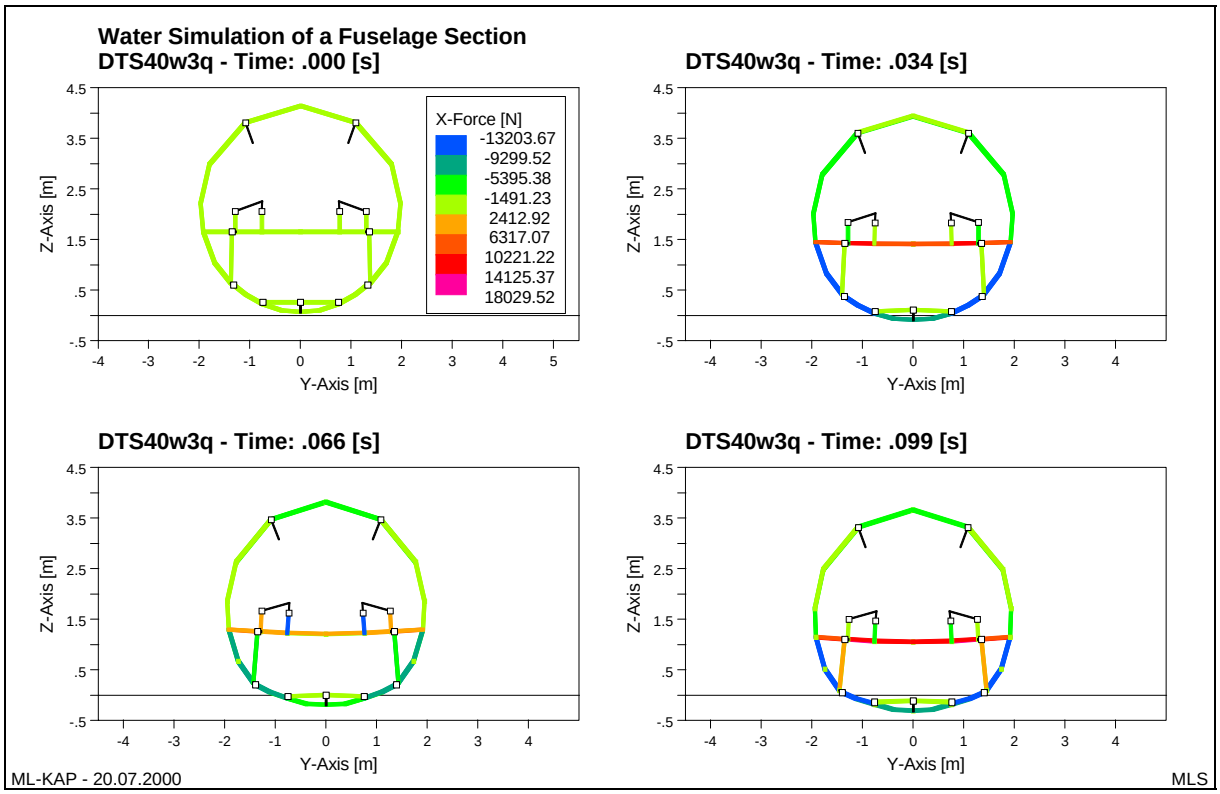

Figure 5-43 : Deformation of the fuselage section at time t = 0 ms, 34 ms, 66 ms and 100 ms (front view); z = 0 is the water surface

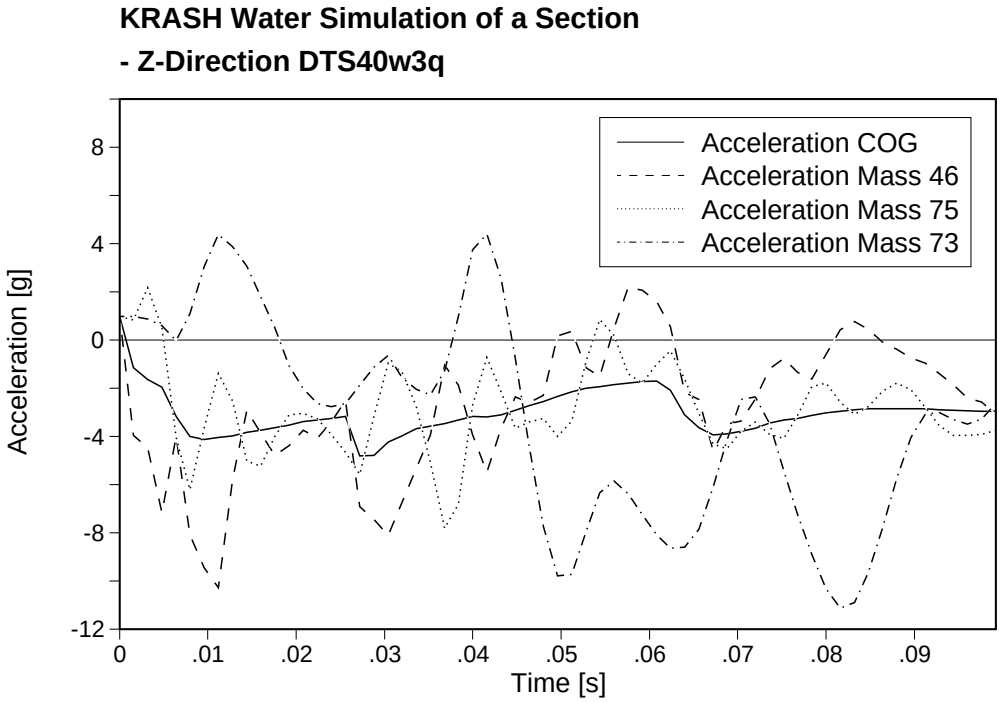

Figure 5-44 : Acceleration at the centre of gravity of the whole fuselage section and at different masses on the floor

5.2.2.4 DRI-KRASH water impact analysis of a full aircraft

In this paragraph, the impact on water of a whole aircraft [51] having a mass of 63,000 kg with a longitudinal velocity component in addition to the vertical one is performed. The half stick-model consists of 42 masses, 41 nodes, 41 beams and 22 hydrodynamic elements, which are defined at each node of the fuselage and at the location of the engines. Figure 5-45 illustrates the model used for the ditching investigation, whereas despite their existence the hydrodynamic elements along the fuselage and at the engines are not shown.

Hydrodynamic element input data are determined according to the geometry:

- position of the frames,
- dimension of the fuselage at the mass considered,
- area perpendicular to the longitudinal flow if the skin breaks,

and according to calibration based on the results obtained for the lower fuselage sub-structure part in § 5.2.2.1 to § 5.2.2.3.

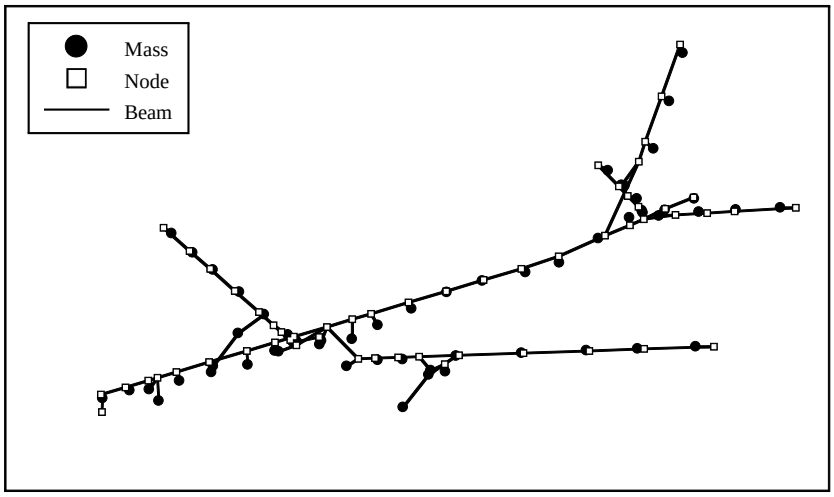

Figure 5-45 : DRI-KRASH full aircraft model [51]

The simulations are performed for an aircraft with retracted landing gear and possible engines separations during ditching. This separation is driven by the horizontal loads applying on them. Calculations which include the landing gear extracted are theoretically possible but necessitate the input of a drag coefficients which can hardly be calculated from a FE simulation.

Conditions and loads that are required to separate the engines from the wings have been taken from [51], in which two conditions of separation have been reported: one due to a horizontal load and one to a vertical one. In the case of an impact on water, it is more likely that the engines separate from the wing because of horizontal load due to the water drag applying on them. The conditions for the separation of the engines from the wings is modelled by defining a maximum pressure on a drag surface located at the engine positions, which after failure is "removed" from the calculation process. Unfortunately, the engine mass itself remains attached to the wing during the simulation, which does not correspond to reality.

Wing lift is considered during the impact. At the beginning the weight of the aircraft is compensated with the wing lift. In the case of 100% lift, the gravitational forces are balanced

with the lift forces, so that the impact is not accelerated. Nevertheless it is possible to consider that the lift is gradually decreased from the beginning of the impact. Suction forces (§ 5.2.3) acting on the fuselage are not taken into account and failure of the fuselage skin is not considered.

Table 5-2 summarises various water impact scenarios investigated. Only scenarios with a longitudinal speed of 70 m/s and with a smooth sea are presented.

Case number	Sink rate speed Vv [m/s]	Pitch angle α [deg]	Lift (%)
1	1	2° nose up	100
2	1	7° nose up	100
3	5	2° nose up	100
4	2	7° nose up	100

Table 5-2 : Investigated impact scenarios

Figure 5-46 shows the simulation sequence of an aircraft with 7 degrees nose up attitude, 2 m/s sink speed and 70 m/s longitudinal speed impacting water (case 4). The line Z = 0 corresponds to the water surface. As it can be observed for this configuration, the aircraft trims down to a near level attitude about 800 ms after the impact and then to a negative attitude. The nose submerges then and a roll over of the aircraft is likely to happen in this case. Due to numerical instabilities, the calculation stops at t = 1.2 s after the impact.

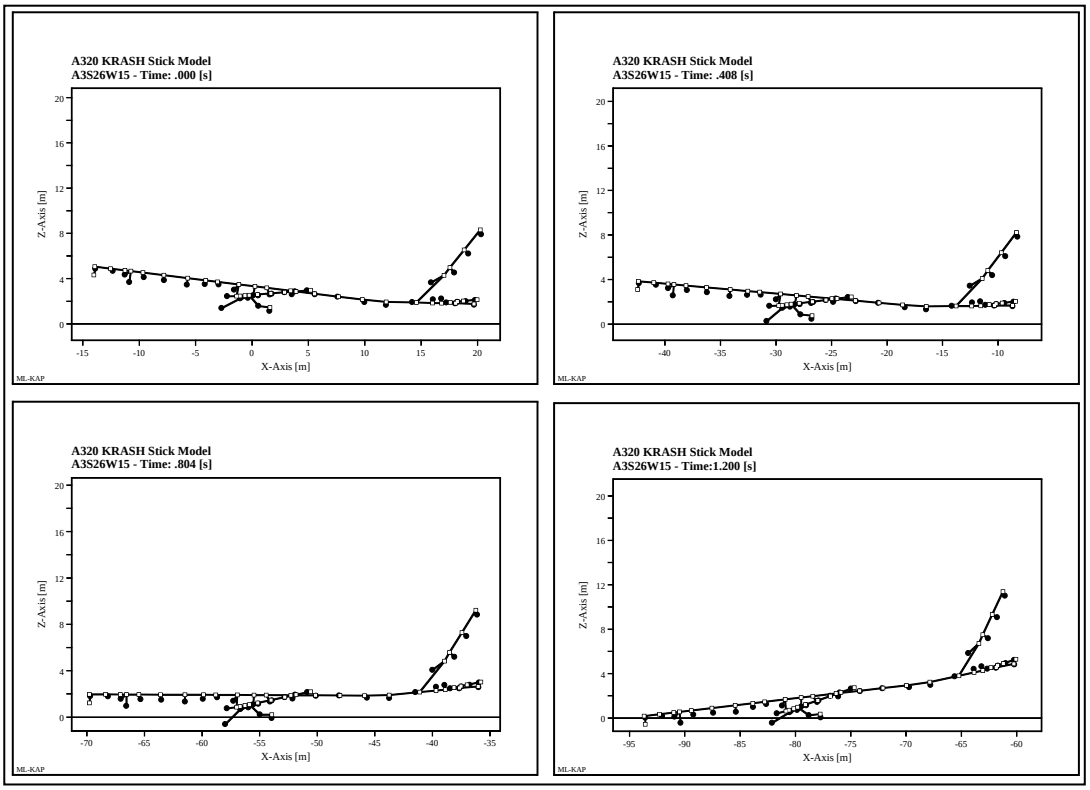

Figure 5-46 : Simulation sequence of the aircraft for the ditching case 4 (t = 0 ms, 400 ms, 800 ms and 1.2 s) [107]

Figure 5-47 and Figure 5-48 depict the longitudinal and vertical accelerations at the centre of gravity of the aircraft for the four scenarios summarised in Table 5-2..

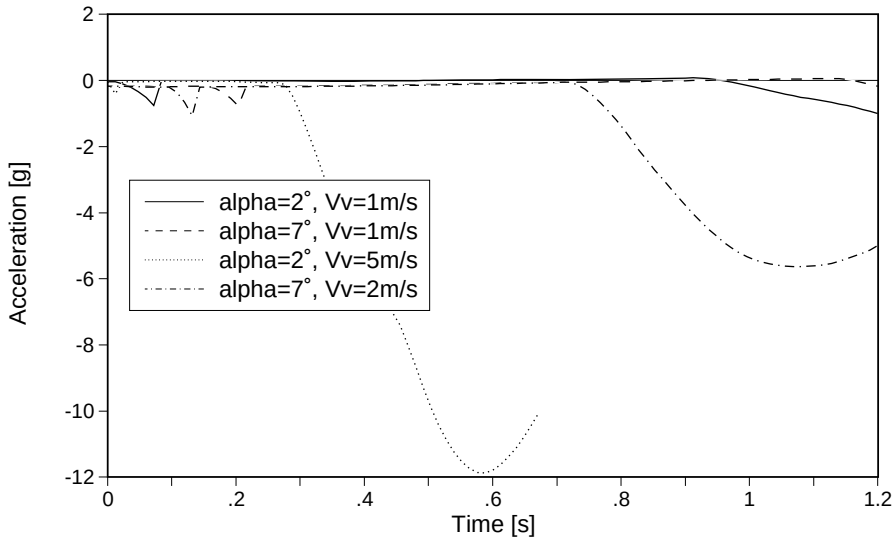

Figure 5-47 : Longitudinal acceleration time history plot at the centre of gravity of the aircraft [107] (cases 1 to 4)

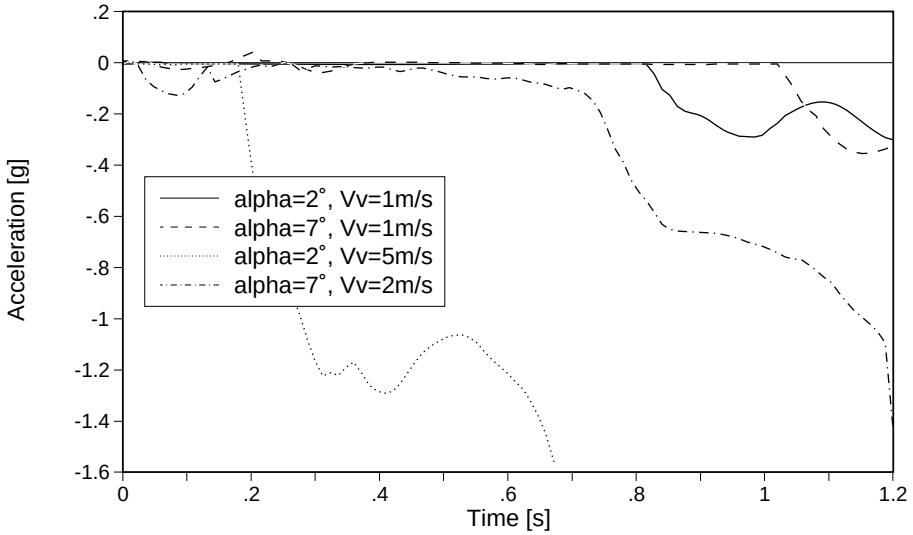

Figure 5-48 : Vertical acceleration time history plot at the centre of gravity of the aircraft [107] (cases 1 to 4)

In the longitudinal acceleration time history plot (Figure 5-47), the first peak varying between 0.7 g and 0.9 g corresponds to the drag caused by the engines which separate from the wing within 8 ms. The second peak occurs when the nose of the aircraft submerges. This can happen depending on the attitude, the sink rate speed and the aircraft configuration. A maximum longitudinal acceleration peak of 12 g is observed for case 3.

In Figure 5-48, the maximum vertical acceleration peak is not reached in the first 1.2 s for cases 3 and 4, corresponding to sink rate speeds of 5 m/s and 2 m/s respectively. Nevertheless vertical accelerations at COG reach 1.6 g at the end of the calculation which terminated by numerical instabilities. Regarding the scenario cases 1 and 2 (sink rate speed of 1 m/s), the

centre of gravity of the aircraft exhibits a maximum vertical acceleration between 0.28 g and 0.35 g until t = 1.2 s.

One point to be mentioned concerns the problems encountered with the hybrid DRI-KRASH calculations which are very easily terminated due to numerical instabilities. These job abortions occur at the moment when the aircraft starts to roll over. This is the reason why simulation sequences have been shown up to 1.2 s after the first contact with the water surface. Nevertheless, this termination time remains well above what could be simulated with a pure FE or FE/SPH code from the computation time point of view.

5.2.2.5 Evaluation of the methodology

It is unfortunately not possible to verify the previous simulation results as no test data are available for comparison. Thus it is proposed in § 5.2.3 to investigate the features of the impact on water involving a forward velocity based on a model test available in the literature.

Nevertheless, the previous simulations based on the local/global methodology show the potential of the route for the application to the ditching numerical analysis. To that aim, a certain effort is necessary including:

- the FE-analysis of structural sub-components to generate necessary input data for the structural model to be investigated with the hybrid code,
- the calibration of the hydrodynamic elements responsible for the restitution of the water/structure interaction,
- the transfer and the fitting of the data to a full-scale hybrid model (e.g. stick model), whose stiffness, mass distribution and hydrodynamic elements should match the real aircraft/rotorcraft full-scale structure.

It is clear that all steps are time consuming especially concerning the generation of the models. Nevertheless, they enable ditching investigations to be performed avoiding any test campaigns, which also cost time and money. Once the models are built, global behaviour of structures can be assessed very quickly with the hybrid code before these structures are built. Extensive parameter studies are very easy to perform for example with the stick model in order to investigate a ditching failure envelope.

5.2.3 Problematic of the impact of an aircraft on water involving a forward velocity

It is shown that in some ditching cases a rapid increase in the attitude of the aircraft at the moment of first impact is observed. It is also noticed that this behaviour depends on the shape of the airframe at the point of impact and on the impact velocity. This phenomenon is due to suction forces caused by an acceleration of the water flow around the impacted area followed by a drop of the water pressure according to the Bernouilli's theorem. If the pressure decreases under the static pressure, cavitation occurs. Based on different test observations, these forces can be high enough to change the attitude of the aircraft and therefore its kinematics. In the following, the importance of the suction forces are evaluated by investigating a test case reported in [108].

5.2.3.1 Test model and setup

In [108], the ditching behaviour of different streamline bodies of revolution representative of common fuselages is experimentally investigated. The fuselages are differentiated by their centrelines, which can be straight, swept up or down to change the curvature of the belly, or split to have a flattened cross-section. The aim of this test campaign is to investigate the influence of the rear-fuselage shape on the ditching behaviour of an aircraft. The hydrodynamic forces developing on this part are particularly interesting because they largely determine the subsequent loads applying on the fuselage and therefore possible damage.

The test model used is designed with a high-wing in order to minimize the influence of the wing on the hydrodynamic behaviour. The horizontal tail is also mounted high on the vertical tail to keep it clear from the water. Finally the tail plane is allowed to break away if it is loaded above the design limits. The fuselage is constructed so that it remains undamaged in all tests. Figure 5-49 shows a picture of the basic configuration of the model, which will be investigated in the simulation presented here.

Concerning the test-setup, the model is catapulted from a monorail into a tank. The water surface is smooth. The control surfaces are positioned so that the model lands at the desired landing speeds, which are between 30 fps and 60 fps (corresponding to 9.14 m/s and 18.28 m/s). In all the tests the attitude at landing is kept the same at 10°. A high speed motion camera registered the course of the tests. Based on the motion-pictures records, data like speed, attitude and centre of gravity height against time could be deduced.

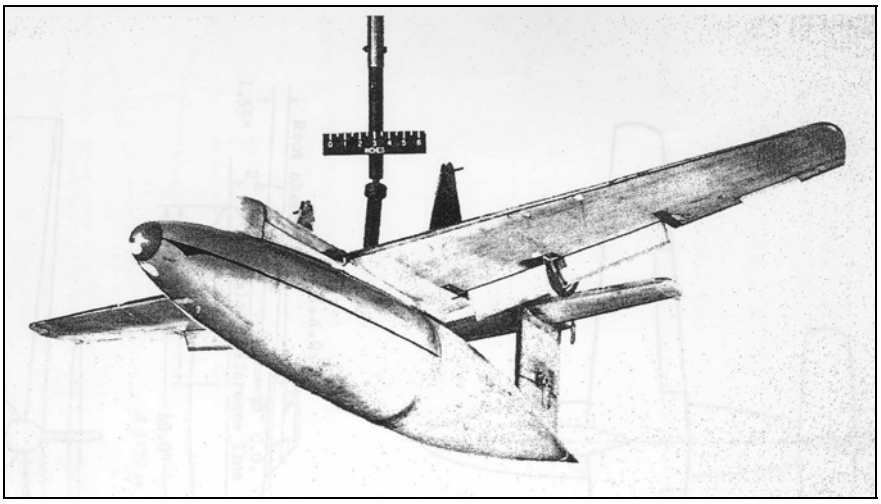

Figure 5-49 : Photograph of the model in its basic configuration [108]

5.2.3.2 Simulation model

Aircraft model

As the test conditions and the model geometry remain symmetric during the various tests, only half of the aircraft model was modelled. In the simulation presented here, a basic configuration consisting of a streamline body of revolution with a maximum radius at 50% of the length is investigated at a speed of 9.14 m/s. The full model is 1.2192 m long, has a maximum radius of 0.1016 m and a wingspan of 1.6764 m, and weights 5.67 kg. The FE model corresponds to the shape of the test model shown in Figure 5-49 and is illustrated in

Figure 5-50. The half model used in the simulation is composed in 1,633 nodes and 1,475 shell elements and is defined as a rigid body.

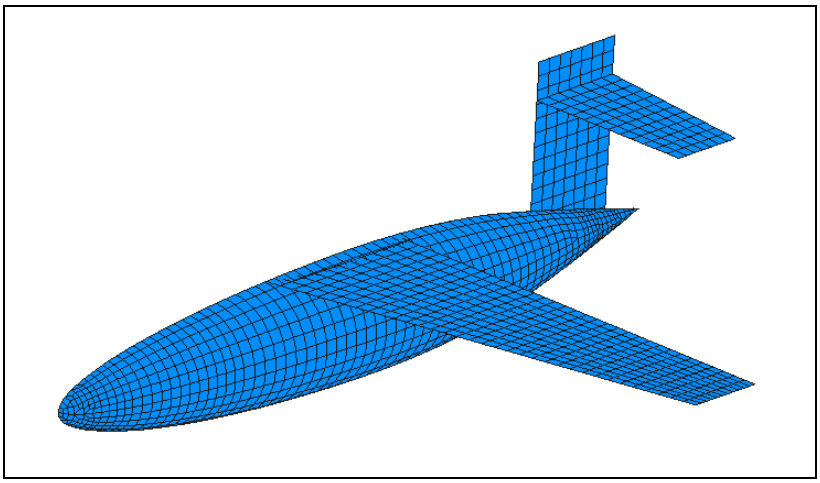

Figure 5-50 : Aircraft half FE model

Water model

The water block is 17.5 m long, 0.6 m wide and 0.6 m deep. The length of the water block is determined by the distance necessary for the aircraft model to come to rest. The central part is modelled with SPH particles and the outpart with solid elements. The material used is the elastic-plastic hydrodynamic elastic plastic material described in § 4.3.1. The mesh consists of 100,800 SPH elements and 12,600 solid elements. Figure 5-51 shows the mesh used and particularly emphasizes the size of the aircraft model compared to the whole water mesh.

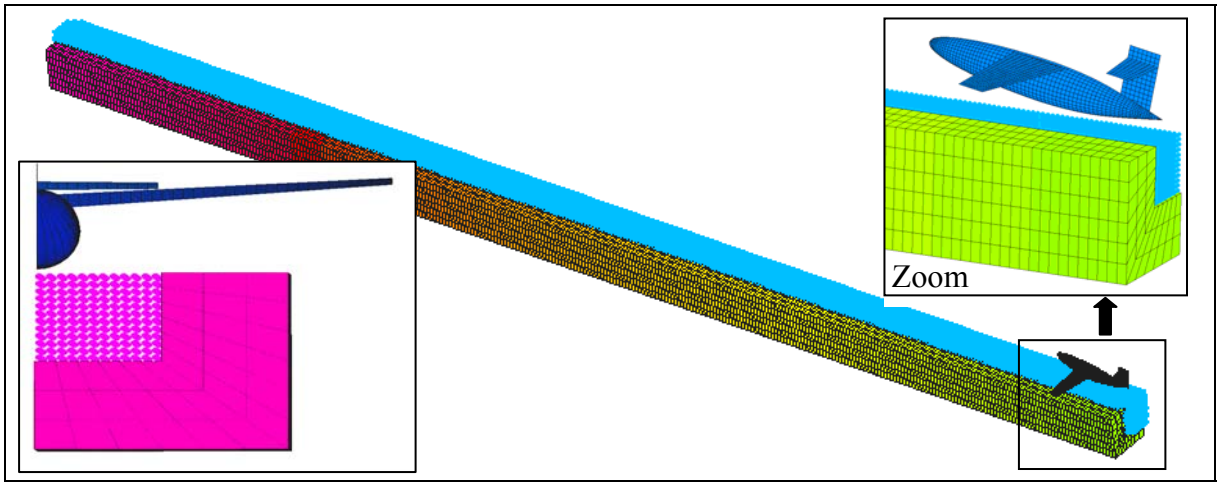

Figure 5-51 : Water and aircraft model

For the ditching simulation involving a forward velocity, the use of a SPH mesh for the water medium in the impact region is most of the time mandatory. The use of a classical FE mesh leads to a dramatic decrease of the time step and therefore to very high computation time. This is caused by the deformation of the individual water solid elements under the vertical and horizontal loads transmitted at the contact interface.

5.2.3.3 Importance of the suction forces acting on the airframe

In the test observations and measurements shown in [108], it can be seen that the aircraft attitude increases very strongly. This indicates that hydrodynamic suction forces act on the rear part of the airframe at the beginning of impact. When the fuselage makes contact with the water surface, the velocity of the water flow increases around the immersed part. This causes a decrease of the pressure (Bernouilli's theorem). If the pressure drops under the available static pressure, cavitation (state, at which vapour or gas- or vapour-filled bubbles, or cavities, become visible and grow) occurs. Additional information on the subject is available in [109].

In order to quantify the effect of the suction forces on the kinematics of the aircraft model, two simulations have been conducted. The first calculation, which is the reference simulation, does not take into account the suction forces. The second calculation has the same boundary conditions as the previous one but includes the suction forces, which are given as a temporary external force applying on the fuselage area, where first impact occurs. This force has been calibrated in order to fit the measured test data (velocity and pitch time histories). To illustrate the effect of the suction forces on the calculated kinematics results, Figure 5-52 shows two simulations sequences comparing the mesh plots at the same time.

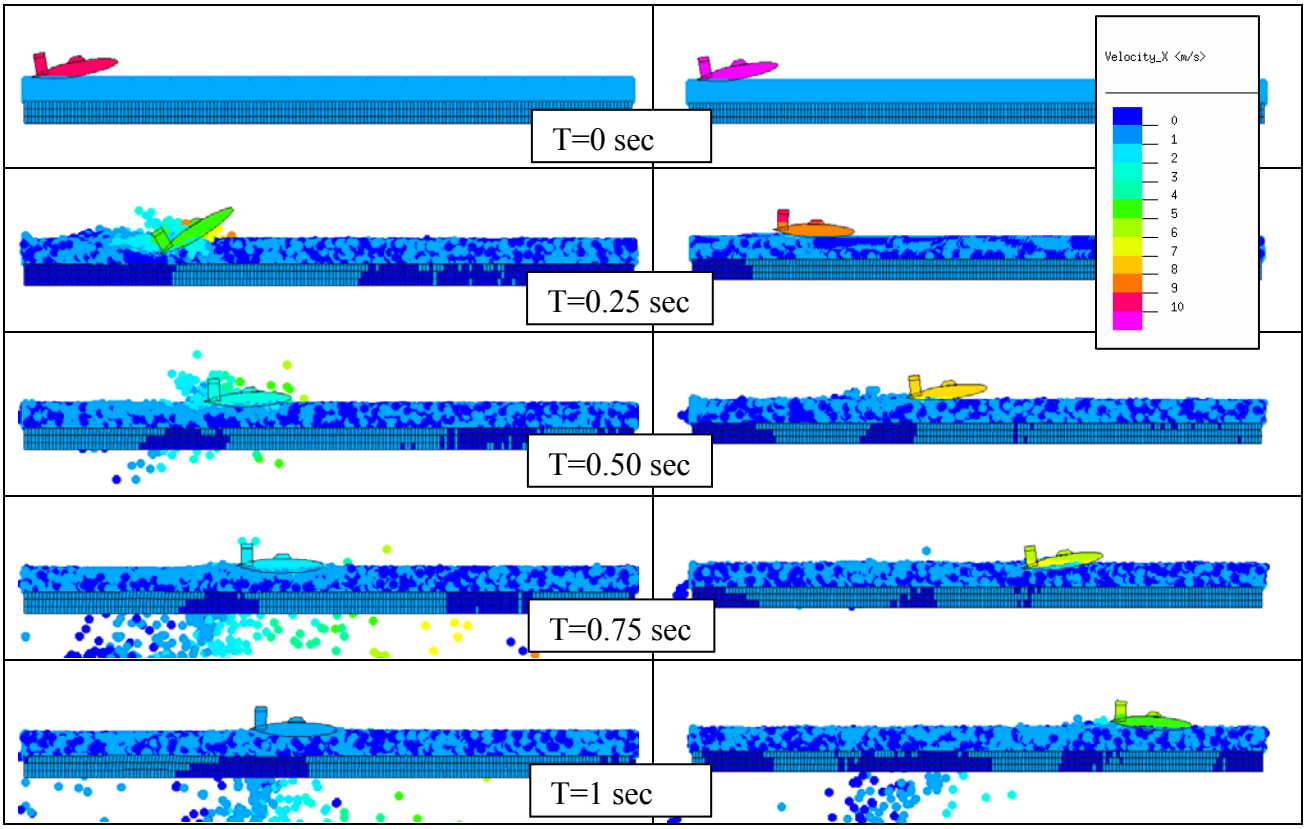

Figure 5-52 : Comparison of the kinematics between two simulations: one taking into account for the suction forces (left column) and the other one without any suction forces (right column)

Figure 5-53 depicts the attitude of the aircraft model calculated in both simulations compared to the results of the test. During the experiment, it can be observed that the aircraft attitude increases from 10° to 38° within about 0.3 sec and then oscillates between -8° and 4° with a period of 0.4 sec. In the simulation without suction forces, the attitude of the aircraft model decreases very quickly from the moment of impact to a negative attitude of -4° within

0.16 sec and oscillates with a period of about 0.35 sec. By contrast on taking the suction forces into account the attitude of the aircraft model increases from 10° to 32°, before decreasing to almost 0° and remaining around this level until rest. These examples show very clearly the importance of the suction forces on the kinematics of the aircraft. Aerodynamic effects are also not taken into account in the FE analysis. To complete these first remarks, Figure 5-54 shows the variation of the velocity during both ditching simulations and the test. During the phase, where the attitude is bigger than 10°, the aircraft velocity decreases from 9.144 m/s to 2.4 m/s in the test. In the simulation, where the suction forces are considered, the velocity-time history curve is very similar to the one of the test until t = 0.6 sec, whereas the velocity remains very high in the basic calculation without suction forces. These observations show that the suction forces constitute a main factor causing high decelerations of the fuselage model in our case (no influence of wings and/or tail planes).

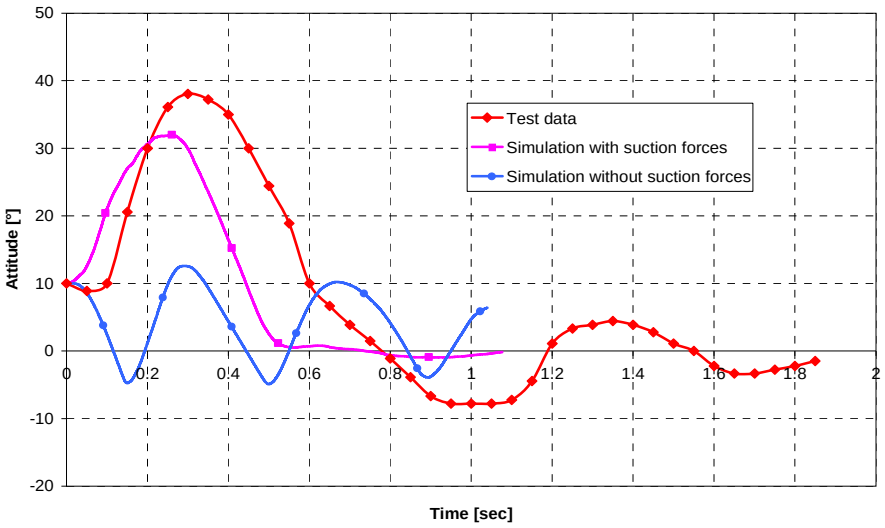

Figure 5-53 : Comparison of the aircraft model attitude between simulations and test

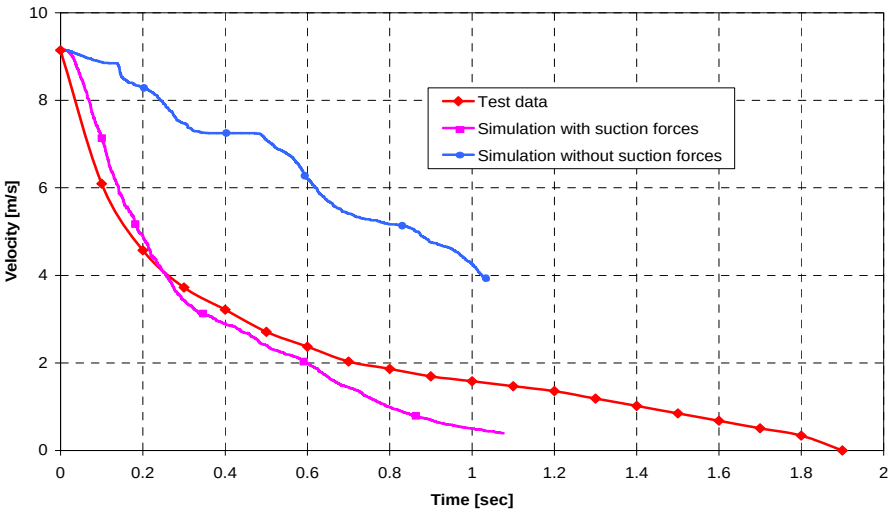

Figure 5-54 : Comparison of the aircraft model velocity between simulations and tests

It is also presumed that the presence of air in the impact region has also an influence on the loading acting on the structure. When the structure is moving forwardly, air is automatically fed into the water, which changes the properties of the continuum at this point. One speaks of

ventilation. The consideration of this phenomenon in the model would need the modelling of air and air/water mixtures requiring additional investigations.

6 Conclusion and outlook

The main aim of this work was to develop and validate numerical methods for simulating the impact of aircraft component or full-scale aircraft on water, in crash conditions relevant to the ditching event of aircraft and helicopters. The emphasis was put on the finite element and the smooth particle methods, which are common techniques used in the crash domain to assess structural deformation. The challenge was then to apply them to the specific domain of "crash" on water.

6.1 Relevance of the subject in aeronautics

In the first chapter, the relevance of impact on water to the area of aeronautics is assessed including aspects like accident conditions and the types of structural damage. To that aim, reported accident data covering the period 1959-2006 is extensively reviewed for fixed wing aircraft whereas the period 1971-1992 is examined for rotorcraft.

The event of impact on water can be classified into two categories: ditching (planned event) and unplanned impact on water. Depending on the category, the types of damage undergone by the structure and the injuries level suffered by the passengers/pilots may be very different. In addition, it is obvious that fixed wing aircraft and helicopter behave very differently when impacting on water. From the structural point of view, fixed wing aircraft have a large cargo volume under the passenger floor, which can absorb energy, may have natural floatation devices (presence of sponsons, low-wing, etc…), which provide additional buoyancy, and the centre of gravity may be sufficiently low to contribute to the aircraft stability in water. For rotorcraft, the sub-floor structure is restricted in height, which limits the capacity to absorb energy and the mass (rotor gear box, motor) is very often concentrated on the top of the structure, which may lead to stability problems in water. From the flight conditions, both fixed wing aircraft and rotorcraft show very different behaviours. For example, whereas forward velocities above 55 m/s are expected for fixed wing aircraft, a helicopter may ditch with a forward speed below 10 m/s. This, of course, makes a large difference in the amount of energy to be absorbed by the structure at impact.

Finally, design guidelines provided mainly by the ditching regulations FAR Part 25 for fixed wing aircraft and FAR Part 29 for transport category rotorcraft to meet crashworthiness objectives in the case of a ditching event are briefly reviewed. They concentrate on three topics: structural integrity, kinematics during impact and floatation characteristics. Until the end of 20th century, demonstration of compliance to ditching requirements have been realised by either testing or comparison to aircraft/rotorcraft of similar design, for which the ditching behaviour has been already certified. Current practices are evolving towards a mix of model testing, analytical investigation and simulation activities, whereas the proportion of numerical simulations in the certification process is increasing. For example, it is probable that the compliance to ditching requirements of the A380 has been exclusively demonstrated numerically.

6.2 Modelling of the impact on water in the literature

In the second chapter, the physics of the phenomenon of impact on water is investigated and the state of the art concerning the modelling of the structure/water interaction presented. This latter includes the analytical and numerical practices used to assess the water impact from the 30's until now.

The phenomenon of impact on water [23, 24] can be divided into two phases: a shock wave (supersonic) phase, where forces are very high on a very short duration and therefore cannot be transmitted to the impacting body and a flow forming (subsonic) phase, where pressure levels are lower but may lead to very high damage in the impacting structure. The notion of added (virtual) mass, to which the impact force is directly connected, is introduced. Consequently, the second phase is focused on in this work.

When considering the vertical impact of aeronautical structure in water, the assessment of the acting forces shows in a first approximation that viscous forces, compressibility and surface tension effects are negligible compared to inertia effects. Based on these assumptions, a mathematical formulation of the problem is proposed which leads to the typical equations solved for hydrodynamic loadings. Despite the fact that the water is considered ideal and incompressible, the flow potential and the structure rigid, the equations remain nonlinear with quadratic terms. In addition, the difficulty is that they are defined on surfaces (free surface and the wetted part of the structure), which themselves are unknowns changing in time and space. Their resolution still remains a challenge today. However, in contrast to a pure vertical impact on water, Troesch and Kang [26] have the opinion that viscous forces may no longer be neglected when considering a horizontal velocity component at impact. This makes the equations of the problem even more complex.

First analytical work about the subject appears in the 30's by Th. Von Karman [34], who proposed an analytical estimate of the impacting force acting on a 2D-wedge impacting vertically on water. His work was then extended by Wagner [35], who additionally considers the formation of a splash at impact and proposes the evaluation of the jet thickness, the water free surface elevation and the pressure distribution of a 2D symmetric wedge of small deadrise angle. Their works are still nowadays the basis of dimensioning tools used for ditching pre-development studies. 3D-analytical or semi-analytical solutions were suggested later by Collopy [36] and Shiffman & Spencer [37, 46] around the 50's. It remained until the 90's for the intuitive work of Wagner to be put on a firm theoretical basis by Cointe [39, 40]. Since then, analytical solutions have been calculated for other simple 2D body shapes [39 - 42] based on the potential flow theory. In these analytical works, the impacting structures have always been considered rigid.

For the resolution of impact on water of 3D complex structure shapes, hybrid techniques involving simple numerical treatments and semi-empirical formule (based on known results from tests or analytical studies conducted on simple bodies) have been developed,. For the specific application of ditching, two codes are used: DRI-KRASH for rotorcraft/fixed wing aircraft crash applications and DITCHER for solely rotorcraft ditching application. On the one hand, DRI-KRASH works with structural models mainly composed of masses/nodes, non-linear beams, springs and plastic hinges reproducing the stiffness and mass distribution of the

global structure. A specific water module for computing the water/structure interaction has been added in order to take into account lift effects (based on planing surface work [53]) and for drag loads (modelled by simple surface standing perpendicular to the forward velocity component) at impact. On the other hand, the DITCHER code considers the effective geometry of the helicopter, which remains rigid during the simulation run. Hydrodynamic forces are computed by considering the submerged volumes and dynamic fluid forces by solving the Morisson equations. Both DRI-KRASH and DITCHER industry oriented codes include effects of waves.

Finally, some advanced numerical techniques able to solve the impact on water of 3D complex flexible structure shapes emerged in the 90's. They involve the coupling (known as the Euler/Lagrange coupling) between the finite volume method for the fluid (Eulerian formulation) and the finite element method for the structure (Lagrangian formulation). For specific applications, some numerical techniques propose an ALE (Arbitrary Lagrange-Euler) formulation for the fluid, which means that the fluid mesh is able to move and the fluid able to "flow" through the moving mesh. Whatever the formulation used for the fluid, the coupling algorithm remains a key issue as it is responsible for the transmission of the contact forces and/or displacements between the fluid and the structure. It consists of a contact tracking phase and a subsequent contact computation phase between the fluid and the structure. In the end, the performance of the coupling algorithm decides the quality of the results. Based on the literature [69, 71, 74 to 76], it is clear that these advanced numerical techniques need further developments before being used for extensive industrial applications such as the impact on water of complex aeronautical structures. Problems of numerical stability and mesh deformation in the case of an ALE formulation have been observed in some cases.

6.3 Simulation of the impact on water with fully Lagrangian techniques

Chapter 3 concentrates on the use of fully Lagrangian formulations to model the water medium as an alternative to the Eulerian or ALE ones described in Chapter 2 and constitutes the main PhD contribution to the subject of impact on water. To that aim, two approaches to simulate the vertical impact on water of simple bodies are evaluated: one based on a pure finite element method and another one based on a meshless method (Smoothed Particle Hydrodynamics) to model the fluid continuum. The main advantages of both approaches are

- the same explicit solver is used for the computation of the fluid and the structure,
- both methods are Lagrangian, which considerably facilitate the computation of the interaction/contact between fluid and structure. No special algorithm is necessary to compute the interaction between both meshes.

In a first study, the water medium is modelled with a finite element mesh consisting of classical eight-node solid where C^0 solid elements are used for computational efficiency. In a second study, it is proposed to model the water medium using the so-called "smoothed particle hydrodynamics" method, which is a meshfree particle method. This latter technique is very suitable for problems where extremely large deformations are expected, which is the case in simulation involving impact on water.
Although the simulations involving SPH are conducted with a Lagrangian solver using a SPH formulation for solid mechanic problems, it is possible to compute the fluid problem by using

the same solver. In that case, the Euler fluid equations are solved in a local Lagrangian reference frame. To that aim, following conditions have to be fulfilled:

- a material model without strength should be used,
- the assumption that the flow can be considered inviscid for the simulations should be appropriate. Only volumetric components of the stress tensor are taken into account.

The second point is in agreement with the statements of Chapter 2 concerning vertical impacts on water and therefore the solver used is adequate for solving the fluid problem in this work.
Besides the formulation used, two material models for water are investigated:

- the isotropic elastic plastic hydrodynamic law, which is adapted to the water properties based on Willbeck's [90] and Heymann's [91] work,
- the Murnaghan equation of state, which is also adapted to the impact problem of interest.

In order to validate the various models, an extensive benchmark study is performed based on test data available from the literature. This latter concerns test campaigns relative to the vertical impact at different velocities of spheres with various densities and sizes. The acceleration time histories at the COG of the spheres were used for comparison. The following parameters are specifically investigated for meshes involving pure FE or SPH: mesh size effects of the water elements, effects of the size of the water pool model, effects of symmetry conditions.

The following statements could be made for a pure classical FE mesh to model water using the isotropic elastic plastic hydrodynamic law:

- the finer the mesh, the better the simulation results correlate with the measurements. Nevertheless, computation time should remain within an acceptable time frame.
- the bigger the model of the water pool, the better the acceleration curves are fitting with the measured ones. As a compromise between result quality and computation time, it was decided for further simulations to use a model twice the size of the structure model to be impacted.
- no significant effects on the result quality could be observed concerning the input of symmetry conditions to minimise the size of the model and therefore the computation time.

When the water medium is modelled with SPH using the same material law, two concepts for the modelling of the water pool have been considered: a pure SPH mesh and a combined SPH/8-node solid mesh, where SPH "elements" are used solely in the region expected to strongly deform. The following could be observed:

- the model of the pool should be at least twice the size (length and width) of the structure to avoid side effects.
- the simulations using a pure SPH mesh are much more time consuming than the pure FE models.
- extending the water pool SPH model with 8-node FE solid elements improves the correlations between test and simulation because side effects are minimised / delayed. Therefore the calculation using the combined meshes for the water pool are preferred.
- the finer the mesh, the better the simulation results correlate with measurements.

To conclude concerning the use of the isotropic elastic plastic hydrodynamic law for water, best results were obtained by using a 5 mm SPH mesh combined with 8-node FE solid elements out of the impact zone. Whereas the acceleration peak could be satisfactorily

predicted by the simulations whatever the technique (SPH or FE) chosen, the acceleration plateau was very often overpredicted by the analyses.

Concerning the simulations using the material model based on the Murnaghan law, very similar results to the ones obtained with the isotropic elastic plastic hydrodynamic law could be obtained and the same conclusions apply. However, a major drawback of the material model is that results are strongly dependent on the "artificial" sound speed chosen for the water. On the one hand, changing this parameter makes this material model attractive because it enables to increase the time step and therefore decreases the computation time. On the other hand, its influence on the quality of the simulation results is too sensitive in my opinion for a reliable use, especially when impact velocities go over a certain value.

Based on the previous recommendations, additional validation work was conducted on other body geometries including a cylinder and wedges with various deadrise angles. The previous statements obtained with the simulations involving the spheres were confirmed. Nevertheless, additional understanding could be reached, especially with the simulations involving the wedges. In the case of a relatively flat wedge (10° deadrise), the possible influence of water compressibility and the importance of an air-layer between the wedge and the water surface, could be emphasised. This latter has a cushioning effect on the impact and therefore decreases the acceleration level acting on the structure. Unfortunately, a full study including the modelling of the air layer could not be conducted for computational limitation.

The extensive investigations in this thesis lead to some guidelines, which are strongly recommended for the simulation of the impact on water of complex aircraft structures:

- the hydrodynamic elastic plastic material model for the water medium should be used,
- a pure FE mesh for the water pool should be preferred to a combined FE-SPH mesh, essentially for reason of computation time,
- the dimensions of the water basin model should be at least twice as big as the dimensions of the structure to be numerically investigated,
- the mesh size should be chosen as fine as possible.

6.4 Simulation of the impact on water of aeronautical structures

Based on the validated methods presented in Chapter 3, two full-scale rotorcraft structures are simulated and numerical results including time histories and deformed structure model compared to test measurements and the crashed components. Aim is to validate the previous modelling work on deformable and representative aeronautical structures.

In a first part, the vertical impact on water of a WG30 helicopter sub-floor component (Aluminium alloys) has been simulated, for which no calibration activities were conducted. Two simulations were performed: one using a full FE model and one using a combined FE-SPH model for the water basin. For computational reasons, the size of the water "elements" (SPH or FE) in the impact zone is chosen five to six times larger than in the simulations presented in § 3.4 and § 3.5. Besides the water model, a considerable effort was also spent on the structure, which is finely meshed especially in the crushing zone. In parallel, adequate advanced material models for the aluminium structure and rivet models have to be incorporated in the structural FE model in order to model the energy absorption mechanisms.

Considering the complexity of the tested structure, correlations between test and analyses results are judged to be very good:

- qualitatively, the folding of the frames and the beams under the impact water loads could be predicted by the simulation. In addition, the typical bending of the skin under the water pressure agrees well between the tested component and the calculated results. These statements apply for the simulation using a pure FE mesh and the one using a combined FE-SPH modelling of the water medium.
- quantitatively, measured pressure time histories at different locations on the skin are available. Depending on the position of the pressure transducers, the quality of the correlations between test and simulation is very variable. Calculated and measured pressure mean levels at soft location agree very well whereas some discrepancies can be observed at stiff locations (e.g. pressure measured directly under a frame). For example pressure peaks are always overpredicted at these places in the numerical analyses whereas the pressure mean level after the peak is acceptably predicted. It can also be observed that the instant of the peak is always advanced in the simulation. Reasons for these differences are the presence of air in the test, which cushion the impact and which is not taken into account in the analysis. This effect is reinforced by the fact that the structure has a flat bottom and the pitch at impact is 0°. When looking at the results issued from the simulation using a combined FE-SPH model for the water, some loss of contact and therefore zero pressure levels are observed after a period of time due to the contact algorithm used. This latter effect tends to push back the particles at the contact between stiff locations and water.

In a second part, the simulation of the vertical impact of a full-scale complete WG30 helicopter is conducted. Due to the size of the structural mesh, only a pure FE mesh for the water basin could be used in order to keep an acceptable computation time. Although no rivet modelling is included in the structural model, similar advanced material models for the aluminium structure are used in order to model the energy absorption mechanisms and the large plastic deformation. The agreement between the test and the calculated results is very good:

- qualitatively, the folding of the frames not only in the sub-floor area but also at the door frames could be reproduced in the simulation. The typical bending of the skin between the frames and keel beams is also very realistic in the calculation.
- quantitatively, the same statements as for the simulation with the WG30 sub-floor apply for the pressure time histories. As acceleration time histories measured at different location on the cabin floor are also available in the test, comparisons with the calculated ones are also conducted. Whereas the measured and calculated time histories agree excellently on the port side, discrepancies are increasing when considering the accelerometers situated on the starboard side. It is thought that the helicopter impacts with a slight roll angle, which of course led to differences between the acceleration levels measured between port and starboard side. This is confirmed by the different pressure levels measured on both sides of the helicopter. This was of course not taken into account in the simulation, which considered a perfectly zero degree attitude at impact and therefore delivers symmetric results.

To conclude, the simulation results (sub-floor and full-scale helicopter) remain conservative compared to the test data and the mean pressure level could be predicted, even if the pressure

peaks were over-predicted at the stiff locations. Nevertheless, the acceleration time histories remain well predicted by the analyses. Due to the reliability of the previously presented method and the validation results, this modelling approach was used in the certification work of the CN235-300M [110].

Based on the experience gained with the full-scale WG30 helicopter, it is clear that the investigation of the impact on water of deformable full-scale structures necessitates very large computation times. If a horizontal velocity at impact should be considered, this would mean a larger model for the water basin and therefore an unacceptable computation time. For this reason, a local/global methodology has been tested involving the hybrid code DRI-KRASH and an explicit FE code (e.g. PAM-CRASH). The main idea is first to investigate the behaviour of critical sub-components of a whole structure with the Finite-Element technique. From the Finite-Element analyses, elaborated input data, usually acquired from tests, like non-linear characteristics for springs and plastic hinges or calibrations of hydrodynamic elements, can be generated for the hybrid code input data. Various scenarios and designs can then be simulated very quickly with DRI-KRASH. However it is important to mention that other input data like the drag coefficient necessary for the definition of the drag surface model DRI-KRASH have still to be determined by tests or empirically.

The application of the methodology to the impact on water is described in the following. In a first step, a characteristic sub-floor sub-structure has been analysed with PAM-CRASH under vertical impact on water. The location of plastic hinges in the structure as well as the calculated contact forces have been used to generate an equivalent DRI-KRASH model of the sub-floor sub-structure and then a full cross-section model. Based on the previous models, a full stick model of the aircraft to simulate ditching could be generated. This is achieved by cutting the fuselage and the wings into sections, each of them being modelled with a single beam with the adapted properties. With such a model, detailed deformations due to the impact occurring in the sub-floor area cannot be reproduced, but the flexibility of the fuselage and of the wing, as well as the rupture of the skin and its consequences could be taken into account. At this stage, various ditching conditions can very easily and rapidly be simulated. The advantage of the methodology is that detailed simulations are conducted on sub-components, which limits the computation time, and full-scale simulations are performed with the hybrid model, which needs very short computation time. Nevertheless, it should be underlined that the procedure (generation of model, calibration, etc …) remains time consuming for the user and needs a certain experience for the generation of the stick model.

The treated case in this work shows that, in principle, the local/global methodology can be successfully applied to simulate the ditching of a full aircraft structure. Due to the absence of test data, validation work could unfortunately not be performed. However, the author would like to highlight the following statement when considering a forward velocity at impact on water. Based on a ditching test campaign with various scaled fuselage shapes [108], the simulation of some tests with a combined FE-SPH mesh necessitates the consideration of suction forces in order to be able to capture the kinematics of the ditching event. These forces act at the structure/water interface and are caused by phenomena of cavitation, whose magnitude depends on the impact velocity and on the fuselage shape at the point of impact. Phenomena of ventilation are also expected but cannot be included in the model as long as air and air/water mixtures are not modelled.

6.5 Outlook

To overcome the problem of computation time limitation, which is rapidly encountered by using a combined FE-SPH mesh for the water, it is meaningful to consider a multi-model coupling technique. This latter would enable to compute the deformation of the water continuum and of the structure with different time steps. The interaction forces between water and structure are then exchanged at a suitable time step, which depends on the impact velocity and both time steps.

It would make sense to develop a special contact algorithm when considering water/structure interaction in order to avoid the loss of contact, which is encountered in the region of high stiffness in the structure. To that aim, a kind of "adhesive conditions" should be included in the contact algorithm so that nodes (FE nodes or SPH nodes) are not accelerated away from the structure when a contact is detected but remain in contact with it.

In this work, pure metallic structures have been investigated at impact on water. The next step could be to apply the methods to composite structures, which show different failure behaviour.

The use of a FE or a combined FE-SPH method is suitable to simulate the pure vertical impact on water of complex structures. Considering a horizontal velocity at impact needs the study of additional phenomena like cavitation and eventually ventilation, whose effects on the water/structure interaction still have to be thoroughly investigated.

Appendix A: Water impact accidents data

Tables A-1 to A-3 review 42 water impact accidents of civil jet transport aircraft for the periods 1959-1979, 1980-1999 and 2000-2006 based on [4], [5] and wide internet research especially in [6]. Only information on accidents involving civil transport aircraft in domestic and international flights as well as scheduled and non-scheduled flights is considered. Ferry, positioning, executive, cargo and military flights are not included. Besides the accident date and location, the type of the involved civil aircraft, the number of occupants onboard and the number of fatalities are reported. Additional information has been added in order to clarify the circumstances of the various water impact accidents.

The flight phase, during which the water impact accident occurred, is identified in the next tables by the following acronyms:

LDG	:	Landing
T/O	:	Take-off
APP	:	Approach
EN ROUTE	:	other phases (climb, cruise or initial descent)

The types of water accidents are classified according to the following categories:

Off runway:
The aircraft runs off the end of the runway or was turned off the runway and comes to stop in water.

CFIT (Control Flight Into Terrain)**:**
The crew has a false opinion of the situation and is not aware of the imminent impact on water.

Ditching:
The aircraft impacts the water as a planned action due to a technical problem.

Loss of control:
The aircraft is not controlled in flight by the crew.

Explosion:
When explosion is involved, it is supposed that the aircraft is severely damaged before impacting on the water.

When the water impact event is not survivable, the event is described in italics in all Tables. For the accidents reported in Table A-1, a supplementary column reveals if the accident was fully survivable or partially survivable based on more detailed information. As discussed in [4] this statement is based on the criteria of a survivable (sufficient) airframe volume (prior to fire), the capability of at least one occupant to withstand the accident environment, the potential for occupant escape and/or a demonstration of structural system performance. Finally, the intentional ditchings are highlighted in bold.

In the accident of a B747 on the 23 June 1985, it is considered that the passengers were primarily killed by the explosion and not by the water impact. For this reason, this event is separately represented in Table A-2.

Date/Aircraft type Accident Location	Year	On-board	Fatalities	Flight Phase Accident type	Occupant survivability
24-Sept-61 B720 Boston	1961	71	0	LDG Off runway	YES
20-Aug-62 DC-8 Rio de Janeiro	1962	105	15	T/O Off runway	YES
21-Aug-63 Tu-124 Neva River, USSR	**1963**	**52**	**0**	**APP Ditching**	**YES**
07-Apr-64 B707 JFK, New-York	1964	145	0	LDG Off runway	YES
17-Apr-64 CVL Dhahran, S. Arabia	*1964*	*49*	*49*	*APP CFIT*	*NO*
16-Aug-65 B727 Lake Michigan	*1965*	*30*	*30*	*EN ROUTE CFIT*	*NO*
04-Feb-66 B727 Tokyo Bay	*1966*	*133*	*133*	*APP CFIT*	*NO*
30-Jun-67 CVL Hong Kong	1967	80	17 [4]/ 24 [6]	APP CFIT	YES
05-Nov-67 CV-880 Hong Kong	1967	137	1	T/O Off runway	YES
22-Nov-68 DC-8 San Fransisco Bay	1968	107	0	LDG CFIT	YES
12-Dec-68 B707 Caracas	*1968*	*51*	*51*	*APP CFIT*	*NO*
13-Jan-69 DC-8 Los Angeles	1969	45	15	APP CFIT	YES
02-Aug-69 CVL Marseille	1969	44	0	LDG Off runway	YES
02-May-70 DC-9 St. Croix, Virgin I.	**1970**	**63**	**25 [4]/ 23 [6]**	**EN ROUTE Ditching**	**PARTIALLY**
27-July-70 DC8 Naha, Okinawa	1970	4	4	APP CFIT	PARTIALLY
22-July-73 B707 Papeete, French Polynesia	*1973*	*79*	*78*	*EN ROUTE CFIT*	*NO*
18-Dec-77 CVL Funchal, Portugal	1977	57	36	APP CFIT	YES
08-May-78 B727 Escambia Bay, Florida	1978	58	3	APP CFIT	YES
23-Dec-78 DC-9 Palermo, Sicilia	1978	129	108	LDG CFIT	UNKNOWN

Table A-1: Water impact accidents of civil jet transport aircraft in the period 1959-1979

Date/Aircraft type Accident location	Year	On-board	Fatalities	Flight Phase Accident type
07-Aug-80 Tu-154 Nouadhibou, Mauritania	1980	168	2 [5]/ 1 [6]	APP CFIT
12-Sept-80, B727 Corfu, Greece	1980	115	0	LDG Off runway
07-May-81 BAC1-11 *Argentina*	*1981*	*30 [5]/* *31 [6]*	*30[5]/* *31 [6]*	*EN ROUTE* *Loss of control*
23-Jan-82 DC-10 Boston	1982	212	2	LDG Off runway
09-Feb-82 DC-8 Tokyo	1982	174	24	APP CFIT
28-Feb-84 DC-10 JFK Airport, New-York	1984	177	0	LDG Off runway
04-Aug-84 BAC1-11 Tacloban, Philippine	1984	80 [5]/ 75[6]	0	LDG Off runway
23-Jun-85 B747 Ireland	1985	325	325	EN ROUTE Explosion
27-Jun-85 DC-10 San Juan, Puerto Rico	1985	270	0	T/O Off runway
16-Feb-86 B737 *Taiwan*	*1986*	*13*	*13*	*APP* *CFIT*
31-Aug-87 B737 *Phuket, Thailand*	*1987*	*83*	*83*	*APP* *Loss of control*
28-Nov-87 B747 *Mauritius*	*1987*	*159*	*159*	*APP* *Loss of control/Fire*
31-Aug-88 Trident Hong Kong	1988	89	7	LDG Off runway
20-Sep-89 B737 La Guardia, New York	1989	63	2	T/O Off runway
20-Feb-91 Bae-146 Puerto Williams, Chile	1991	72 [5]/ 73 [6]	20	LDG Off runway
01-Jul-93 Fokker F-28 Sorong-Jefman, Indonesia	1993	43	41	APP CFIT
12-Sep-93 B747 Papette, French Polynesia	1993	272	0	LDG Off runway
04-Nov-93 B747 Hong Kong	1993	396	0	LDG Off runway
05-Nov-94 Yakovlev 40 Saposoa Airport, Peru	1994	31	6	LDG Off runway
23-Nov-96 B767 **Comoros**	**1996**	**175**	**125**	**APP** **Ditching**

Table A-2: Water impact accidents of civil jet transport aircraft in the period 1980-1999

Accident date/aircraft type/location	Year	On-board	Fatalities	Flight Phase Accident type
30-Jan-00 A310 Abidjan, Ivory Cost	2000	179	169	EN ROUTE CFIT
16-Jan-02 B737 Yokyakarta, Indonesia	**2002**	**60**	**1**	**APP Ditching**
20-Apr-05 B707 Tehran-Mehrabad, Iran	2005	169	3	LDG Off runway

Table A-3: Water impact accidents of civil jet transport aircraft in the period 2000-2006

Appendix B: Analytical investigations of the impact on water of a sphere

As validation of the method described in § 3.2.4 and 3.2.5, a set of experimental results from the literature have been compared to the analytical results obtained with Collopy's [36] and Shiffman & Spencer [47] approaches. Configurations of various spheres impacting on water are summarised in Table B-1.

Origin of the test data	Weight [kg]	Diameter [mm]	Type of impact	Impacting velocity [m/s]
Anghileri [73]	3.76	109	vertical	11.8
Troesch [26]	33.12	251	vertical	3.46
Troesch [26]	33.12	251	vertical	4.89
Troesch [26]	33.12	251	vertical	5.99
McGehee [36]	975.2	3,200	vertical	9.144
Troesch [26]	33.12	251	oblique	3.46
Troesch [26]	33.12	251	oblique	4.89

Table B-1: Summary of the test data for various spheres

In this paragraph, the force time history of various spheres at different striking velocities will be calculated using the Collopy's analytical formulas and compared to test data. The applied procedure is given in the following.

From the geometry of the sphere, the radius of the disk situated at the intersection of the sphere and the undisturbed water surface (Figure B-1) is given by:

$$r = \sqrt{2Rz - z^2} \qquad \text{(B-1)}$$

Inserting (B-1) in the equations (3-35), (3-36) and finally (3-20a), it is possible to calculate the induced mass, the velocity and the impact force of the sphere as a function of the immersion depth. Knowing the velocity, the elapsed time from the first contact of the sphere on water can be deduced by applying an advance difference time integration scheme and therefore the impact force as a function of the time obtained.

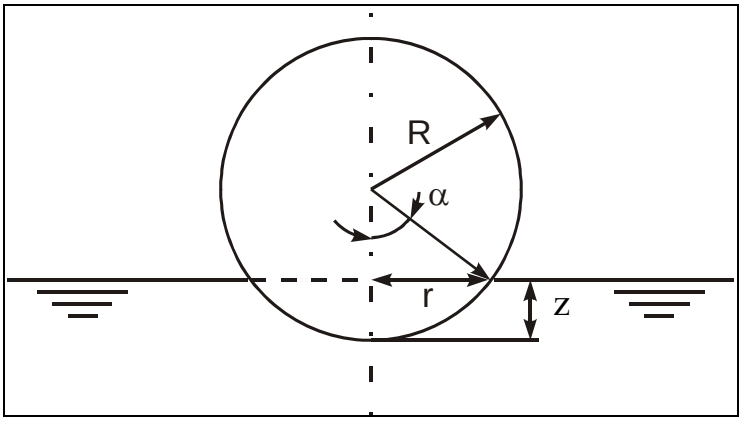

Figure B-1: Parameters used for a sphere impacting on water

Calculated acceleration curves from Figures B-2 to B-4 were generated with an excel program according to this procedure. It can be seen that results from the Collopy's analytical formula agree well with the experimental results. The overall behaviour of the impact force as well as the time of the peak correlate excellently.

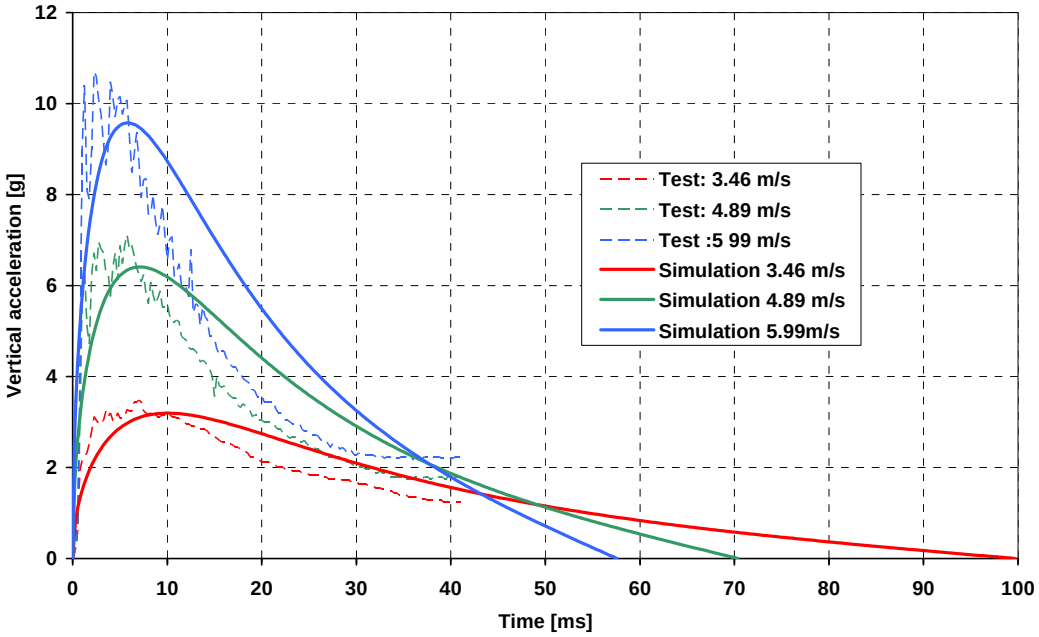

Figure B-2: Comparison between test data and analytic results from Collopy's formula for a sphere with a weight of 33.12 kg and a radius of 251 mm impacting water at the following velocities: V= 5.99/4.89/3.46 m/s

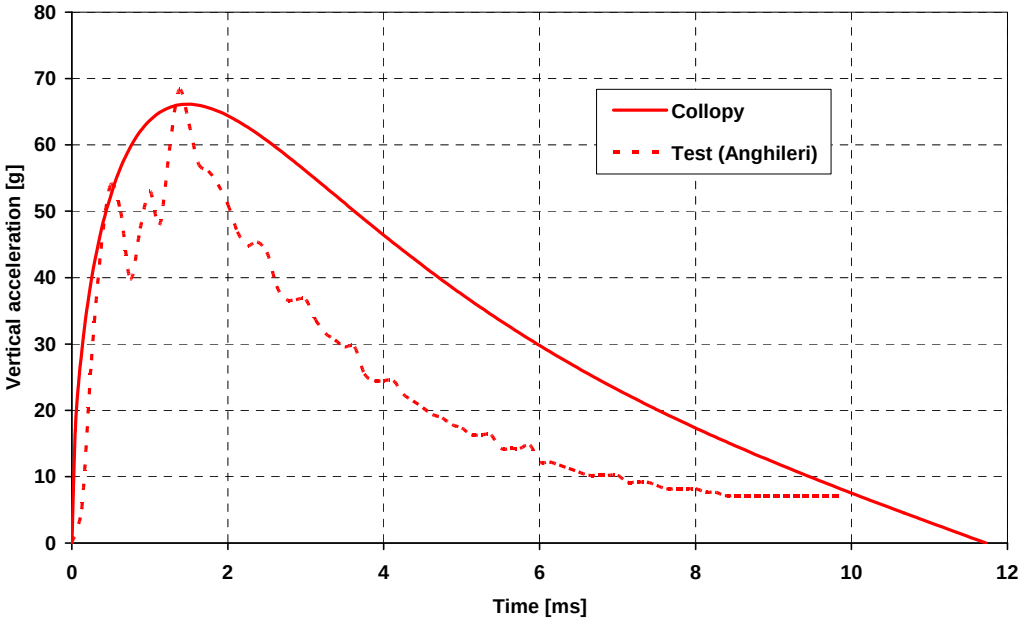

Figure B-3: Comparison between test data and analytic results from Collopy's formula for a sphere with a weight of 3.76 kg and a radius of 109 mm impacting water at 11.8 m/s

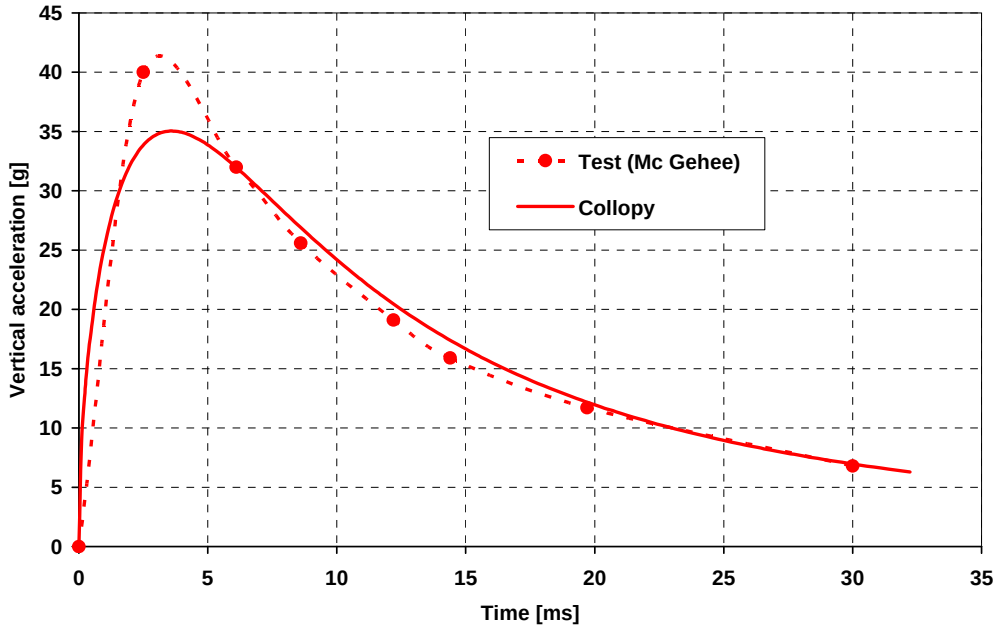

Figure B-4: Comparison between test data and analytic results from Collopy's formula for a sphere with a weight of 975.2 kg and a radius of 3,200 mm impacting water at 9.1 m/s (●: measured point)

In addition, the method of Shiffman & Spencer has been investigated. The maximum accelerations have been calculated from Figure 3-8 for the different spheres' configurations and obtained results are presented in Table B-2.

Origin of test data	Maximum measured acceleration	Prediction from Shiffman & Spencer's approach	Percentage of error
Anghileri	67 g	63.7 g	-4.9 %
Troesch	3.49 g	3.5 g	0.3 %
	7.1 g	7.0 g	-1.4 %
	10.7 g	10.5 g	-1.9 %
McGehee	40 g	--	--

Table B-2: Comparison between Shiffman & Spencer's and test results

Calculated acceleration is not available for the McGehee test result because geometrical sphere data lay outside the range of the curves in Figure 3-8. Comparison between test data and results from the graphical method of Shiffman & Spencer leads also to excellent results. The error between calculated and tested acceleration maximums remains below 5 %.

Appendix C: Numerical investigations

Influence of the mesh density of the body impacting on water on the simulation results

Figure C-1 shows the influence of the sphere mesh size on the acceleration time histories by comparing the simulation results of the test case described in [73]. When the mesh size of the water pool is kept unchanged, running simulations with varying mesh sizes of the sphere deliver acceleration time histories at the center of gravity of the sphere very close to each other. It can then be assumed that the mesh density of the rigid sphere barely influences the simulation results. Nevertheless, this supposes that the mesh is still able to describe sufficiently the geometry of the impacting body.

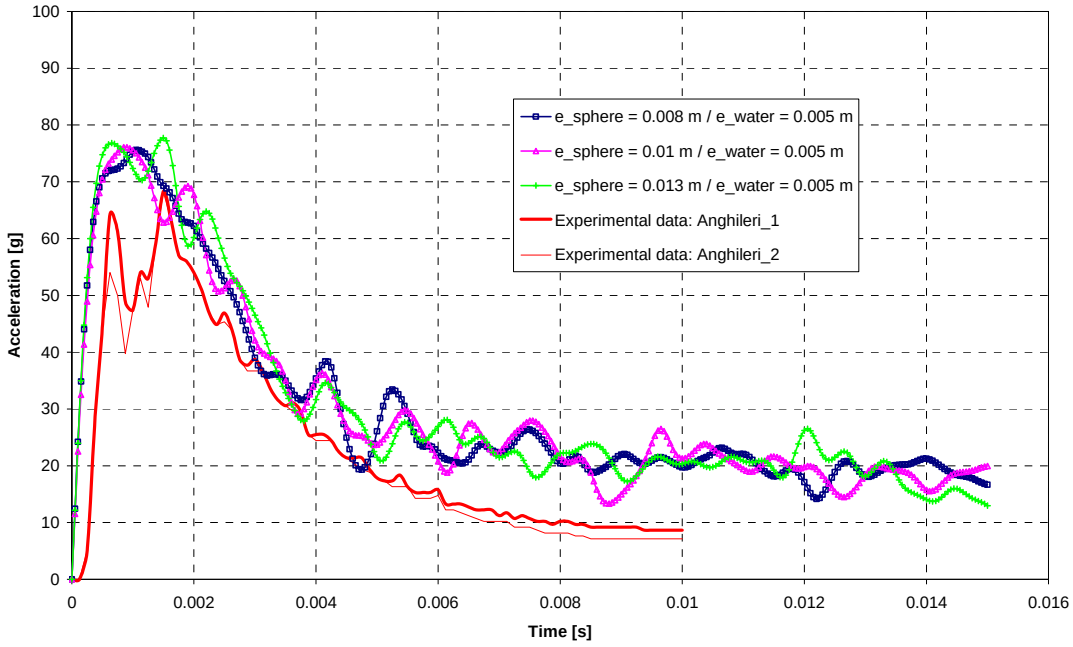

Figure C-1: Influence of the mesh density of the sphere on the calculated acceleration time histories at COG (pure FE models)

Appendix D: Comparison between test and simulation of a sub-floor structure impacting on water using a combined FE-SPH mesh for the water basin

Simulation model

Figure D-1 gives an overall view of the model used for the simulation of the impact of the sub-floor structure on water using a combined FE-SPH mesh. The same boundary conditions as for the simulation with the pure FE mesh for the water basin are applied (§ 5.1.1.2).

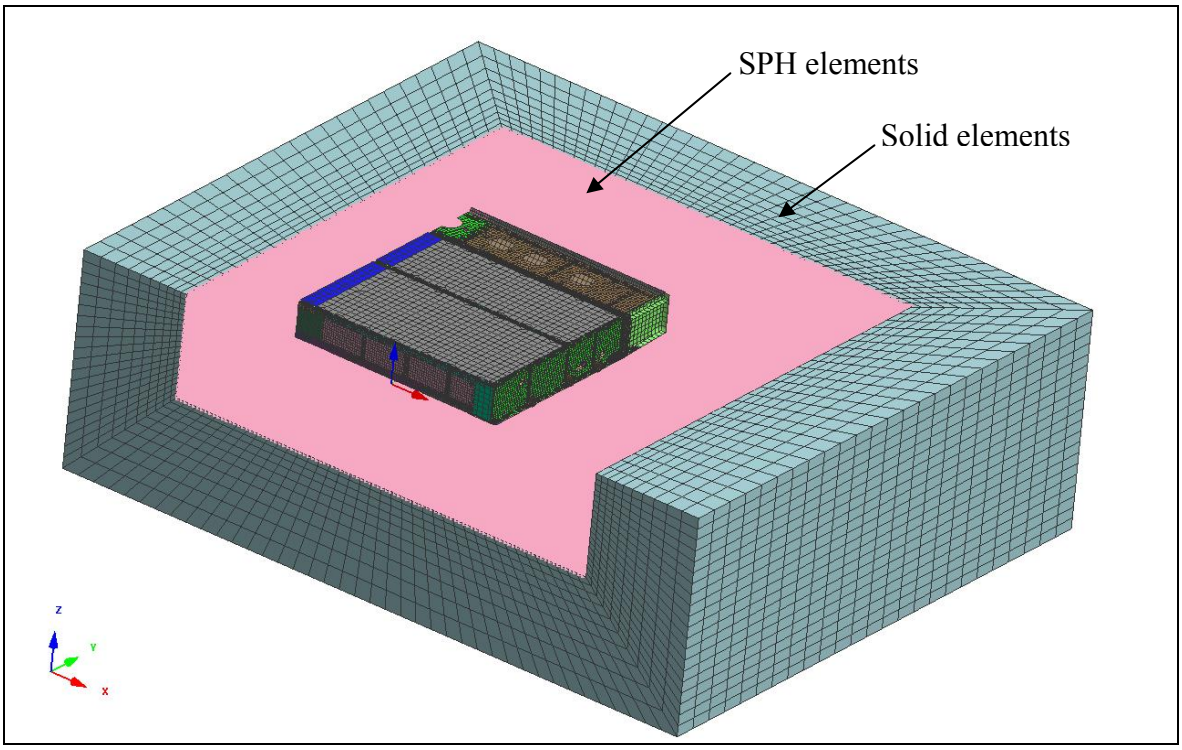

Figure D-1: Picture of the model including the half sub-floor structure and the combined FE-SPH mesh

Correlation between test and analysis results

In Figure D-2, the simulation using SPH elements shows a realistic splash effect at impact and predicts velocities above 16 m/s for some particles. Nevertheless, no experimental data are available for comparison.

Figures D-3 and D-4 show comparison of the deformations sustained by the sub-floor structure between test and calculation. The same comments as made for the simulation conducted with the pure FE water mesh apply. The buckling of the frames and the bending of the skin can be well predicted by the computational analysis.

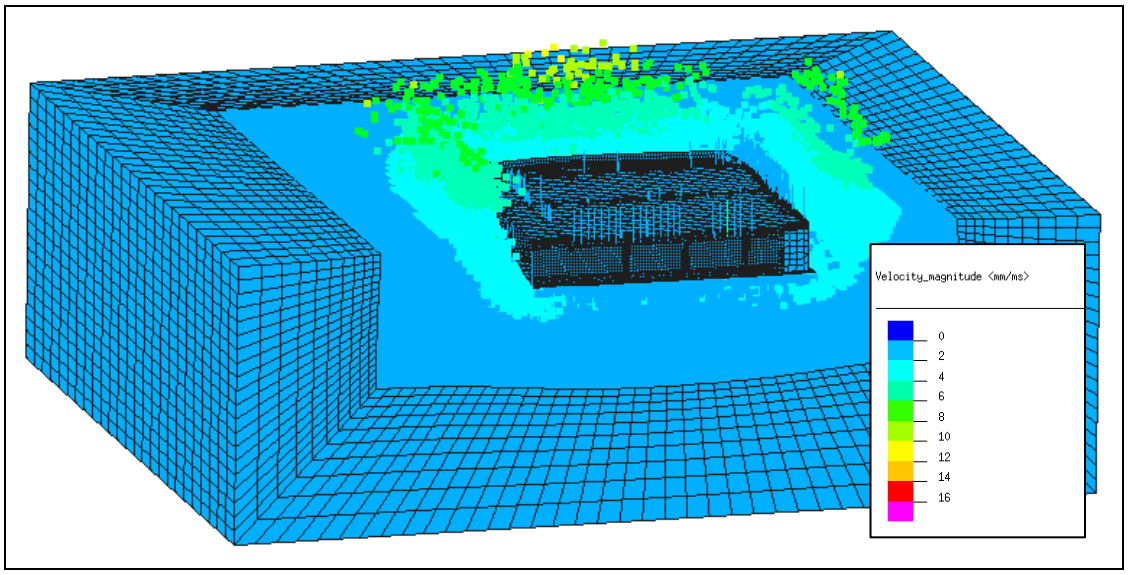

Figure D-2: Deformation of the water surface at impact (t = 40 ms)

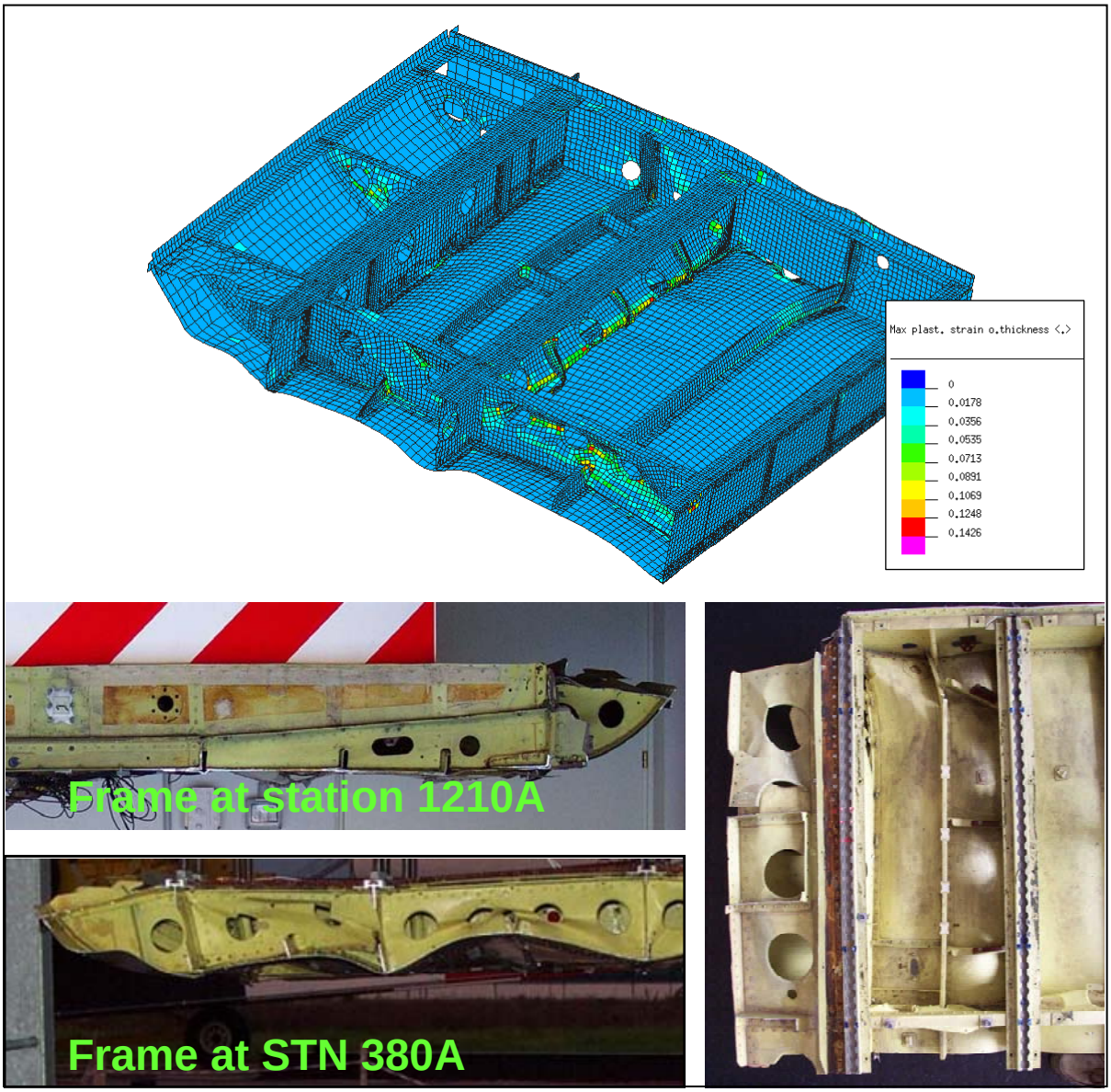

Figure D-3: Upper view of the sub-floor deformations in the analysis at t = 40 ms and pictures of the damage after the test

Figure D-4: Lower view of the sub-floor deformations in the analysis at t = 40 ms and after the test

Figures D-5 to D-8 show the comparisons between measured and calculated pressures at locations P2, P3, P6 and P8 respectively, which were computed but not included in the main text (§ 5.1.1) for clarity. For Figure D-5 the same comments as for Figure 5-13 apply whereas for Figures D-6 and D-7, the same comments as for Figure 5-11 apply. In Figure D-8, the simulation using a pure FE mesh for the water basin strongly underestimates the measured pressures. This is explained by the fact that the skin at this location deforms more in the simulations compared to the test. In addition, the pressure transducer shows a suspicious behaviour giving negative pressures, which were never observed in the 20 first milliseconds of the impact with the other transducers.

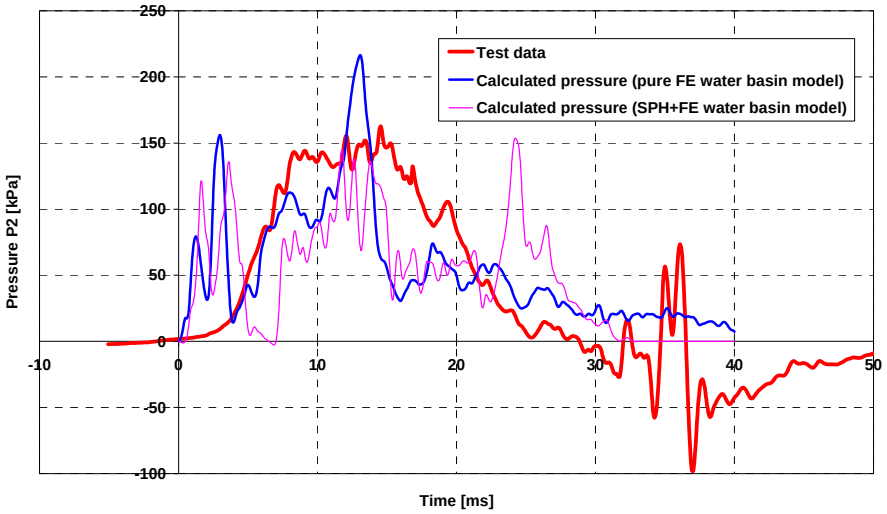

Figure D-5: Measured and calculated pressures at location P2 (soft location)

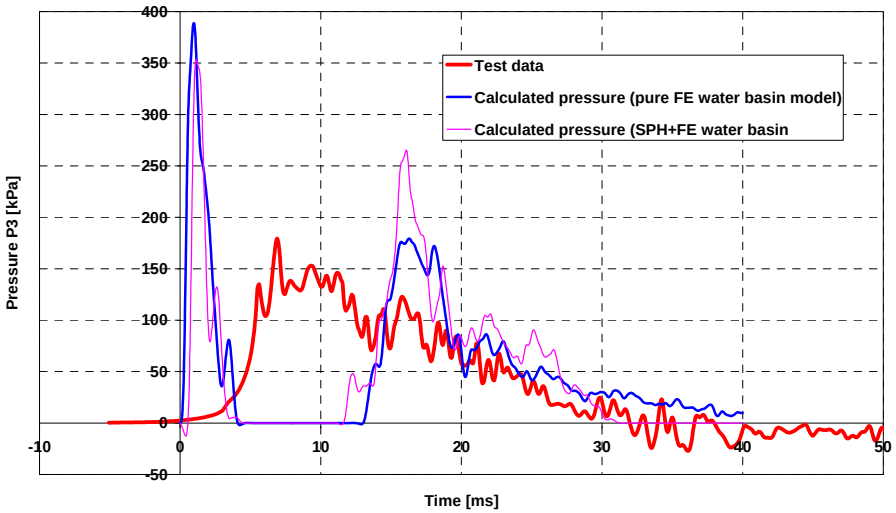

Figure D-6: Measured and calculated pressures at location P3 (very stiff location)

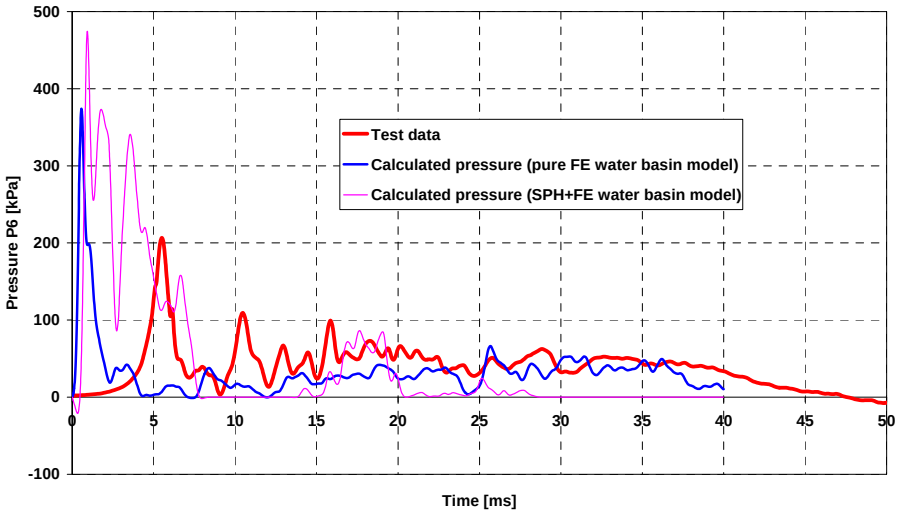

Figure D-7: Measured and calculated pressures at location P6 (very stiff location)

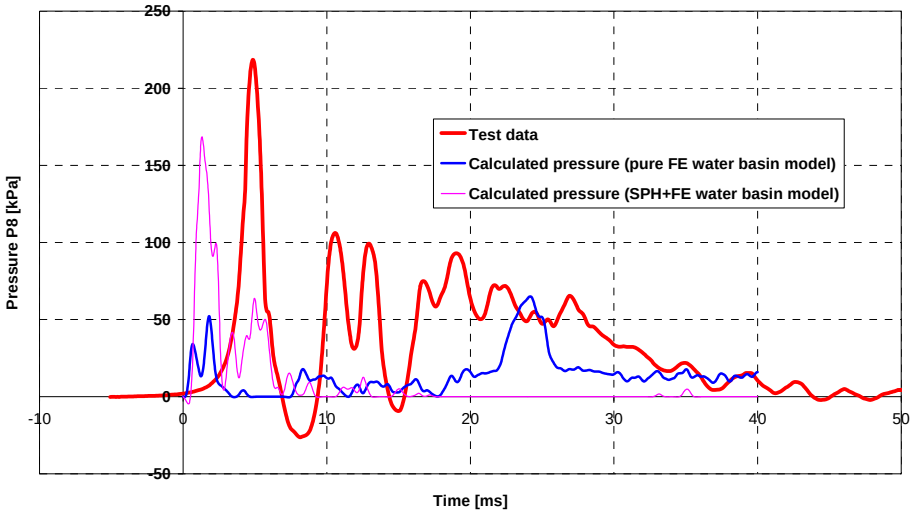

Figure D-8: Measured and calculated pressures at location P8 (very stiff location)

The comparisons between the calculated and measured pressures at locations P9 to P14 are not reported here because they were not calculated with the combined FE-SPH water mesh (half model).

Appendix E: Comparison between test and simulation of a full-scale WG30 helicopter impacting on water using a pure FE mesh for the water basin

Simulation model

Figure E-1 shows a global view of the full-scale WG30 helicopter model whilst Figures E2 and E3 illustrate more precisely the difference of mesh densities between the tail, the roof, the upper part of the cockpit and the sub-floor area. This latter is of special interest to acquire the acceleration levels reached on the seat rails and therefore the risk of injury on the passengers.

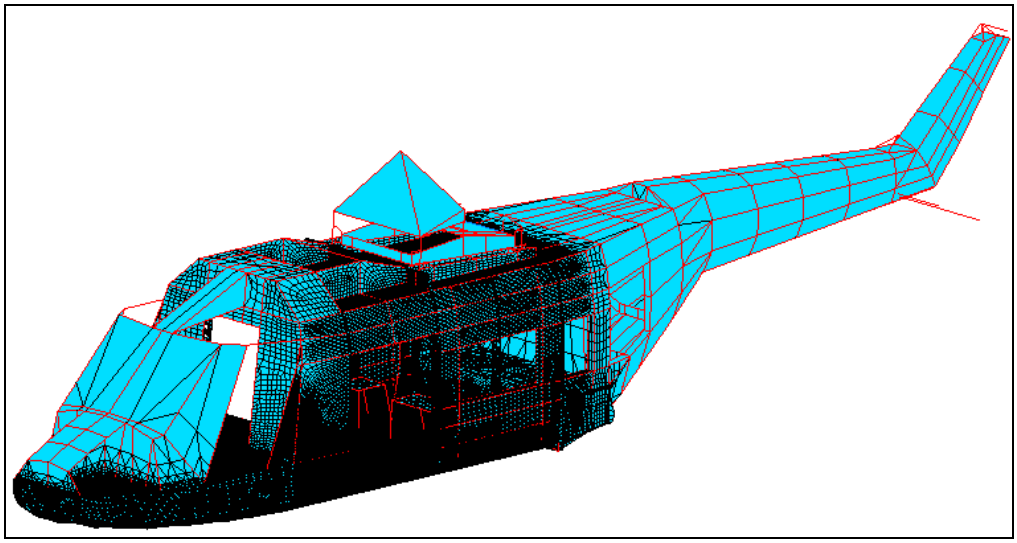

Figure E-1: Global view of the WG30 helicopter FE model

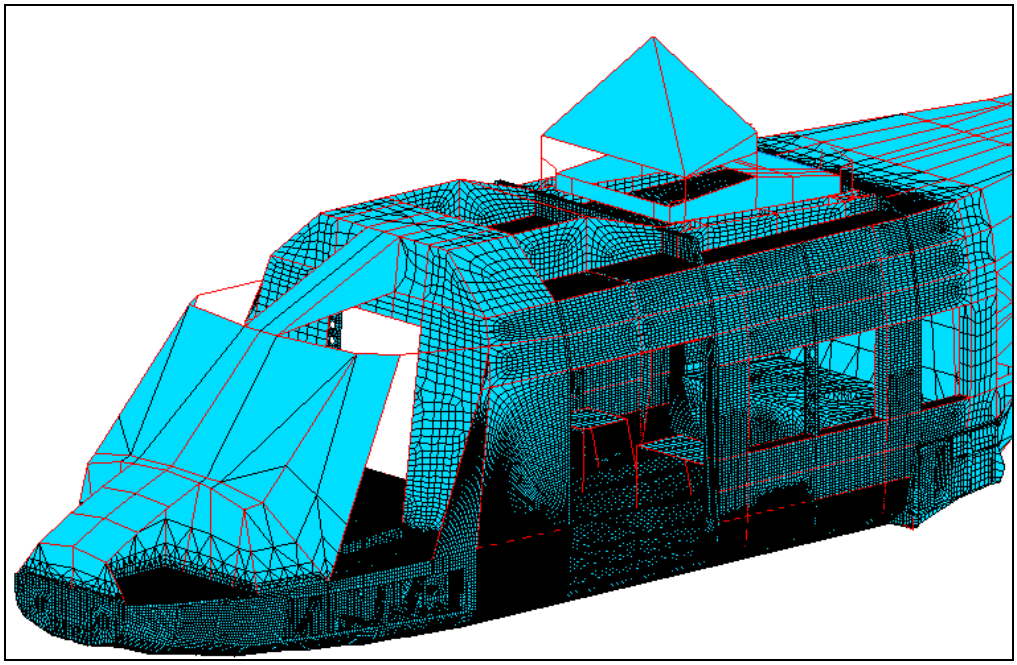

Figure E-2: Zoom on the cabin area of the WG30 helicopter FE model

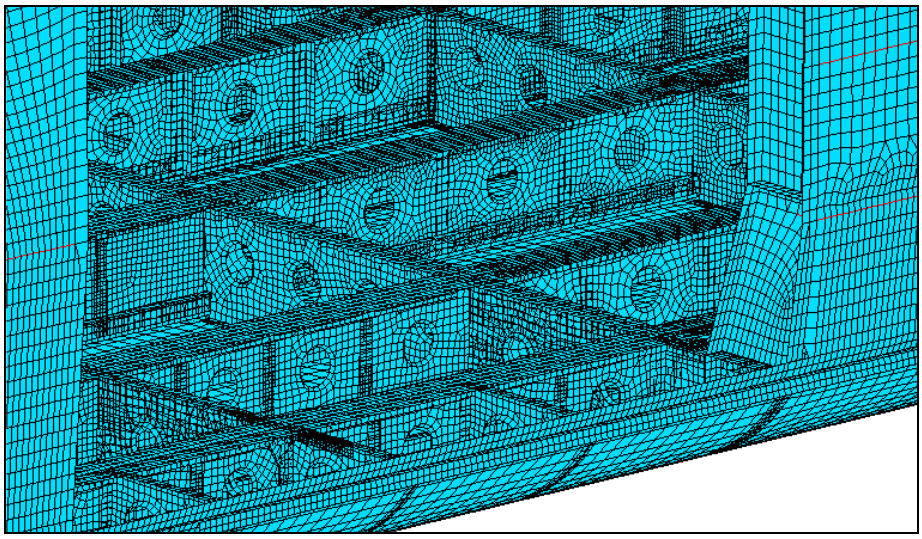

Figure E-3: Details of the mesh in the sub-floor area of the WG30 helicopter

Correlation between test and analysis time history results

Figure E-4 shows the position of the accelerometers on the seat rails, whose signals are used for the evaluation of the impact on water. They are positioned in the cabin and in the cockpit. Only the acceleration time histories on the seat rails are illustrated because they concern a zone of interest and therefore are modelled with great care (very fine mesh). In this region, the accelerations which are transmitted to the seats of the passengers/pilot/co-pilot, can be directly determined. Figures E-5 to E-12 depict a comparison between acceleration time histories measured and calculated on the cabin floor, which are not reported in § 5.1.2. Data are filtered with a CFC60 filter as recommended for full vehicle test in [103, 104]. The same conclusions as in § 5.1.2.3 apply. Correlations between test and simulations are very satisfactory at the accelerometers situated along the centre (BL. 0) showing differences of 20 % in the acceleration peaks. On the starboard side (BL. -830), the agreements between test and measures are not as good exhibiting differences for the acceleration peak of up to 45 % between test and analysis. Reasons can be many if the complexity of the model is considered. An explanation can be: a slight roll and pitch attitude of the helicopter at impact, which is not taken into account in the simulation, can lead to lower acceleration levels on the starboard side of the helicopter in the test. Although the impact was planned perfectly normal to the water surface, all the accelerometers on the starboard side show lower peak levels compared to the accelerometers on the port side (see a11 and a9, a14 and a12, a17 and a15).

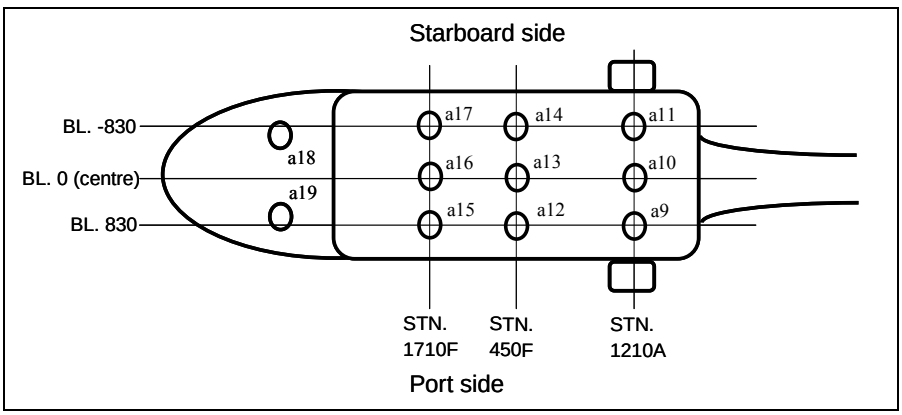

Figure E-4: Position of the accelerometers on the seat rails of the WG30 helicopter's floor (not in scale)

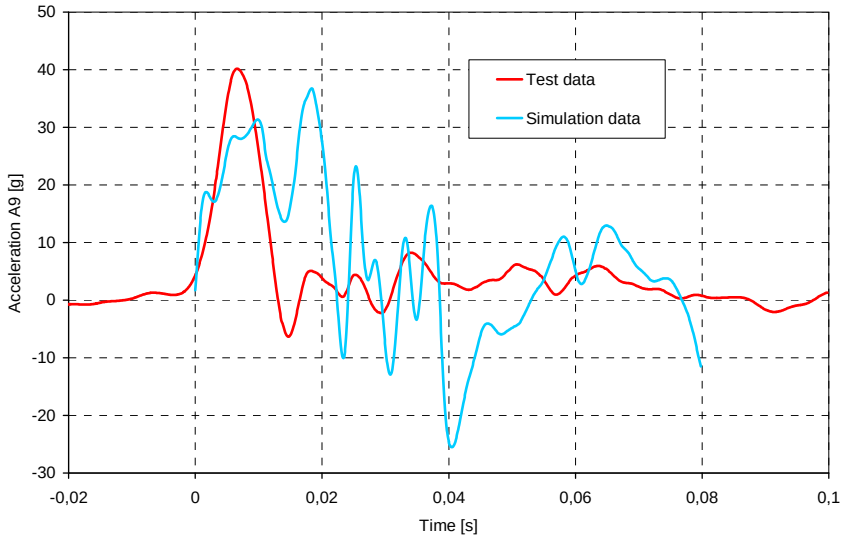

Figure E-5: Acceleration time histories on the cabin floor STN 1210A, WL –802, BL 830 (location A9)

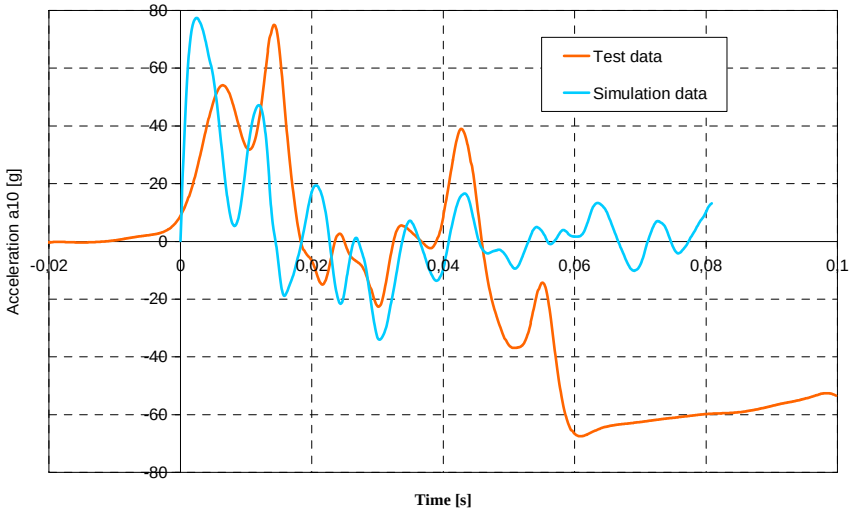

Figure E-6: Acceleration time histories on the cabin floor STN 1210A, WL –802, BL 0 (location A10)

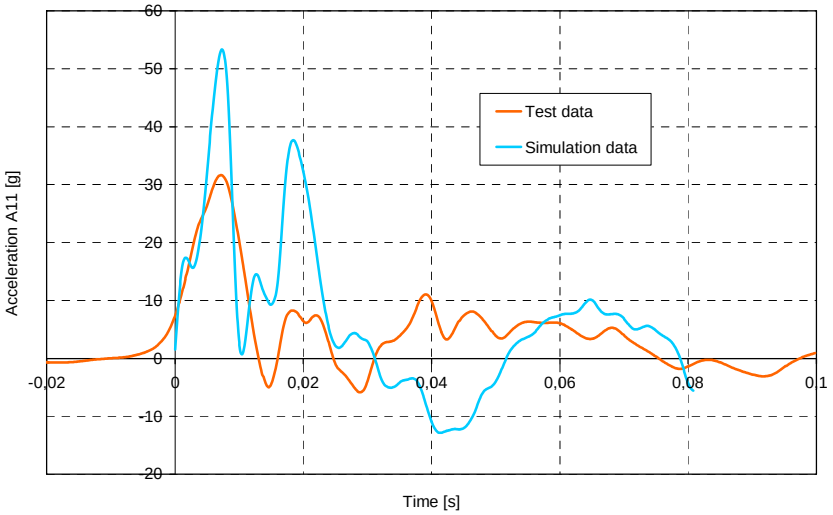

Figure E-7: Acceleration time histories on the cabin floor STN 1210A, WL –802, BL -830 (location A11)

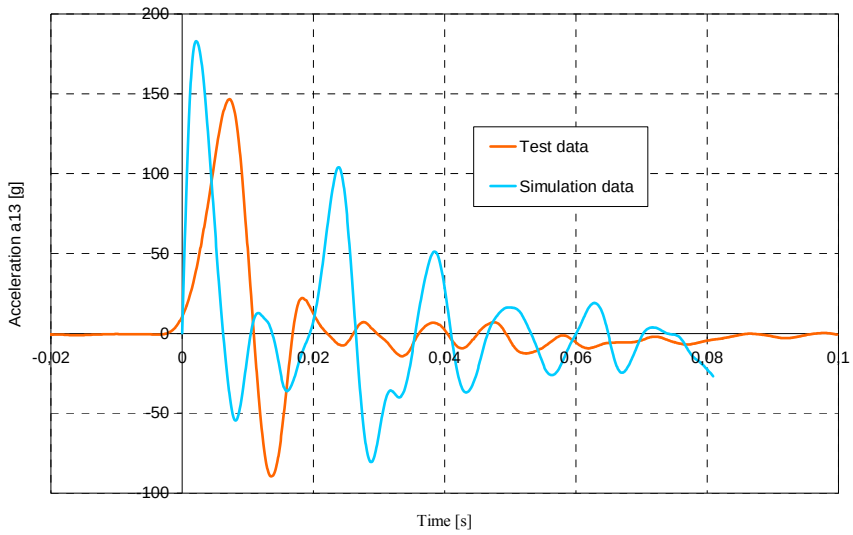

Figure E-8: Acceleration time histories on the cabin floor STN 450F, WL –802, BL 830 (location A13)

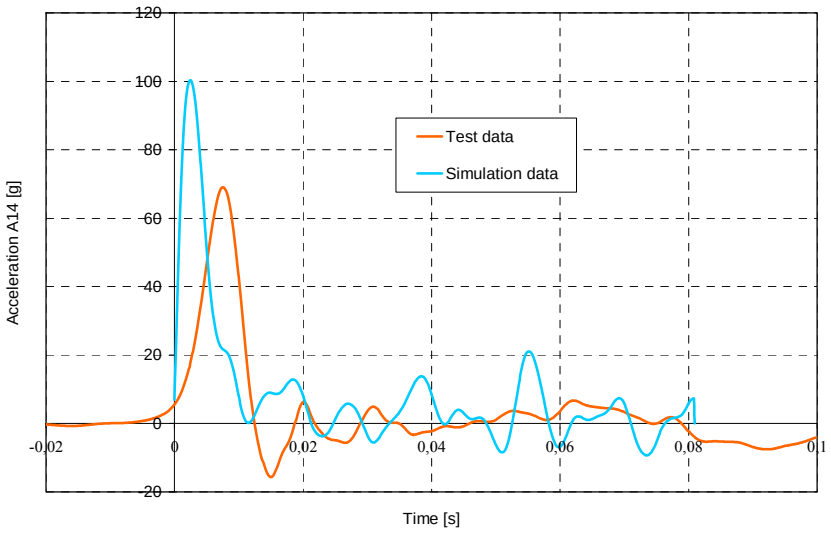

Figure E-9: Acceleration time histories on the cabin floor STN 450F, WL –802, BL 0 (location A14)

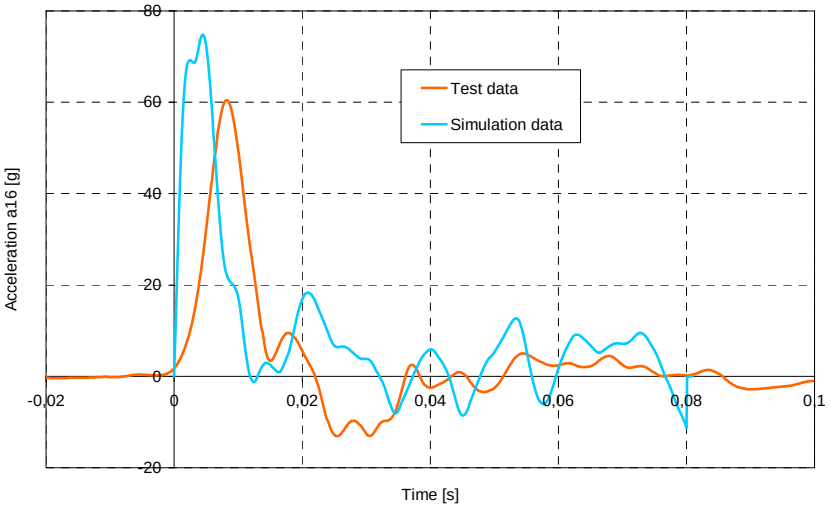

Figure E-10: Acceleration time histories on the cabin floor STN 1710F, WL –802, BL 0 (location A16)

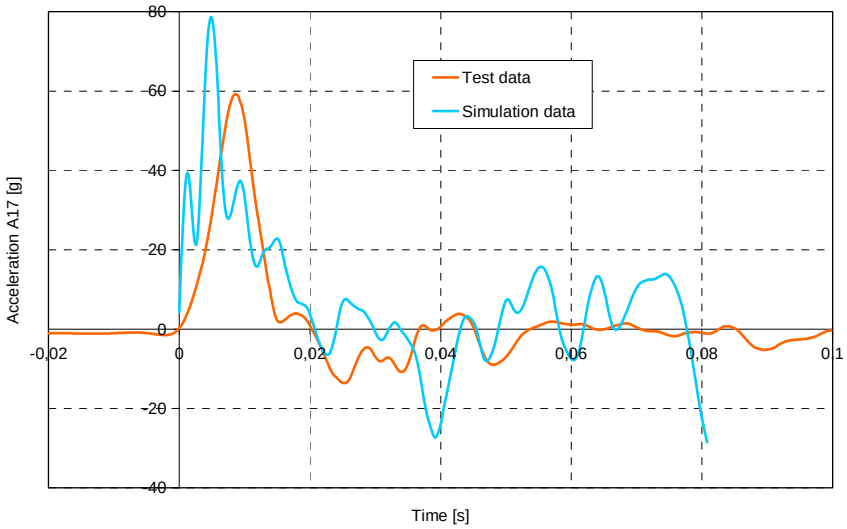

Figure E-11: Acceleration time histories on the cabin floor STN 1710F, WL –802, BL -830 (location A17)

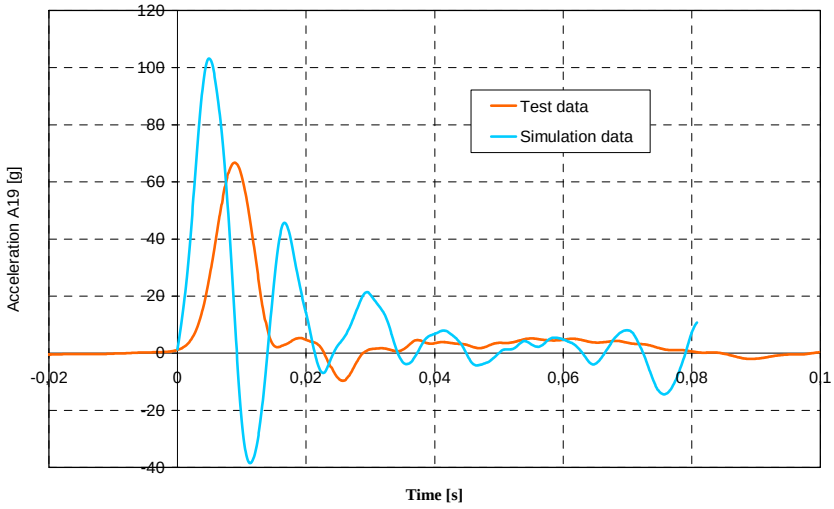

Figure E-12: Acceleration time histories on the co-pilot floor (location 19)

Figure E-13 shows the position of the pressure transducers on the skin. They are located directly under frames, which corresponds to a stiff location in the structure. Based on the statements made in § 5.1.1.3 concerning the simulation of the sub-floor structure impacting on water, an overestimation of the pressure peak is expected in the simulation. This is confirmed by Figures E-14 to E-22, which depict the comparison between pressure time histories measured and calculated on the skin. Only the graphs not reported in § 5 are shown in this Appendix. The same filter (CFC180) as for the test data is used for the calculated data. It can be observed that the pressure transducers P3, P7, P9 and P10 are defective shortly after the impact.

In the test, the pressure maxima are slightly higher on the port side (BL. 800) than on the starboard side (BL -800). This is in agreement with the statements made for the accelerometers, which show higher acceleration peaks on the port side than on the starboard side.

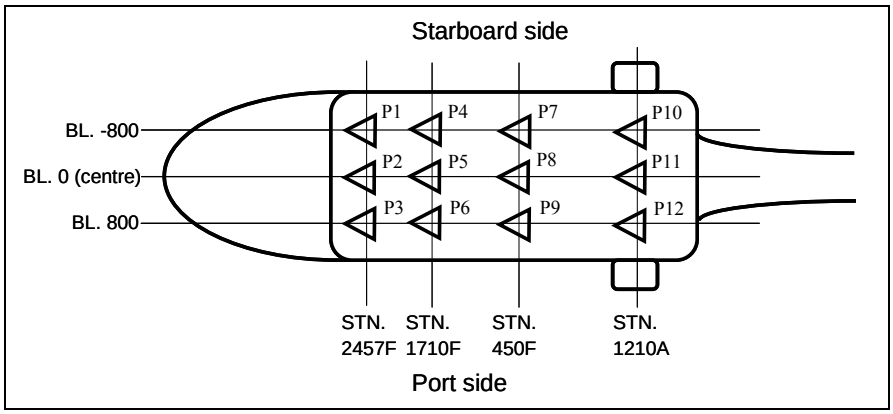

Figure E-13: Position of the pressure transducers on the skin of the helicopter (upper view, not in scale)

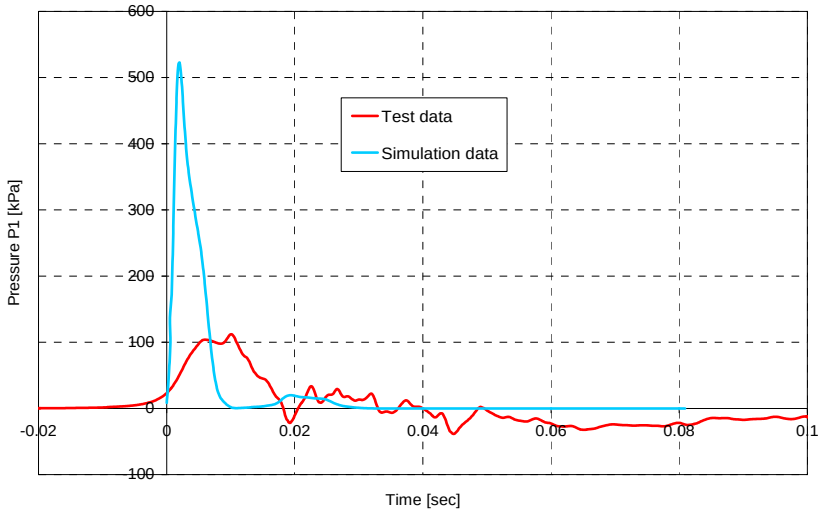

Figure E-14: Calculated and measured pressure time histories at location P1 (STN 2457F, BL -800)

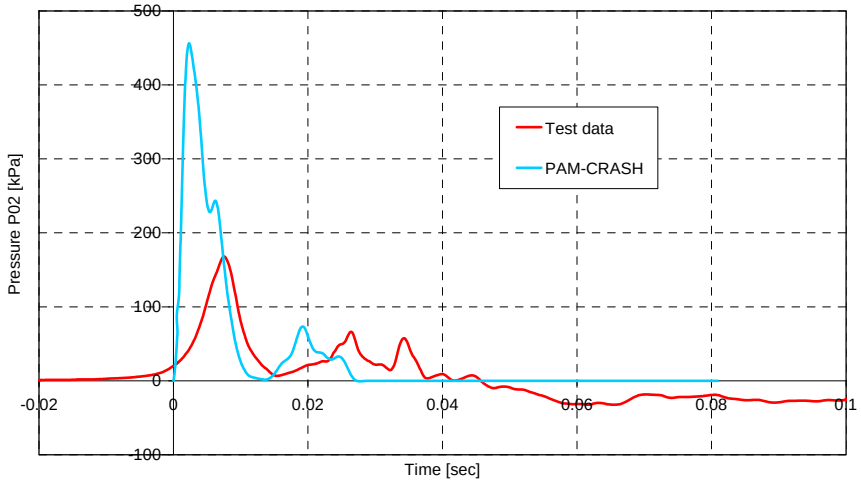

Figure E-15: Calculated and measured pressure time histories at location P2 (STN 2457F, BL 0)

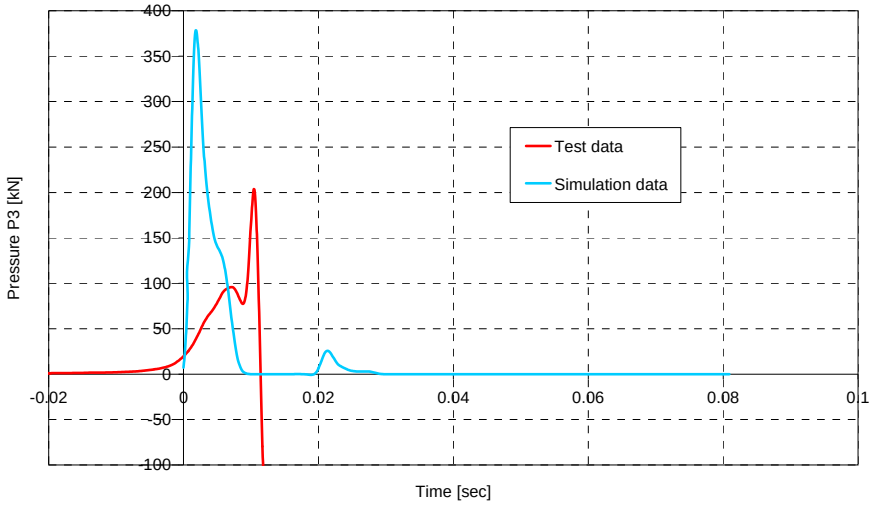

Figure E-16: Calculated and measured pressure time histories at location P3 (STN 2457F, BL 800)

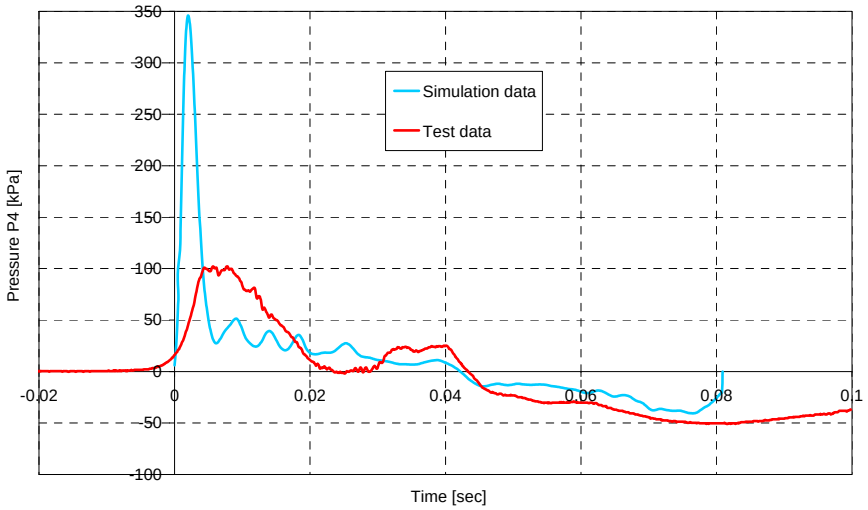

Figure E-17: Calculated and measured pressure time histories at location P4 (STN 1710F, BL -800)

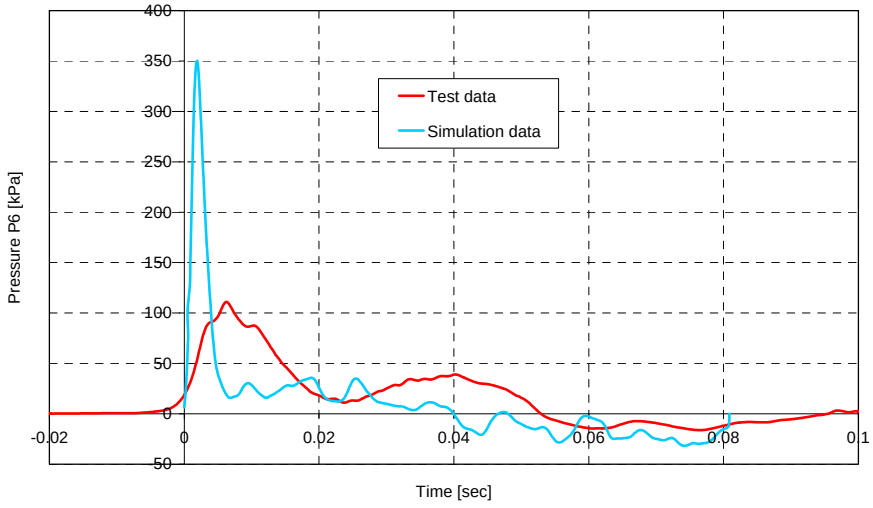

Figure E-18: Calculated and measured pressure time histories at location P6 (STN 1710F, BL 800)

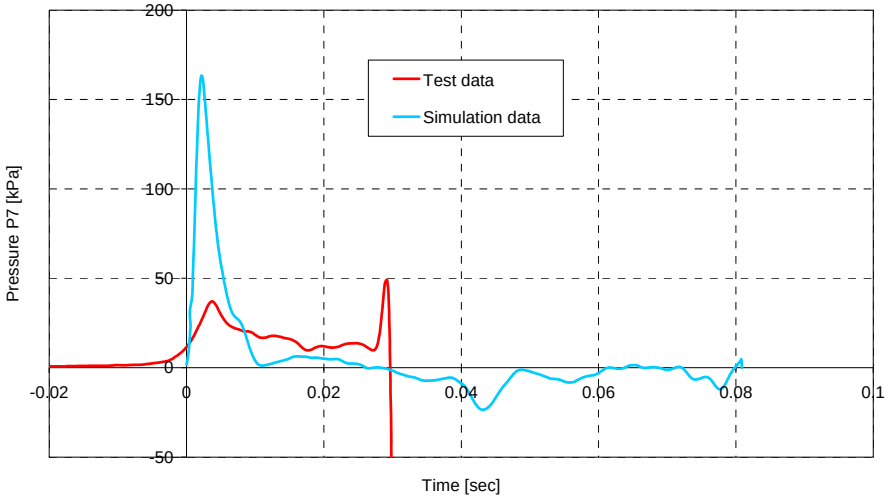

Figure E-19: Calculated and measured pressure time histories at location P7 (STN 450F, BL -800)

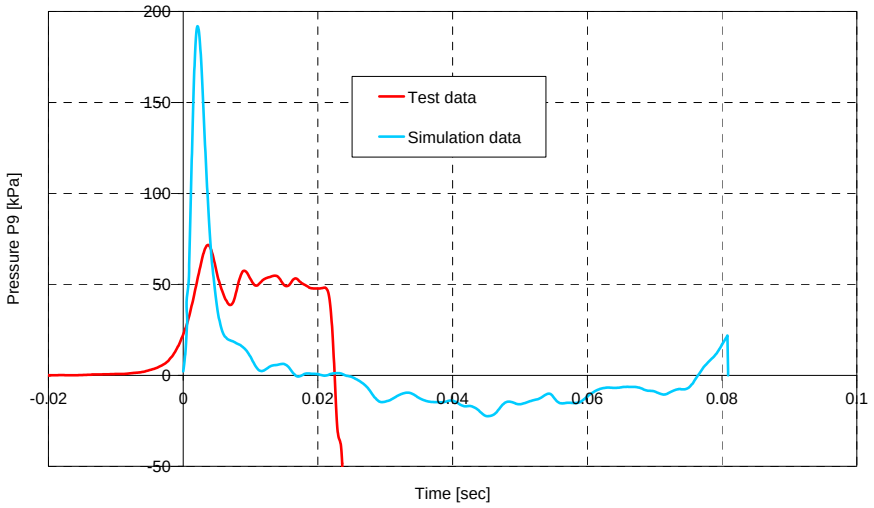

Figure E-20: Calculated and measured pressure time histories at location P9 (STN 450F, BL 800)

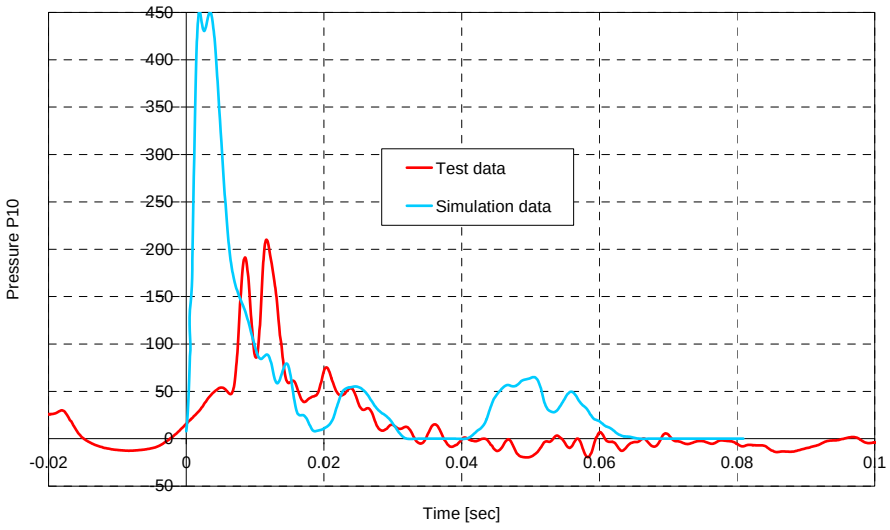

Figure E-21: Calculated and measured pressure time histories at location P10 (STN 1210A, BL -800)

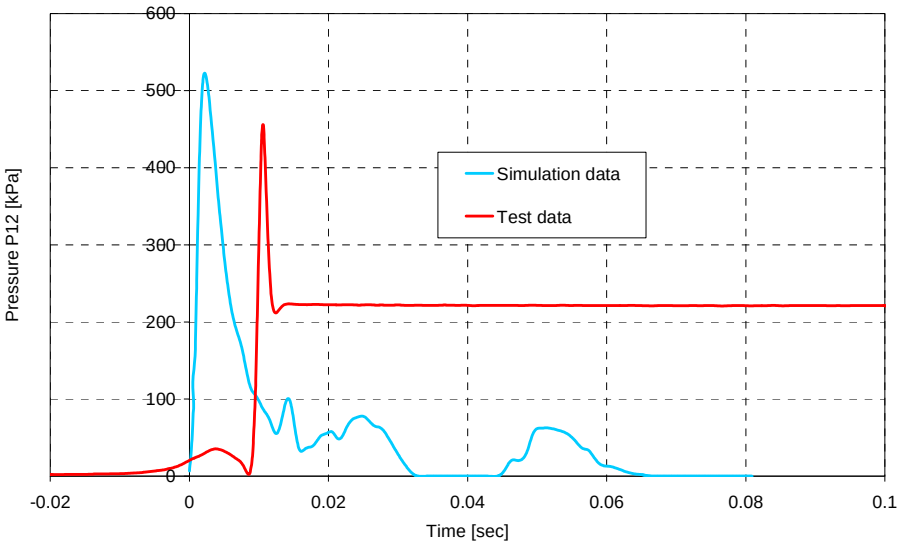

Figure E-22: Calculated and measured pressure time histories at location P12 (STN 1210A, BL 800)

Bibliography

[1] Westland Helicopters Limited, “An analysis of the response of helicopter structures to water impact”, Stress department report SDR156, CAA contract 7D/S/915, March 1995

[2] Pentecote, N., Vigliotti, A. “Crashworthiness of helicopters on water: Test and simulation of a full-scale WG30 impacting on water”, Int. J. of Crashworthiness, Vol. 8, No. 6, pp. 559-572, 2003

[3] “Room to improve”, Flight International, pp 36-42, 22-28 July 2003

[4] Johnson, D., “Study on Transport Airplane Unplanned water contact”, Report No. DOT/FAA/CT-84/3, Federal Aviation Administration, Technical Center, Atlantic City, January 1984

[5] Patel, A.A., Greenwood, R.P.Jr., „Transport Water Impact and Ditching performance“, Report No. DOT/FAA/AR-95/54, March 1996

[6] -, http://aviation-safety.net, 2006

[7] - “I may have to ditch this aircraft”, Air Disaster, Volume 1, Chapter 8, pp 67-73, 1994

[8] - “Summary Report on Helicopter Ditching and Crashworthiness Research”, CAA PAPER 2005/06, Civil Aviation Authority, Safety Regulation Group, December 2005

[9] Westland Helicopters Limited, “A review of UK Military and World Civil Helicopter Water Impacts over the Period 1971-1992”, Stress department report SDR146, November 1993

[10] Civil Aviation Authority, Review of Helicopter Offshore and Survival (RHOSS), CAP 641, London, February 1995

[11] Mc Bride E.E., Fisher L.J., “Experimental Investigation of the Effect of Rear-fuselage shape on ditching behaviour”, National Advisory Committee for Aeronautics, Technical Note 2929, Langley Aeronautical Laboratory, Langley Field, Virginia, April 1953

[12] Fisher L.L., Hoffman E.L., “Ditching Investigations of Dynamic Models and Effects of Design Parameters on Ditching Characteristics”, National Advisory Committee for Aeronautics, Technical Note 3946, Langley Aeronautical Laboratory, Langley Field, Virginia, February 1957

[13] Thompson, W.C., “Ditching investigation of a 1/30 Scale Dynamic Model of Heavy Jet Transport airplane”, NASA Technical Memorandum TM X-2445, National Aeronautics and Space Administration, February 1972

[14] Richards, M.K.; Kelley, E.A. “Development of a Water Impact dynamic Test facility and Crash testing a UH-1H Aircraft on a water Surface”, American helicopter society, 53rd Annual Forum, Virginia Beach, Virginia, May 25-May 27, 1999

[15] Federal Aviation Administration, “Transport Airplane Cabin Interiors Crashworthiness Handbook”, Advisory Circular AC25-17, pp. 401-403, 15 July 1991

[16] Federal Aviation Administration, “FARs Part 25 -- Airworthiness standards : Transport Category Airplanes”, Special Federal Aviation Regulation No. 13, 19 December 2000

[17] Federal Aviation Administration, “FARs Part 29 -Airworthiness Standards Transport Category Rotorcraft”, 7 August 2006

[18] Federal Aviation administration, “Certification of Transport Category Rotorcraft“, Advisory circular AC29-2A, Change 2, pp. 553-559, 24 September 1991

[19] Civil Aviation Authority, “Emergency Alighting on water”, British Civil Airworthiness Requirements, Paper No. G779, 7 October 1985

[20] Smith A.G., Warren C.H.E., Wright D.F., “Investigations of the Behaviour of Aircraft When Making a Forced Landing on Water (Ditching)”, Aeronautical Research Council, Reports and Memoranda No. 2917, 1957

[21] Fisher, L.J., “Factors affecting ditching of new transport airplanes”, NASA-SP-270 pp 1-10, May 1971

[22] Goodwin, J.F., “DC-10 Airplane: Design Ditchability, Structural aspects”, Pacific Air Safety Search and Rescue Symposium, San Francisco, pp. 19-23, October 1968

[23] May, A. "water entry and the cavity running behaviour of missiles", AD-A020 429, SEHAE, Technical Report 75-2, 1975

[24] Korobkin, A.A. & Pukhnachov V.V. „Initial stage of water impact“, Ann. Rev. Fluid Mech. 20, pp. 159-185, 1988

[25] Zukas, J. A. „ Impact dynamics“, Krieger Publishing Company, (1982), reprint edition 1992

[26] Troesch, A.W., Kang, C.-G. “Hydrodynamic Impact Loads on Three-Dimensional Bodies”. In 16th Symposium on Naval Hydrodynamics, Berkeley CA, 1986

[27] Verhagen, J.H.G. “The impact of a flat plate on a water surface”, J. Ship Res. 11, pp. 211-223, 1967

[28] Lewison, G.R.G. “On the reduction of slamming pressures”, Trans. RINA 112, pp. 285-306, 1970

[29] Troesch, A.M.; Kang C.-G. “Evaluation of Impact Loads Associated with Flare Slamming”, Spring Meeting/STAR Symposium/3rd IMSDC, Pittsburgh, Pennsylvania, June 8-10, 1988

[30] Zhao, R., Faltinsen, O. “Water entry of two-dimensional bodies”, J. Fluid Mech., Vol. 246, pp. 593-612, 1993

[31] Le Méhauté, B. “An introduction to hydrodynamics and water waves”, Springer Verlag, 1976

[32] Newman, J.N. “Marine hydrodynamics”, The Massachussetts Institute of Technology, MIT Press, 1977

[33] Wang, M.L., Troesch, A.W., Maskew, B. “Comparisons of two different mixed Eulerian-Lagrangian Schemes Based on the Study of Flare-Slamming Hydrodynamics”. In: Transactions of the ASME, Vol. 118, Aug. 1996

[34] Von Karman, Th. "The impact on seaplane floats during landing", NACA TN-321, October 1929

[35] Wagner H. „Über Stoß- und Gleitvorgänge an der Oberfläche von Flüssigkeiten“. In: Zeitschrift für angewandte Mathematik und Mechanik, 1932

[36] Collopy, F.H. "Determination of the water impact shock environment". In Shock and Vibration Bulletin 35, Part 7, April 1966

[37] Shiffman, M., Spencer, D.C. “The force of impact on a cone striking a water surface (vertical entry)”, Communication on Pure and Applied Mathematics, Vol. 4, pp. 379-417, 1951

[38] Fabula, A. G. “Ellipse fitting approximation of two-dimensional, normal symmetric impact of rigid bodies on water”, In: proceedings of 5th Mid-Western Conference on fluid mechanics, Univ. of Michigan, 1957

[39] Cointe, R., Armand, J.L. “Hydrodynamic impact analysis of a cylinder”, ASME J. Offshore Mech. Arc. Engng, Vol. 109, pp. 237-243, 1987

[40] Cointe, R. “Two-dimensional water-solid impact”, ASME J. Offshore Mech. Arc. Engng, Vol. 111, pp. 109-114, 1989

[41] Howison, S.D., Ockendon, J.R., Wilson, S.K. “Incompressible water-entry problems at small deadrise angles”, J. Fluid Mech., Vol. 222, pp. 215-230, 1991

[42] Donguy, B. “Etude de l’interaction fluide structure lors de l’impact hydrodynamique”, Ecole Centrale de Nantes, PhD, 2002

[43] Greenhow, M. “Water-entry and -exit of a horizontal circular cylinder”, Applied ocean research, vol. 10, No. 4, pp. 191-198, 1988

[44] Greenhow, M.; Yanbao, L. “Added masses for circular cylinders near or penetrating fluid boundaries - review, extension and application to water entry, -exit and slamming”, Ocean engineering, Vol. 14, No. 4, pp. 325-348, 1987

[45] Lamb, H., “Hydrodynamics”, Dover Publication, 1945

[46] Moghisi, M., Squire, P.T. “An experimental investigation of the initial force of impact on a sphere striking a liquid surface”, J. Fluid Mechanics, Vol. 108, pp. 133-146, 1981

[47] Shiffman, M & Spencer D.C. “The flow of an ideal incompressible fluid about a lens”. In: Quart. Appl. Math. 5, pp. 270-288, 1947

[48] Miloh, T. “Wave slam on a sphere penetrating a free surface”, J. Engineering Mathematics, Vol. 15, No. 3, pp. 221-240, 1981

[49] Wilson, S. “The mathematics of ship slamming”, PhD, University of Oxford, 1989

[50] Korobkin, A. “Wave impact on the bow end of a Catamaran wet deck”, Journal of Ship Research, Vol. 39, pp. 321-327, 1995

[51] Lützenburger, M. “Generation of an A320 Full Aircraft Stick Model and Simulations Using the Hybrid Code KRASH”, Institute of Structures and Design, Stuttgart, IMT Program “Crashworthiness for Commercial Aircraft”, Contract No. AER2-CT92-0030, March 1996

[52] - “DRI-KRASH: THEORY ADDENDUM, APPENDICES”, Krash version 9601, Dynamic Response Inc. Sherman Oaks, CA. 91403, January 1996

[53] Mercier, J.A. “Impact Loads on warped planing surfaces landing on smooth and rough water”, Report SIT-DL-71-1514, Davidson laboratory, Stevens Institute of Technology, Castle Point Station, Hoboken, New Jersey 07030, March 1971

[54] Brown, P.W. “Seaplane Impact theory” Short Brothers and Harland Limited, Hydrodynamics Notes No. 46, August 1954

[55] - “DRI-KRASH Users Manual Input format - Krash Version 9601”, Dynamic Response Inc, Sherman Oaks, CA. 91403, July 1997

[56] Wittlin, G., Schultz, M., Smith, M.R. „Rotary wing aircraft water impact test and analyses correlation“, American Helicopter Society, 56th annual Forum, Virginia Beach, Virginia, May 2-4, 2000

[57] Wittlin, G., Gamon, M. “Ditching analysis Using DRI-KRASH”, 2000

[58] Martin, Y., Sarlin, P., Demoulins, J.F., Garbay, Ph. “Helicopters and Aircraft Ditching: Ways to Modelling of Floatation Systems and Structural Loading Evaluation”

[59] Carden, H.D., Fasanella, E.L., Jones, L.E. “Analysis of the Space Shuttle Orbiter Skin Panels under Simulated Hydrodynamic Loads”, NASA Langley Research Center Hampton, NASA Technical Memorandum 4082, 1988

[60] Ghaffari,F. “An analytical Method for ditching analysis of an airborne vehicle”, NASA Langley Research Center Hampton, NASA Contractor Report 4120, February 1988

[61] Adler, C.O., Coopersmith, M. “Development of a hydrodynamic free surface capability in a low order aerodynamic panel method”, AIAA-95-1910-CP, AIAA 13th Applied Aerodynamics Conference, San Diego, CA, June 19-22, 1995

[62] Souli, M., Ouashine, A., Lewin, L. “ALE formulation for fluid-structure interaction problems”, Computer Methods in Applied Mechanics and Engineering, 190, pp. 659-675, 2000

[63] Aquelet, N., Souli. M., Gabrys, J., Olovson, L. ”A new ALE formulation for sloshing analysis”, Vol. 16, No. 4, Structural Engineering and Mechanics, pp. 423-440, 2003

[64] Souli, M. “LS-DYNA ALE and Fluid-Structure Interaction”, Seminare, CAD-FEM GmbH, Leinfelden-Echterdingen, 17-18 Juni 2004

[65] Zhong, Z.-H. “Finite Element Procedures for Contact Impact Problems”, Oxford Science Publications, 1993

[66] Aquelet, N: “Modélisation de l’impact hydrodynamique par un couplage fluide-structure″, Laboratoire de Mécanique, Villeneuve d’Ascq, PhD thesis, 2004

[67] Wagner, S. “Der Höchstleistungsrechner - Unverzichtbares Werkzeug zur numerischen Simulation der Strömungs-Struktur-Wechselwirkungen an Hubschrauberrotoren”, Sonderdruck aus Schriften der Sudetendeutschen Akademie der Wissenschaften und Künste Band 28, Forschungsbeiträge der Naturwissenschaftlichen Klasse, München, 2008

[68] Ribet, H. “Modélisation et simulation numérique en dynamique rapide d’interactions entre fluide et structure souple - Application à l’amerrissage d’un avion”, PhD thesis, Université Paul Sabatier de Toulouse, 1997

[69] Ribet, H., Laborde, P., Mahé, M. ”Numerical modelling of the impact on water of a flexible structure by explicit finite element method - Comparisons with Radioss numerical results and experiments”, Aerospace Science and Technology, No. 2, pp. 83-91, 1999

[70] Portemont, G. “Contribution au développement des méthodes numériques de traitement des interactions corps dur/corps mous - Application au Crash, aux collisions ou au chocs”, PhD, Université de Valenciennes et du Hainaut Cambrésis, January 2004

[71] Candy, E.G., Kirk, N.E., Murrell, P.J. “Airframe Water Impact Analysis”, American Helicopter Society, Proceedings of the National Crashworthiness Specialists’ Meeting, September 14-16, 1998

[72] -, “MSC-Dytran Version 4.0 User’s Manual”, The MacNeal-Schwendler Corporation (MSC), 1997

[73] Anghileri, M., Spizzica, A. "Experimental Validation of Finite Element Models for Water Impacts", Second International Krash Users' Seminar, Cranfiled Impact Centre Ltd, England, 26-28 June 1995

[74] Clarke, C.W., Shen, Y.-C, "The development of a rotorcraft water-impact analysis methodology", American Helicopter Society, Proceedings of the National Crashorthiness Specialist's meeting, Phoenix, Arizona, Spetember 14-16, 1998

[75] Sareen, A., Smith M.R., Hashish, E. "Crash Analysis of an Energy-Absorbing Subfloor During Ground and Water Impact, American Helicopter Society, 55th Annual Forum, Montréal, Quebec, Canada, May 25-27, 1999

[76] Vignjevic, R., Meo, M. "Simulation of helicopter under-floor structure impact on water", International Journal of Crashworthiness, Vol. 6, No. 3, 2001

[77] Souli, M., Zolesio, J.P. "Arbitrary Lagrangian-Eulerian and free surface methods in fluid mechanics", Computer Methods in Applied Mechanics and Engineering, Vol. 191, pp. 451-466, 2001

[78] "PAM-SCL™ (Solid Core Library) - Version 2000 - Theory notes manual", Pam System International, 2000

[79] Lucy, L.B. "Numerical approach to testing the fission hypothesis", Astronomical journal, 82, pp. 1013-1024, 1977

[80] Gingold, R.A., Monaghan, J.J. "Smoothed particle hydrodynamics: Theory and application to non-spherical stars", Monthly Notices of the Royal Astronomical Society, 181, pp. 375-389

[81] Monaghan, J.J. "Smoothed Particle Hydrodynamics", Annu. Rev. Astrophys. 30, pp. 543-574, 1992

[82] Stellingwerf, R.F., Wingate C.A., "Impact modelling with smooth particle hydrodynamics", Int. J. Impact Engng, Vol. 14, 1993, pp. 707-718

[83] Johnson, G.R., Stryk, R:A., Beissel, S.R. "SPH for high velocity impact computations", Comput. Methods Appl. Mech. Engrg., Vol. 139, 1996, pp. 347-373

[84] Kamoulakos, A., Groenenboom P. "Moving from FE to SPH for space debris impact simulations - experience with PAM-SHOCk", Proceedings European Conference on Space Structures, Materials and Mechanical Testing, Braunschweig, Germany, 4-6 November 1998

[85] Liu, G.R., Liu, M.B. "Smoothed Particle Hydrodynamics. A meshfree particle method", World Scientific Publishing, 2003

[86] Benz, W. “Smooth particle hydrodynamics: A review”, NATO Workshop, Les Arcs, France, 1989

[87] Monaghan, J.J., Gingold, R.A. “Shock simulation by the particle method SPH”, J. of computational physics, Vol. 52, 1983, pp. 374-389

[88] Fulk, D.A. “A numerical analysis of smoothed particle hydrodynamics”, Air Force Institute of Technology, Air University, AFIT/DS/ENC/94-1, Dissertation, September 1994

[89] Monaghan, J.J. “Interpolation from particles”, School of mathematical sciences, Monash University, Lecture note, 2004

[90] Wilbeck, J.S, “Impact behaviour of low strength projectiles”, AFML-TR-77-134, Air Force Material laboratory, Air Force Wright Aeronautical laboratories, Wright-Patterson Air Force Base, Ohio 45433, July 1978

[91] Heymann, F.J. “On the shock wave velocity and impact pressure in high speed liquid-solid impact”, Transation of the ASME, Series D, Vol. 90, July 1968, p 400

[92] “Introduction to MSC/DYTRAN”, Seminar Notes, The MacNeal-Schwendler Corporation, 1999

[93] Massey, B.S. “Mechanics of fluid”, 5th edition, Van Nostrand Reinhold (UK) Co. Ltf, 1983

[94] Monaghan, J.J. “Simulating free surface flows with SPH”, J. Computational physics, Vol. 110, no. 2, February 1994

[95] “Hydrodynamic Impact Analysis” EPRI (Electric Power Research Institue), NP-824, Projects 812-1, 2, 3 and 965-3, June 1978

[96] Bisplinghoff, R.L., Doherty, C.S. “A Two-Dimensional Study of the Impact of wedges on a Water Surface”. Massachusetts Institute of Technology, Contract No. Noa(s)-9921, 1950

[97] Rothermel, T. “Untersuchung der Smooth Particle Hydrodynamics Methode zur berechnung des Crashverhaltens von Hubschrauberstrukturen beim Aufprall auf nachgiebige Oberflächen“, Diplomarbeit, Institut für Statik und Dynamik, Universität Stuttgart, 2005

[98] CAST project “Crashworthiness of Helicopters on Water: Design of Structures Using Advanced Simulation Tools, funded by the European Union under the Aeronautics par of the GROWTH RTD programme (Contract G4RD-CT1999-01728)

[99] Pentecote, N., Vigliotti, A. « Simulation of the impact on water of a sub-floor component and a full-scale WG30 helicopter », American Society 58th Annual Forum, Montréal, Canada, June 11-13, 2002

[100] Pentecote, N., Kindervater, C.M., Arendts, F.J., “Airframe Water Impact Analysis”, CEAS Forum on “Crash Questions”, CIRA, Capua, Italy, 14-15 February 2000

[101] Vigliotti, A., Pentecote, N., Clifford, S. “Crashworthiness of rotorcraft on water: an experimental test campaign”, 28th European Rotocrfat Forum, Bristol, September 2002

[102] - “PAM-CRASH PAM-SAFE: Solver Notes Manual”, PAM System International, 2000

[103] - “Instrumentation for Impact Test, SAE Recommended Practice”, SAEJ211 OCT 88, The Engineering Society for Advancing Mobility Land Sea Air and Space, Revised October 1988

[104] Reichert, J.K.; Landolt, J.P. “Digital and Analog Filters for Processing Impact Test Data”, SAE Technical Paper Series 810813, Passenger Car Meeting, Dearborn, Michigan, June 8-12, 1981

[105] Kohlgrüber, D., Lützenburger, M. „Numerical simulation of Dynamic Test I“, Subtask 2-1-2.2 (IMT), DLR-IB 435-95/22, January 1996

[106] Lützenburger, M. “Simulation of the A320 Section drop test using the hybrid code DRI-KRASH”, Sub-Task 3.1 (IMT), DLR-IB 435-95/24, December 1995

[107] Pentecote, N., Kindervater, C.M. “Airframe water impact analysis using the local/global methodology”, American Helicopter Society 55th Annual Forum, Montréal, Québec, 25-27 May 1999

[108] McBride E.E. and Fisher L.J. 'Experimental investigation of the effect of rear-fuselage shape on ditching behaviour', NACA Technical Note 2929, Washington, April 1953

[109] Pentecote, N. “Ditching simulation: Investigation regarding CPU time, cavitation and ventilation”, DLR-IB 435-2003/3, Institut für Bauweisen- und Konstruktionsforschung, DLR Stuttgart, November 2003

[110] Climent, H., Benitez, L., Rosich, F., Rueda, F., Pentecote, N. “Aircraft ditching numerical simulation”, 25th International Congress of the Aeronautical Sciences, ICAS 2006, Hamburg, 3-8 September 2006

Nathalie Renée Solange TOSO née PENTECOTE,
born on August 1st 1971 in Saint-Dié, France

Education

1994 Engineer Diploma from "Fondation EPF - Ecole d'ingénieurs" with specialisation in aeronautics and space

1994 Thesis "optimization of an ultra-lightweighted mirror" at the Institute of Aircraft Design, University of Stuttgart

1993-1994 one year study at the University of Stuttgart, Fakultät der Luft-und Raumfahrt

1989 Baccalauréat scientifique (equivalent to A-level in Mathematics, physics and chemistry)

Experience

2000-2008: Research scientist at the "German Aerospace Center" in Stuttgart (DLR, Deutsches Zentrum für Luft- und Raumfahrttechnik)
Investigation of the impact on water of various helicopter structures within the EU project CAST ("Crashworthiness of Helicopters on Water: Design of Structures Using Advanced Simulation Tools" 2000-2004), PhD "Modellierung und Simulation von Wasseraufprall auf Flugzeugstrukturen/Contribution to the Modelling and Simulation of Aircraft Structures Impacting on Water", application of the developed methodologies for industrial applications, numerical investigation of composite behaviour in future aircraft components under high velocity impact.

1997-2000: Research Scientist as "Jungwissenschaftlerin" (young scientist) at DLR sponsored jointly by DLR Stuttgart and DASA (Deutsche Aerospace)
Evaluation and optimisation of the energy absorption capabilities of an aircraft sub-cargo floor within the EU project CRASURV ("Commercial Aircraft Design for Crash Survivability" 1997-2000), first investigations of the impact on water of aeronautical structures.

1994-1997: Scientific assistant at Institute of Aircraft Design, University of Stuttgart
Static studies of components of the ICARÉ I, the solar powered aircraft of the University of Stuttgart, investigations on a pre-development design tool for aircraft including structure, performances and costs.

Grants and awards

Sept. 1996: Amelia Earhart Award from the Zonta International Foundation Committee (Chicago)

July 1996: Hermann-Reissner grant from the Fakultät der Luft- und Raumfahrttechnik, University of Stuttgart

Oct. 1995-July 1996: DAAD fellowship from Deutschen Akademischen Austauschdienst (German Academic Exchange Service)